UNIVERSITÀ
DEGLI STUDI
DI PADOVA

University of Padova

Department of Chemical Sciences

Doctoral Course in Science and Engineering of Materials and Nanostructures

CICLO XXXII

Synthesis and characterization of materials for PEM-FC, based on Pt alloyed nanoparticles supported on next generation mesoporous carbon.

Director: Ch.mo Prof. Giovanni Mattei

Supervisor: Prof. Christian Durante

Student: Brandiele Riccardo

Index

1 Figures Index

2 Tables Index

3 Abstract

Proton Exchange Membrane (PEM) Fuel Cells are a promising technology for the clean energy production, especially in the automotive field. Actually, the main commercial catalysts employed in this system are based on Pt Nanoparticles supported on high surface area Carbon. The main issues associated to PEM Fuel Cells deal with the sluggish kinetic of oxygen reduction (ORR) at Platinum based electrode, with the low stability of both the carbon support and the metal phase, that tend respectively to oxidize and dissolve or diffuse and with the high cost due to rare and expensive Pt. In fact, nowadays high costs and low durability are the two factors that make PEM fuel cells still not competitive with internal combustion engine. For these reasons, research now focuses on obtaining more stable material with higher performances toward ORR. Two strategies are possible to improve catalyst for oxygen reduction. The first one deals with the enhancing of Pt activity modifying its electronic properties by alloying Pt with other transition metal (ligand effect) or by reducing the Pt-Pt distance (geometric effect). In both cases a Pt d-band shift occurs, which is responsible for the modification of adsorption and desorption energies of all species involved in ORR and has as a direct consequence a modulation in the electrochemical activity. The second strategy deals with the utilization of supports more stable respect to corrosion, like graphene, carbon nanotubes or mesoporous carbons. Furthermore, doping of carbon support with heteroatoms like N or S, can help to stabilize the metal nanoparticles. In fact, doping creates homogeneous and narrow dispersion of small metallic nanoparticles, strongly bound to the surface of carbon support and with a higher resistance to agglomeration. Furthermore, doping has as well an influence on the electronic structure of the Pt catalyst, resulting in a modulation of its electrochemical activity. Doping is not beneficial only in noble-metal catalyst but may also modify properties of the carbon support in which heteroatoms are present. Wettability, electrical conductivity and electrochemical activity are generally boosted when heteroatoms are inserted in carbonaceous substrates such as carbon blacks (CBs).

The topics of this PhD thesis are Platinum NPs on doped carbon and Platinum-Yttrium alloy NPs on carbon.

The goal consists in the understanding how the different synthesis parameters can influence the Pt-Y alloy formation and can modify the NPs growing. An increment of interact means increasing the electrochemical performance vs. the Oxygen Reduction Reaction (ORR). The Platinum deposition investigation is conducted via solid state reduction of several Platinum and Yttrium salts, in order to find the best conditions which, allow to have a good Pt NPs distribution over all surface of the carbon support. The synthetized Pt_xY@C catalysts are characterized by TEM, SEM, ICP, XRD, XPS and TGA techniques. Cyclic Voltammetry in steady conditions and with Rotating Disk Electrode are employed for the determination of electrochemical surface area (ECSA) and catalytic activity toward ORR, respectively, and compared to a commercial Pt/C catalyst.

The catalytic activity of pure platinum can be increase by interaction with heteroatoms which permits to modify the absorption energy of oxygen and increase the Oxygen Reduction Reaction rate. The typical heteroatoms which interact very strongly with the platinum are sulphur and nitrogen. Platinum on nitrogen doped carbon was synthetized via solid state synthesis using particular platinum complex which contain nitrogen ligand. The goal consists in the synthesis of catalysts with a nitrogen surface distribution very close to the platinum NPs for increasing the Pt-N interaction and so for increasing the electrochemical performance.

The metal-support interactions (MSI) between sulphur doped carbon and Pt nanoparticles (NPs) were investigated, for understanding how sulphur functional groups can improve the electrocatalytic activity of Pt NPs towards the oxygen reduction reaction (ORR). Sulphur doped carbons were synthetized by hard template method, tailoring the density of sulphur functional groups, and Pt NPs were deposited by thermal reduction of $Pt(acac)_2$. The metal-support interaction was evaluated and proved by X ray photoelectron spectroscopy and X ray diffraction, the analysis revealed a strong electronic interaction between Pt and S proportional to the density of sulphur group. The combination between the micro-strain and the electronic effects resulted in a high catalytic activity of Pt NPs vs. ORR, showing a correlation of the electrochemical activity with the sulphur content in the carbon support. Sulphur affords a clear metal support interaction between Pt NPs and the doped carbon support; the NPs dimension and distribution are influence by heteroatom concentration in the support but especially by the morphology (in terms of surface area, pore dimension and pose distribution) of the carbon matrix. The surface area of sulphur doped carbon was modify by steam treatment. The carbon matrixes were completely physic-chemical characterized with TEM, Raman BET, AE. The platinum NPs were deposited by high temperature solid state synthesis with $Pt(acac)_2$ using a temperature of 300 °C for 3 h and 8% H_2. XPS, XRD and N_2 Adsorption/Desorption analysis show a double correlation between the electrochemical activity and the sulphur concentration and the carbon morphology.

3.1 Reading Guide

- ***Chapter 1***: The chapter introduce the thesis arguments, in particular the different types of Fuel Cell. The Fuel Cell are distinguished based on the working condition such as the electrochemical reaction or the electrolyte or the catalyst. The chapter describe the pros and cons of the main Fuel Cells. In the second part, the Proton Exchange Membrane Fuel Cell is totally described from the reactions in the anodic and cathodic compartment to the Fuel Cells assembling.
- ***Chapter 2***: The chapter explain the Oxygen Reduction Reaction, in particular is focused on the different mechanisms in acid and alkaline electrolyte. In the second part the OR Reaction is evaluated considering a PGM and a non-PGM catalysts. The PGM and non-PGM material catalysed the ORR with a different mechanism, in the final part the different intermediates are explained.
- ***Chapter 3***: The purpose of this part is explaining the different way act to improve the catalytic activity of a platinum based material. The main problem for the PGM catalysts is the cost the platinum, so different methods are developed for increase the catalytic activity and reduce the mass loading on the catalysts. The chapter evaluate the influence of the dimension and shape of platinum NPs on the catalytic activity.
- ***Chapter 4:*** The chapter explain the techniques used for characterized the catalysts from a theoretical point of view. Electrochemical Techniques, TGA, TEM, SEM, XRD, ICP-MS and Nitrogen Adsorption/Desorption Analysis are fundamental for evaluated a platinum based materials. The chapter briefly describes the theory of these techniques.
- ***Chapter 5***: The chapter connect the characterization technique explain in the previous chapter to the platinum based material. The purposes are explained which result are possible obtained in each technique, and how interpret the results. The different techniques are evaluated considering the analysis on a platinum based materials.
- ***Chapter 6***: The chapter describe the synthesis of the carbon used as NPs support and the platinum NPs deposition. The carbon supports are synthetized by hard template method using different carbon precursors and/or silica. The Platinum NPs are deposited in a tubular furnace at high temperature and in a reduction atmosphere. The chapter show the synthesis procedure and the main parameters which influence the properties of the resulting materials.
- ***Chapter 7***: The chapter describe the synthesis and the characterizations of a Platinum NPs on nitrogen mesoporous carbon catalyst. The catalysts show an high interaction between the platinum NPs and the nitrogen group due to the, particular, platinum precursors. The catalysts are fully characterized with EC techniques, TGA, XPS and XRD to evaluated how the nitrogen groups can modify the platinum catalytic activity vs. ORR. The resulting materials show the increment of the catalytic activity with the increment of the interaction Pt-N.

- ***Chapter 8***: Sulphur as nitrogen show a strong impact on the carbon support conductibility and can prevent the platinum NPs aggregation. Sulphur concentration and surface area show an influence on the platinum catalytic activity, in the chapter 8, the influence of these parameters on the catalytic activity vs. ORR are evaluated. The catalysts show an increment of the catalytic activity with the increment of heteroatoms and show a double correlation between the Surface Area and the sulphur concentration.
- ***Chapter 9***: An innovative platinum based material which show a high catalytic activity vs. the Oxygen Reduction Reaction is the platinum alloy catalysts. The chapter describe the influence the synthesis temperature, platinum and yttrium precursors and the carbon support on the alloy formation and on the catalytic activity. The catalysts are fully characterized to understand the influence of the synthesis parameters on the Pt NPs dimension and on Platinum crystallography.
- ***Chapter 10***: Platinum and Palladium NPs were synthetized with Laser Ablation; the chapter show an innovative method for the synthesis of metal NPs applied in the ORR catalysis. The NPs show particular behaviour during the electrochemical characterization due to the core-shell structure, the catalyst was fully characterized for understand the influence of the NPs structure on the catalytic activity vs. the Oxygen Reduction Reaction.

1 Introduction

With the global population swelling and industrialisation on the rise in developing nations, humanity's hunger for energy has reached unprecedented levels. Half of electric energy comes from fossil fuels extracted from deep within the Earth's crust. It is estimated that since commercial oil drilling began in the 1850s, we have sucked up more than 145 billion tonnes for oil to automotive, fuel our power stations and heat our homes. Burning of coal, oil and gas has been inextricably linked to the rising levels of greenhouse gases in the atmosphere and is a leading contributor of climate change [1].

Figure 1: Impact of pollution; industry to produce textile fibers for car seats.
Data Source: https://www.nationalgeographic.com/environment/2018/09/news-air-quality-brain-cognitive-function/

The world's scientists agree that we are on a path towards disaster that can only be stopped by weaning ourselves of our fossil fuel habit. At today, around a fifth of the world's primary energy supply already comes from renewable sources such as hydrothermal, solar, wind and geothermal. Electricity produced from RES (renewable energy sources**)** is available only when the sun shines or the wind blows: RES energy supply fluctuates significantly and does not match energy demand [2]. If we want a shot at transitioning to renewable energy, we'll need one crucial thing: technologies that can convert electricity from wind and sun into a chemical fuel for storage and vice versa. Commercial devices that do this exist, but most are costly and perform only half of the equation. Now, researchers have created lab-scale systems that do both jobs. If larger versions work as well, they would help make it possible or at least more affordable to run the world on renewables. Some utilities are beginning to install massive banks of batteries in hopes of storing excess energy and evening out the balance sheet. But batteries are costly and store only enough energy to back up the grid for a few hours at most. Another option is to store the energy by converting it into hydrogen fuel. Devices called electrolysers do this by using electricity ideally from solar and wind power to split water into oxygen and hydrogen gas, a carbon-free fuel. A second set of devices called fuel cells can then convert that hydrogen back to electricity to power cars, trucks, and buses, or to feed it to the grid.

The fuel cell is one of the most promising sources of renewable energy. They can be considered as green power because they are environmentally clean, have low emission of NO_x and SO_x [3, 4]. In addition, they can provide energy in a controlled way with higher efficiency than conventional power plants. Fuel cells can be used in a wide range of applications, including transportation, material handling, stationary, portable, and emergency backup power applications. Fuel cells have several benefits over conventional combustion-based technologies currently used in many power plants and passenger vehicles. Fuel cells can operate at higher efficiencies than combustion engines and can convert the chemical energy in the fuel to electrical energy with efficiencies of up to 60%. Fuel cells have lower emissions than combustion engines. Hydrogen fuel cells emit only water, so there are no carbon dioxide emissions and no air pollutants that create smog and cause health problems at the point of operation. Also, fuel cells are quiet during operation as they have fewer moving parts Increasing the local capacity of the FCH sector is an attractive option to tap into a growing market, drive local economic growth and create new jobs. In the German state of Baden-Württemberg, for example, the potential value added by the FCH sector is estimated at around EUR 680 million through 2030 [5]. Opportunities for local economic growth arise along the entire FCH value chain. In the long term, a large international market is expected to evolve that is projected to create 30 million jobs and USD 2,000 billion in annual sales worldwide by 2050.

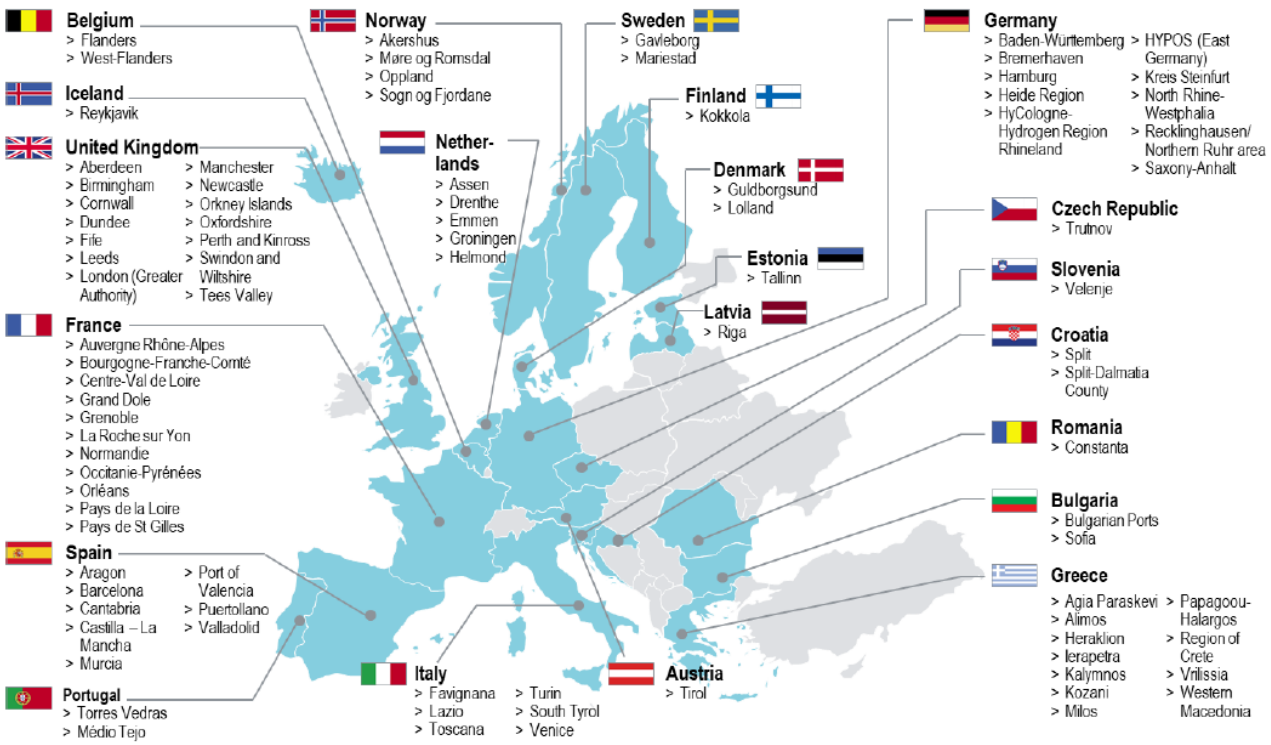

Figure 2: Overview of participating regions and cities in "Fuel Cell in Bus", December 2018.

Data Source: http://www.hydrogenfuelnews.com/h2-mobility-opens-new-hydrogen-fuel-station-in-germany/8534212/

1.1 Fuel Cell

There are five types of fuel cells being known or available on the market. All devices have the same basic design and structure, but different chemicals are used as the electrolyte or the input (in the anodic and cathodic compartments) fuel (Figure 3). Others important differences between the fuel cell are the working temperature and the anodic/cathodic catalyst [6].

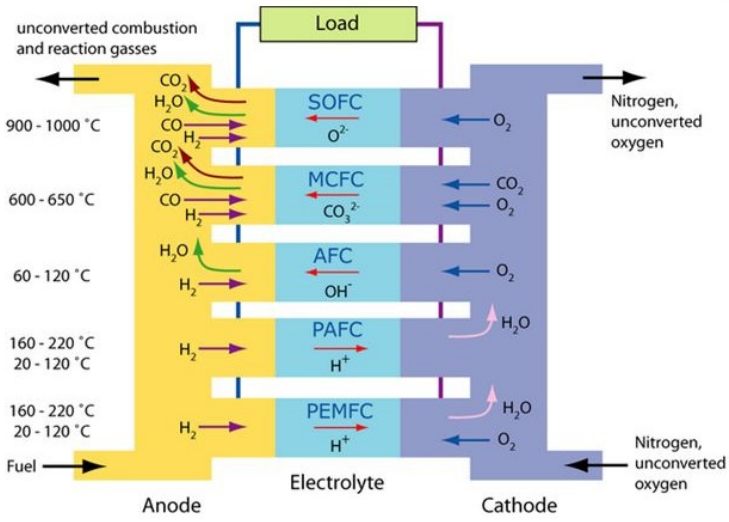

Figure 3: Operating mechanisms of the main fuel cells and working condition

Data Source: https://www.doitpoms.ac.uk/tlplib/fuel-cells/types.php

The main fuel cells are: Alkaline Fuel Cell (AFC), Phosphoric Acid Fuel Cell (PAFC), Molten Carbonate Fuel Cell (MCFC), Solid Oxide Fuel Cell (SOFC) and Proton Exchange Membrane Fuel Cell (PEMFC).

(1) Alkaline fuel cells (AFCs) were one of the first fuel cell technologies developed in the U.S. Space Program to produce electrical energy and water on spacecraft (1960, Apollo Mission). These fuel cells use an aqueous solution of Potassium hydroxide (KOH) as the electrolyte and can use a variety of non-precious metals as a catalyst at the anode and cathode compartments (Nickel or Cobalt). In recent years, novel AFCs that use a polymer membrane as the electrolyte have been, successfully developed [7]. The alkaline fuel cells are closely related to conventional PEM fuel cells, except the electrolyte solution. These devices also demonstrated efficiencies above 60 %, only, in space applications. The high performance of AFCs is due to the rate at which electro-chemical reactions take place in the anodic and cathodic compartment. The typical operating temperatures are around 70 °C, but the optimal operating range is 90 °C – 100 °C [8]. Generally, the AFC work at a temperature lower than the optimal one to preserve the structure, even the conversion efficiency decrease. A key challenge for this fuel cell type is that it is susceptible to poisoning by carbon dioxide (CO_2). In fact, even the small amount of CO_2 in the air can dramatically affect cell performance and durability due to carbonate formation. Alkaline cells with liquid electrolytes can work in

a recirculating mode, which allows for electrolyte regeneration to help reduce the effects of poisoning in the electrolyte. The liquid electrolyte systems also suffer from additional concerns including wettability, increased corrosion, and difficulties handling differential pressures. The advantages are the faster cathodic reaction in alkaline solution, which leads to high performance and the low cost of the component. AFCs are being considered for applications in the W to kW scale, the stack size produces and power of 10 kW - 100 kW [9, 10]. Challenges for AMFCs include tolerance to carbon dioxide, membrane conductivity and durability, higher temperature operation, water management, power density, and anode electrocatalysis.

(2) Phosphoric acid fuel cells (PAFCs) use liquid phosphoric acid (H_3PO_4) as electrolyte, the electrolyte is contained in a Teflon-bonded silicon carbide matrix. The typical catalysts for Phosphoric acid fuel cells are platinum based material, which is generally used in both anodic and cathodic compartments. The PAFC is considered the "novel generation" of modern fuel cells. It is one of the most mature cell types and the first to be used commercially. This type of fuel cell is typically used for stationary power generation, but some PAFCs have been used to power large vehicles such as city buses. PAFCs are more tolerant of impurities in fossil fuels that have been reformed into hydrogen than for example Proton Membrane Fuel Cells, which are easily "poisoned" by carbon monoxide (carbon monoxide binds to the platinum catalyst at the anode, decreasing the fuel cell's efficiency) [11]. PAFCs are more than 85% efficient when used for the generate electricity and heat but they are less efficient at generating only electricity (37% - 42%). PAFC efficiency is only slightly more than that of combustion based power plants, which typically operate at around 33% efficiency. The PAFCs operate at high temperatures of around 180 ºC, the optimal temperature for PAFC is in the range 150 °C and 200 °C [12, 13]. PAFCs are also less powerful than other fuel cells, given the same weight and volume. As a result, these fuel cells are typically large and heavy. PAFCs are also expensive because require much higher loadings of expensive platinum catalyst than other types of fuel cells do, which raises the cost. This type of fuel cell can produce 100 kW for stack module.

(3) Molten carbonate fuel cells (MCFCs) are currently being developed for natural gas and coal based power plants for electrical utility, industrial, and military applications. MCFCs are high-temperature fuel cells that use an electrolyte composed of a molten carbonate salt (lithium carbonate, potassium carbonate and sodium carbonate) mixture suspended in a porous chemically inert ceramic lithium aluminium oxide matrix. The system operates at high temperatures of 650°C and non-precious metals can be used as catalysts at the anode and cathode for this reason the costs are reduced. Improved efficiency is another reason MCFCs offer significant cost reductions over phosphoric acid fuel cells [14, 15]. Molten carbonate fuel cells, when coupled with a turbine, can reach efficiencies approaching 65%, considerably higher than the 37% - 42% efficiencies of a phosphoric acid fuel cell. When the heat, generated during the working, is accumulated and used, fuel efficiencies can be over 85%. Unlike

alkaline, phosphoric acid, and PEM fuel cells, MCFCs can work without an external transformer to convert the light hydrocarbons to hydrogen. The cost can be reduced at high temperatures at which MCFCs can operate, CH_4 and other light hydrocarbons in the input fuels are converted to hydrogen, the conversion process is called "internal reforming" [16]. The main advantage is the possibility to use several fuels for anodic and cathodic sides, in fact H_2 or CO can be used in anodic compartment and O_2 or CO_2 in cathodic compartment. The main disadvantage of Molten Carbonate fuel cells technology is the durability. At working temperature, especially in internal reforming, the corrosion proprierties of the electrolyte accelerates the component breakdown and corrosion, decreasing cell life. Scientists are currently exploring new resistant materials for components as well as fuel cell designs that double cell life from the current 40000 hours (ca. 5 years) without decreasing performance. The MCFC show a very high power, the production can vary between 300 kW to 2 MW, however the fuel cell shows an high start-up time and a very low power density [17].

(4) Solid oxide fuel cells (SOFCs) use a non-porous ceramic compound as the electrolyte (zirconium oxide stabilised with yttria). SOFCs are around 60% efficient for the conversion fuel/energy. In applications when a heat system capture is used the efficiencies could top 85% [18]. SOFCs operate at very high temperatures as 1000 °C. High temperature operation removes the need for PGM catalyst (because high temperature significant high kinetic reaction), so reducing cost. The SOFCs can work with several input fuels so reducing the cost associated with adding a reformer to the system to convert the input fuel. SOFCs are also the most sulphur resistant fuel cell type; the system can tolerate several orders of magnitude more sulphur than other cell types can. In addition, SOFCs are not poisoned by carbon monoxide, which can even be used as fuel. High temperature operation has disadvantages. It results in a slow start-up [19]. The development of low cost materials with high durability at cell operating temperatures is the key for an utilization increment of these systems. Scientists are currently focused on lower-temperature SOFCs operating below of 700 °C that have fewer durability problems and cost less. Lower temperature SOFCs have not yet matched the performance of the higher temperature systems, however, and stack materials that will function in this lower temperature range are still under development. Summarized, the SOFC shows an high efficiency and input fuel flexibility, the anodic and cathodic reaction can be catalysed by different catalysts based on non-precious materials and the electrolyte in solid state can increase the security however increase also the corrosion effect. The SOFC show an working durability higher than 10000 h. However, the high working temperature leads to fast corrosion process of the structural components and an high start-up time [20, 21, 22].

(5) Polymer electrolyte membrane (PEM) fuel cells also called proton exchange membrane fuel cells deliver high power density and offer the advantages of low weight and volume compared with other fuel cells. PEM fuel cells use a solid polymer as an electrolyte and porous carbon electrodes containing

a platinum or platinum alloy catalyst [23]. For the high cost of the electrode catalysts the research is focused on low PGM material and on non-PGM catalysts. They need only hydrogen, oxygen from the air, and water to operate. They are typically fuelled with pure hydrogen supplied from storage tanks or reformers. PEM fuel cells operate at relatively low temperatures, around 80°C. Low temperature operation allows them to start quickly (less warm-up time) and results in less wear on system components, resulting in better durability. However, it requires that a noble-metal catalyst be used to separate the hydrogen's electrons and protons, adding to system cost. The platinum catalyst is also extremely sensitive to carbon monoxide poisoning, making it necessary to employ an additional reactor and filter to reduce carbon monoxide in the fuel gas if the hydrogen is derived from a hydrocarbon reforming [24]. The PEM fuel cell, generally, can produce 1 kW - 2 MW. The durability at maximum performance is evaluated be 3000 h. The actual system can work with an efficiency of 50 % - 60 %, these efficiencies can be reached using a platinum base material as catalysts, the catalysts material is the main problem of this type of fuel cell because increase the cost of the system and despite show and high catalytic activity and durability present an fast poisoning [25, 26].

1.2 Proton Exchange Membrane Fuel Cell (PEM-FC)

PEM fuel cells are used primarily for transportation applications and stationary applications. Due to their fast start-up time and favourable power to weight ratio, PEM fuel cells are particularly suitable for use in passenger vehicles, such as cars and buses. We should look for a renewable energy source to resolve the problem of fossil fuel consumption and pollution. The burning of fossil fuels has caused serious environmental problems such as air pollution, oil spillage and global warming. Using fuel cells to replace fossil fuels as primary energy source can solve a lot of energetic and environmental problems because fuel cells:

(1) Are clean energy source.
(2) Have high efficiency, 50% - 60% of the chemical energy being converted to electricity.
(3) Use a different fuel e.g. hydrogen or methanol or hydrocarbons.
(4) Are reliable, maintainable and durable.

PEMFCs have been developed for use in small distributed power generators in hospitals, hotels and office buildings because of their compact design (typical power for these devices are between 1 kW - 5 MW). These systems can be used in portable electronic devices because they are lighter and smaller than batteries or accumulator, have longer operating and faster output time compared to batteries and do not need recharging from the grid (20 mW -100 mW).

The polymer electrolyte fuel cell, also named proton exchange membrane (PEM) fuel cell, can be considered a good alternative on vehicles since have an easy structure, high specific power, a lower working temperature, non-corrosive electrolyte and rapid start-up at different temperatures. A PEM fuel cell is constituted by a stack

with a central membrane able to conduct protons. PEM-FCs are considered safe systems, which do not involve damage or danger [27, 28]. The typical structure of a PEM-FC is shown in Figure 4.

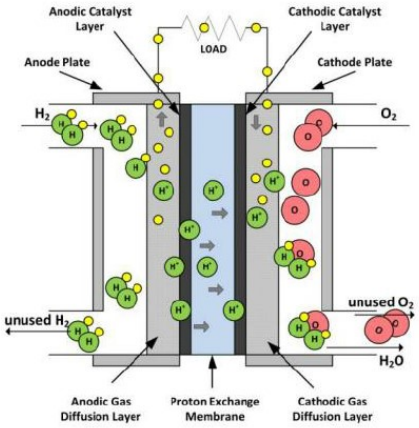

Figure 4: Schema for Proton Exchange Membrane Fuel Cell (PEM-FC)

Data Source: A. Abaspour, N. Tadrisi Parsa, M. Sadeghi, A New Feedback Linearization-NSGA-II based Control Design for PEM Fuel Cell, Int. J. Comput. Appl. 97 (2014) 25–32. doi:10.5120/17044-7354.

The basic PEMFC stack consists of Membrane Electrode Assemblies (MEAs) that are sandwiched by bipolar plates encompassed at both ends by current collector. The MEAs at the heart of the PEMFC, it is included between two electrodes: anodes and cathodes on either side, where electric power is generated from the electrochemical redox reactions whenever hydrogen and air (as oxygen input) are supplied, Figure 5. The set of layers is pressed by two conductive plates containing some channels in which the reactants flow [29].

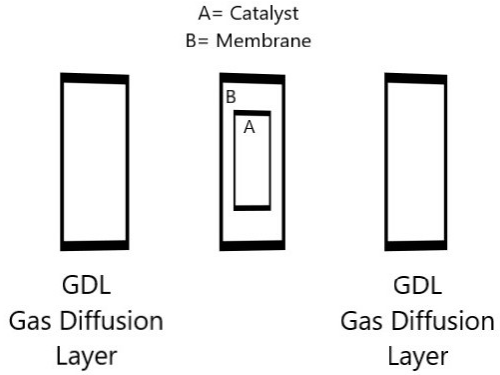

Figure 5: Schema of a standard MEA

The electrodes are composed by a gas diffusion layer and a catalyst layer. Both layers have a porous and partially hydrophobic structure, these are fundamental characteristic for the catalyst deposition. The central membrane works as a electrolyte that performs both the functions of transferring H^+ from the anode to the cathode and permits the reactant separation.

$$H_2 \rightarrow 2H^+ + 2e^- \quad (1.1)$$

$$O_2 + 4H^+ + 4e^- \rightarrow 2H_2O \quad (1.2)$$

$$2H_2 + O_2 \rightarrow 2H_2O \quad (1.3)$$

Hydrogen fuel is processed at the anode where electrons are separated from protons on the surface of a electrodic material (Hydrogen Oxidation Reaction, HOR, {1.1}). The protons pass through the membrane (MEA) to the cathode side of the cell while the electrons travel in an external circuit, generating the electrical output of the cell. On the cathode side (Oxygen Reduction Reaction, ORR, {1.2}), another precious metal electrode combines the protons and electrons with oxygen to produce water, which is expelled as the only waste product; oxygen can be provided in a purified form or extracted at the electrode directly from the air.
The electrodes at the MEA are usually made of a gas diffusion layer consisting of carbon paper or cloth, and a catalyst layer consisting of catalysts such as Pt at the anode and a PGM material at the cathode, which are impregnated in NPs form on carbon materials such as activated carbons (ACs), carbon nanotubes (CNTs) and carbon nanofibers (CNFs). Metal Nanoparticles and a porous carbon support are fundamental for obtain a catalyst with an high active area.

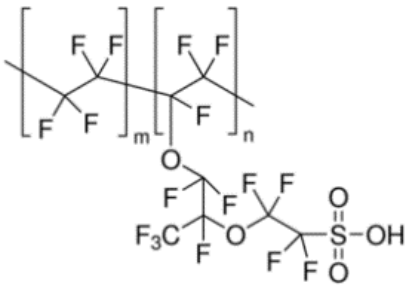

Figure 6: Chemical structure of perfluorosulfonic acid (PSFA)

The proton exchange membrane or solid polymer electrolyte is usually a proton conducting polymer that is impermeable to gas and electron, such as perfluorosulfonic acid (PSFA) or Nafion® (Figure 6), which is an excellent proton conductor that keeps gas crossover and electron short circuit to a minimum, but its effective operating temperature is limited to 80 °C and 90 °C [30]. The membrane conducts protons from the anode to the cathode to complete the electrical circuit with electrons that are conducted from the anode through the external load to the cathode, where both react with oxygen to form water.

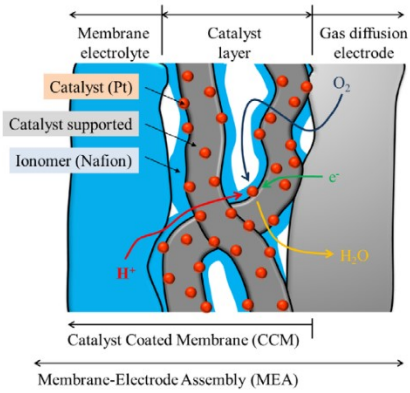

Figure 7: Sketch of the main components of a MEA: membrane electrolyte, catalyst layer and GDE.
Data Source: M. Eguchi, K. Baba, T. Onuma, K. Yoshida, K. Iwasawa, Y. Kobayashi, K. Uno, K. Komatsu, M. Kobori, M. Nishitani-Gamo, T. Ando, Influence of ionomer/carbon ratio on the performance of a polymer electrolyte fuel cell, Polymers (Basel). 4 (2012) 1645–1656. doi:10.3390/polym4041645.

Degradation of MEA components are due to (i) electrocatalyst sintering via (a) thermal induced growth following surface migration over the carbon support material (the process lead to the formation of areas with a greater NPs population and area in which the catalytic material is not present), and (b) "Ostwald Ripening" which follows a dissolution deposition mechanism, the NPs aggregate and the total active surface area decrease; (ii) agglomeration of platinum particle caused by corrosion of the carbon support (the carbon corrosion lead to a mechanical instability, and the NPs can be incorporate inside the matrix structure resulted inactive); (iii) electrocatalyst poisoning, surface segregation and morphology changes due to presence of strong surface chemisorption by species such as carbon monoxide, sulphur compounds, derivates of methanol oxidation, etc. (the absorption causes a drastically reduction of the active site, consequently the performance decrease, generally the poisoning in these catalysts is irreversible).; (iv) self-segregation of elements in mixed metal oxides or alloys (generally the oxide formation is a favourite process, it can form during the catalysts synthesis or during the fuel cell working, the process is irreversible and brought the catalyst deactivation); (v) degradation of ion conducting component including membrane and smaller aggregates present alongside the electrocatalyst in the reaction layer due to free radical species as H_2O_2 generated at the interface MEA/electrode (Figure 8) and (vi) an local temperature increment can dry the MEA, and reduce the ions transfer [31, 32].

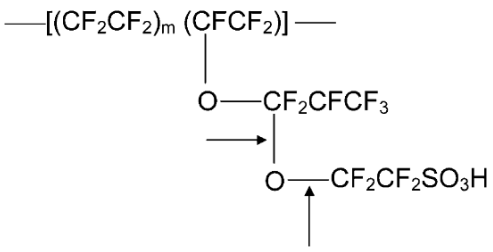

Figure 8: Nafion degradation due to the free radical attack

Theoretically, a single fuel cell produces 1.23 V of electrical potential in open circuit, but when connected to a load, it decreases as the load draws current from the cell and the usual operating voltage ranges from 0.6 to 0.7 V. The voltage loss is caused by several factors: electrode polarization caused by slow electrochemical reactions at both the anode and the cathode, ohmic polarization losses caused by hydrogen crossover or electron short circuit, mass transport polarization caused by hydrogen and oxygen concentration gradients at both electrodes when the reactants are consumed rapidly and ohmic losses caused by the internal resistance of the cell. Durability and low costs are primary challenges in proton exchange membrane fuel cell (PEMFC) technology and must be met concurrently. Actually, a series of freshly signed political and economic agreements are expected to boost the use of Proton Exchange Membrane FC technology and expand the range of applications. However, despite their great promise in terms of both energy efficiency and environmental control, the wide spread of PEMFCs is still hindered by the bottleneck of the oxygen reduction reaction (ORR). Carbon supported platinum or platinum alloys nanoparticles are commonly used as catalyst on both the anode and the cathode of PEMFC.

1.3 Bibliography

[1] M.S. Masnadi, H.M. El-Houjeiri, D. Schunack, Y. Li, J.G. Englander, A. Badahdah, J.C. Monfort, J.E. Anderson, T.J. Wallington, J.A. Bergerson, D. Gordon, J. Koomey, S. Przesmitzki, I.L. Azevedo, X.T. Bi, J.E. Duffy, G.A. Heath, G.A. Keoleian, C. McGlade, D. Nathan Meehan, S. Yeh, F. You, M. Wang, A.R. Brandt, Global carbon intensity of crude oil production, Science (80-.). 361 (2018) 851–853. doi:10.1126/science.aar6859.

[2] G. Baskar, I. Aberna Ebenezer Selvakumari, R. Aiswarya, Biodiesel production from castor oil using heterogeneous Ni doped ZnO nanocatalyst, Bioresour. Technol. 250 (2018) 793–798. doi:10.1016/j.biortech.2017.12.010.

[3] A. Baroutaji, T. Wilberforce, M. Ramadan, A.G. Olabi, Comprehensive investigation on hydrogen and fuel cell technology in the aviation and aerospace sectors, Renew. Sustain. Energy Rev. 106 (2019) 31–40. doi:10.1016/j.rser.2019.02.022.

[4] J.T. Pukrushpan, H. Peng, A.G. Stefanopoulou, Control-Oriented Modeling and Analysis for Automotive Fuel Cell Systems, J. Dyn. Syst. Meas. Control. 126 (2004) 14–25. doi:10.1115/1.1648308.

[5] A.. Fallis, Summary for Policymakers, in: Intergovernmental Panel on Climate Change (Ed.), Clim. Chang. 2013 - Phys. Sci. Basis, Cambridge University Press, Cambridge, 2013: pp. 1–30. doi:10.1017/CBO9781107415324.004.

[6] J. Larminie, A. Dicks, Fuel Cell Systems Explained, John Wiley & Sons, Ltd,., West Sussex, England, 2003. doi:10.1002/9781118878330.

[7] C. Coutanceau, L. Demarconnay, C. Lamy, J.M. Léger, Development of electrocatalysts for solid alkaline fuel cell (SAFC), J. Power Sources. 156 (2006) 14–19. doi:10.1016/j.jpowsour.2005.08.035.

[8] G.F. Mclean, T. Niet, N. Djilali, An assessment of AFC technology, Int. J. Hydrogen Energy. 27 (2002) 507–526.

[9] S. Maurya, C.H. Fujimoto, M.R. Hibbs, C. Narvaez Villarrubia, Y.S. Kim, Toward Improved Alkaline Membrane Fuel Cell Performance Using Quaternized Aryl-Ether Free Polyaromatics, Chem. Mater. 30 (2018) 2188–2192. doi:10.1021/acs.chemmater.8b00358.

[10] Z. Sun, B. Lin, F. Yan, Anion-Exchange Membranes for Alkaline Fuel-Cell Applications: The Effects of Cations, ChemSusChem. 11 (2018) 58–70. doi:10.1002/cssc.201701600.

[11] Y. Manoharan, S.E. Hosseini, B. Butler, H. Alzhahrani, B.T.F. Senior, T. Ashuri, J. Krohn, Hydrogen fuel cell vehicles; Current status and future prospect, Appl. Sci. 9 (2019). doi:10.3390/app9112296.

[12] P. Stonehart, Development of alloy electrocatalysts for phosphoric acid fuel cells (PAFC), J. Appl. Electrochem. 22 (1992) 995–1001. doi:10.1007/BF01029576.

[13] M.W. Ellis, M.R. Von Spakovsky, D.J. Nelson, Fuel Cell Systems: Efficient, Flexible Energy Conversion for the 21st Century, Proc. IEEE. 89 (2001) 1808–1817. doi:10.1109/5.975914.

[14] L. Mastropasqua, L. Pierangelo, M. Spinelli, M.C. Romano, S. Campanari, S. Consonni, Molten Carbonate Fuel Cells retrofits for CO_2 capture and enhanced energy production in the steel industry, Int. J. Greenh. Gas Control. 88 (2019) 195–208. doi:10.1016/j.ijggc.2019.05.033.

[15] A.H. Mamaghani, B. Najafi, A. Shirazi, F. Rinaldi, Exergetic, economic, and environmental evaluations and multi-objective optimization of a combined molten carbonate fuel cell-gas turbine system, Appl. Therm. Eng. 77 (2015) 1–11. doi:10.1016/j.applthermaleng.2014.12.016.

[16] A. Lanzini, H. Madi, V. Chiodo, D. Papurello, S. Maisano, M. Santarelli, J. Van herle, Dealing with fuel contaminants in biogas-fed solid oxide fuel cell (SOFC) and molten carbonate fuel cell (MCFC) plants: Degradation of catalytic and electro-catalytic active surfaces and related gas purification methods, Prog. Energy Combust. Sci. 61 (2017) 150–188. doi:10.1016/j.pecs.2017.04.002.

[17] K. Czelej, K. Cwieka, J.C. Colmenares, K.J. Kurzydlowski, Catalytic activity of NiO cathode in molten carbonate fuel cells, Appl. Catal. B Environ. 222 (2018) 73–75. doi:10.1016/j.apcatb.2017.10.003.

[18] N. Mahato, A. Banerjee, A. Gupta, S. Omar, K. Balani, Progress in material selection for solid oxide fuel cell technology: A review, Prog. Mater. Sci. 72 (2015) 141–337. doi:10.1016/j.pmatsci.2015.01.001.

[19] Y. Zhang, R. Knibbe, J. Sunarso, Y. Zhong, W. Zhou, Z. Shao, Z. Zhu, Recent Progress on Advanced Materials for Solid-Oxide Fuel Cells Operating Below 500 °C, Adv. Mater. 29 (2017). doi:10.1002/adma.201700132.

[20] S.Y. Gómez, D. Hotza, Current developments in reversible solid oxide fuel cells, Renew. Sustain. Energy Rev. 61 (2016) 155–174. doi:10.1016/j.rser.2016.03.005.

[21] Y. Zheng, J. Wang, B. Yu, W. Zhang, J. Chen, J. Qiao, J. Zhang, A review of high temperature co-electrolysis of H 2 O and CO 2 to produce sustainable fuels using solid oxide electrolysis cells (SOECs): advanced materials and technology, Chem. Soc. Rev. 46 (2017) 1427–1463. doi:10.1039/C6CS00403B.

[22] X. Zhang, L. Liu, Z. Zhao, B. Tu, D. Ou, D. Cui, X. Wei, X. Chen, M. Cheng, Enhanced oxygen reduction activity and solid oxide fuel cell performance with a nanoparticles-loaded cathode, Nano Lett. 15 (2015) 1703–1709. doi:10.1021/nl5043566.

[23] Y. Liu, W. Lehnert, H. Janßen, R.C. Samsun, D. Stolten, A review of high-temperature polymer electrolyte membrane fuel-cell (HT-PEMFC)-based auxiliary power units for diesel-powered road vehicles, J. Power Sources. 311 (2016) 91–102. doi:10.1016/j.jpowsour.2016.02.033.

[24] B. Smitha, S. Sridhar, A.A. Khan, Solid polymer electrolyte membranes for fuel cell applications - A review, J. Memb. Sci. 259 (2005) 10–26. doi:10.1016/j.memsci.2005.01.035.

[25] M.T.D. Jakobsen, J.O. Jensen, L.N. Cleemann, Q. Li, Durability Issues and Status of PBI-Based Fuel Cells, in: High Temp. Polym. Electrolyte Membr. Fuel Cells, Springer International Publishing, Cham, 2016: pp. 487–509. doi:10.1007/978-3-319-17082-4_22.

[26] J. Zhao, A. Ozden, S. Shahgaldi, I.E. Alaefour, X. Li, F. Hamdullahpur, Effect of Pt loading and catalyst

type on the pore structure of porous electrodes in polymer electrolyte membrane (PEM) fuel cells, Energy. 150 (2018) 69–76. doi:10.1016/j.energy.2018.02.134.

[27] D.J. Kim, M.J. Jo, S.Y. Nam, A review of polymer–nanocomposite electrolyte membranes for fuel cell application, J. Ind. Eng. Chem. 21 (2015) 36–52. doi:10.1016/j.jiec.2014.04.030.

[28] Y. Wang, K.S. Chen, J. Mishler, S.C. Cho, X.C. Adroher, A review of polymer electrolyte membrane fuel cells: Technology, applications, and needs on fundamental research, Appl. Energy. 88 (2011) 981–1007. doi:10.1016/j.apenergy.2010.09.030.

[29] S. Yuk, J. Yuk, T.H. Kim, Y.T. Hong, D.H. Lee, J. Hyun, S. Choi, G. Doo, D.W. Lee, H.T. Kim, External reinforcement of hydrocarbon membranes by a three-dimensional interlocking interface for mechanically durable polymer electrolyte membrane fuel cells, J. Power Sources. 415 (2019) 44–49. doi:10.1016/j.jpowsour.2019.01.048.

[30] J. Maiti, N. Kakati, S.P. Woo, Y.S. Yoon, Nafion® based hybrid composite membrane containing GO and dihydrogen phosphate functionalized ionic liquid for high temperature polymer electrolyte membrane fuel cell, Compos. Sci. Technol. 155 (2018) 189–196. doi:10.1016/j.compscitech.2017.11.030.

[31] E. Padgett, V. Yarlagadda, M.E. Holtz, M. Ko, B.D.A. Levin, R.S. Kukreja, J.M. Ziegelbauer, R.N. Andrews, J. Ilavsky, A. Kongkanand, D.A. Muller, Mitigation of PEM fuel cell catalyst degradation with porous Carbon supports, J. Electrochem. Soc. 166 (2019) F198–F207. doi:10.1149/2.0371904jes.

[32] A. Kneer, J. Jankovic, D. Susac, A. Putz, N. Wagner, M. Sabharwal, M. Secanell, Correlation of changes in electrochemical and structural parameters due to voltage cycling induced degradation in PEM fuel cells, J. Electrochem. Soc. 165 (2018) F3241–F3250. doi:10.1149/2.0271806jes.

2 Oxygen Reduction Reaction

2.1 General Mechanism

The oxygen reduction reaction (ORR) taking place on the cathode has sluggish kinetics, which give a major contribution to the efficiency loss of the fuel cell. High amount of catalyst is required on the cathode to reach sufficient activity compared to the fast hydrogen oxidation reaction on the anode. Catalysts are required to accelerate the reactions; Pt based materials are the best H_2 oxidation reaction (HOR) catalyst at today. Hydrogen oxidation reaction (HOR) as the key reaction in the anodic compartment of fuel cell and ultra-low platinum catalysts Pt (2 μg cm^{-2}) is required for increase the electrochemical performance and reduce the cost. Similarly, the best electrocatalysts known for oxygen reduction reaction (ORR) is again the platinum best materials. However, still the ORR is six or more orders of magnitude slower than the anode hydrogen oxidation reaction. The research is focused on the oxygen reduction reaction (ORR) because it is the main source of kinetic losses in low temperature PEM fuel cells. Oxygen reduction in aqueous solutions (both alkaline both acid solution) occurs mainly through two different mechanisms: either a four-electron reduction pathway where O_2 is reduced to H_2O and/or a two-electron pathway from O_2 to H_2O_2 and after at lower potential H_2O_2 is reduced at H_2O. The mechanism pathways are different in refer to acid or alkaline electrolyte. The rection rate and pathway are different in alkaline and acid electrolyte. In PEMFCs, a four-electron transfer is preferred, because the formation of hydrogen peroxide can damage the MEA, and decrease the total efficiency of the PEM-FC [33, 34].

The ORR mechanisms is alkaline media versus reversible hydrogen electrode (RHE) at 25°, and its thermodynamic potentials at standard conditions are showed as follows:

$$O_2 + 2H_2O + 4e^- \rightarrow 4OH^- \qquad (1.4)$$

The hydrogen peroxide formation follows the next pathway:

$$O_2 + H_2O + 2e^- \rightarrow HO_2^- + HO^- \qquad (1.5)$$

$$HO_2^- + H_2O + 2e^- \rightarrow 3HO^- \qquad (1.6)$$

The ORR in acidic electrolyte can follow a 4 or 2 electron pathway, depending by the catalyst.

Direct four-electron reduction :

$E^\theta = 1.229$ V $\qquad O_2 + 4H^+ + 4e^- \rightarrow 2H_2O \qquad (1.7)$

The hydrogen peroxide formation occurs with the follow pathway:

$E^{\theta} = 0.770$ V $$O_2 + 2H^+ + 2e^- \rightarrow H_2O_2 \quad (1.8)$$

$E^{\theta} = 1.760$ V $$H_2O_2 + 2H^+ + 2e^- \rightarrow 2H_2O \quad (1.9)$$

The hydrogen peroxide can react with H^+ ions and reducing itself to water, H_2O can be form also through chemical decomposition:

$$2H_2O_2 \rightarrow 2H_2O + O_2 \quad (1.10)$$

Full Oxygen Reduction is a dissociative adsorption process which begins with the adsorption of O_2 on the catalyst surface. Following O_2 adsorption, the first electron transfer in the form of hydrogen addition takes place resulting formation of HOO^*. After a second electron transfer occur, again in the form of hydrogen addition with the final formation of HO^* and O^*. Depending on whether this second hydrogen addition takes place at the oxygen molecule adsorbed to the catalyst or if it takes place at the oxygen already bound to the hydrogen determines how the reaction moves forward.

$$O_2 \rightarrow O_2^* \quad (1.11)$$

$$O_2^* + H^+ + e^- \rightarrow HOO^* \quad (1.12)$$

If the second hydrogen addition takes place at the oxygen adsorbed to the catalyst (Figure 9a), it results in two adsorbed HO^* groups. Subsequent electron transfers in the form of hydrogen addition take place at each HO^* group resulting in the production of two water molecules.

$$HOO^* + H^+ + e^- \rightarrow 2HO^* \quad (1.13)$$

$$2HO^* + 2H^+ + 2e^- \rightarrow 2H_2O \quad (1.14)$$

If the second hydrogen addition takes place at the oxygen already bound to the first hydrogen (Figure 9b), this results in desorption of a water molecule and an adsorbed O atom. Two electron transfers in the form of hydrogen ({1.16} and {1.17} addition to the O* follow resulting in desorption of a second water molecule.

$$HOO^* + H^+ + e^- \rightarrow H_2O + O^* \quad (1.15)$$

$$O^* + H^+ + e^- \rightarrow HO^* \quad (1.16)$$

$$HO^* + H^+ + e^- \rightarrow H_2O \quad (1.17)$$

DFT simulations of the two pathways show that the first pathway is thermodynamically favoured for the direct oxygen reduction to water, and it is therefore the more realistic method. Mechanism (b) involves a two electron pathway resulting in the production of adsorbed hydrogen peroxide by the reaction of water with O* intermedia.

$$H_2O + O^* \rightarrow H_2O_2 \qquad (1.18)$$

In Mechanism b, if the H^+ attack faster than O* dissociation, the reaction evolves with the hydrogen peroxide formation.

$$HOO^* + H^+ + e^- \rightarrow H_2O_2 \qquad (1.19)$$

The result is partial reduction of O_2, Oxygen is first adsorbed on to the catalyst surface. Then, two hydrogen additions take place resulting in an adsorbed H_2O_2 molecule [35, 36]. The hydrogen peroxide product can then undergo further reduction to produce two water molecules, or it can simply dissociate resulting in a free H_2O_2 molecule.

$$H_2O_2 \rightarrow H_2O + O^* \qquad (1.20)$$

$$H_2O_2 \rightarrow 2\,HO^* \qquad (1.21)$$

Mechanism a follows a more efficient four electron pathway which does not involve the production of H_2O_2 or radical species. The radical species can attack the C-O bond of the Nafion, reduced the ion conduction of the MEA. Considering the high reactivity of hydrogen peroxide compared to the stability of water, the 4 direct pathway is sought when choosing a catalyst for the ORR.

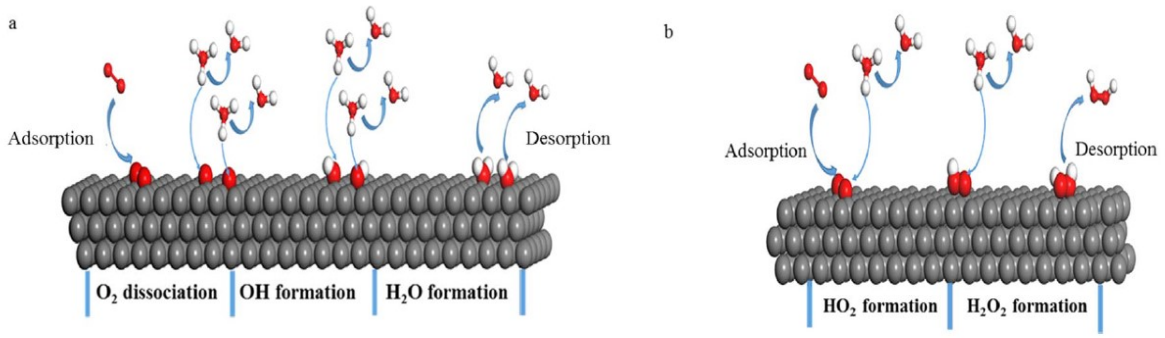

Figure 9: Mechanisms of Oxygen Reduction, a) 4 electron mechanism and H_2O desorption; b) 4 electron mechanism and H_2O_2 desorption.

It is desirable for the ORR to occur at potentials close to thermodynamic potentials as much as possible. ORR is the slowest reaction in any condition of the fuel cells. There are several reasons associated with this case. One of them is the higher bond energy of the oxygen molecule, $\Delta H^0 = +\,498\ kJ\ mol^{-1}$.

$$O_2\ (g) \rightarrow 2O(g) \qquad (1.22)$$

This activation barrier should overcome to get a higher current density from the cathode. The entropy change (ΔS) of dissociation of O_2 is always positive (increase the randomness). Hence, oxygen dissociation is more favourable at higher temperatures (decrease the ΔG).

$$\Delta G = \Delta H - T\Delta S \qquad (1.23)$$

However, the ΔS for the overall reaction is negative (reactant in gaseous state produce a liquid) hence, $-T\Delta S$ becomes positive. Therefore, at higher temperatures the ΔG increases (negative value of ΔG decreases) so that the efficiency will be reduced.

2.2 Catalyst for Oxygen Reduction Reaction

A catalyst for ORR must induce a direct reduction of O_2 to water by utilising the protons that permeate in the MEA from the anode. Pt is the most used electrocatalyst for ORR reactions, as it is the only commercially available catalyst with an high activity, stability and durability for PEMFCs, although it offers limited commercialisation on the market of the fuel cells due to its low availability and high cost. Pt standard based material shows over potentials of over 400 mV from the equilibrium reversible potentials (1.19 V at 80°C). These high potentials lead to a formation of adsorbed species on a Platinum active sites that restrain the ORR and hence result in performance decrement. The charge transfer kinetics of the Oxygen Reduction Reaction must be quick as possible [37, 38].

The optimal catalyst should be sufficiently reactive to activate the O_2 gas molecule and at the same time sufficiently noble to release oxygen and the reaction products in the form of H_2O. Pt is the pure metallic element with the highest ORR activity, in terms of kinetic and thermodynamic. More reactive metals as for instance Pd, Cu or Ir bind oxygen or HOO^- too strongly while others noble metals as Ag or Au adsorb oxygen too weakly so the reaction rate decrease.

If the M (generic metal)-O_2 bond is strong, the H^+ can't react and form HO^-, while if the bond is weak the reaction with ion leads to the HOO^- formation. Volcano plot (Figure 10) is a representation of Metal Oxygen bond, which rank the catalysts considering the energy of the bond. The optimal catalyst, at the peak of the volcano plot, should have an oxygen absorption energy of 0.2 eV lower than that of pure Pt. A density

functional theory (DFT) studio can explains the volcano vertex as a trade-off between the desorption of HO^- on strong binding materials such as Platinum or Palladium, and the reaction between O_2 and H^+ activation on weak binding materials such as Au. In contrast, kinetic experiments on Pt point towards the first electron transfer to O_2 being rate-determining, suggesting O_2 activation rather than OH removal is limiting ORR activity [39].

Density functional theory (DFT) calculations indicate that the binding energy between oxygen intermediates and the catalyst surface is related to catalytic efficiency for ORR. The Volcano plot is based on the Sabatier principle. The Sabatier principle is the idea that a reactant must bind strongly enough to the catalyst for the reaction to take place, but weakly enough that the product will dissociate, and the catalyst surface will not be poisoned by either the reactant or intermediates. So, in this case the oxygen species must bind tightly enough to the catalyst that the reaction can take place on the surface, but not so tightly that oxygen intermediates poison the catalyst. Based on both theoretical calculations and experimental data, "volcano plots", can be constructed comparing catalytic activity to Oxygen binding energy. These plots can then be used to find the optimal ΔE_O for an ORR catalyst [40, 41]. Figure 10 show the Volcan Plot for metal generally used for catalysed the Oxygen Reduction Reaction.

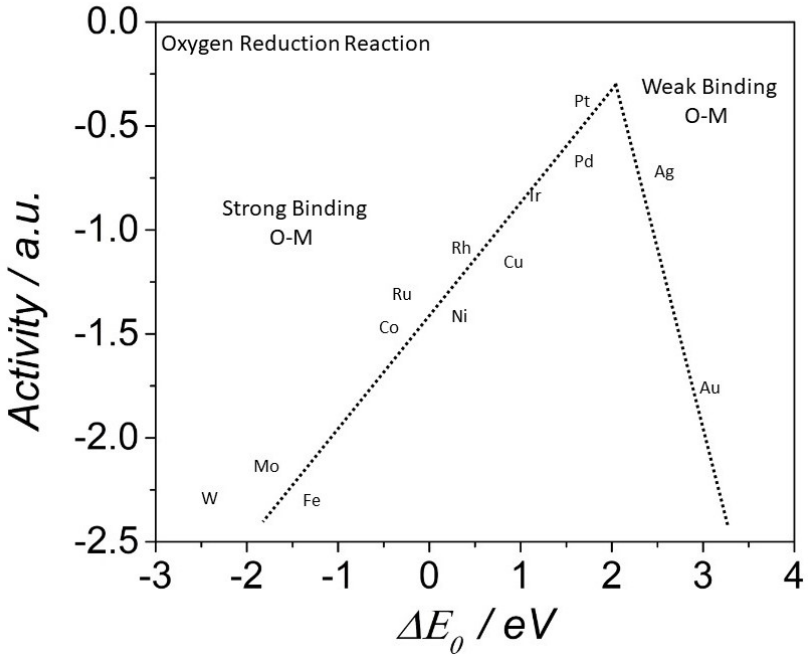

Figure 10: Volcano plot for Oxygen Reduction Reaction

Using published Bronsted-Evans-Polanyi Theory, the kinetic model may be generalized using the HO^-(or O*) formation energy as a descriptor for the ORR activity. As hydroxylic species binding is weakened, the ORR activity initially increases, under a thermodynamic rate control, with the OH removal until in the situation

where $M - OH$ bind becomes too weak to activate O_2 through the formation of HOO^-. The ORR catalysed by a generic metal can evolve in two mechanism, dissociative and associative.
Dissociative mechanism:

$$O_2 + 2M^* \rightarrow 2O^* \quad (1.24)$$

$$O^* + H^+ + e^- \rightarrow HO^* \quad (1.25)$$

$$HO^* + H^+ + e^- \rightarrow H_2O + M^* \quad (1.26)$$

In this mechanism, no H_2O_2 is formed. On the Metal surface, the O_2 adsorption breaks the O-O bond and forms adsorbed atomic O* with further gain of two electrons, in the two consecutive steps, forming H_2O. Because there is no adsorption of O_2 on the surface, no H_2O_2 can be formed. This mechanism can be considered as the direct four-electron reduction reaction. Platinum is more metal used because H_2O_2 is unstable on the surfaces and it will immediately dissociate to OH if formed during ORR, unless the cleavage of the O-O bond is inhibited by adsorbed spectator species.

The associative mechanism can be explained with the following reactions.

$$O_2 + H^+ + e^- + M^* \rightarrow HOO^* \quad (1.27)$$

$$HOO^* + H^+ + e^- \rightarrow O^* + H_2O \quad (1.28)$$

$$O^* + H^+ + e^- \rightarrow HO^* \quad (1.29)$$

$$HO^* + H^+ + e^- \rightarrow M^* + H_2O \quad (1.30)$$

Where M^* indicates the active site on a catalytic surface and the adsorbed intermediates in the case of HOO∗, HO* and O*, all bound through an oxygen atom. The kinetic rate is due to the adsorption of O_2 on the metal, while the thermodynamic control is connected to the reduction of *OH to H_2O. Adsorption of O_2 is one of the major steps in ORR. The three types of models most considered for O_2 adsorption are (Figure 11): End-on adsorption (i), Bridge (ii) and Top-on adsorption (iii) model. The end on adsorption leads to series pathway through H_2O_2 and bridge adsorption results in direct four electron pathway [42].

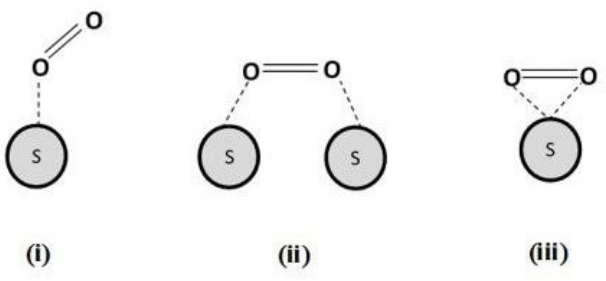

Figure 11: Different absorption mechanisms of O_2 on an active site (S)

The presence of three different intermediates explains the higher level of complexity with respect for instance to the HOR (with the single intermediate H*) and therefore the difficulties of finding good catalysts. At today, 142 different intermedia was evaluated for the oxygen reduction reaction. Even if trivial, an efficient ORR catalyst should bind each of these intermediates optimally, neither too strongly nor too weakly. A better catalyst binds HOO* more strongly and OH* weakly, but thermodynamically is impossible. In particular, an ideal material for Oxygen Reduction Reaction would show a flat free energy diagram at the equilibria potential: 1.23 V at 25 °C and atmospheric pressure. This would mean in high ORR kinetics currents at slightly more negative potentials and low losses. A metal which binding strongly to HO* will also bind strongly to HOO* and vice versa, because metal in all two cases bind through an O atom.

The dissociation of M-OOH into M-OH and/or M-O occurs easily without any activation barrier to overcome. The M-OOH is adsorbed as top-bridge, after dissociation two top sites are formed M-OH and M-O. The OH species moves to bridge site whereas the O is block in a top-on configuration due to formation of hydrogen bond with H_2O and HO^-. After, H^+ is transferred to OH species and forms H_2O*. Due to formation of hydrogen bond between H^+ and H_2O, the water molecules travels to O* species to give two atoms adsorbed OH species. It is also possible an end-on configuration, which leads to the formation before of HOO- and after to HOO*H. The formation of an end-on configuration for HOO*H species, lead to hydrogen peroxide formation.

After the formation of HOO*H species, this can desorb as H_2O_2 or dissociates to give one atom adsorbed *OH and another bridge adsorbed *OH species. Also, *OH species formed in this way are r unstable than that formed by O* and H^+. One of the adsorbed *OH species can react with a proton to give H_2O*. The last reduction step shows a proton and an electron transfer to *OH species giving two H_2O* adsorbed species which are bonded to each other by hydrogen bond.

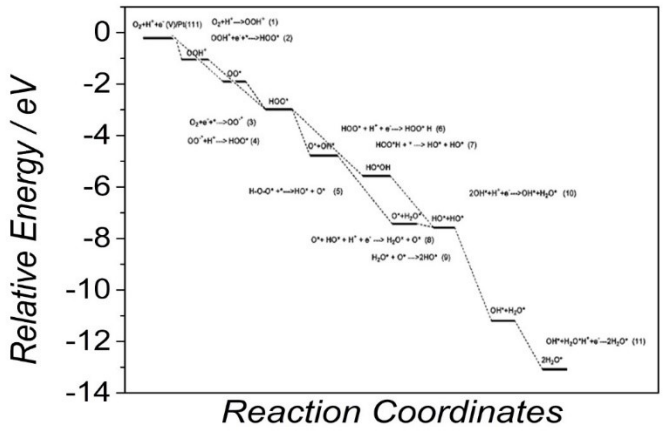

Figure 12: Oxygen Reduction Reaction for Pt(111) catalyst

The catalysts for Oxygen Reduction Reaction can be divided in two class, Platinum Group Metal (PGM), and free-Platinum group metal (non-PGM). The main different can be calcsilicate in “catalysts cost” and “catalyst performance”, the first describe the material in terms of price, availability, dangerousness and accessibility.

The catalysts performance describes the active materials only in terms of catalytic activity, stability and durability [43, 44]. Considering these differences, the research is based on:

(1) reduce the costs of fuel cells, which is one of the stumbling blocks in fuel cell commercialisation using low-cost non-Pt catalysts such as supported platinum group metals Pd, Ir and Ru;

(2) improve the electrocatalytic activity of the cathode catalyst, which includes using bimetallic alloy catalysts, transition metal macro cyanides, transition metal chalcogenides and metal oxides, in order to, improve the ORR kinetics on the new catalyst;

(3) fabricate Pt with novel nanostructures such as nanotubes, graphene and carbon nanofibers (CNFs), as it is known that supports may significantly affect the performance of the catalyst.

2.3 Oxygen Reduction Reaction on PGM Catalysts

The platinum group metals (PGM), consist of six elements: platinum, palladium, rhodium, iridium, ruthenium, and osmium. An estimated 30% of the cost of PEMFC is driven by the use of Platinum (Pt) as a very effective hydrogen oxidation and oxygen reduction catalyst in low temperature PEMFC fuel cells. In addition, Pt is sensitive to contamination as carbon monoxide by impurities in the hydrogen and certain air contaminants. Many projects are focused on the decrement of Pt loading in MEAs, and on the increment of the catalytic activity. At the potential between 0.8 and 0.9 V, under which PEMFCs typically operate, oxygen molecules adsorb on the surface layer of catalysts, following by the break of O-O bond and the formation of HO- species adsorbed. The process can occur through three mechanisms. The conclusion step is the reaction of the absorbed hydroxyl with a proton to produce water [45, 46].

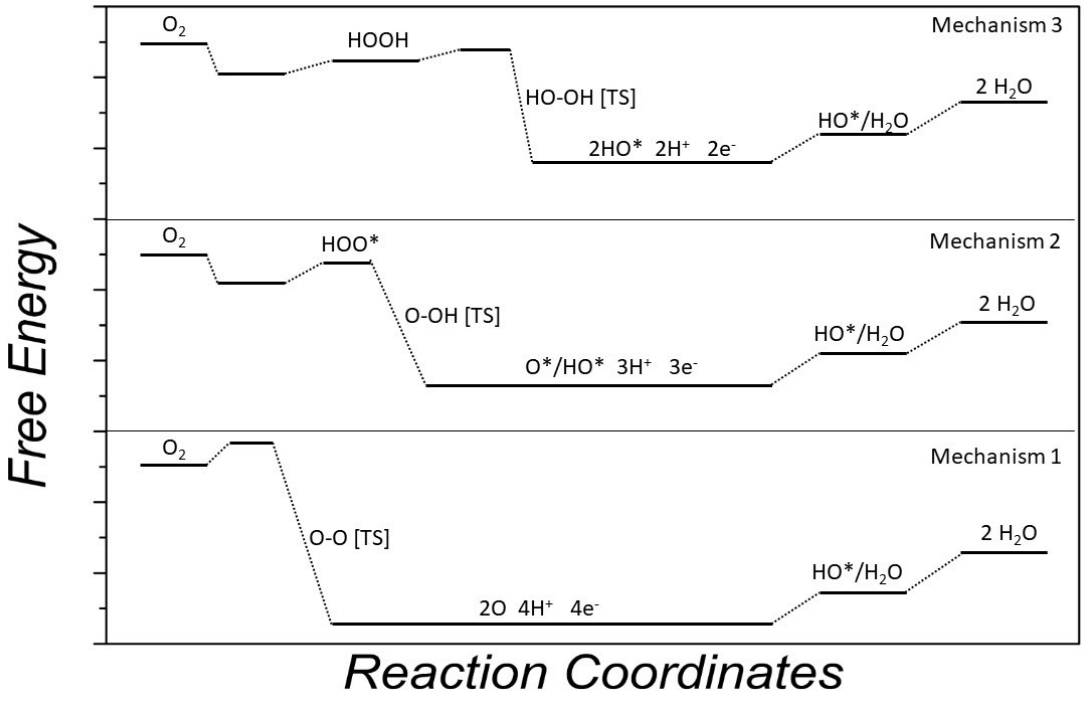

Figure 13: Mechanisms for ORR in a PGM catalyst

The Oxygen Reduction Reaction can occur through three different mechanism (in acid condition) in a platinum surface, as show in Figure 13. All three were identified as the four electron processes that involve the adsorbed oxygen species, including *OOH, *OH and HOO*H. Major challenge for PGM is to develop new Pt-containing catalysts that have ultrahigh activity and durability for reduce the metal loading in the catalysts so reduce the catalysts cost.

Typical electrocatalysts, developed recently, are metal alloy based nanocrystals in various forms on carbon-based materials including quinone and its pyrolytic derivative, transition metals macrocyclic compound,

transition metals chalcogenide, transition metals carbide, oxide, and perovskite. The number of catalysts which can catalyses the ORR is very high but Pt-based nanoparticles remain as the most practical catalysts in strong acidic media.

The kinetic current of a metal, and Pt in particular, can be increased by modulating the electronic density of the catalyst nanoparticles (NPs) by interaction with the support or morphological defects or by alloying with a other metal, especially early or late transition metals [47]. The effects which modify the catalytic activity of a metals can by summarized as, electronic and geometric effect. These catalysts can show a higher catalytic activity than bulk platinum with lower metal loading. As described in the previous chapter, in order to improve the ORR activity of Pt, the binding of the intermediates HO* and HOO* has to be weakened slightly. One way to do it is to alloy Pt with other materials, such as Co, Ni, Fe, and, more recently, with lanthanides such as Gd and Y. Pt alloys exhibit an improved activity over Pt because of their weaker interaction with O. The electronic interaction modifies the d-band energy of the platinum, increasing the performance; from a graphic point of view, the platinum alloy catalysts are shifted to the vertex of volcano plot. In Platinum metal alloy the insertion of a second element in the crystal structure lead to a variation of the platinum-platinum interatomic distance. Compressive strain can weaken the Pt surface atoms' binding to the ORR intermediates. When the core is composed of a compound with a lattice parameter smaller than that of Pt, the Pt surface atoms will tend to contract laterally. In this case, the overlayer's d-band centre is lower than the Fermi level, which in turn increases the occupancy of the Pt-adsorbate antibonding states. Electronic effects occur when the Pt surface atoms interact with the metal atoms with a different composition, which also weakens the binding of the Pt surface atoms to O*, *OH and *OOH. In other words, electronic effects are caused by the electronic interactions between the surface Pt atoms and the alloying materials due to the different electronegativity. If the electronegativity of alloying metal is lower than platinum, an electron transfer from the metal to the platinum occur, vice versa a charge transfer from the secondo metal to platinum is observed when the different of electronegativity of platinum is lower than the alloying metal. In most Pt alloy ORR catalysts, such as Pt_3Ni, Pt_3Co and dealloyed PtCu, the weakening of the Pt-O bond can be at least partially attributed to compressive strain: each has a smaller lattice parameter than pure Pt. The point is the electronic interaction between the bulk (where the alloy metal is present) and the Pt overlayer is responsible for the shift of the d-band center. On a real surface the two effects often co-exist, and it is difficult to separate them [47,48]. Figure 14 show the influence of the lattice parameter for different platinum alloy catalysts on the kinetic current.

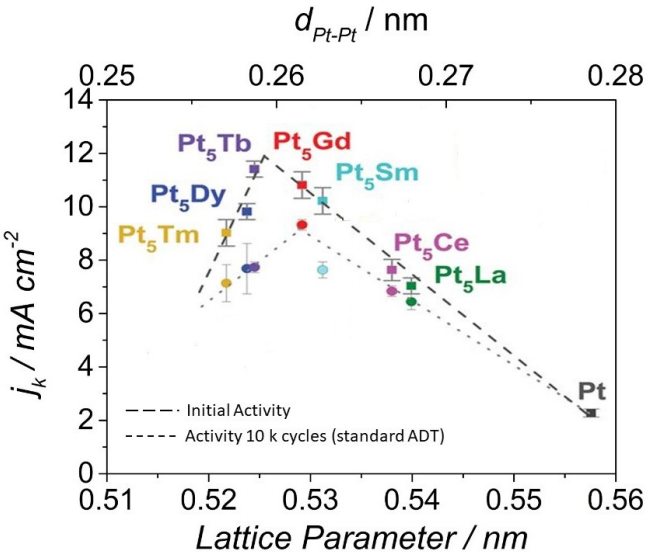

Figure 14: Volcano Plot for Platinum alloy materials

Generally, Platinum catalysts are deposited on nanostructured carbon support in order to increase the specific surface area, the process is fundamental to obtain an acceptable catalytic performance. The surface physicochemical properties and the structure of carbon materials play an important role on the activity and the stability of the resultant carbon supported Pt NPs because the interaction between carbon active sites and Pt NPs can modify the physicochemical and electronic structure of Pt which in turn influences the catalytic activity and durability [49].

Generally, the requirements for catalyst support material are:

- High surface area to improve the metal NPs dispersion.
- High electrical conductivity to provide a low ohmic resistance.
- High stability.
- Good interaction between support and metal NPs.

2.4 Oxygen Reduction Reaction in non-PGM catalysts

The cost of precious Pt-based catalysts used at the anode and the cathode contributes significantly to the cost of a fuel cell. Thus, cost-effective catalyst design should include less expensive non-precious metals in order to make the fuel cell a viable and common technology for power generation. Even though Pt has shown the best catalytic performance, its high cost and the production areas have limited a large scale application. Therefore, rich of an inexpensive and non-noble metal catalysts to substitute Pt-based catalyst has become a critical and fundamental issue in the PEM-FCs research field. For increase the PEM Fuel Cells commercialization, several substitutes for Pt have been considered, including Pd-based catalysts and non-noble metals and functionalized carbon materials. Among the non-noble metal catalysts, Fe, Co, and Mn are the most studied material. Other noble metals, such as Pd, Ag, Rh, Ir and Ru, have also been used as cathode materials for ORR. Among these, Pd, which has the same electron configuration and lattice constant as Pt, as they belong to the same row in the periodic table, showed the most improved ORR. The noble metals in terms of ORR activity follow the trend: Pt > Pd > Ir > Rh. Ag is reported to show less electrocatalytic activity towards ORR compared to Pt but is more stable than Pt cathodes during long-term operations [50, 51]. Transition metal (TM) and nitrogen carbon (TM–N_x–C) materials are considerable studied as alternatives to Pt-based catalysts with good activity towards cathode reaction (ORR). Cobalt and iron phthalocyanine on microporous carbon are the most-used transition metals as centres for macro cycling complex rings as catalysts for ORR in fuel cells. Co phthalocyanine has demonstrated similar ORR kinetics as commercial Pt/C, as it also leads to a four-electron pathway but with a reaction rate lower than platinum bulk. The ORR on TM–N_x/C electrocatalysts has been assumed to proceed through an associative mechanism which involves the adsorption of molecular O_2 onto the transition metal (TM) followed by its hydrogenation.

The homolytic O - O bond scission in O on a single TM of a TM–N_x site is unfaourable in catalysts that contain widely dispersed TM–N_x sites since two TM-adsorption sites are needed for the adsorption. Fe–N_x–C electrocatalysts can promote an associative ORR pathway by two mechanisms[52].

Mechanism 1	Mechanism 2
$O_2 + TM^* \rightarrow O_2^*$	$O_2 + TM^* \rightarrow O_2^*$
$O_2^* + H^* + e^- \rightarrow HOO^*$	$O_2^* + H^* + e^- \rightarrow HOO^*$
$HOO^* + H^+ + e^- \rightarrow O^* + H_2O$	$HOO^* + H^* + e^- \rightarrow 2HO^*$
$O^* + H^+ + e^- \rightarrow HO^*$	$2HO^* + H^+ + e^- \rightarrow HO^* + H_2O$
$HO^* + H^+ + e^- \rightarrow H_2O + TM^*$	$HO^* + H^+ + e^- \rightarrow H_2O + TM^*$

In acidic medium, the fundamental step in ORR after O_2 adsorption is the hydrogenation to form a peroxyl (OOH) intermediate. Further hydrogenation of peroxyl results in O–O bond scission either to form O and H_2O in reaction pathway 1, as shown in the scheme below. The hydrogenation of *O and *OH results in the

formation of H_2O. H_2O_2 may form as a product of the third reaction in both reaction pathways 1 and 2 due to selective hydrogenation of *OOH and can desorb as a stable intermediate.

$$HOO^* + H^+ + e^- \rightarrow H_2O_2 + TM^* \qquad 1.31$$

Fe–N_x or Co-N_x sites are expected to promote a single site 4e^- ORR.

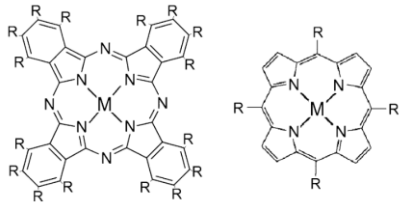

Figure 15: Typical metal nitrogen complexes, which catalysed the ORR

2.5 Bibliography

[33] D.H. Lim, J. Wilcox, Mechanisms of the oxygen reduction reaction on defective graphene-supported Pt nanoparticles from first-principles, J. Phys. Chem. C. 116 (2012) 3653–3660. doi:10.1021/jp210796e.

[34] I. Roche, E. Chaînet, M. Chatenet, J. Vondrák, Carbon-supported manganese oxide nanoparticles as electrocatalysts for the Oxygen Reduction Reaction (ORR) in alkaline medium: Physical characterizations and ORR mechanism, J. Phys. Chem. C. 111 (2007) 1434–1443. doi:10.1021/jp0647986.

[35] J.A. Keith, T. Jacob, Theoretical studies of potential-dependent and competing mechanisms of the electrocatalytic oxygen reduction reaction on Pt(111), Angew. Chemie - Int. Ed. 49 (2010) 9521–9525. doi:10.1002/anie.201004794.

[36] V. Tripković, E. Skúlason, S. Siahrostami, J.K. Nørskov, J. Rossmeisl, The oxygen reduction reaction mechanism on Pt(1 1 1) from density functional theory calculations, Electrochim. Acta. 55 (2010) 7975–7981. doi:10.1016/j.electacta.2010.02.056.

[37] B. Wang, Recent development of non-platinum catalysts for oxygen reduction reaction, J. Power Sources. 152 (2005) 1–15. doi:10.1016/j.jpowsour.2005.05.098.

[38] G. Wu, P. Zelenay, Nanostructured nonprecious metal catalysts for oxygen reduction reaction, Acc. Chem. Res. 46 (2013) 1878–1889. doi:10.1021/ar400011z.

[39] F. Calle-Vallejo, J.I. Martínez, J. Rossmeisl, Density functional studies of functionalized graphitic materials with late transition metals for oxygen reduction reactions, Phys. Chem. Chem. Phys. 13 (2011) 15639–15643. doi:10.1039/c1cp21228a.

[40] Y. Okamoto, O. Sugino, Hyper-volcano surface for oxygen reduction reactions over Noble metals, J. Phys. Chem. C. 114 (2010) 4473–4478. doi:10.1021/jp9087805.

[41] M. Shao, P. Liu, J. Zhang, R. Adzic, Origin of enhanced activity in palladium alloy electrocatalysts for oxygen reduction reaction, J. Phys. Chem. B. 111 (2007) 6772–6775. doi:10.1021/jp0689971.

[42] T. Ikeda, M. Boero, S.F. Huang, K. Terakura, M. Oshima, J.I. Ozaki, Carbon alloy catalysts: Active sites for oxygen reduction reaction, J. Phys. Chem. C. 112 (2008) 14706–14709. doi:10.1021/jp806084d.

[43] S. Kattel, P. Atanassov, B. Kiefer, A density functional theory study of oxygen reduction reaction on non-PGM Fe-Nx-C electrocatalysts, Phys. Chem. Chem. Phys. 16 (2014) 13800–13806. doi:10.1039/c4cp01634c.

[44] Y.J. Wang, N. Zhao, B. Fang, H. Li, X.T. Bi, H. Wang, Carbon-Supported Pt-Based Alloy Electrocatalysts for the Oxygen Reduction Reaction in Polymer Electrolyte Membrane Fuel Cells: Particle Size, Shape, and Composition Manipulation and Their Impact to Activity, Chem. Rev. 115 (2015) 3433–3467. doi:10.1021/cr500519c.

[45] J. Wu, H. Yang, Platinum-based oxygen reduction electrocatalysts, Acc. Chem. Res. 46 (2013) 1848–1857. doi:10.1021/ar300359w.

[46] C. Wang, N.M. Markovic, V.R. Stamenkovic, Advanced platinum alloy electrocatalysts for the oxygen reduction reaction, ACS Catal. 2 (2012) 891–898. doi:10.1021/cs3000792.

[47] M. Shao, A. Peles, K. Shoemaker, Electrocatalysis on platinum nanoparticles: Particle size effect on oxygen reduction reaction activity, Nano Lett. 11 (2011) 3714–3719. doi:10.1021/nl2017459.

[48] A. Kulkarni, S. Siahrostami, A. Patel, J.K. Nørskov, Understanding Catalytic Activity Trends in the Oxygen Reduction Reaction, Chem. Rev. 118 (2018) 2302–2312. doi:10.1021/acs.chemrev.7b00488.

[49] B. Cai, R. Hübner, K. Sasaki, Y. Zhang, D. Su, C. Ziegler, M.B. Vukmirovic, B. Rellinghaus, R.R. Adzic, A. Eychmüller, Core–Shell Structuring of Pure Metallic Aerogels towards Highly Efficient Platinum Utilization for the Oxygen Reduction Reaction, Angew. Chemie - Int. Ed. 57 (2018) 2963–2966. doi:10.1002/anie.201710997.

[50] U. Martinez, S. Komini Babu, E.F. Holby, P. Zelenay, Durability challenges and perspective in the development of PGM-free electrocatalysts for the oxygen reduction reaction, Curr. Opin. Electrochem. 9 (2018) 224–232. doi:10.1016/j.coelec.2018.04.010.

[51] I. Matanovic, K. Artyushkova, P. Atanassov, Understanding PGM-free catalysts by linking density functional theory calculations and structural analysis: Perspectives and challenges, Curr. Opin. Electrochem. 9 (2018) 137–144. doi:10.1016/j.coelec.2018.03.009.

3 Mechanisms to improve the activity vs. ORR in a Platinum based Catalysts

To improve the catalytic activity, stability, and utilization of Pt Nanoparticles catalysts, high surface area carbon black particles have been considered to be the best choice as the electrocatalyst support due to their large specific surface area favouring the dispersion of an active component, good electric conductivity (a great electrical conductivity permits to expedite electron transfer in numerous redox reaction) , porous structure, and low cost. The best strategies for increase the catalytic activity (Figure 16) for ORR include (1) controlling of Pt-based NPs dimension with size in the range of 3 nm − 5 nm to yield a high electrochemical active area and catalytic activity, an high surface area for the catalyst particles permits to ensure their effective immobilization in a well-dispersed route, (2) controlling the shape of Pt- catalysts to give more complex morphologies such as cube, dendritic NPs which permits to increase the surface area and limiting the less active crystallographic faces (3) obtaining specific index facets in catalysts, such as (110) or (110), favouring high activity and stability during the application in Fuel Cell, (4) designing controlled architectures such as core-shell structure, Platinum skin or Platinum monolayer on non-noble metals, (5) developing new support materials with high conductivity, chemical stability, and surface area, and (6) obtaining a uniform distribution of Pt or Pt-alloy nanoparticles on the support materials [53, 54]. The supports strongly influence catalytic activity, the support materials play a crucial role in the catalytic behaviour of catalysts. Strong catalyst-support interactions to not only enhance catalyst effectiveness but also facilitate electron transfer, as well as excellent electrical conductivity to promote electron transfer in redox reactions. However, the support must have certain characteristic as surface area, or pore distribution referring by the type of metal NPs deposited.

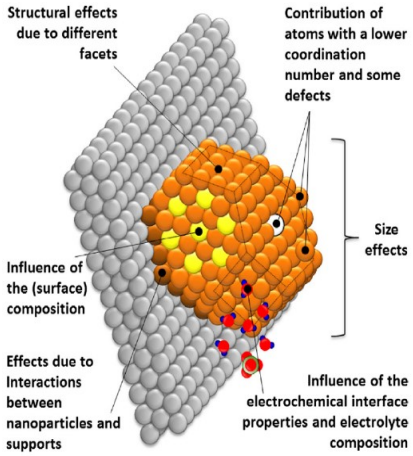

Figure 16 :Sketch of the main interaction which can modify the stability and the activity of the catalysts

Data Source: A.S. Bandarenka, M.T.M. Koper, Structural and electronic effects in heterogeneous electrocatalysis: Toward a rational design of electrocatalysts, J. Catal. 308 (2013) 11–24. doi:10.1016/j.jcat.2013.05.006.

At present, platinum free catalysts such as iron or cobalt nitrogen materials (FeN_x or CoN_x) showed lower activity and stability than platinum bulk. Platinum catalyst occupy the most optimal position in the Volcano plot, but it is not at the peak. One method to modify the adsorption energies of oxygen species is adjusting the centre of the d-band, or conductive band, of the catalyst. The d-band acts as a descriptor of the electronic properties of the solid, and it has been shown to correlate with the Oxygen adsorption energies so with the catalytic activity for Oxygen Reduction Reaction. Therefore, huge efforts are focused to improve the Pt catalyst activity, so that to reduce its loading, for example by tailoring different shape metal particle, or by development of many different types of Pt alloy materials. Other methods for modify the d-band energy is increase the interaction between the metal NPs and the support, where the extend of the interaction depends on the type (graphitized or amorphous), structure (mesostructured or microstructured), and composition of the support (doping). The metal support interaction (MSI) can, generally, affect the catalytic activity by influencing the NPs morphology and dimension, inducing strain on the NP due to lattice mismatch and changing the electronic structure via charge transfer processes between the carbon and the metal site [55]. For examples, it was demonstrated how nitrogen doped carbon exerts a strong interaction with the supported Pt NPs triggering their electronic properties and catalytic activity, the conductibility of the system is closely connected to the nitrogen concentration, high concentration increases the resistivity of the material and makes it unsuitable for the application as a catalyst. Also, sulphur affords a clear metal support interaction between Pt NPs and the carbon support. Sulphur doped supports significantly improve the kinetics and the stability of Pt catalysts for ORR.

Mechanism to improve the catalytic activity in a Platinum-based material for Oxygen Reduction Reaction:

- Pt_xM alloy nanoparticles with transition metal. Platinum alloys have two distinct advantages over pure Pt catalysts: i) interactions between the two metals give rise to modifications to the electronic properties of the material, some of which result in higher ORR activity; ii) incorporation of another metal in the noble metal structure leads a decrement of platinum loading while the catalytic activity and therefore a higher mass activity can being maintained or improved [56].
- Increased of the metal carbon interaction. The properties of a supported materials can be tuned by control of particle size, using the metal-support interaction. The support acts as a “supramolecular ligand” and has been claimed to promote specific electronic properties and geometrical features of the sized supported metal particles. The effect is based in the interaction between the d-band of the metal and the molecular orbitals of carbon support [57, 58].
- Tuning Pt structur in terms of shape, size and crystallography. Each crystal plane shows a specific surface energy, and therefore different binding energies to reactants and so different ORR performance. Pt (111) single crystal catalyst show an ORR activity 10 times higher than state of the art Pt@C catalysts with a mixture of facets on the catalyst surface. Morphology is also an important factor when optimizing a catalyst. For reduce the NPs dimension and maintaining a good stability the ratio surface area on pore volume of the support must increase [59, 60].

3.1 Platinum alloy Nanoparticles on Carbon

The platinum alloying induces strain and electronic effects, modifying the interactions with adsorbates. Many alloys between Pt and transition metals shows an increment of the catalytic activity. Pt_xM (where M = Ti, V, Fe, Co and Ni) show higher activity than pure Pt for the Oxygen Reduction Reaction. Generally, the less noble metal is not thermodynamically stable under the acidic conditions of a PEMFC and/or at the typical cathode potentials. The alloys have a specific stoichiometric ratio between the two metals, different values lead to different catalytic properties. The metals alloy in acid environmental tend to dissolve into the electrolyte, the process is known as "dealloying". The resulting surface of these catalysts is Pt enriched and it typically consists of a Pt overlayer protecting the less noble metal in the bulk from the dissolution. Platinum Nickel or Platinum Aluminium show a very fast dealloying process, in the other hand in Pt_xCo or Pt_xTi the dealloying is unfavourable. In general, two kinds of surface structures can be distinguished: Pt-skeleton and Pt-skin structures, Figure 17 [61, 62].

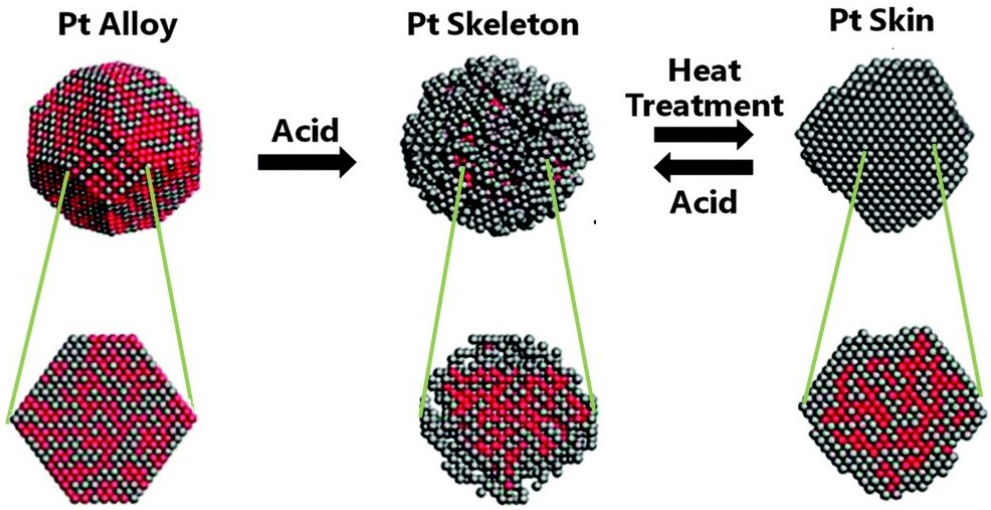

Figure 17: Sketch of different platinum structures

Data Source: Y. Nie, L. Li, Z. Wei, Recent advancements in Pt and Pt-free catalysts for oxygen reduction reaction, Chem. Soc. Rev. 44 (2015) 2168–2201. doi:10.1039/c4cs00484a.

PGM are resistant to attack by common aqueous chemical reagents, the overlayer of Pt help to stabilizes the bulk structure by protecting the core alloy from further oxidation. The skeleton structure can be obtained as dissolution of the less noble metals atoms; these leached surfaces typically exhibit a 1-2 nm thick Pt overlayers containing negligible amounts of other metals. In Platinum skin, the external surface consists in a single monolayer and that is stable under electrolyte exposure. These Pt-skin structures are highly ordered and typically show a very high crystallography. From the second layer the less noble metal concentration increase, however the concentration profile shows an oscillatory behaviour in the surface layers after the top layer [56].

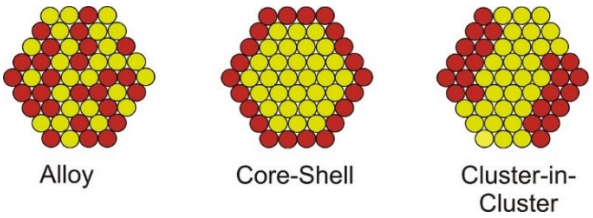

Figure 18: Different structures of metals alloy

Data Source: https://phys.org/news/2014-03-atomic-layer-deposition-bimetallic-nanoparticles.html

The dealloying process can be executed with an electrochemical way, applying an cathodic potential, or via chemical using strong acid as HF. The electrochemical dealloying produces a uniform Pt rich overlayer, an order structure and a smooth surface, the Platinum structure can be modify changing the electrochemical parameters. The chemical dealloying leaves no ordered structure, a typical structure is the spongy structure. Both structures are more active that pure Pt with the electrochemically dealloying, the catalyst show a highest specific activity. When the dealloying is obtaining with chemical reaction, the resulting catalyst show an increment of surface area and mass activity.

The main characteristic of an alloy process is the insertion of a second metal in the platinum structure. During the insertion, the binding energy is modifying by two mechanisms: Strain effects and the electronic effect. The two mechanisms can be explained by the d-band model that describes how the position of the d-band, in transition metals, directly influence adsorbates binding energies. Shifting the d-band centre down will weaken the adsorbates interaction with the surface, while an upwards shift will increase the interaction. The weakening of the binding energies of adsorbates on the surface of platinum can be achieved through alloying; so, the electronic structure of the Pt atoms will change. In the case of ORR in a platinum based material, if the d-band shift is to lower energy the reaction rate increase while if the binding energy shift to higher value, the reaction becomes unfavourable [63, 64].

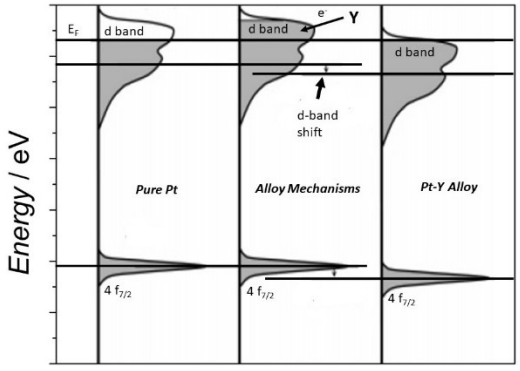

Figure 19: Electronic effect in Platinum Yttrium alloy

The insertion of the second metal with different electronegativity changes the center of the d-band and thereby alters the binding energy of the adsorbates. Depending on the less noble metal the binding of the adsorbates can be weakened or strengthened; for example, in Platinum yttrium alloy the ORR rate is increased while in PtGd the reaction rate is considerably decrease. For metals where the d-band is more than half filled, compressive strain increases the overlap between the atoms d-orbitals. The d band center will move down as the filling degree cannot change, weakening the interaction with adsorbates. The Figure 19 show the interaction between cobalt and platinum, the electronegativity of platinum and cobalt are 2.28 and 1.88, respectively. After the insertion, the cobalt donates electronic density to the d-band of platinum, caused an increment of electronic density (the process is favourable thanks to the band overlap). To compensate the increment of population in the d-band, this one will shift to smaller binding energy [65]. The insertion of the second metal in the platinum structure causes a variation of platinum-platinum interatomic distance. Considering the kagome structure, increasing the covalent radius the platinum-platinum interatomic distance decrease. Generally, decreasing the atomic number of the metal, decrease the covalent radio. Figure 20 show the platinum overlayer compression due to the expansion of platinum-platinun distance in thenars neighbours atoms.

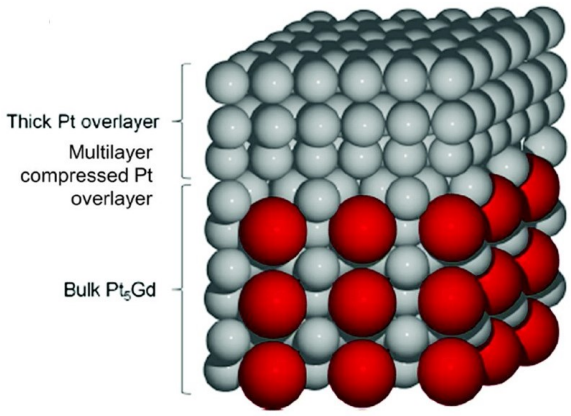

Figure 20: Sketch of "geometric effect" of a Pt_5Gd alloy

Data Source: S.G. Peera, T.G. Lee, A.K. Sahu, Pt-rare earth metal alloy/metal oxide catalysts for oxygen reduction and alcohol oxidation reactions: An overview, Sustain. Energy Fuels. 3 (2019) 1866–1891. doi:10.1039/c9se00082h.

The high levels of strain in lead to a dislocation in the Pt overlayer. This relaxation explains the decrease in activity observed for Platinum-Tb, Platinum-Dy and Platinum-Eu. Alloys of Pt and late transition metals with their promising ORR activities, solve some of the problems involved in the development of efficient PEMFCs. The stabilization of the Pt overlayers that would ensure the necessary long-term stability of the cathode is still a big challenge. The problem is in the synthesis of these catalysts which show an high overlayer stabilization; the more commonly methods used are in UHV, this makes the catalyst not usable in fuel cells.

The common durability of a platinum catalysts in a PEM-Fuel Cell is ca. 3000 h. These observations motivated many groups to carry out a theoretical DFT screening study in search of new Pt alloys for the ORR which have

a higher stability. The results show as the resulting alloy, considering a Pt/M ratio of 3, must satisfy the follow requirements

- Pt (or Pd) overlayers with binding energy vs. the HO adsorption about 0.1 eV weaker than the one of pure Pt.
- The heat of alloy formation, defined as the amount of energy gained during the bulk alloy formation by its constituents, must be as negative as possible.

This new class of catalysts, constituted by Pt and an early transition metal, is characterized by extremely negative heats of alloying formation. Pt_3Y, Pt_3Ni, Pt_3Fe and Pt_3Co owns an binding energy higher of 0.08 eV – 0.12 eV than platinum, as showing in Volcano plot in Figure 21b.

Interestingly, the heat of alloy formation of Pt_3Co and Pt_3Ni, as for most of the alloys of Pt and late transition metals, is basically negligible and explain their dealloying tendency. The stability is strongly connected to the dissolution of less noble metals [65, 66, 67].

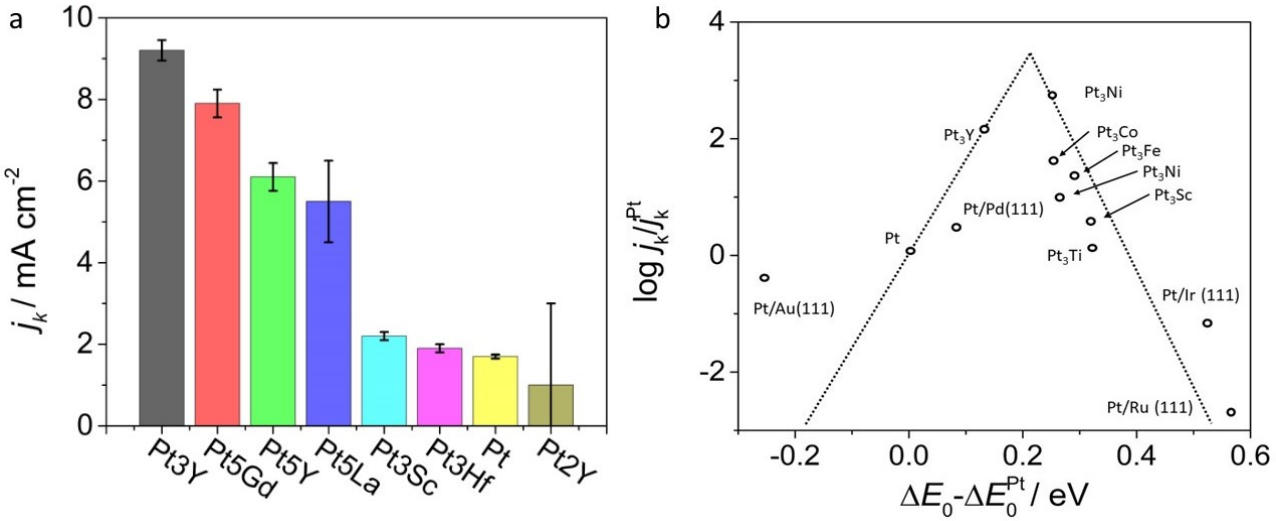

Figure 21: a) Electrochemical Activity vs. ORR for the most popular alloys; b) Volcano plot for platinum alloy materials

3.2 Effect of Carbon Support on the Catalytic Activity for ORR

A platinum nanoparticles catalyst needs a carbon support with an high specific surface area due to the mesoporosity, an high graphitization, medium hydrophobic proprieties, an high graphitization and a low cost (Figure 22). The carbon support is not a total inert material and it can favour the electron transfers the electrode-electrolyte interface, so accelerate or decelerate the electrode processes. In the carbon-supported Pt system, the interaction between the carbon and platinum favour the electron transfer from Pt active sites to oxygen atoms adsorbed on carbon surface. In many cases, chemical bonds can be formed due to the charge transfer between the contacting phases. [68, 69].

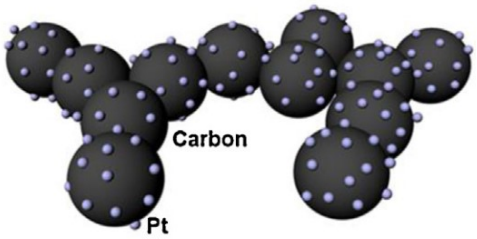

Figure 22: Sketch of distribution of Pt NPs on Carbon matrix

The carbon support may affect the geometry and electronic structure of Pt nanoparticles. The electrons in a carbon supported Pt system have been proved to transfer not only within Pt, but also from Pt sites to carbon. The basic properties of carbon support are (1) high electrical conductivity, (2) high specific surface area and high porosity, (3) good interaction of support with Pt (Pt-alloy), and (4) easy metal recycling in the used electrocatalyst. The carbon support may not only modify the electronic character of the Pt but also influence the shape and distribution of the deposited Pt NPs. It has been found that the specific surface area, pore size distribution, and surface properties of carbon material strongly influence the size, size distribution of Pt particles, surface structure and morphology, and alloying degree and therefore the structure and morphology of the catalyst, affecting the number of the active sites on the catalyst surface and thus ORR activity in PEMFCs. The specific surface area of the support as well as the oxygen surface groups affected the particle size and dispersion and catalytic performance. Carbon support may cause a sintering/agglomeration of Pt nanoparticles under fuel cell operation and thus the decrease of electrocatalytic surface area, resulting in the degradation of catalyst and the decrease of catalytic activity and fuel cell performance (Figure 23) [70, 71, 72].

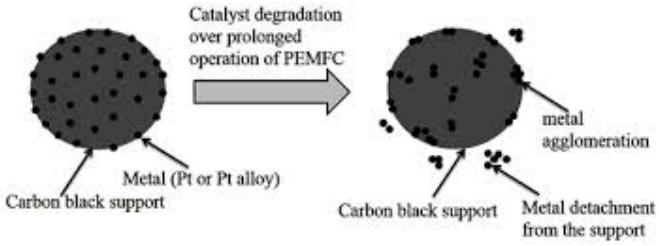

Figure 23: Platinum NPs on carbon support degradation

The morphological aspects most investigated are the surface area and the pore dimension and interconnection or distribution. In fact, high surface area is necessary for optimizing the Pt active phase dispersion, whereas wide and interconnected pores are desirable for improving mass transport of reagents or the products. The modification of the support chemical properties generally consists in the introduction of surface functional groups of heteroatoms such as nitrogen, boron, phosphorus and sulphur, a process that is commonly known as doping. For an high NPs stabilization and a good mass transport, the carbon must show a mesoporous structure. Mesoporous carbons are ideal materials for electrocatalysis since they have large surface area from 200 m^2 g^-

[1] to 1000 m^2 g^{-1}, uniform and adjustable pore size, which allows a favourable mass transport and they can be easily doped.

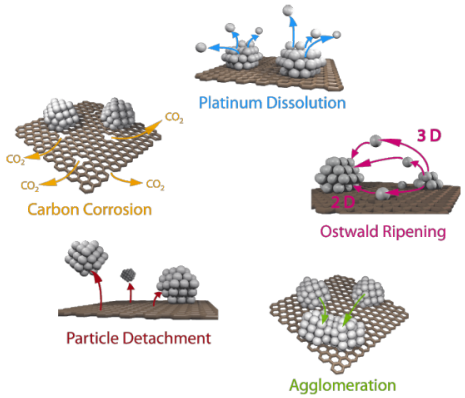

Figure 24: Sketch of the main catalysts degradation

Data Source: T.W. Napporn, A. Mokrini, F.J. Rodríguez-Varela, Introduction: Low-Temperature Fuel Cells, in: Adv. Electrocatal. Low-Temperature Fuel Cells, Springer International Publishing, Cham, 2018: pp. 1–49. doi:10.1007/978-3-319-99019-4_1.

For stabilized the NPs and prevent the typical aggregation or detachment process (Figure 24) the carbon support must have a mesoporous volume higher by two times than the micropore volume. These parameters are in close contact with the total surface area; considering the same number of porous, the microporous have a stronger impact on the total surface than the mesoporous. Other important parameters are the pore volume (micro and meso porous) and the pore dimensional distribution. Considering the pore geometry and the pore dimension, the pore volume describes how the channel propagates inside the carbonaceous structure. In a platinum base material, the optimal NPs dimensions are in the range 2 nm – 8 nm; the NPs must be distributed not only in the external surface of the carbon particles but also inside the pore structure. Generally, a carbon must have an high mesoporous structure to host the metal nanoparticles, the correct pore dimension is between 8 nm - 15 nm. The carbon used for Pt deposition, for catalysed the ORR, have a total surface area from 150 m^2 g^{-1} to 500 m^2 g^{-1}. Lower surface area is connected to an too low pore volume for hosting metal NPs or a low pore number (for area unit). Higher surface area can be obtained increasing the microporous ($d_{pore} < 2$ nm) or increase the total pore number, however, the process destabilizes the carbon structure, making the carbon mechanically more fragile and subject to structural collapse. The collapse is a negative process which can occlude the NPs inside the carbon structure (in an area inaccessible to the electrolyte solution) and decrease the number of active sites [72, 73].

3.2.1 Carbon Support Modification

Activated carbon is a carbonaceous, highly porous adsorptive medium that has a complex structure composed primarily of carbon atoms. The networks of pores in carbons are channels created in a rigid skeleton layers of carbon atoms. The typical structure is highly porous structure which nooks, crannies, cracks and crevices between the carbon layers. Carbon surface area, mesoporosity or microporosity can be modify with different treatment i.e steam or CO_2 at high temperature or with a KOH activation. The most common process is steam activation; at around 1000°C steam molecules selectively burn holes into the carbonized raw material, thus creating a multitude of pores inside the carbonaceous matrix. The chemical reaction between the carbon and steam takes place at the internal surface of the carbon, removing carbon from the pore walls and thereby enlarging the pores. In the steam treatment the time reaction has a stronger impact on the morphology than the synthesis temperature. Increasing the time, new pores are created, and the pore structures increase its dimension. The size increment depends by the graphitization of the carbon support. Currently, steam treatment is the best process for increase the mesoporous structure, but in the other hand is dangerous because the treatment corrodes also the external structure, decreasing the mechanical proprieties of the carbon, so increasing collapse effect [74].

$$C + H_2O \rightarrow H_2 + CO \quad (3.1)$$

$$C + 2H_2O \rightarrow 2H_2 + CO_2 \quad (3.2)$$

$$C + CO_2 \rightarrow 2CO \quad (3.3)$$

$$CO + H_2O \rightarrow CO_2 + H_2 \quad (3.4)$$

Carbon dioxide activation mainly causes the creation of microporosity and its increment. Activation by carbon dioxide creates not only a larger number of groups evolving as CO but also these groups are thermally more stable than those produced by steam activation. Activated carbons prepared by carbon dioxide activation exhibit a larger micropore volume and a narrower micropore size distribution than those pre- pared by steam activation [75]. The nature of the activating agent hydrogen, steam or carbon dioxide and the way the contact between the agent and the fuel occurs, may influence significantly the yield and the quality of the products. Steam or a mixture of steam and carbon dioxide, favours efficient removal of the volatile products from the carbonising material and formation of a product with increased surface area.

Chemical activation is generally made by mixing carbon materials with chemical activating agents i.e. KOH, H_3PO_4, $ZnCl_2$, followed by the carbonization at 400 °C - 900 °C. The chemical activation of various carbon sources using KOH as the activating reagent is very promising because of its lower activation temperature and higher yields, and well defined micropore size distribution [76, 77].

$$2KOH \rightarrow K_2O + H_2O \quad (3.5)$$

$$C + H_2O \rightarrow CO + H_2 \quad (3.6)$$

$$CO + H_2O \rightarrow CO_2 + H_2 \quad (3.7)$$

$$CO_2 + K_2O \rightarrow K_2CO_3 \quad (3.8)$$

$$K_2CO_3 \rightarrow K_2O + CO_2 \quad (3.9)$$

$$K_2CO_3 + 2C \rightarrow 2K + 3CO \quad (3.10)$$

$$K_2O + C \rightarrow 2K + CO \quad (3.11)$$

Based on the above reaction, three main activation mechanisms for KOH activation of carbon are confirmed:
(a) Etching the carbon framework by the redox reactions between various1 potassium compounds as chemical activating reagents with carbon, called chemical activation, is responsible for generating the pore network;
(b) the formation of H_2O and CO in the activation system positively contributes to the further development of the porosity through the gasification of carbon, namely physical activation;
(c) the as prepared metallic K, efficiently intercalating into the carbon lattices of the carbon matrix during the activation, results in the expansion of the carbon lattices.

3.3 Platinum Loading on Mesoporous Carbon

The loading method of Pt on carbon support can determine the catalytic properties of the final product. The choice of loading method to prepare carbon supported Pt based materials indeed depends on the physical and chemical characteristics desired in the final composition. The metal loading is connected to the carbon characteristics as porosity, surface area. Moreover, low surface area (around 250 $m^2 g^{-1}$) carbon material may not enough to accommodate Pt nanoparticles with a dimension of 10 nm and with a loading in the range 20 % - 35%$_w$. Moreover, due to corrosion of carbon, Pt nanoparticle on the carbon support agglomerates and loses the support material (carbon). Generally, the carbons for Platinum NPs deposition shows a surface area in the range 220 m2 g-1 – 450 m2 g-1, such as Vulcan XC-72 or Carbon Black Acetylene [78, 79].
The most common methods for the Pt deposition are chemical precipitation, impregnation, colloidal, microemulsion, electrodeposition, pulse electrodeposition, vapor phase method, sputter deposition technique, cationic exchange, sonochemistry and ultrasonic spray pyrolysis, supercritical fluids, high energy ball milling, etc. The goal is the obtaining of stable and robust catalysts which can preserve their initial morphologies under fuel cell operation over long periods, the catalysts must show a low NPs aggregation and a narrow Pt particle size distribution. The synthesis method can modify also the crystallinity and the shape of the nanoparticles [80, 81, 82].

Considering the platinum metal loading, the platinum based materials for ORR can by divided in three categories:

1. Low Platinum Catalysts, the platinum loading is in the range 0.5 %w – 5 %w. In these catalysts the NPs owns a dimension < 1 nm. Despite the low loading, the materials show an high active surface area. The carbon used for the metal deposition must have an microporosity from 1 nm to 3 nm, and an high graphitization for stabilize the NPs growing.
2. Medium Platinum catalysts, the loading most often used in a catalyst for PEM-Fuel Cell. The loading range is from 15 % to 35 %. A surface area of 350 m2 g-1 and an high mesoporous structure are basic requirements for obtain a good NPs distribution without the aggregate formation. The NPs, generally, show a dimension from 1.5 nm to 7.5 nm.
3. Ultra-Platinum catalysts, the platinum content is higher than 40%. The problem in this type of catalysts is the NPs size control. The dimension distribution can vary from 2 nm to 50 nm, depends by the carbon support. For carbon with a surface area < 50 m^2 g^{-1}, the optimal NPs dimension is higher than 40 nm and only distributed in the external surface and not inside the pores. When the carbon support shows a medium surface area and an equal meso/micropores distribution, the catalysts show a multimodal size distribution.

3.4 Impact of NPs size on the catalytic activity vs. ORR

Carbon-supported Pt catalysts, in the form of nanoparticles, can provide much higher surface area, or in other term an high number of active sites, for the reacting molecules in an electrochemical reaction. The electrocatalytic activity was significantly affected by nanoparticle size. The optimal dimension can change refer to the reaction and to the metal used as catalysts. For example, the catalysts used for the CO_2 reduction is Tin or Au based material; the maximum performance in tin oxide material are obtained with NPs size of 35 nm, while for gold the optimal dimension is around 12 nm. In the Oxygen Reduction Reaction two commons catalysts are Platinum and Gold, with increasing particle size, the catalytic rate for Au particles increase, whereas a decrease was observed for Pt particles. In platinum based material the correlation between the NPs dimension and the catalytic activity show a trend at maximum. For a Pt NPs the best electrochemical performance, in terms both activity both stability, can be obtained with a size of 1.5 nm – 2.5 nm, for Pt_3Y alloy NPs the best dimension for the increasing only the activity are 7 nm – 10 nm, in Pt_5Gd the best dimension is 9 nm – 13 nm [83, 84]. This difference resulted from a volcano-shaped relationship between electrocatalytic activity and the electronic state of the atoms. Platinum on carbon catalysts were more useful in practical industrial applications than the semi-infinite surfaces because the catalysts can provide a larger surface area in which the catalytic reaction can run simultaneously with higher activities. The size of these catalyst particles might range from <1 nm to 10 nm in diameter, which is strongly dependent on the catalytic effect of extended surfaces on those nanoparticles [47].

Higher mass activities can be achieved by raising the level of catalyst dispersion (for example, the number of active sites per mass of catalyst) or by raising the intrinsic activity, in terms of area, per active site (specific activity). Unfortunately, in most cases these two quantities are connected and so they cannot modify independently. Another crucial problem in the small NPs (< 2 nm) is the agglomeration process during the electrochemical working, the NPs can aggregate for Ostwald Ripening, in this case the NPs size increase and the surface active area and mass activity collapse drastically. In the case of pure Pt nanoparticles, for instance, a higher dispersion can be reached by decreasing the particle size. However, while the catalyst dispersion increases for smaller sizes, increase also thee number of active sites, with an under coordination, on the surface favouring so the agglomeration. On these sites (e.g. steps, edges and kinks) the ORR intermediates (for instance HO*) bind more strongly, causing higher overpotentials and lower specific activities. The combination of these two opposite trends generates a maximum of mass activity at a particle size of about 3 nm, which is not optimal in terms of catalyst stability [85, 86].

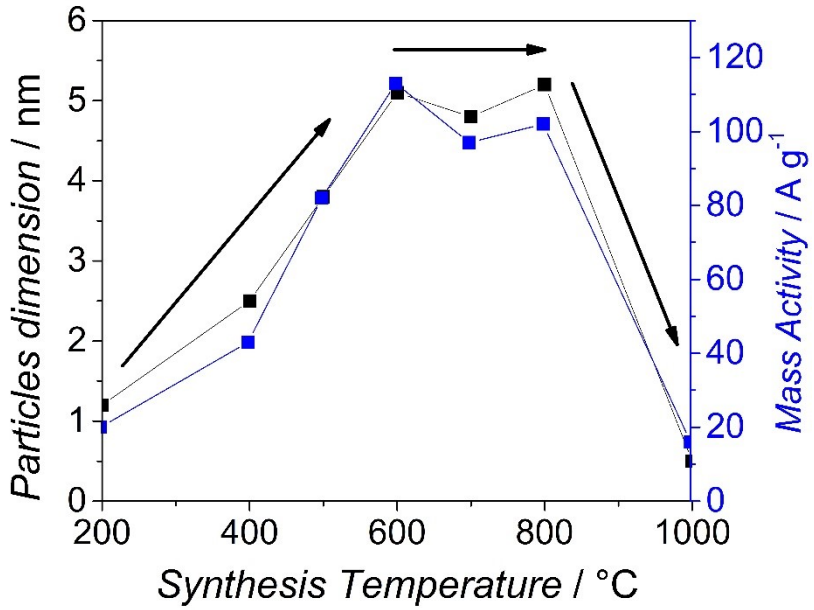

Figure 25: Size correlation between temperature in a solid state synthesis and electrochemical performance vs. ORR of a Pt_3Ni catalyst

Some of the most important challenges in synthesizing carbon supported Pt nanoparticles are the different nucleation and growth rates of different elements, which are directly related to the formed nanoparticle size and size distribution, and thus to ORR activity. Typically, the reduction of the Pt precursor (e.g., platinum acetylacetonate, $Pt(acac)_2$) occurs faster than 3d transition metals such as Mn, Fe, Ni, Co, and Cu, in the synthesis of carbon supported Pt alloy particles because Pt has a much higher reduction potential, for the Pt^{2+}/Pt, $E^0 = +1.2$ V, than 3d transition metals where E^0 is in the range - 0.2 V and - 0.4 V). As a result, the precious metal is prone to nucleate first and grow into separate nanoparticles or form Pt-rich regions in the product. In the synthesis of carbon-supported Pt alloy nanoparticles, nucleation can be induced by increasing temperature, adding a precursor, and adding a secondary metal precursor (Figure 25). The activity of a catalyst

for the ORR is inversely proportional to the particle size, while the active sites area is independent by the particle size. A broad size distribution and relatively large particle size will lead to nonuniform chemical composition among alloy nanoparticles and thus decrease the catalyst's ORR activity. It is not easy to control particle size and size distribution, since very small particles (< 2 nm) are significantly prone to agglomeration or corrosion under practical synthesis conditions. Recently, much research has been devoted to developing various new methods to reduce Pt-alloy size and narrow down particle size distribution to enhance catalytic performance, including thermal evaporation in a vacuum and pulsed laser deposition, chemical vapor deposition, gas condensation, electrochemical deposition and impregnation. Each synthesis has a different impact on the particles size and on the distribution on the carbon support [85, 54].

3.4.1 Control size factor

The critical factors for the size and distribution control are:

- pH
- Protective agent
- Temperature of synthesis
- Time
- Reactant composition

A homogeneous deposition (HD) strategy for the synthesis of carbon-supported Pt nanoparticles can be realized by in situ hydrolysis of urea, in which a gradual increase in pH lead to a NPs size increment. As a result, a Pt complex species with small particle sizes was uniformly deposited onto the carbon support. A nanoparticle size of 18 nm was achieved in a pH range of 10 ÷ 12 due to the good balance between the formation and growth steps. However, at a pH of around 13, the nanocrystal growth stopped [87, 88].
At pH < 7 the situation is different, with a decrease in pH from 4.0 to 1.5, the size of Pt NPs increased without aggregate formation, at pH < 1 the size control fails, and the Nanoparticles tend to aggregate. For platinum alloy based material the situation is more complex because the size of binary Pt alloys is closely related also to the type of the second metal.
Heat treatment has been extensively studied as a means of controlling particle size in the synthesis of various carbon-supported Pt_xM. The role of heat treatment is mainly to assist alloy formation by increasing the mobility of the metal particles. Obviously, the particle size considerably increases with the heat treatment temperature; the same considerations can be doing for the time synthesis. Increasing the time, the NPs can grow and rising the formation probability of aggregate. The degree of alloying is found to be dependent on the lattice constant and is also a function of the treatment temperature, the lattice constant decreases with increasing temperature. Therefore, the degree of alloying can be controlled by adjusting the heat treatment temperature, even though high temperature may increase the particle size [89]. The control size factor depends by the synthesis; Laser

Ablation is an fast and easy method for the NPs synthesis of Pt, Pd, Co or Fe the NPs. The NPs distribution show a multimodal dimension, in a very wide range, using appropriate protection agents is possible modulate the size. Lin at all. show the synthesis of Platinum and Palladium NPs by LAS in a aqueous solution of NaCl. The salt addition modulates the NPs growing and permits to obtain a unimodal size distribution. The NaCl solution endows the Pd NPs with neat charges which depress the aggregation of NPs. In addition, the particle dimension decreases with the increment of NaCl concentration, and the structure transforms from polycrystalline to monocrystalline at NaCl concentration of 0.1 M. The dimensional distribution can be narrowed with annealing treatment in N_2, the thermal treatment increases also the crystallinity [90].
Finally, in bimetallic system the salts precursor plays an important role on the NPs size, generally an reduction process both in wet environmental both in solid state provides the degradation of the ligand and the reduction from M^{n+} to metal state. The two processes occur concurrently, inorganic ligands, such as NO_3^-, Cl- or SO_4^{2-} stabilize better than organic ligands (such as acetate or acetylacetonate) the NPs growing. Inorganic ligands permit to obtained NPs with a dimension lower than when organic ligands are used. In addition, with organic ligand the aggregate population increase. The effect is connected to the ligand degradation, the dissociation of inorganic ligand is most fast and provide less intermedia. Platinum alloy system show different stoichiometric ratio, different metal ratio can influence the NPs size. The Platinum alloy NPs show a core shell structure, with a platinum shell and a alloy core. The NPs size increase with the increment of the concentration of the second metal. Increasing the second metal, the core is most stretched, and the NPs show an increment of size. However, an high increment of the concentration can increase the dimension but reduce the NPs density [91].

3.5 Impact of NPs shape on the catalytic activity vs. ORR

Morphology control plays a key role in developing high performance catalysts with unique physical and chemical properties. These nanostructures correspond to a precise particle shape and controlled particle size, with different surface areas and crystallographic facets. The catalytic performance of Pt-based is directly connected to their crystal facets. Many shaped PGM alloy nanoparticles show extraordinary catalytic property comparing to the same metal alloy without morphology control. The effect of nanosized induced surface contraction on facet dependent oxygen binding energy [92]. The platinum index has also a strong impact on the catalyst durability, high index planes such as (311) or (220) are instable, the NPs tend to grow over limit and decrease the electrochemical performances. The moderately compressed (111) facets were most conducive to ORR on small nanoparticles, which could result in the compressive strain effect and thus enhance the ORR activity. In addition, it is suggested that a nanostructure with high-index facets exhibits higher catalytic activity than common nanostructures with low-index facets. Shape controlled Pt-alloy catalysts are much more complicated and challenging than the size control both in experimental preparation and both in characterization [86]. Generally, the shape of nanoparticles in carbon-supported Pt NPs catalysts is determined by thermodynamics and kinetics during the synthesis process: it is also dependent on the intrinsic structural

properties of the Platinum and the reactants, such as the solvent, capping agent, and reducing agent or temperature/ time synthesis, used in the production process. During the formation of Pt nanoparticles, some facets similar to 111 planes (for examples, (100), (110), and (111)) often form to minimize surface energy and total excess free energy. The different planes of a Pt exhibited different ORR activities. The ideal determinate shapes of Pt and Pt alloy based material NPs may have certain low index planes for obtained high performance for ORR. The typical shapes obtained for platinum based material are: (1) tetrahedron, (2) cube, (3) octahedron, (4) truncated cube, (5) cuboctahedron, (6) truncated octahedron, (7) bipyramid, (8) decahedron, (9) rod and (10) icosahedron [86, 93]. Figure 26 show the common structure for a platinum catalyst.

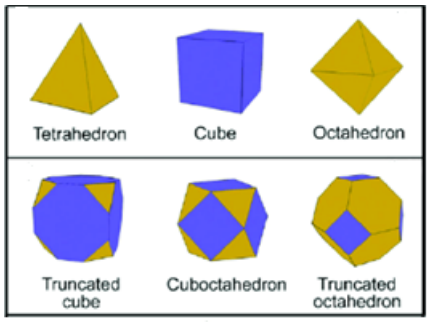

Figure 26: Typical Platinum structures

Most of the successes in preparing shaped PGM nanoparticles have been achieved using wet chemistry, which involves the reduction of metal precursors in a solvent and the use of organic surfactants for confining the formation of particle morphology. For example, sodium polyacrylate confine the growth of Pt (100) planes. With a low concentration of sodium polyacrylate, Cubic Pt nanoparticles were obtained. A mixture of cubic and tetrahedral Pt particles were synthesized when the organic surfactant concentration is increased. A material with an homogeneous crystallography is impossible to obtained. The influence of substrates on the particle size could be attributed to their different surface chemistry, which can alter the reduction and nucleation process of metals and consequently their growth kinetics [94].

3.5.1 Factor Shape

For control the particle shapes different methods are available:

- Organic capping agent
- Templating approaches
- Inorganic ions

In wet chemistry, organic capping agents as hydrocarbons with long chain, can provide a barrier to limit the direct contact between relatively high energy metallic surfaces which can react and therefore stabilize the metal nanoparticles. Because the capping agent is adsorbed thus lead to a decrement of agglomeration process but

especially limit the further growth of the particles. In other words, the morphology of the nanocrystals can be controlled only after the selective adsorption of the capping agent onto a specific type of facet [95, 96].

Typical capping agent are long alkene chain ammines, generally used for obtained cubic and truncated octahedral nanoparticles. In addition to the use of different alkane chain length, a combination of strong or mild reduction agents was used to effectively adjust the nucleation and growth rate.

Inorganic ions and other small molecules can also prevent metal nanoparticle size from increasing and affect the shape of formed metal nanoparticles. However, after they are adsorbed onto specific facets of metal nanoparticles, inorganic species cannot afford the counterpart in the interaction to promote or inhibit further growth along given directions. Typically, inorganic ions such as bromide or iodide are adsorbed on the surface of Pt nanoparticles, favouring the stabilization of the (100) facet and thus the formation of monodispersed Pt tetrahedrons and cubes with dimension lower than 10 nm.

This effect is commonly used in Lased Ablation for control the NPs shape. Template synthesis approaches have been considered the best way to prepare shape controlled Pt-based materials. Both chemical and physical templates can offer confined spaces and/or functionalized structures for the formation and growth of a Pt structure. The templates are often classified into two basic categories: hard and soft. The hard templates (e.g., anodic aluminium oxide, mesoporous silica, and lithographically patterned templates) consist of spatially well-defined physical structures, while the soft templates include self-assembled and self-organized structures in solution [97]. The obtained shape of a Pt or Pt-alloy nanocrystals is a competition in surface energies of the different facets. The preparation of shaped PGM nanoparticles using wet chemistry methods often encounters several crucial problems, including complex synthetic procedure, scale-up difficulty, and surface contamination of made particles, which have largely hindered practical applications of these materials. Another synthetic route where is possible control the platinum shape is high temperature solid state synthesis in assisted reduction atmosphere, for example using a mixture of H_2 and CO. The different surface exposure of PGM nanoparticles is attributed to the different interaction between CO and the faces, which altered the surface growth rate and led to specific particle morphology. Carbon monoxide absorption was found more energy favourable on the (100) planes of Pt, which tailored the growing Pt particles into cubic shape. It causes the slowest growth rate of the (111) planes, which consequently become the exposure surface and confine the particle growth into octahedral morphology [93, 97]. Different platinum structure such as cube, octahedron or truncated octahedron show different index plane (**Errore. L'origine riferimento non è stata trovata.**), which own a different stability and, so, have different activity vs. the ORR.

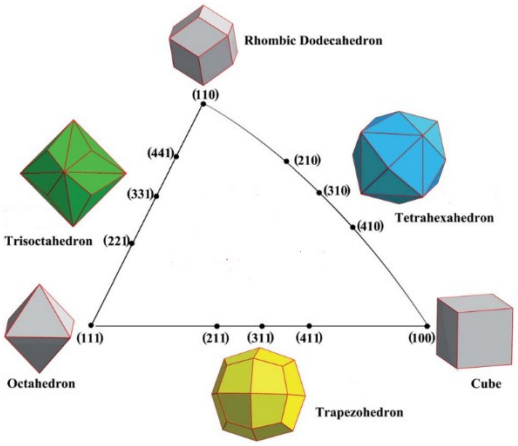

Figure 27: Typical planes index for the different platinum structures

Data Source: X.M. Zeng, R. Huang, G.F. Shao, Y.H. Wen, S.G. Sun, High-index-faceted platinum nanoparticles: Insights into structural and thermal stabilities and shape evolution from atomistic s

3.6 Parameters for a high catalytic activity vs. ORR

There are different types of ORR electrocatalysts developed in the past 2 decades. However, the following requirements are essential for a good ORR electrocatalyst.

- High catalytic activity towards ORR
- High electrical conductivity of the support
- High mesoporous surface area
- High chemical and electrochemical stability
- Should not dissolve in the electrolyte (insoluble in acidic or basic aqueous solutions)
- Favourable optimum structural composition, morphology, high specific surface area, small particle size, high porosity, and uniform distribution of catalyst particles on the support
- Particle shape and crystallographic selectivity
- High interaction between the catalyst particle and the support surface
- High catalytic stability

All these factors dictate what materials and synthetic strategy will be selected, to achieve technological breakthroughs in the microstructure and performance of ORR catalysts.

3.7 Bibliography

[52] K. Sasaki, J.X. Wang, H. Naohara, N. Marinkovic, K. More, H. Inada, R.R. Adzic, Recent advances in platinum monolayer electrocatalysts for oxygen reduction reaction: Scale-up synthesis, structure and activity of Pt shells on Pd cores, Electrochim. Acta. 55 (2010) 2645–2652. doi:10.1016/j.electacta.2009.11.106.

[53] K. Jukk, N. Kongi, P. Rauwel, L. Matisen, K. Tammeveski, Platinum Nanoparticles Supported on Nitrogen-Doped Graphene Nanosheets as Electrocatalysts for Oxygen Reduction Reaction, Electrocatalysis. 7 (2016) 428–440. doi:10.1007/s12678-016-0322-1.

[54] M. Shao, Q. Chang, J.P. Dodelet, R. Chenitz, Recent Advances in Electrocatalysts for Oxygen Reduction Reaction, Chem. Rev. 116 (2016) 3594–3657. doi:10.1021/acs.chemrev.5b00462.

[55] O.T. Holton, J.W. Stevenson, The role of platinum in proton exchange membrane fuel cells, Platin. Met. Rev. 57 (2013) 259–271. doi:10.1595/147106713X671222.

[56] I.E.L. Stephens, A.S. Bondarenko, U. Grønbjerg, J. Rossmeisl, I. Chorkendorff, Understanding the electrocatalysis of oxygen reduction on platinum and its alloys, Energy Environ. Sci. 5 (2012) 6744–6762. doi:10.1039/c2ee03590a.

[57] I. Jiménez-Morales, S. Cavaliere, D. Jones, J. Rozière, Strong metal-support interaction improves activity and stability of Pt electrocatalysts on doped metal oxides, Phys. Chem. Chem. Phys. 20 (2018) 8765–8772. doi:10.1039/c8cp00176f.

[58] S. Zhang, Z. Xia, T. Ni, Z. Zhang, Y. Ma, Y. Qu, Strong electronic metal-support interaction of Pt/CeO2 enables efficient and selective hydrogenation of quinolines at room temperature, J. Catal. 359 (2018) 101–111. doi:10.1016/j.jcat.2018.01.004.

[59] B. Garlyyev, K. Kratzl, M. Rück, J. Michalička, J. Fichtner, J.M. Macak, T. Kratky, S. Günther, M. Cokoja, A.S. Bandarenka, A. Gagliardi, R.A. Fischer, Optimizing the Size of Platinum Nanoparticles for Enhanced Mass Activity in the Electrochemical Oxygen Reduction Reaction, Angew. Chemie - Int. Ed. (2019) 9596–9600. doi:10.1002/anie.201904492.

[60] S. Akbar, A. Anwar, M.Z. Noon, J.M. Elliott, A.M. Squires, Platinum as an electrocatalyst: effect of morphological aspects of Pt/Pt-based materials, Mater. Sci. Technol. (United Kingdom). 35 (2019) 1–11. doi:10.1080/02670836.2018.1495878.

[61] D. Van Der Vliet, C. Wang, M. Debe, R. Atanasoski, N.M. Markovic, V.R. Stamenkovic, Platinum-alloy nanostructured thin film catalysts for the oxygen reduction reaction, Electrochim. Acta. 56 (2011) 8695–8699. doi:10.1016/j.electacta.2011.07.063.

[62] Q. Jia, M.K. Bates, S. Mukerjee, W. Liang, P. Mani, W. Lee, Activity descriptor identification for oxygen reduction on platinum-based bimetallic nanoparticles: In situ observation of the linear composition-strain-activity relationship, ACS Nano. 9 (2015) 387–400. doi:10.1021/nn506721f.

[63] A. Oh, H. Baik, D.S. Choi, J.Y. Cheon, B. Kim, H. Kim, S.J. Kwon, S.H. Joo, Y. Jung, K. Lee, Skeletal

octahedral nanoframe with cartesian coordinates via geometrically precise nanoscale phase segregation in a Pt@Ni core-shell nanocrystal, ACS Nano. 9 (2015) 2856–2867. doi:10.1021/nn5068539.

[64] P. Hernandez-Fernandez, F. Masini, D.N. McCarthy, C.E. Strebel, D. Friebel, D. Deiana, P. Malacrida, A. Nierhoff, A. Bodin, A.M. Wise, J.H. Nielsen, T.W. Hansen, A. Nilsson, I.E.L. Stephens, I. Chorkendorff, Mass-selected nanoparticles of Ptx y as model catalysts for oxygen electroreduction, Nat. Chem. 6 (2014) 732–738. doi:10.1038/nchem.2001.

[65] J. Ma, A. Habrioux, Y. Luo, G. Ramos-Sanchez, L. Calvillo, G. Granozzi, P.B. Balbuena, N. Alonso-Vante, Electronic interaction between platinum nanoparticles and nitrogen-doped reduced graphene oxide: Effect on the oxygen reduction reaction, J. Mater. Chem. A. 3 (2015) 11891–11904. doi:10.1039/c5ta01285f.

[66] M.P. Hyman, J.W. Medlin, Effects of electronic structure modifications on the adsorption of oxygen reduction reaction intermediates on model Pt(111)-alloy surfaces, J. Phys. Chem. C. 111 (2007) 17052–17060. doi:10.1021/jp075108g.

[67] E. Antolini, J.R.C. Salgado, M.J. Giz, E.R. Gonzalez, Effects of geometric and electronic factors on ORR activity of carbon supported Pt-Co electrocatalysts in PEM fuel cells, Int. J. Hydrogen Energy. 30 (2005) 1213–1220. doi:10.1016/j.ijhydene.2005.05.001.

[68] M. Watanabe, H. Sei, P. Stonehart, The influence of platinum crystallite size on the electroreduction of oxygen, J. Electroanal. Chem. 261 (1989) 375–387. doi:10.1016/0022-0728(89)85006-5.

[69] S. Nayak, I.J. McPherson, K.A. Vincent, Adsorbed Intermediates in Oxygen Reduction on Platinum Nanoparticles Observed by In Situ IR Spectroscopy, Angew. Chemie - Int. Ed. 57 (2018) 12855–12858. doi:10.1002/anie.201804978.

[70] M. Inaba, M. Ando, A. Hatanaka, A. Nomoto, K. Matsuzawa, A. Tasaka, T. Kinumoto, Y. Iriyama, Z. Ogumi, Controlled growth and shape formation of platinum nanoparticles and their electrochemical properties, Electrochim. Acta. 52 (2006) 1632–1638. doi:10.1016/j.electacta.2006.03.094.

[71] J. Speder, A. Zana, I. Spanos, J.J.K. Kirkensgaard, K. Mortensen, M. Hanzlik, M. Arenz, Comparative degradation study of carbon supported proton exchange membrane fuel cell electrocatalysts - The influence of the platinum to carbon ratio on the degradation rate, J. Power Sources. 261 (2014) 14–22. doi:10.1016/j.jpowsour.2014.03.039.

[72] P. Ehrburger, O.P. Mahajan, P.L. Walker, Carbon as a support for catalysts. I. Effect of surface heterogeneity of carbon on dispersion of platinum, J. Catal. 43 (1976) 61–67. doi:10.1016/0021-9517(76)90293-1.

[73] M.A. Fraga, E. Jordão, M.J. Mendes, M.M.A. Freitas, J.L. Faria, J.L. Figueiredo, Properties of carbon-supported platinum catalysts: Role of carbon surface sites, J. Catal. 209 (2002) 355–364. doi:10.1006/jcat.2002.3637.

[74] V. Minkova, S.P. Marinov, R. Zanzi, E. Björnbom, T. Budinova, M. Stefanova, L. Lakov, Thermochemical treatment of biomass in a flow of steam or in a mixture of steam and carbon dioxide,

Fuel Process. Technol. 62 (2000) 45–52. doi:10.1016/S0378-3820(99)00065-X.

[75] C.A. Toles, W.E. Marshall, L.H. Wartelle, A. McAloon, Steam- or carbon dioxide-activated carbons from almond shells: Physical, chemical and adsorptive properties and estimated cost of production, Bioresour. Technol. 75 (2000) 197–203. doi:10.1016/S0960-8524(00)00058-4.

[76] T. Otowa, Y. Nojima, T.K. Coke, Development of Koh Activated High Surface Area Carbon and Its Application To Drinking, Science (80-.). 35 (1997) 1315–1319.

[77] M. Li, W. Li, S. Liu, Hydrothermal synthesis, characterization, and KOH activation of carbon spheres from glucose, Carbohydr. Res. 346 (2011) 999–1004. doi:10.1016/j.carres.2011.03.020.

[78] S.L. Knupp, W. Li, O. Paschos, T.M. Murray, J. Snyder, P. Haldar, The effect of experimental parameters on the synthesis of carbon nanotube/nanofiber supported platinum by polyol processing techniques, Carbon N. Y. 46 (2008) 1276–1284. doi:10.1016/j.carbon.2008.05.007.

[79] K. Wikander, H. Ekströrn, A.E.C. Palmqvist, A. Lundblad, K. Holmberg, G. Lindbergh, Alternative catalysts and carbon support material for PEMFC, Fuel Cells. 6 (2006) 21–25. doi:10.1002/fuce.200500092.

[80] E.P. Ambrosio, C. Francia, M. Manzoli, N. Penazzi, P. Spinelli, Platinum catalyst supported on mesoporous carbon for PEMFC, Int. J. Hydrogen Energy. 33 (2008) 3142–3145. doi:10.1016/j.ijhydene.2008.03.045.

[81] E. Higuchi, H. Uchida, M. Watanabe, Effect of loading level in platinum-dispersed carbon black electrocatalysts on oxygen reduction activity evaluated by rotating disk electrode, J. Electroanal. Chem. 583 (2005) 69–76. doi:10.1016/j.jelechem.2005.01.041.

[82] S. Taylor, E. Fabbri, P. Levecque, T.J. Schmidt, O. Conrad, The Effect of Platinum Loading and Surface Morphology on Oxygen Reduction Activity, Electrocatalysis. 7 (2016) 287–296. doi:10.1007/s12678-016-0304-3.

[83] Detailed description of the benchmark measurements at TUM_1 - Unknown - Unknown, (n.d.).

[84] F.J. Nores-Pondal, I.M.J. Vilella, H. Troiani, M. Granada, S.R. de Miguel, O.A. Scelza, H.R. Corti, Catalytic activity vs. size correlation in platinum catalysts of PEM fuel cells prepared on carbon black by different methods, Int. J. Hydrogen Energy. 34 (2009) 8193–8203. doi:10.1016/j.ijhydene.2009.07.073.

[85] B.E. Hayden, D. Pletcher, J.P. Suchsland, L.J. Williams, The influence of support and particle size on the platinum catalysed oxygen reduction reaction, Phys. Chem. Chem. Phys. 11 (2009) 9141–9148. doi:10.1039/b910110a.

[86] M. Nesselberger, M. Roefzaad, R. Fayçal Hamou, P. Ulrich Biedermann, F.F. Schweinberger, S. Kunz, K. Schloegl, G.K.H. Wiberg, S. Ashton, U. Heiz, K.J.J. Mayrhofer, M. Arenz, The effect of particle proximity on the oxygen reduction rate of size-selected platinum clusters, Nat. Mater. 12 (2013) 919–924. doi:10.1038/nmat3712.

[87] F. Delime, J.M. Léger, C. Lamy, Optimization of platinum dispersion in Pt-PEM electrodes:

Application to the electrooxidation of ethanol, J. Appl. Electrochem. 28 (1998) 27–35. doi:10.1023/A:1003289516328.

[88] B. He, Y. Ha, H. Liu, K. Wang, K.Y. Liew, Size control synthesis of polymer-stabilized water-soluble platinum oxide nanoparticles, J. Colloid Interface Sci. 308 (2007) 105–111. doi:10.1016/j.jcis.2006.12.031.

[89] I.N. Leontyev, V.E. Guterman, E.B. Pakhomova, P.E. Timoshenko, A.v.guterman, I.N. Zakharchenko, G.P. Petin, B. Dkhil, XRD and electrochemical investigation of particle size effects in platinum-cobalt cathode electrocatalysts for oxygen reduction, J. Alloys Compd. 500 (2010) 241–246. doi:10.1016/j.jallcom.2010.04.018.

[90] J.-Y. Lin, C. Xi, Z. Li, Y. Feng, D.-Y. Wu, C.-K. Dong, P. Yao, H. Liu, X.-W. Du, Lattice-strained palladium nanoparticles as active catalysts for the oxygen reduction reaction, Chem. Commun. 55 (2019) 3121–3123. doi:10.1039/C9CC00447E.

[91] R. Brandiele, C. Durante, E. Grądzka, G.A. Rizzi, J. Zheng, D. Badocco, P. Centomo, P. Pastore, G. Granozzi, A. Gennaro, One step forward to a scalable synthesis of platinum–yttrium alloy nanoparticles on mesoporous carbon for the oxygen reduction reaction, J. Mater. Chem. A. 4 (2016) 12232–12240. doi:10.1039/C6TA04498K.

[92] G.J. Leong, M.C. Schulze, M.B. Strand, D. Maloney, S.L. Frisco, H.N. Dinh, B. Pivovar, R.M. Richards, Shape-directed platinum nanoparticle synthesis: Nanoscale design of novel catalysts, Appl. Organomet. Chem. 28 (2014) 1–17. doi:10.1002/aoc.3048.

[93] C. Wang, H. Daimon, T. Onodera, T. Koda, S. Sun, A general approach to the size- and shape-controlled synthesis of platinum nanoparticles and their catalytic reduction of oxygen, Angew. Chemie - Int. Ed. 47 (2008) 3588–3591. doi:10.1002/anie.200800073.

[94] V.R. Stamenkovic, B.S. Mun, M. Arenz, K.J.J. Mayrhofer, C.A. Lucas, G. Wang, P.N. Ross, N.M. Markovic, Trends in electrocatalysis on extended and nanoscale Pt-bimetallic alloy surfaces, Nat. Mater. 6 (2007) 241–247. doi:10.1038/nmat1840.

[95] C.M. Sánchez-Sánchez, J. Solla-Gullón, F.J. Vidal-Iglesias, A. Aldaz, V. Montiel, E. Herrero, Imaging structure sensitive catalysis on different shape-controlled platinum nanoparticles, J. Am. Chem. Soc. 132 (2010) 5622–5624. doi:10.1021/ja100922h.

[96] Z. Peng, H. Yang, Designer platinum nanoparticles: Control of shape, composition in alloy, nanostructure and electrocatalytic property, Nano Today. 4 (2009) 143–164. doi:10.1016/j.nantod.2008.10.010.

[97] L. Zhang, L.T. Roling, X. Wang, M. Vara, M. Chi, J. Liu, S.-I. Choi, J. Park, J.A. Herron, Z. Xie, M. Mavrikakis, Y. Xia, Platinum-based nanocages with subnanometer-thick walls and well-defined, controllable facets, Science (80-.). 349 (2015) 412–416. doi:10.1126/science.aab0801.

4 Materials characterization Theory

4.1 Electrochemical characterization

Electrochemistry is a powerful tool to evaluate the reactions which involving electron transfers. Electrochemistry relates the electrons transfer to chemical changes. The different voltammetric techniques are distinguished by the potential applied to the working electrode which drive the reaction, and by the material used as the working electrode. The equipment to perform cyclic voltammetry consists of a conventional potentiostat connected to an electrode system, constituted by two or three electrodes (working, reference and counter) immersed in a test solution call electrolyte. The potentiostat applies and maintains the potential between the working and reference electrode while at the same time measuring the current at the working electrode. Another working system is the galvanostatic techniques where a current is applied and maintain constant while the potential variation is measured.

The typical electrochemical techniques used during the PhD are:

- Cyclic Voltammetry (CV)
- Linear Sweep Voltammetry (LSV) with Rotating Disc Electrode (RDE)
- Potentiometric Electrochemical Impedance Spectroscopy (PEIS)

4.1.1 Cyclic Voltammetry

Cyclic voltammetry (CV) is a powerful and popular electro-chemical technique commonly employed to investigate the reduction and oxidation processes of molecular species. The interest in cyclic voltammetry derive from its ability to rapidly provide considerable informations on the thermodynamics of redox processes, on the kinetics of heterogeneous electron-transfer reactions, and on coupled chemical reactions or adsorption processes. The potential of the working electrode is measured against a reference electrode which maintains a constant potential. A cyclic voltammogram is obtained by measuring the current at the working electrode during the potential scans. A cyclic voltammogram is obtained by applying a linear potential sweep between the working electrode and the reference electrode. The experiment is usually started at a potential where no electrochemical reaction occurs (E_i), and the potential is scanned with a fixed scan rate to the potential. When an electrochemically active specie is present in the solution phase, scanning the potential, an anodic current peak at the potential E_{pa} is detected with the peak current I_{pa}. When the potential is swept back during the reverse scan a further current peak at the potential E_{pc} may be observed with a cathodic peak current I_{pc}. The Cyclic Voltammetry involves sweeping the electrode potential between potential limits E_1 and E_2 at a known sweep rate. On reaching limit E_2 the sweep is reversed until E_i.

$$R \rightarrow O + ne^- \quad (4.1)$$

$$O + ne^- \rightarrow R \quad (4.2)$$

In cyclic voltammetry, a species that undergoes a reduction during a cathodic polarization of working electrode in static solution is re-oxidised by applying a reverse (anodic) scan. Cyclic voltammetry makes possible the elucidation of the kinetics of electrochemical reactions taking place at electrode surface. The important parameters of a cyclic voltammogram are the magnitudes of anodic peak current (I_{pa}), the cathodic peak current (I_{pc}), the anodic peak potential (E_{pa}) and cathodic peak potential (E_{pc}). At the start of the experiment, the electrolyte solution contains only the reduced species (R), point A in Figure 28. Scanning the potential in anodic direction and approaching the peak, first the current is kept constant and then begins to grow approaching point B. As R is converted into O (4.1), concentration gradients are set up for both R and O, and diffusion occurs down these concentration gradients. At the anodic peak (point C), R is oxidized to O, generating a current i_{pa}, which is a function of the mass transport of the electrochemically active species. After the anodic peak (point C), the current continues to decay, because the reduction species is converted to O. If a redox system remains in equilibrium throughout the potential scan, the electrochemical reaction is said to be reversible. Point B, generally is call “upper vertex potential” or “ inversion potentil”. In cathodic scan, the cathodic peak correspond to the convernsion from O to R. In other words, equilibrium requires that the concentrations of O and R in the electrode surface are maintained at the values required by the Nerst Equation.

$$E = E^0 + \frac{RT}{nF} ln \frac{[O]}{[R]} \quad (4.3)$$

where E is the applied potential difference and E^o is the standard electrode potential (the value is tabulated, for each redox couple, R is gas constant 8.31 J K^{-1} mol $^{-1}$, T is the temperature expressed in Kelvin (generally, the experiments are conduct at 298.15 K), F is the Faraday constant (96485 C), [O] and [R] are the concentration of the oxidized and reduced species, respectively and n is the number of electron exchange.

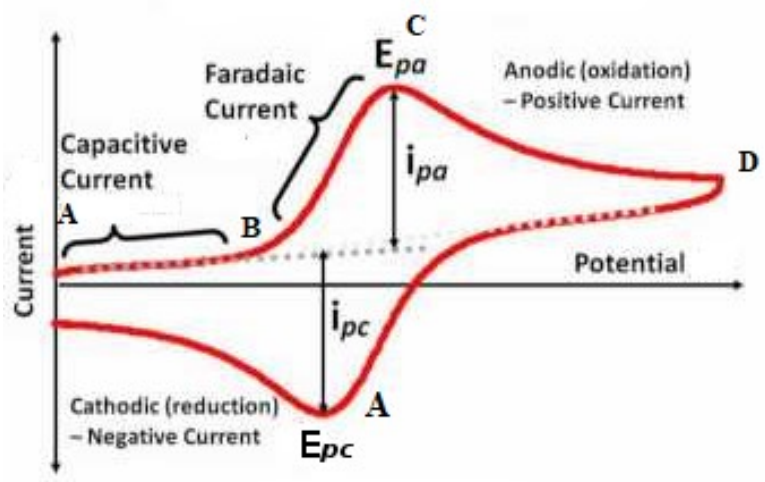

Figure 28: Typical CV at three electrode in "American Convention", the measurement show a reversible process

In a reversible system, the peak potential separation (E_{pa} - E_{pc}) is 59/n mV for all scan rates where n is the number of electron equivalents transferred during the redox process.

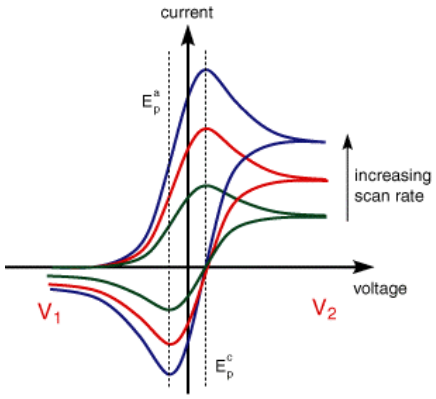

Figure 29: Effect of the Scan Rate on the Cyclic Voltammetry

Data Source: https://www.ceb.cam.ac.uk/research/groups/rg-eme/Edu/linear-sweep-and-cyclic-voltametry-the-principles

In a reversible redox couple, increasing the scan rate the E_{pa} - E_{pc} is constant. The peak current increase follows the Randles Sevcik Equation. The Randles Sevcik Equation connect the current peak (i_p) to the scan rate, the concentration, diffusion of analyte species. The peak current for a reversible couple (at 25°C), can be calculated as:

$$i_p = 0.4463\, nFAC \left(\frac{nFvD}{RT}\right)^{1/2} \qquad (4.4)$$

where n is the number of electrons, A the electrode area (in cm^2), C the concentration (in mol/cm^3), D the diffusion coefficient (in cm^2/s), and v the scan rate (in V/s). Accordingly, the current is directly proportional

to concentration and increases with the square root of the scan rate. Generally, the Randles Sevcik Equation is used for determinate the Diffusion Parameter of an unknow species or for determinate the electrode active surface area. A catalytic process can be classified in Reversible, Quasi-Reversible and Irreversible processes depending by the electrochemical response (Figure 30).

Irreversible system in electrochemistry is obtained with a sluggish charge-transfer step, i.e., the standard rate constant and exchange current density are very small. In a non-ideal system, the chemical reactions are coupled to the redox process or adsorption process on the electrode can occurs. Mass transport plays a fundamental role, because "control" the concentration of redox species; the expressions for reversible processes can be applied also for quasi-reversible processes. The voltammograms of a quasi-reversible process exhibit a higher peak-to-peak separation than in the reversible processes. The peak current increase with $\nu^{1/2}$ but is not linear and ΔE is greater than 0.059/n V. In reversible process, current, for an oxidation or reduction, is associated directly to the mass transport; in quasi-reversible process, current is influenced by both the mass transport and charge transfer kinetics. In a stationary Cyclic Voltammetry, the species migrate only for concentration gradient from the electrode surface to the bulk or from the bulk to the electrode [98, 99, 100].

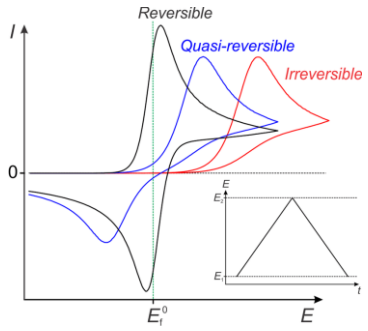

Figure 30: Cyclic Voltammetry for different electrochemical process: reversible, quasi- reversible and irreversible

Cyclic voltammetry is an excellent technique to survey the reactivity of new materials or compounds and can provide information about:

1. the potential at which oxidation or reduction processes occur
2. the oxidation state of the redox species
3. the number of electrons involved
4. the rate of electron transfer
5. possible chemical processes associated with the electron transfer
6. adsorption effects.

4.1.2 Lineal Sweep Voltammetry

Linear sweep voltammetry is a electrochemical technique where the current at a working electrode is measured while the potential between the working electrode and a reference electrode is swept linearly in time, the description is very similar to cyclic voltametry. However, in LSV the voltage is scanned from a lower limit to an upper limit, unlike the CV where the potential is scanned both in anodic both in cathodic sweep.
The potential is swept linearly from the starting potential, E_i, with a scan rate ν.

$$E(t) = E_i + \nu t \qquad (4.5)$$

where v = dE/dt (in V s^{-1} units) is the sweep rate, E_i is the initial potential, E(t) is the potential at time t.
LSV essentially only the first half-cycle of a cyclic voltammogram is executed. Scanning starts at a potential where no electrochemical reaction occurs. Current can be observed at the potential where the charge transfer begins, which increases with the potential, however, after a maximum value (peak current or plateau) it starts to decrease due to the depletion of the reacting species at the interface. The LSV is used for evaluated only the oxidation or reduction of an electroactive species.

4.1.2.1 Linear Sweep Voltammetry with Rotating Disk Electrode (RDE)

LSV is employed in the rotating disk electrochemistry (RDE) for eliminate the natural mass transport due to the different concentration between the bulk solution and the electrode surface. A rotating disk electrode is rotated in the electrolyte solution, the current depends on the solution flow rate, or in other terms by the rotation rate. The typical experimental set up is show in Figure 31.

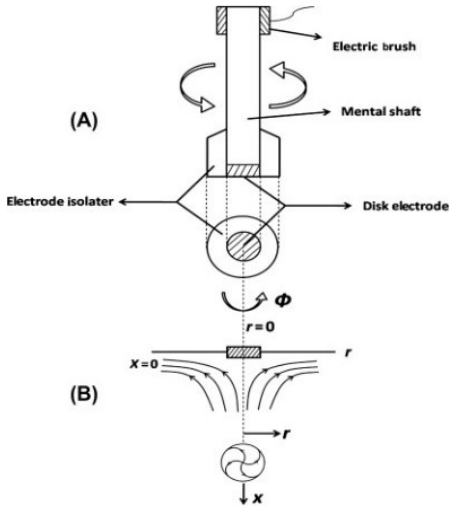

Figure 31: a) Sketch of Rotating Disk Electrode, b) Mass transport phenomena

The laminar flow at a rotating disk electrode conveys a steady stream of material from the bulk solution to the electrode surface. While the bulk solution far away from the electrode remains stirred by the convection mass transport due to the disk rotation, the portion of the solution nearer to the electrode surface rotate with the electrode. The rate of mass transport at the rotating disk electrode is modificated altering the disk rotation speed. The components of the fluid velocity depend by the angular velocity of the disk, which is given by $\omega = 2\pi f$, where f is the rotation speed in rotation per minutes (rpm) or rotation frequency in hertz.
Mathematic method, in specific convection-diffusion concept of fluid dynamic, can be used for describing the movement of the electroactive species in the electrolyte. Mass transport of material from the bulk solution into the stagnant layer occurs by forced convection, due to electrode rotation. The electroactive species present, in the stagnant layer, moves closer to the electrode surface; and so, convection becomes less important and diffusion becomes more important

Electrochemical reactions are heterogeneous reactions; the reaction takes place at the interface between the electrolyte and the electrode. In our case, two successive processes are happening:

1) Diffusion of the electroactive ion across the diffusion layer – the mass transport.
2) Charge transfer across the electrolyte-electrode interface – the kinetics

The current associated to case 1 is call diffusion current, i_d (or density current diffusion, if it is normalized for the electrode area), while the current in the case 2 is call kinetic current and is associated to the electron transfer (i_k or j_k). Consider two cases, first, when the mass transfer is slow (or the kinetics is very fast) and so j_d is small. Then $1/j_d >> 1/j_k$ ($i_k >> i_d$) and the process is governed by j_d. This case is called the mass-transfer limited reaction because the process is practically limited by the comparably slow mass transfer. The second case follows naturally, when the mass transfer is much faster than the kinetics of the reaction and so $1/j_k >> 1/j_d$ ($i_d >> i_k$). The process is kinetically limited. When an electrode reaction is governed only by mass transfer, the concentration of the electroactive ion at the surface of the electrode is zero. It is because the reaction is fast enough to instantly consume any reactant that arrives on the electrode. A general equation of the disk current, considering both mass transport and electron transfer kinetics can thus be given as the Koutecky-Levich equation

$$\frac{1}{j} = \frac{1}{j_k} + \frac{1}{j_L} \qquad (4.6)$$

$$\frac{1}{j} = \frac{1}{j_k} + \left(\frac{1}{0.62nFD^{2/3}\upsilon^{-1/6}\,C}\right)\omega^{-\frac{1}{2}} \qquad (4.7)$$

Where j is the total current density of the system, j_k is the kinetic current density, j_L (or j_d) is the diffusion current density, n is the number of electrons involves in the redox reaction, F is the Faraday constant, D is the

diffusion coefficient for the redox specie, *v* is the scan rate, C is the concentration of the redox specie and ω is the rotation rate expressed in rad s^{-1}.

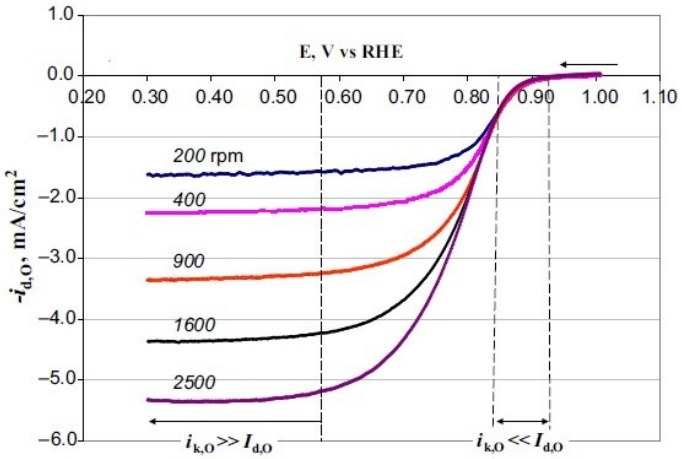

Figure 32: Effect of the RDE rotation rate on the LSV, the graph show, also, the kinetic and diffusion regions.

The rotation rate owns an impact only on the limited current, because increasing the rotation speed the redox species concentration increase the current increase follow the Koutecky-Levich equation. The Figure 32 show the impact of different rotation rate on a LSV with RDE. The region between the kinetic and diffusion zone is call mixed control region. This zone presents a control due to the electroactive species diffusion and the charge transfert [100, 101, 102, 103].

4.1.3 Potentiometric Electrochemical Impedance Spectroscopy

Impedance spectroscopy is considered a powerful technique for investigating electrochemical systems and processes. The impedance technique is based on disturbing an electrochemical cell at equilibrium or steady state with alternating signal of small magnitude and measuring the current response. This disturbance can come from a wide range of parameters such as applied potential or applied current. If the disturbance due to an applied voltage at a frequency (ω) to the electrochemical cell is considered:

$$E(t) = E_0 + \sin \omega t \qquad (4.8)$$

where E (t) is voltage at time t, E_0 is the voltage amplitude, and ω is the radial frequency. Generally, for E_0 is chosen a potential where no redox reaction occurs. The current response will take the form with a phase shift denoted by θ

$$I(t) = I_0 \sin(\omega t + \theta) \qquad (4.9)$$

Where I (t) is the current at time t, I_0 is the current amplitude, and θ is the phase shift.

The impedance of the system is the ratio Z.

$$Z = \frac{E_t}{I_t} \qquad (4.10)$$

Considering $Z_0 = E_0/I_0$ and a phase shift (θ), the equation present itself as a vector quantity. The complex notation for impedance will be:

$$Z = Z_0(\cos\theta + a\sin\theta) \qquad (4.11)$$

$$Z = Z' + aZ'' \qquad (4.12)$$

Where a = √ (-1), Z' is the real part and Z" is the imaginary part.

Graphical presentation of the measured impedance data is usually presented as Nyquist plot, where the real (Z') and imaginary (-Z") parts of the complex impedance (Z) are graphited as x and y axes respectively. Increasing the frequency, the imaginary and real components of the impedance decrease [103]. The Nyquist plot can be divided in three zones (Figure 33):

1. Ohmic Phenomena, which correspond to the resistance of electrolyte solution between the reference and working electrodes.
2. Charge transfer which describe the double-layer capacitance
3. Mass Transport, resulting from the semi-infinite diffusion of ions to the electrode surface

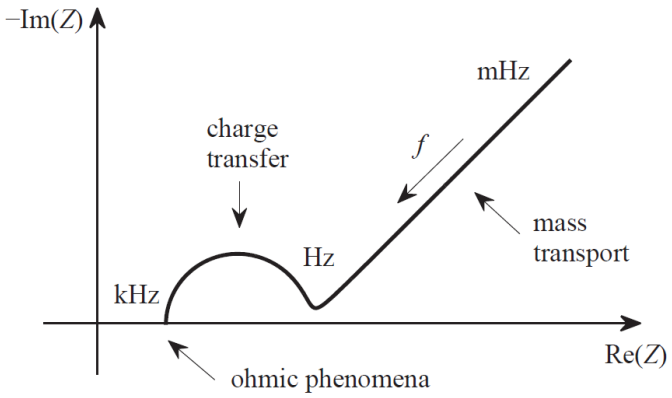

Figure 33: Impedance spectra

4.2 Thermogravimetric Analysis (TGA)

Thermogravimetric Analysis is a technique in which the mass of a substance is evaluated in function of temperature or time. The sample specimens are subjected to a controlled temperature program in a controlled atmosphere. A TGA consists of a sample pan that is supported by a precision balance. That pan resides in a furnace and is heated or cooled during the experiment. The mass of the sample is monitored during the experiment. A sample purge gas controls the sample environment. These instruments can quantify loss of water, loss of solvent, loss of plasticizer, decarboxylation, pyrolysis, oxidation, decomposition, weight % filler, amount of metallic catalytic residue remaining on carbon nanotubes, and weight %.

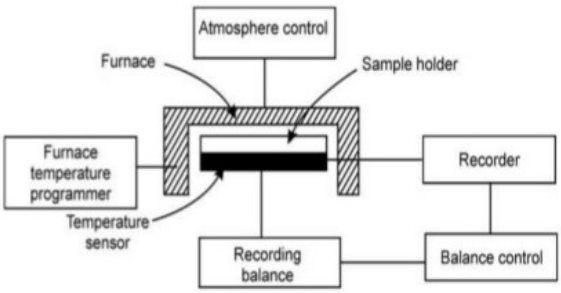

Figure 34: Main component in a TGA instrument

The analysis is performed by gradually raising the temperature and plotting the substances weight against temperature. The abscissa (X-axis) can be displayed as time or temperature and the ordinate (Y-axis) can be displayed as weight (mg) or weight percent (%). The descending TGA thermal curve indicates a weight loss occurred. The degradation temperature is evaluated reporting the 1st derivate of mass loss vs the temperature [104].

4.3 Nitrogen Absorption/Desorption at 77 K

BET measures surface area based on gas adsorption. Brunauer, Emmett, and Teller found a way to calculate the specific surface area of a sample including the pore size distribution from gas adsorption. BET theory is an evolution of the Langmuir theory, which describe the adsorbed gas only as monolayer, BET theory, instead, consider the adsorbed gas in a multilayer system and after rationalized to a monolayer increasing the dimension. The volume of gas (usually nitrogen) adsorbed to the surface of the particles is measured at the boiling point of nitrogen (77 K). At this temperature the nitrogen gas condenses on the surface of the particles. It is assumed that the gas condenses onto the surface in a monolayer and considering the size of the gas atom/molecule, the total surface area of the particles including pores at the surface (inaccessible pores are not detected) is correlated to the condensed gas. The isotherms derived by the nitrogen adsorption can be classified

in six type (Figure 35). BET method is applicable only to adsorption isotherms of type II (disperse, nonporous or macroporous solids) and type IV (mesoporous solids, pore diameter between 2 nm and 50 nm).

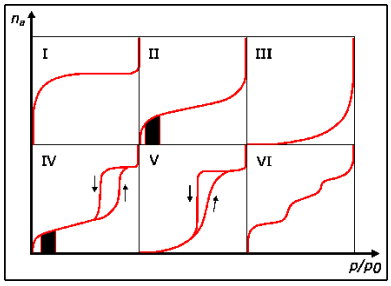

Figure 35: Typical adsorption and desorption isotherms

Type I isotherms are given by microporous solids having relatively small external surfaces (e.g. activated carbons, molecular sieve zeolites, COFs/MOFs and certain porous oxides), the limiting uptake being governed by the accessible micropore volume rather than by the internal surface area. The reversible Type II isotherm is the normal form of isotherm obtained with a non-porous or microporous adsorbent. The reversible isotherm type III show lateral interactions between adsorbed molecules are strong in comparison to interactions between the adsorbent surface and adsorbate. Type IV and V isotherms show a multilayer adsorption process followed by capillary condensation on the micropore. Characteristic feature of the Type IV isotherm is hysteresis loop, which is associated with capillary condensation taking place mainly in mesopores. The initial part, at P/P_0 ratio lower than 0.2. of the Type IV isotherm is attributed to monolayer adsorption. The distinction between Types IV and V is due to the interation between the adsorbent surface and adsorbate. The hysteresis is usually attributed to a network effects, the hysteresis is due to a different adsorption/desorption rate. The hysteresis can be classified in 4 class (Figure 36), depending by the interaction and the pore dimension. H1: correspond to agglomerates or big spherical particles with cylindrical pore geometry and orderly pore uniformly distributed with an high interconnection; H2 correspond to pores with narrow size distribution, relatively uniform channel length and a complex pore network; H3: aggregates of plate like particles forming slit-like pores and H4: narrow slit-like pores, particles with internal voids of irregular shape and broad size distribution, hollow spheres [105, 106].

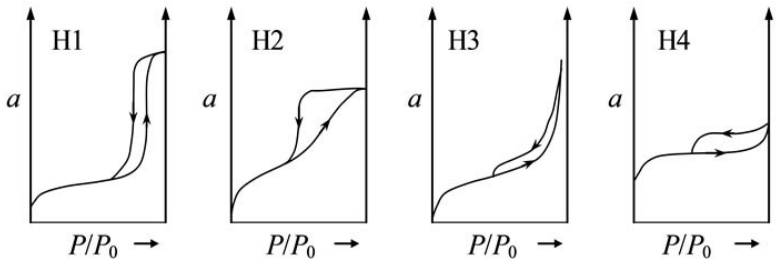

Figure 36: Typical hysteresis

The BET equation was derived on the following hypotheses:

(1) Surface is energetically homogeneous; all adsorption sites on the active surface have the same adsorption energy
(2) There is no lateral interaction between adsorbed molecule
(3) The adsorption energies in the second and all higher layers are equal to condensation energy of adsorptive

The BET equation can be formalized as following:

$$\frac{p}{n_a(p_0 - p)} S_{tot} = \frac{1}{n_m C} + \frac{C-1}{n_m C} \frac{p}{p_0} \qquad (4.13)$$

Where p and p_0 are the equilibrium and the saturation pressure of adsorbates at the temperature of adsorption, the adsorbed gas quantity is described by n_a.
The calculated quantities are: the n_m (the monolayer capacity) and the BET constant, C. The BET constant (C) is also calculated from the intercept and gradient and is related to the energy of adsorption in the first adsorbed layer. Consequently, the value of C is an indication of the magnitude of the adsorbent/adsorbate interactions. C is normally between 100 – 200, if it is lower than around 20 there is significant adsorbent/adsorbate and the BET method is invalid. With value greater than 200, the sample may contain significant porosity. To calculate these values the BET equation is plotted as an adsorption isotherm (4.14) typically at a relative pressure (p/p_0) between 0.05-0.35.

$$S_{tot} = \frac{n_m N_A}{V} \qquad (4.14)$$

Where N_A is Avogadro's number, s the adsorption cross section of the adsorbing species, and V the molar volume of the adsorbate gas. Considering the equation 4.13 and 4.14 is possible calculated S_{tot}, which is connected (considering the pore geometry and the material structure) to the external surface area and the internal surface area (pore surface). The total surface area is calculated as sum of external and pore surface [107]. From BET equation, several new equations are developed for calculate the pore dimensional distribution or absorption energy. Typical equation used are (Linear DFT for low area material, Non-Linear DFT for medium and high area material, PFVAS equation, or PLDD4 equation.

4.4 ICP-MS

Inductively coupled plasma mass spectrometry (ICP-MS) is an elemental analysis technology used for detecting most elements of the periodic table at milligram to nanogram levels per liter of solution. The Inductively Coupled Plasma (ICP) is an ionization source that fully decomposes a sample into ions.

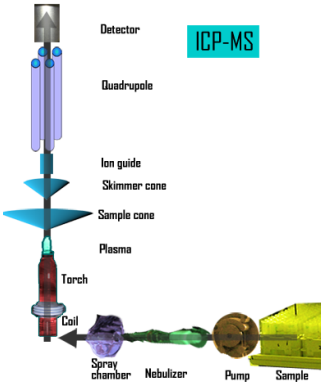

Figure 37: ICP-MS instrumentation

To be processed efficiently in the plasma, samples must be in either gas or vapor (aerosol) form. The gases can be analysed directly by the plasma, solids and liquids have to be converted to aerosol form (for liquids) or an mineralization device (for solids). With solid samples, digestion in strong and hot acids is the typical protocol for eliminated the matrix. The acids themselves range from simple nitric acid or sulphuric acid (for easy matrices) to hydrofluoric acid. External calibration uses a range of separate (external) standards of known concentration of the analyte to generate a calibration curve of instrument response. The calibration curve, which is usually a linear regression, is then used to back-calculate the concentration of analyte in unknown samples based on their instrument response [108, 109].

4.5 Elemental Analysis

Elemental Analysis is an easy, fast and popular techniques where a material is analysed for its elemental. Elemental analysis can be qualitative and quantitative. EA often refers to CHNX analysis: the determination of the mass fractions of carbon, hydrogen, nitrogen, and heteroatoms (X) (halogens, sulfur). For instance, carbon and hydrogen are determined in organic compounds by combustion to carbon dioxide and water. Likewise, the nitrogen species are converted to nitrogen gas.

4.6 Transmission Electron Microscopy (TEM)

The TEM (Transmission Electron Microscope) is a very important, fundamental and crucial tool for material science. A energy beam, with an energy higher than 300kV, of electrons through a sample, and the interactions between the electrons and the atoms present in the sample can be used to observe the material structure. When an electron beam passes through a thin section specimen of material, the electrons are scattered, and the electron after are focused by a system of electromagnetic lenses, for generate an image or diffractogram patter [110, 111].

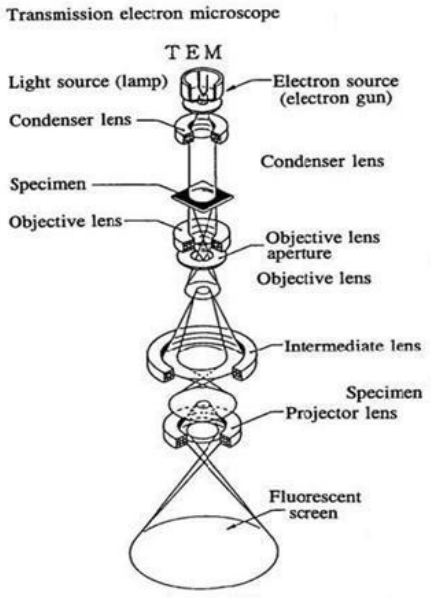

Figure 38: Main TEM components

4.7 Scanning Electron Microscopy (SEM)

The scanning electron microscope (SEM) uses a focused high energy electron beams to evaluate the external morphology (texture), chemical composition, and crystalline structure and orientation of materials generate a variety of signals at the surface of solid specimens. The SEM system is similar to the TEM analysis.

The interaction between the electronic beams the specimen generates secondary electron which are focused in a CCD camera. Secondary electrons show the morphology and the topography on samples and the backscattered electrons are most valuable for illustrating contrasts in composition in multiphase samples. The resolution of a SEM depends by the electron size and varies between 1 nm and 20 nm. SEM analysis, as TEM, is considered a “non-destructive” technique. The energy of electrons is included in the range100 eV and 30 keV, they are, generally, generated by a tungsten filament an high temperature, the energy of the beam in is lower than in the TEM analysis.

Secondary electrons are detected by scintillator type detectors, which are charged with a positive voltage in order to attract electrons. The chamber is kept under vacuum during the measurement, in order to, avoid obstacles to electrons path. High vacuum (10^{-5} – 10^{-7} torr) is required for high resolution measurement [111].

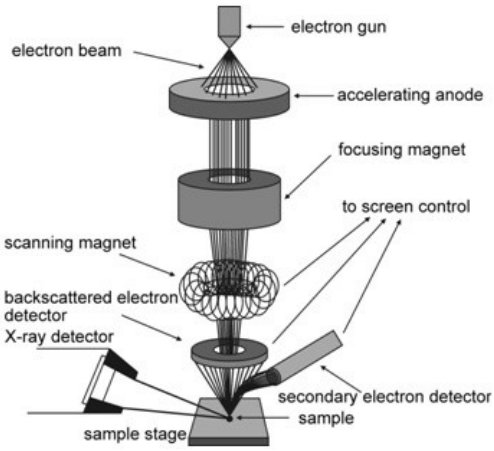

Figure 39: Main components for a SEM instrument

4.8 Raman Spectroscopy

Raman spectroscopy is used for evaluating the structure and properties materials, the technique is based on the inelastic light scattering by molecules. The incident photons interact transiently with atoms and are scattered in all directions. During the interaction with molecules, photons change their energy for the interaction with the atoms. The laser beam can be considered an oscillating electromagnetic wave characterized by a frequency v_0, its interaction with the material induces an electric dipole moment. The interaction causes a molecular vibration with the characteristic frequency "v_m".

When the molecule absorbs a photon with frequency "v_0", the excited molecule returns back to the same vibrational state and emits light with the same frequency of the excitation source, this interaction is called elastic Rayleight Scattering. Raman scattering can occur in two different ways. Stokes scattering, when the emitted radiation shows lower frequency than the incident radiation. The resulting frequency of scattered light is reduced by "$v_0 - v_m$", this Raman frequency is called Stokes frequency (Figure 40). And anti-Stokes scattering if the emitted radiation shows a frequency higher than the incident radiation. When a photon with frequency "v_0" is absorbed by an molecule already in the excited vibrational states the molecule returns to the fundamental state with a frequency "$v_0 + v_m$", anti-Stokes frequency (Figure 40). A very small amount of the scattered light (ca. 10^{-5} % of the incident light intensity) is shifted in energy from the laser frequency due to interactions between the incident electromagnetic waves and the vibrational energy levels of the molecules in the sample.

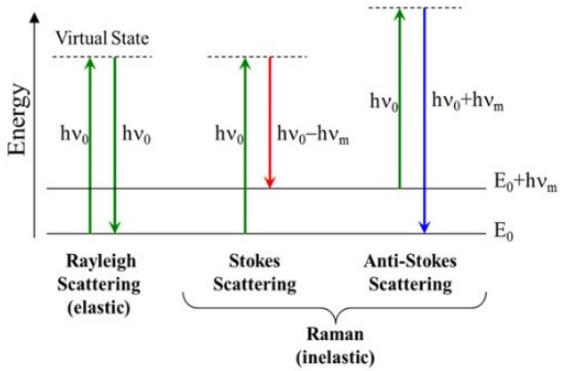

Figure 40: Typical interaction in RAMAN Spectroscopy after the photon adsorption

The oscillating molecule emits photons of different wavelengths (Raman scattering) that can be measured by detector. The energy difference between the initial and final vibrational levels or Raman shift in wave numbers, is calculated through intensity of incident radiation and intensity of the scattered radiation, expressed in wavelengths. A Raman spectrum is obtained plotting of the intensity of Raman scattered radiation as a function of its frequency difference from the incident radiation (usually in units of wavenumbers, cm^{-1}); because it is a difference value, the Raman shift is independent of the frequency of the incident radiation [112].

4.9 X-Ray Photoelectron Spectroscopy

In photoelectron spectroscopy the X-Ray source produces photons with an energy depending by the element of the source, in Mg Kα photon with an energy of 1253.6 eV and Al Kα photon with an energy of 1486.6 eV. When the electron absorbs enough energy, they are expelled from atoms (photoelectrons) of the sample. Photoelectric effect is the emission of an electron from an atom due to absorption of a photon. The photoelectrons emitted by photons are unique because they are ejected from the valence or the inner orbitals (such as K orbital) and have an energies characteristic of the atom emitter. When the core electron is ejected, an external electron fills the core hole. The transition energy is balanced by the emission of an Auger electron or a characteristic X Ray. XPS can determined the elemental and chemical composition of the specimen. If the absorbed energy of the photon, $h\nu$, is sufficient for the electron to overcome its binding energy E_b and the work function of the material's, electron emission can occur. The kinetic energy E_k of the emitted electron is related to its initial binding energy which is characteristic of a certain element and of a certain chemical state [113].

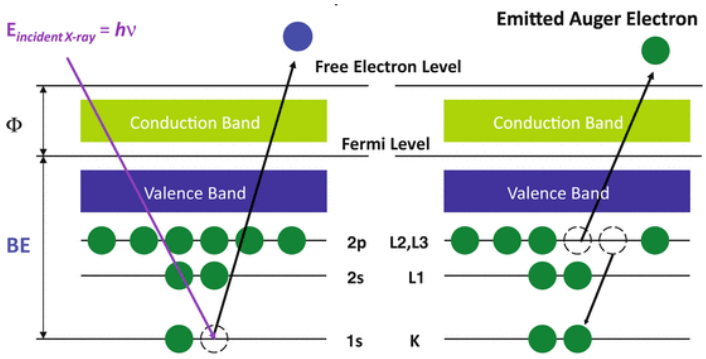

Figure 41: Differents emission processes after the photon adsorption

The position and intensity of the peaks in an energy spectrum provide the desired chemical state and quantitative information. In XPS, the distribution of kinetic energies of the emitted electrons is measured, typically by a hemispherical analyser.

$$E_k = h\upsilon - E_b - \phi \qquad (4.15)$$

$$E_b = h\upsilon - E_k - \phi \qquad (4.16)$$

Where E_b is the binding energy; the photon energy, hv, is the energy of X-ray photons being used by the spectrometer, and E_k is the the kinetic energy of the ejected electrons. The work function is a correction factor for the instrument and correlates to the minimum energy required to eject an electron from an atom. From the binding energies it is possible differentiate the elements and their chemical state. The surface sensitivity of XPS correspond to length of the electron mean free paths, which is in the range of 5 Å – 20 Å; in other words, only, the electrons emitted from atoms very close to the surface can be detected. The energy corresponding to each peak is characteristic of an element present in the sampled volume. The area under a peak in the spectrum is a measure of the element concentration. The peak shape and precise position indicate the chemical state for the element. Semi-quantitative analysis is possible by measuring the peak areas of specific elemental core lines (i) and by applying appropriate atomic sensitivity factors (S), also known as relative sensitivity factors (RSF), using the general equation:

$$C_x = \frac{{}^{i_x}/_{S_x}}{\sum {}^{I_i}/_{S_i}} \qquad (4.17)$$

where C_x is the atomic fraction of element x in a sample and i_x is the peak intensity of the x element.

4.10 X-ray Diffraction

X-ray powder diffraction (XRD) is used for defeminated and identify the crystallinity of the material and can provide information on unit cell dimensions. X-ray diffraction is based on constructive interference of monochromatic X-rays on a crystallite or semi crystallite sample. The interaction of the incident rays with the sample produces constructive interference (and a diffracted ray) when conditions satisfy Bragg's Law, Figure 42.

$$n\lambda = 2d \sin\theta \qquad (4.18)$$

The Bragg's Law connect the wavelength of electromagnetic radiation (λ) to the diffraction angle (θ) and the lattice spacing (d) in a crystalline sample. Scanning the sample in 2θ angles range, is possible individuated all possible diffraction directions of the lattice, with an orderly or random structure [114].

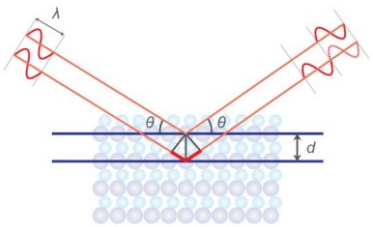

Figure 42: Sketch of the Bragg law

XRD is consisted by a X-ray source, a sample holder, and an X-ray detector. X-rays are generated in a cathode ray tube by heating a tungsten filament, the electrons are accelerated toward a target by applying a voltage. When electrons have enough energy to dislodge inner shell electrons of the target material, the characteristic X-ray spectra are produced. Copper is the most common target material for single-crystal diffraction, with Cu K_α radiation = 1.5418 Å. The sample and detector are in rotation. When the geometry of the incident X-rays satisfies the Bragg Equation, constructive interference occurs, and the recorded signal correspond to a specific crystallographic face. For typical powder patterns, data is collected at 2θ from ~5° to 90°.

XRD technique can be used for determinate:

- unit cell dimension
- sample purity
- lattice mismatch between film and substrate
- crystal structure
- stress and strain effect
- thickness, roughness and density of film
- grains orientation in polycrystalline sample

4.11 Bibliography

[98] N. Elgrishi, K.J. Rountree, B.D. McCarthy, E.S. Rountree, T.T. Eisenhart, J.L. Dempsey, A Practical Beginner's Guide to Cyclic Voltammetry, J. Chem. Educ. 95 (2018) 197–206. doi:10.1021/acs.jchemed.7b00361.

[99] G.A. Mabbott, An introduction to cyclic voltammetry, J. Chem. Educ. 60 (1983) 697–702. doi:10.1021/ed060p697.

[100] R.S. Nicholson, Theory and Application of Cyclic Voltammetry for Measurement of Electrode Reaction Kinetics, Anal. Chem. 37 (1965) 1351–1355. doi:10.1021/ac60230a016.

[101] D. Jahn, W. Vielstich, Rates of Electrode Processes by the Rotating Disk Method, J. Electrochem. Soc. 109 (1962) 849. doi:10.1149/1.2425567.

[102] U.A. Paulus, T.J. Schmidt, H.A. Gasteiger, R.J. Behm, Oxygen reduction on a high-surface area Pt/Vulcan carbon catalyst: A thin-film rotating ring-disk electrode study, J. Electroanal. Chem. 495 (2001) 134–145. doi:10.1016/S0022-0728(00)00407-1.

[103] A.J. Bard, L.R. Faulkner, Electrochemical Methods: Fundamentals and Applications (2nd ed), Wiley. 2001.

[104] BROIDO A, Simple, Sensitive Graphical Method of Treating Thermogravimetric Analysis Data, J Polym Sci Part A-2 Polym Phys. 7 (1969) 1761–1773.

[105] A. Lecloux, J.P. Pirard, The importance of standard isotherms in the analysis of adsorption isotherms for determining the porous texture of solids, J. Colloid Interface Sci. 70 (1979) 265–281. doi:10.1016/0021-9797(79)90031-6.

[106] M.F. De Lange, T.J.H. Vlugt, J. Gascon, F. Kapteijn, Adsorptive characterization of porous solids: Error analysis guides the way, Microporous Mesoporous Mater. 200 (2014) 199–215. doi:10.1016/j.micromeso.2014.08.048.

[107] M. Thommes, K. Kaneko, A. V. Neimark, J.P. Olivier, F. Rodriguez-Reinoso, J. Rouquerol, K.S.W. Sing, Physisorption of gases, with special reference to the evaluation of surface area and pore size distribution (IUPAC Technical Report), Pure Appl. Chem. 87 (2015) 1051–1069. doi:10.1515/pac-2014-1117.

[108] Y. Liu, Z. Hu, S. Gao, D. Günther, J. Xu, C. Gao, H. Chen, In situ analysis of major and trace elements of anhydrous minerals by LA-ICP-MS without applying an internal standard, Chem. Geol. 257 (2008) 34–43. doi:10.1016/j.chemgeo.2008.08.004.

[109] R. Thomas, Practical Guide to ICP-MS, CRC Press, 2013. doi:10.1201/b14923.

[110] L. Reimer, Transmission Electron Microscopy: Physics of Image Formation and Microanalysis, Springer Berlin Heidelberg, 2013. https://books.google.it/books?id=CUfsCAAAQBAJ.

[111] T.E. Microscopy, Transmittion, 2009.

[112] A.C. Ferrari, Raman spectroscopy of graphene and graphite: Disorder, electron-phonon coupling, doping and nonadiabatic effects, Solid State Commun. 143 (2007) 47–57. doi:10.1016/j.ssc.2007.03.052.

[113] J.F. Watts, J. Wolstenholme, An Introduction to Surface Analysis by XPS and AES, John Wiley & Sons, Ltd, Chichester, UK, 2003. doi:10.1002/0470867930.

[114] J.I. Goldstein, D.E. Newbury, P. Echlin, D.C. Coy, C.E. Lyman, E. Lifshin, L. Sawyer, J.R. Michael, Scanning Electron Microscopy and X-Rays Microanalysis, Kluwer Academy, New York. 2003

5 Materials characterization of PGM catalysts

5.1 Electrochemical characterization of Platinum based material.

The Pt/C catalysts was characterized in a conventional electrochemical cell, in argon and oxygen saturated electrolyte. The electrochemical surface area of the catalyst is normally measured in the electrolyte solution saturated with inert gas Ar and the electrode is at static state (not rotated). The purpose is to obtain information about the redox activity of the catalyst itself or some information about the catalyst surface behavior, such as the catalyst electrochemical active surface area (for Pt-based catalysts) or the concentration of catalyst active sites (for non-noble metal catalysts). Instead, in oxygen saturated solution the kinetic parameters for the Oxygen Reduction Reaction was determinate.

The electrode coated with the Platinum catalyst is immersed into the three-electrode cell (working, reference and counter electrodes) containing the deaerated acid or alkaline electrolyte, a platinum net or a graphite bar as the counter electrode, and a reversible hydrogen Electrode (RHE) or a standard SCE as the reference electrode. For a reproducible signal the Pt/C must be electrochemical activated. The electrode is cycled for more than 100 times between 0 V vs RHE and 1.2 V vs RHE using cyclic voltammetry method with a scan rate of 200 mV s^{-1} for removing the possible surface contaminant and activate the platinum surface. The electrochemical measurements should be conducted in a thermostatic situation at 25 °C. After the electrochemical activation, the cyclic voltammograms (CVs) were recorded at different scan rate (200 mV s^{-1} – 100 mV s^{-1} – 50 mV s^{-1} – 20 mV s^{-1} – 10 mV s^{-1} and 5 mV s^{-1}), for determinate the Electrochemical Platinum Surface Area (EPSA) [115, 116].

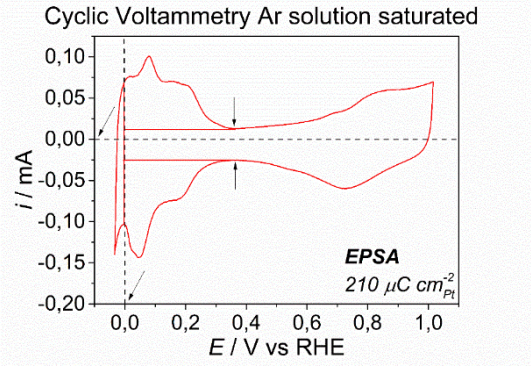

Figure 43: Example of CV of platinum catalyst

The voltammograms of a Platinum on carbon catalyst are characterized by three different voltammetric region; the left side (from 0 V vs RHE and 0.3 V vs RHE) corresponds to the H_2 adsorption (in cathodic current) / desorption (in anodic current) and H_2 evolution (which start at potential less than 0 V vs RHE), the middle zone, generally from 0.35 V vs. RHE to 0.6 V vs. RHE to the double layer charging current and the right side to the platinum oxide/hydroxide formation and reduction.

The intensity and position of peaks in the H_2 adsorption/desorption region show the type and the crystallographic surface sites. A platinum base material can show different peaks in the H_2 adsorption/desorption area depending by its crystallography or the NPs dimension. The synthesis parameter affects the intensity and the position of the H_2 adsorption/desorption peaks, indicating a poor and high selectivity towards the formation of crystallographic domains. In particular, in Figure 43 (100) sites are not formed since no peaks are present in the potential range between 0.2 and 0.3 V. The peaks are mainly located in the potential range between 0.0 and 0.13 V, which can be attributed to (110) sites and (111) sites.

The EPSA is evaluated based on the electric charge of the hydrogen desorption or the average of hydrogen desorption/desorption. The standard charge quantity of monolayer hydrogen desorption on a polycrystalline platinum layer is 0.21 mC cm^{-2} at 25 ° C, this parameter permits to convert the hydrogen adsorption/desorption charge into platinum surface area. The EPSA of the catalyst layer is measured in hydrogen adsorption/desorption between 0.05 and 0.4 V vs RHE. For calculate the EPSA, the adsorption/desorption area must be correct by the double layer charge.

$$Q = \frac{A_{desH_2}}{v} = \frac{mA \cdot V}{V\ s^{-1}} = mA\ s = mC \tag{5.1}$$

$$EPSA = \frac{Q\ mV}{0.21\ mC\ cm_{Pt}^{-2}} \tag{5.2}$$

The platinum based material, where the catalysts is synthetized with a platinum loading between 20 % and 35 % show a electrochemical platinum surface area (EPSA) from 0.5 cm^2 to 3 cm^2. ECSA is the ElectroChemical Surface Area, it is an indication of the Pt-active site density: the larger the ECSA value, the more active the catalyst layer should be. The ECSA is generally meaningful for pure Pt catalysts, whereas in the case of Pt alloys this value should be considered more carefully [115]. The ECSA is obtained normalized the EPSA with the platinum loading.

$$ECSA = \frac{EPSA}{Platinum\ Loading} \tag{5.3}$$

The typical ECSA values for carbon-supported Pt-based catalysts range from 50 $m^2\ g^{-1}$ to 100 $m^2\ g^{-1}$ depending on the type of the catalysts and the preparation of the catalyst layer. EPSA and ECSA are the fundamental parameters for describe the concentration of active sites on the platinum catalyst.

In oxygen saturated electrolyte is possible evaluated the kinetic parameter for the ORR, which are connected to the catalysts deposited on the electrode surface.
To study the ORR kinetics catalysed by the catalyst, the Linear Sweep Voltammetry with Rotating Disk Electrode are normally recorded at different electrode rotating rates (800 rpm – 1200 rpm – 1600 rpm – 2000 rpm and 2400 rpm) at 20 mV s^{-1} (or less scan rate). In order to obtain the steady state curves, the controlled potential scan rate is

normally slow, lower than 50 mV s^{-1}. In order to maintain the O_2 concentration inside the electrolyte solution, Oxygen bubbling is maintained over the electrolyte solution during the data collection. The electrochemical data can be determinate for each scan rate, but for the convention a rotation rate of 1600 rpm is used [117]. The main parameters which describe the kinetic are the half wave potential, $E_{1/2}$ and the onset potential, E_{on}. Figure 44 show the Linear Sweep Voltammetry with RDE at 1600 rpm and 20 mV s^{-1} for a platinum standard catalyst; the current is normalized by the electrode area, and the potential is referred to the standard Reversible Hydrogen Electrode.

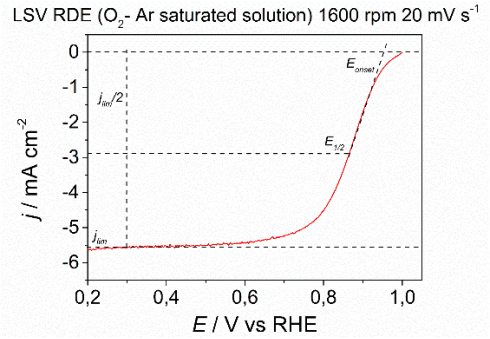

Figure 44: Example of LSV with RDE of a platinum catalyst

The half-wave potential ($E_{1/2}$), and the limiting current density (j_{lim} or j_L) for the ORR were determined at a RDE (at 1600 rpm) by recording linear sweep voltammograms (LSVs) at a scan rate of 20 mV s^{-1} in the potential range 0.05 V vs RHE - 1.05 V vs. RHE in O_2 saturated electrolyte solution. The limiting current was determined graphically in the diffusion limited region (0.1 V vs RHE - 0.6 V vs. RHE) after the subtraction of the background current recorded in Ar saturated electrolyte under otherwise the same experimental conditions, as scan rate, angular velocity and potential window. The kinetic current density (j_k), is the current density in the kinetic region corrected for the mass transfer contribution, is, generally, calculated from LSV recorded at 1600 rpm and a scan rate of 20 mV s^{-1}. Generally, for platinum based materials, the kinetic current is calculated at 0.9 V vs. RHE.

$$i_{k,0.9VvsRHE} = \frac{|i_L| * |i_{0.9VvsRHE}|}{|i_L| - |i_{0.9VvsRHE}|} \tag{5.4}$$

At a potential of 0.9 V vs. RHE, the influence of mass transport is negligible. The kinetic current density at 0.9 V vs. RHE is commonly referred to as specific activity (SA) if normalized for the EPSA.

$$SA = \frac{i_k}{EPSA} \tag{5.5}$$

Another important parameter is the mass activity (MA), which is determined normalizing the kinetic current calculated at 0.9 V vs. RHE by the Pt loading.

$$MA = \frac{i_k}{Platinum\ Loadig} \tag{5.6}$$

When the current passes though the electrode surface, there will be a current distribution between the working electrode surface and the counter electrode surface. The effect is due to the electrolyte resistance (R), it will cause an inconsistency between the controlled electrode potential ($E_{control}$ vs Reference electrode) and the actual electrode potential (E vs reference electrode).

$$E = E_{control} \pm iR \tag{5.7}$$

where "±" is used to take care of the current direction. This iR can cause a measurement error. The iR compensation depends by the electrode surface, the electrolyte, the distance between the electrodes. For correct determination of all electrochemical parameters, the electrochemical measurement must be compensate. Generally, the compensation in perchloric acid 0.1 M is around 6 Ω and 3 Ω in sulphuric acid 0.5 M [116, 117].

5.2 Electrochemical Procedure for Platinum based material catalysts

Catalysis testing is very sensitive to the operating conditions applied. A number of different aspects have to be considered correctly in order to obtain reliable results. How to test catalysts for the oxygen reduction reaction in low temperature fuel cells was discussed in many papers. Therefore, it is necessary to carry out the experiments accurately, carefully following a number of procedures for each single step of the testing. In the following, such a procedure is recommended. A standard electrochemical cell with the typical three electrode configuration was used. The cell was furnished with a water jacket attached to a hot water bath to control the temperature: all reported electrochemical measurements were performed at 25 °C. All glassware was cleaned for 24 h in a mixture of H_2SO_4 Trace Select and Nocromix, followed by multiple cycles of heating and rinsing with ultrapure water (Millipore Milli-Q, 18.2 M cm^{-1}) to remove residual sulphates. For all measurements the electrolyte consisted of a 0.1 M $HClO_4$ (Trace Select) electrolyte also prepared with ultrapure water or H_2SO_4 0.5 M or KOH 0.1 M prepared always with ultra-pure water. The working electrode was mounted on a rotating disk electrode (RDE). A Pt electrode was used as counter electrode while the reference electrode was a RHE electrode. The reference electrode, to which all reported potentials are referred, was a reversible hydrogen electrode (RHE). The electrode was prepared in situ before each experiment applied an current of -2 mA vs. counter electrode. All potentials of this thesis are referred to the reversible hydrogen electrode (RHE) and are corrected for ohmic losses [116, 117].

Catalyst testing for the ORR comprises several different steps:

1. Cleaning of the glassware and other parts in contact with the electrolyte
2. Polishing and cleaning of a glassy carbon disc electrode for use in a rotating disc electrode
3. Preparation of the catalyst ink.
4. Catalyst Layer preparation of RDE glassy carbon disc electrode
5. Preparation of the RHE (alternatively a Pt disc electrode needs to be used first in the same type of electrode under H_2 bubbling, and the potential of the used reference can be calibrated with respect to RHE).
6. Condition of the catalyst by carrying out cyclic voltammetry under inert gas conditions
7. Determination of the ohmic resistance, either by impedance spectroscopy or by the current interrupt
8. Determination of the catalyst active surface area by H_{UPD} from cyclic voltammetry under inert gas conditions
9. RDE cyclic voltammetry under inert gas conditions under electrode rotation at same conditions as subsequently ORR measurements are carried out
10. ORR measurements

A commercial glassy carbon (GC) rotating disk electrode (RDE) (5 mm diameter tip, geometric surface area 0.196 cm^2), was used as a working electrode, WE. The GC tip was preliminarily polished with diamond pastes (3 µm, 1 µm, and 0.25 µm) and sonicated in milli-Q water for 5 min at 20 °C. The prepared catalysts were characterized as thin films drop-casted on a GC collector electrode (Figure 45). The ink used for drop-casting was formulated by mixing 1.25 mg of catalyst, 2.1 mL of milli-Q water, 0.1 mL isopropanol and 5 µL of a Nafion (5 % in EtOH) solution. The ink before the deposition was sonicated for 2 h. maintaining a temperature lower than 20 °C. Temperature higher than 30 °C can damage the ink, favourable detachment or leaching process. A thin film of Pt based material catalysts was obtained by drop-casting 12 µL -15 µL of ink onto a clean GC electrode and drying overnight. The catalyst ink was formulated to obtain a Pt loading on the electrode of $15 mg_{Pt}\ cm^{-2}$. After the drop casting, the electrode has been rotated at 500 rpm until the completely evaporation of the solvent.

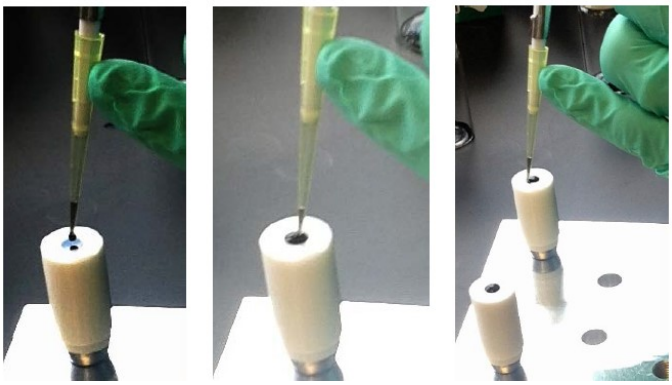

Figure 45: Example of drop casting

Condition for Impedance spectroscopy

- Measure OCV (Open Circuit Potential) for 5 min
- Measure the impedance from 200 kHz to 0.1 Hz for the determination of the electrolyte resistance. Apply an amplitude of 5 mV. The resulting value can be used for compensation of the electrolyte resistance *R* during the measurement, if the equipment provides this option. One should then use 85% of the value obtained for the correction, as otherwise there is a risk of oscillations. Alternatively, the potential can be corrected later by subtracting *I•R*. Generally, the iR compensation in HClO4 0.1 M for is 6 Ω.

Conditions for ORR testing

In Argon saturated condition (20 minutes in 60 mL of electrolyte solution)

1. Activation 100 cc at 200 mV s^{-1} between 0 V vs. RHE and 1.2 V vs RHE.
2. Cyclic Voltammetry at 200 mV s^{-1}, 100 mV s^{-1}, 50 mV s^{-1}, 20 mV s^{-1} and 5 mV s^{-1} between 1 V vs. RHE and 0 V vs. RHE.
3. Cyclic Voltammetry at 200 mV^{-1} in the same previous condition.
4. LSV with RDE at 1600 rpm and 20 mV s^{-1} and 5 mV s^{-1} from 1.05 V vs. RHE to 0.05 V vs. RHE
5. LSV with RDE at 20 mV s-1 and 800 rpm, 1200 rpm, 1600 rpm and 2000 rpm from 1.05 V vs. RHE to 0.05 V vs. RHE
6. Cyclic Voltametry at 200 mV^{-1} in the same previous condition of point 2.

In Oxygen saturated electrolyte (30 minutes in 60 mL of electrolyte solution)

1. LSV with RDE at 1600 rpm and 20 mV s-1, the start potential to 1.05 V and the lower potential to 0.05 V, and measure 5 cycles in oxygen saturated solution.
2. LSV with RDE at 5 mV s-1 and 1600 rpm, from 1.05 V vs. RHE for 2 cycles
3. Cyclic Voltammetry at 200 mV^{-1} between 1 V vs. RHE and 0 V vs. RHE
4. LSV with RDE at 20 mV s-1 and 800 rpm, 1200 rpm, 1600 rpm and 2000 rpm from 1.05 V vs. RHE to 0.05 V vs. RHE
5. Cyclic Voltammetry at 200 mV^{-1} between 1 V vs. RHE and 0 V vs. RHE

5.2.1 Instrumentation

Electrochemical measurements were recorded using an Autolab Potentiostat/Galvanostat 101N, Biologic SP200. The electrochemical activity was evaluated in a standard three cell. A glassy carbon (GC) rotating disk electrode (RDE, Pine Electronics) (5mm diameter tip, geometric surface area 0.196 cm^2) and a rotating GC disk (5mm diameter tip, geometric surface area 0.196 cm^2) Pt ring electrode (RRDE, Metrohm) were used as working electrodes. A Pt ring (Amel instruments for Electrochemistry) was used as a counter electrode. The reference electrode was an home made reversible hydrogen electrode (RHE) that was freshly prepared before each experiment. Alternatively, a Hg/HgO reference electrode (AMEL instruments for Electro- chemistry) was employed in the alkaline electrolyte.

5.3 Thermogravimetric analysis of Platinum based material

Thermogravimetric Analysis (TGA) involves the continuous weight loss monitoring of the sample in function of temperature, which varies from room temperature to 1000 °C. The measurement can be done under N_2 or O_2 flow, depending on the stability of the sample. The heating is divided in three steps: in the first one the sample is kept at 100 °C till all the volatile components, for example water, are eliminated, then the sample is heated till 1000 °C, and this temperature is maintained for 20 minutes. TGA was performed on 1 mg of sample with a heating rate of 10 °C min^{-1} from 50 °C to 1000 °C in N_2 environment to determinate the thermal stability. The TGA of a only carbon supports show the carbon degradation peak, where the carbon start to decompose form CO, CO_2 or ash (Figure 46a). In a platinum based material support on carbon, the parameters analysed are the temperature peak which correspond to the carbon support degradation and the residue at the end of the measurement which correspond to the amount of metal phases.

TGA was used, also, for determinate the degradation temperature of the precursor salts of platinum or yttrium used for the synthesis, the analysis was fundamental for determinate the temperature which permits the ligand losses. Figure 46b show the TGA of platinum (II) acetylacetonate.

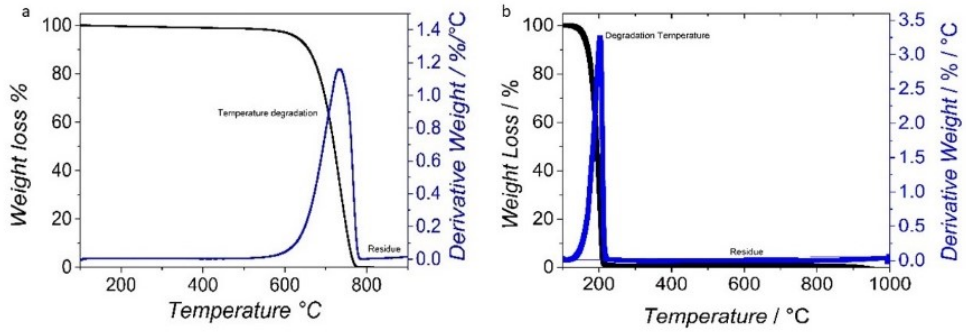

Figure 46: a) TGA of a standard mesoporous carbon Vulcan XC-72; b) TGA of Pt(ACAC)2

5.3.1 Instrumentation

Thermogravimetric analysis (TGA) was performed using a Q5000IR (TA Waters)

5.4 Nitrogen Adsorption/Desorption at 77 K of Platinum based material

BET analysis was used for determinate the carbon characteristic, in terms of surface area, micro-mesoporous volume and the pore distribution. Porous materials are divided into three kinds according to the pore size: the pore size less than 2 nm are microporous materials, the pore size of 2 nm – 50 nm are mesoporous materials, and the pore diameter greater than 50 nm are large porous material. For a platinum base material, the carbon support must have a mesoporous structure, in fact the metal NPs have a dimension of 2 nm and the carbon pores must host the metal nanoparticles. Surface area and porosity play major role in metal NPs distribution. The specific surface area is increased as the carbon particle size becomes small. Surface area, pore volume and pore distribution play a key role in the stabilization of platinum NPs and consequently on the resulting catalytic activity vs. ORR [119, 120, 121].

5.4.1 Instrumentation

N_2 adsorption/desorption isotherms were recorded at 77 K using an ASAP 2020. Specific surface area of the samples was calculated by a multipoint Brunauer-Emmett-Teller (BET) analysis; total volume pore and micropore volume were obtained from application of Gurvitsch law at $p/p_0 \sim 0.95 - 1$ and t-plot method, respectively. Pore size distribution curves were derived using density functional theory (DFT) methods and finally the number of mesopores was calculated as the difference between the total and micropore values. Considering the pore size, a Langmuir analysis is not applied for the carbon structure evaluation.

5.5 ICP-MS of Platinum based material

The platinum content was evaluated with ICP-MS. Platinum based material was digested in a mixture of HNO_3, HCl and H_2SO_4. Generally, 2 g of HNO_3 69%, 6 g of HCl 37% and 3 g of H_2SO_4 conc were add to 2.5 mg of platinum on mesoporous carbon (considering an theoretical platinum loading of 30%). The strong oxidation mixture is obligatory for a totally platinum and carbon oxidation, the carbon oxidation is important because the platinum can be encapsulated in inaccessible carbon particles, so the platinum loading is understimate. The mixture was digested at 220 °C for 10 minutes with a pressure of 100 psi and medium stirring. After the treatment the sample was diluted and filter; finally analysed in ICP-MS [122, 123].

5.5.1 Instrumentation

A Microwave Digestion System (CEM EXPLORER SP-D PLUS) was used for the acid digestion.
ICP-MS Agilent serie 7700x. (Agilent Technologies International Japan, Ltd., Tokyo, Japan). The instrument is equipped with an octupole collision cell operating in kinetic energy discrimination mode, which was used for the removal of polyatomic interferences and argon-based interferences.
RF power 1550 W, RF matching 1.8 V, Plasma gas flow rate 15 l min-1 Ar, Auxiliary gas flow rate 1.0 l min-1 Ar, Carrier gas flow rate 1.05 l min-1 Ar, Make-up gas flow rate 0.0 l min-1 Ar, He gas flow 4.3 ml/min, CeO+/Ce+ 0.902%, Ratio(2+) 70/140 0.944%, Nebuliser Microflow PFA nebuliser, Spray chamber Scott double-pass type at 2 °C and Torch Quartz glass torch.

5.5.2 Calibration

IMS-103. Multi-element calibration standard-3 (Ultra-scientific multi standard ICP-MS IMS-103), 100 mL: 10 mg/L. Sb, Au, Pt, Rh, Hf, Ru, Ir, Te, Pd and Sn; matrix 10% HCl / 1% HNO_3 COD: 8500-6948
Ag 1. Multi-element calibration standard-1, 100 mL: 10 mg/L of Ce, Dy, Er, Eu, Gd, Ho, La, Lu, Nd, Pr, Sc, Sm, Tb, Th, Tm, Y, Yb; matrix 5% HNO_3 N° 8500-6944

5.6 Elemental Analysis of Platinum based material

Elemental analysis consists in the V_2O_5 catalysed combustion of carbonaceous compounds in order to determine their atomic composition. The sample is located close to a CuO and Cu column, where O_2 is fed and the temperature is raised to 950 °C to promote combustion. This generate H_2O, CO_2, NO_x and SO_x. Molecular-exclusion chromatography is carried out for gas separation, then a Wheatstone bridge is employed as detector. Elemental analysis was used for determinate the amounts of carbon, hydrogen but especially sulphur and nitrogen in the carbon support. The functionalization of the carbon support consists in the introduction of heteroatoms such as nitrogen, boron, phosphorus and sulphur on a carbon matrix, the process is commonly call doping. It was largely demonstrated how nitrogen doped carbon exerts a strong interaction with the supported Pt NPs triggering their electronic properties and catalytic activity. Also, sulphur affords a clear metal support interaction between Pt NPs and the carbon support. The specific effect of sulphur doping on the electronic properties of Pt improve the kinetics and the stability of Pt catalysts for ORR. Knowing the content of heteroatoms in the carbonaceous matrix of a platinum based material is fundamental for studying its catalytic activity.

5.7 TEM and SEM of Platinum based material

The catalytic properties of nanoparticles usually depend on their crystal structures, size distributions and exposed surfaces, edges, corners, shaper ore structure. TEM is the preferred method to directly measure nanoparticle size, grain size, size distribution, and morphology. The dimensional distribution and the distribution of platinum NPs is a fundamental parameter for describe a material and can influence directly the Mass and Specific Activity. TEM and SEM are fundamental also for evaluated the carbon and its porosity [124]. Figure 47 show a the SEM image of Pt NPs on a homemade mesoporous carbon and b) the TEM image of Pt_xY alloy on carbon black. The NPs dimensional distribution calculated from the TEM images can be deconvoluted with different fitting such as Gaussian, Lorentzian and LogNormal. The type of fitting corresponds to a different growing process of the NPs. The Gaussian and Lorentzian fitting, generally, are attributed to an homogeneous particles dimension, in these two cases, the NPs, during the syntheses process, have the same growing rate. In the gaussian fitting is applied when the NPs show an higher dimensional variation, in contrast when the NPs show small variation of diameter, a Lorentzian fitting can be applied. The LogNormal fitting is used when the NPs show a multimodal dimensional distribution.

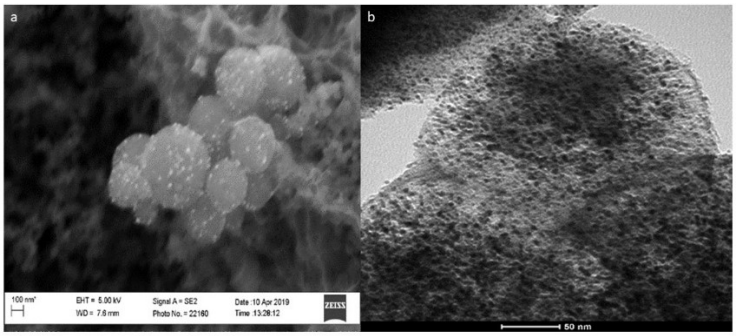

Figure 47: a) SEM image of Platinum NPs on carbon; b) TEM image of Platinum NPs on carbon

5.7.1 Instrumentation

Transmission electron microscopy (TEM) was performed with a FEI Tecnai G2 12 operating at 100 kV and equipped with a TVIPS CCD camera. Samples were prepared by drop casting on copper grids coated with amorphous carbon films. The surface morphology was also studied by a scanning electron microscope (SEM-FEG, JSM 7001F, JEOL).

5.8 Raman Spectroscopy analysis of Platinum based materials

Raman Spectroscopy is used for evaluating the structural composition of a carbon support, a typical Raman spectrum of a carbon support for the platinum NPs deposition show two intense bands at ~1600 cm^{-1} and at ~1350 $cm^{-1,}$ which correspond to the G (graphitic, E2g) and the D1 band (defect, A1g). Raman spectra can be interpreted using the three-stage model, that shows the evolution of the G band position and of the D1/G ratio along an amorphization trajectory going from graphite to tetrahedral amorphous carbon.

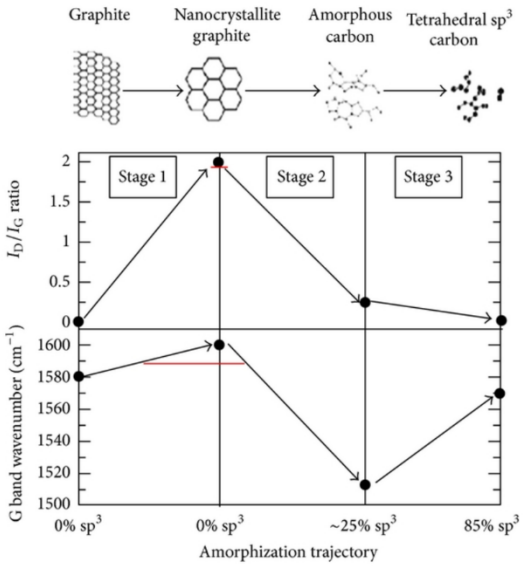

Figure 48: Three Stage Raman model for carbons material

In the first stage, graphite transforms into nano crystalline graphite (NC-graphite), where the three-dimensional order is lost due to the formation of nanosized graphite crystallites. The Raman spectra accompanying this process exhibit a shift of the G-band peak from about 1580 cm^{-1} to about 1600 cm^{-1}. In the second stage nanocrystalline graphite coverts into amorphous carbon (G band around 1500 cm^{-1}), that consists of mainly sp^2 sites in puckered ring-like configurations and in the third stage, amorphous carbon converts into tetrahedral amorphous carbon (G band around 1560 cm^{-1}), in which the carbon sp2 sites is gradually converted from rings to olefin chains. The stage three show the conversion from amorphous carbon to tetrahedra carbon sp3.

In order to recognize individual components in the Raman spectra, deconvolution analysis has been carried out. In the literature, commercial carbon has been fitted with three bands and other carbon materials with four or five bands. Generally, four bands were necessary to obtain a good fit: however, letting all parameters free, the fit became ambiguous, and depending on the starting values and on the band, shape adopted, the fit reached several minima, all with a very good and similar adjusted R2 but corresponding to different band combinations. This probably arises from the overlap of the bands used to deconvolute the spectrum.

The frequency of the two bands corresponding to D1 and G were constrained between 1300 cm^{-1} and 1400 cm^{-1} and between 1550 cm^{-1} and 1650 cm^{-1}, respectively. The frequency of the other two bands were fixed at 1500 cm^{-1} (D3

band) and 1200 cm^{-1} (D4 band). The D3 band is assigned to amorphous carbon and the D4 one has been tentatively related to the presence of polyenes or ionic impurities. All band shapes were chosen Gaussian and FWHMs let free. Raman was used for evaluated the carbon component, in fact the different components such as graphitic or amorphous have a different impact on the platinum NPs. An high graphitic component means an low capacitive current and an high electron transfer between the Pt NPs and the carbon support, but also a low NPs stabilization which can grow without control. In the other hand, an amorphous carbon shows an high capacitance, in fact they generally applied in the supercapacitor sector. In a total amorphous mesoporous carbon, the electronic interactions between the metal NPs and the carbon active site are lacking [125, 126].

5.8.1 Instrumentation

The excitation wavelength used in the experiments was 514 nm. The size of the laser spot at the sample was about 3 mm by 80 µm and the power at the sample about 12 mW (Intensity = 5 W cm^{-2}). Cyclohexane was used as a frequency standard for the calibration of the Raman shift. Every spectrum was acquired as the average of a minimum number of 10 spectra with a minimum of 10 s integration time. A minimum of three points on the sample were recorded and all spectra turned out to be identical. Test measurements were recorded also with a home-built Micro-Raman setup operating at 514 nm with a 20x objective and showed that also in this configuration the spectra do not depend on the illuminated point of the sample.

5.9 XPS of Platinum based material

XPS is a fundamental technique in the Platinum based material analysis. XPS permits to determinate the oxidation state of the metal and the amount of each component. In adding, the XPs permits to evaluate the electronic interaction of the platinum with other species, such as yttrium in the case of Platinum-Yttrium alloy or with Nitrogen or Sulphur in the case of platinum on doped mesoporous carbon. The interaction is evaluated as binding energy shift of the platinum component, in fact when the electronic density of the noble metals is varied, the energy of the valence state can increase or reduce.

The XPs signal was fitted with a Gaussian-Lorentzian curve, generally for the metal component, the resulting line shape is composed by 70 % of Gaussian behaviour and 30 % of Lorentzian. The Gaussian function describe the instrumental response, the doppler and thermal broadening, the Lorentzian function explain the natural broadening due to the different lifetime. The effect of the material on the fitting process is due to the spin-orbital coupling, electron-photon interaction or different surface charging. The XPS instrumentation such as the XPS electron analyser or the non-total monochromatic X ray source causes an asymmetry in the signal. For these two reason a double function must be used for fitting the signal. For the metal signal, the situation can be complicated by a peak asymmetry. A XPS peak, generally, is described by two components the FWHM (Full Width at Half Maximum), the Lorentzian/Gaussian ratio.

The main elements evaluated, in this PhD thesis, by XPS are Pt, Pd, Y, S, N, C and O.

In Platinum Yttrium alloy catalysts, alloy formation was evaluated by XPS analysis. the Pt 4f peak of the Pt_xY NPs can be fitted with 3 components: the first one, at lower B.E. belongs to metallic Pt, the other components centered at 72.1 eV and 73.2 eV are assigned to Pt (II) and Pt (IV) species, respectively, Figure 49a. The core level peak of the Pt NPs on MC sample is shifted of 0.3 eV to higher B.E. with respect a common catalysts Pt/C. The Pt (0) shift is the first indication of the formation of Platinum-Yttrium alloy. The Y 3d peak has been rationally fitted with 3 components centred at B.E. of 156.3 eV, 157.4 eV and 158.4 eV, and corresponding to metal Y in alloy Pt_xY, Y-C and Y_2O_3, respectively [127]. Yttrium not in alloy form show a Y (0) component peaked at 156.6 eV, the lower binding energy evaluated in Pt_xY catalysts correspond to the Pt-Y interaction, Figure 49b.

In a Platinum material the component of the carbon support, typically, analysed are C 1s, N 1s, S 2s and O 1s. The C 1s can be fitted with three main components, which are assigned to C sp^2 species at 284.4 eV, to C sp^3 species at 284.9 eV (generally, associated to C-H and C-C bonds) and to C sp^3 species bound to an heteroatom (B.E. = 286.5 eV).

Similarly, the broad O 1s peak can be fitted with four components corresponding to carbonyl oxygen in esters group at 530.8 eV; oxygen atoms in hydroxyls or ethers at 531.6 eV, the ether oxygen atoms in esters at 532.6 eV and carboxyl groups 533.7 eV [128].

N 1s XPS region show three different components centred at 398.4 eV (pyridinic), 399.6 eV (pyrrolic) and 400.7 eV (N graphitic). A fourth component peaked at 401.6 eV, which correspond to oxidized nitrogen.

XPS scan of the S 2p signal can be fitted with a single component at 163.9 eV, which is assigned to carbon sulphur group or thiophenic group. The interactions occurring between a catalyst material and the support play a significant role in terms of nanoparticle size and catalysts dispersion because the properties of the support directly affect the nucleation and growth processes during preparation. Nitrogen or sulphur containing carbon can tremendously influence the affinity of noble metal precursors onto carbon supports via electronic interactions, the size of the cluser, the dissolution of the platinum or the platinum particles is directly influence by the electronic interaction.

Considering all these effects, XPS is a crucial technique for determinate the electronic modifications, evaluated in terms of binding energy shift or signal increment, between metal active phase and the heteroatoms, which are connected to the catalytic activity of the resulting material. The electrochemical performance in an platinum based material can be connected to the binding energy shift [129].

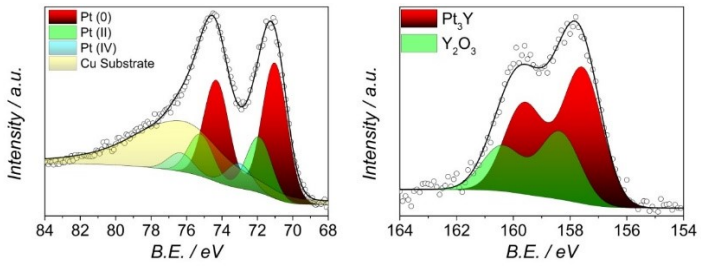

Figure 49: Examples of Platinum 4f and Yttrium 3d XPS analysis

To perform XPS measurements, 2.5 mg of the Pt based material powders were dispersed in Milli-Q water or ethanol, depending by the hydrophobic of the carbon support and sonicated for 45 min in order to efficiently disperse the

powders; the solutions were then drop-cast on electropolished polycrystalline copper or GC substrates (with a surface area of 1 cm^2). Thus, the samples were first dried overnight under nitrogen flux to obtain homogeneous films.

5.9.1 Instrumentation

X-ray photoemission spectroscopy (XPS) measurements were performed in a UHV chamber (base pressure < 5 x10-9 mbar), equipped with a double anode X-ray source (Omicron DAR-400) and a hemispherical electron analyzer (Omicron EA-125) at r.t., using non-monochromatized Mg-Ka radiation (hν =1253.6 eV) and a pass energy of 50 eV and 20 eV for the survey and the high resolution spectral windows, respectively. The calibration of the Binding Energy (B.E.) scale was carried out using Au 4f as the reference (B.E. Au 4f = 84.0 eV).

5.10 XRD of Platinum based material

X-Ray diffraction (XRD) is used in combination with transmission electron microscopy (TEM) and, for fuel cell electrocatalysts, electrochemical methods such as cyclic voltammetry, in the characterisation of supported platinum catalysts. The catalytic activities of Pt catalyst or Pt based catalysts can be described by multiple parameters as the NPs size, the electronic interaction, the NPs shape or crystallography. The Oxygen Reduction Reaction occur with different kinetic rate on the various crystallography platinum faces, so knowing the crystallography is very important for analysed the catalytic activity. Platinum shown different diffraction peaks at the Bragg angles of 39°, 46°, 67° and 81° which are in good agreement with the (111), (200), (220), and (311) facets, Figure 50.

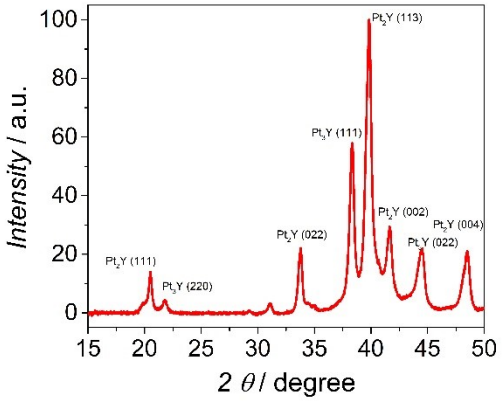

Figure 50: Typical XRD diffractogram of Platinum-Yttrium alloy NPs on mesoporous carbon

The XRD peaks of Pt nanoparticles were broad and comparable to those of the corresponding bulk Pt material. The average Pt crystallite dimensions can be calculated by measuring the full width half maximum of the Pt X-ray powder diffraction peaks, using the Debye–Scherrer equation.

$$L = 0.94\frac{\lambda}{\beta \cos\theta} \tag{5.8}$$

where L is the mean size of Pt crystallites, λ is the X-ray wavelength (1.5418 Å), θ is the angle of the peak, and β is the half-peak width.

Pt_xY alloy formation can be evaluated also with XRD, diffraction peaks show a slight shift, with respect to the Pt pure metal crystallographic peaks. The crystallographic peak shift was reported to be an evidence for the alloy formation between Pt and Y. XRD is a fundamental technique for determine the influence of the heteroatoms on the growing of specific active facets [130, 131, 132, 133].

5.10.1 Instrumentation

XRD measurements were performed using a Panalytical X'Pert Pro diffractometer equipped with a Co anode X-ray tube (40 kV, 40 mA), Bragg-Brentano optical module and X'Celerator detector (with a detecting length of 2.122° 2 theta). Diffraction patterns were collected in the 5 ° - 130 ° 2θ range, with 0.033° 2θ virtual step size, counting an equivalent time of 100 s per step. The average dimension of ordered crystalline domains (crystallite sizes) were estimated by line profile analysis using the W-H plot method as implemented in HighScore Plus v. 3.0.

5.11 Bibliography

[115] K. Shinozaki, J.W. Zack, R.M. Richards, B.S. Pivovar, S.S. Kocha, Oxygen reduction reaction measurements on platinum electrocatalysts utilizing rotating disk electrode technique: I. Impact of impurities, measurement protocols and applied corrections, J. Electrochem. Soc. 162 (2015) F1144–F1158. doi:10.1149/2.1071509jes.

[116] K. Shinozaki, J.W. Zack, S. Pylypenko, B.S. Pivovar, S.S. Kocha, Oxygen reduction reaction measurements on platinum electrocatalysts utilizing rotating disk electrode technique II. influence of ink formulation, catalyst layer uniformity and thickness, J. Electrochem. Soc. 162 (2015) F1384–F1396. doi:10.1149/2.0551512jes.

[117] Y. Garsany, O.A. Baturina, K.E. Swider-Lyons, S.S. Kocha, Experimental methods for quantifying the activity of platinum electrocatalysts for the oxygen reduction reaction, Anal. Chem. 82 (2010) 6321–6328. doi:10.1021/ac100306c.

[118] A. Guha, W. Lu, T.A. Zawodzinski, D.A. Schiraldi, Surface-modified carbons as platinum catalyst support for PEM fuel cells, Carbon N. Y. 45 (2007) 1506–1517. doi:10.1016/j.carbon.2007.03.023.

[119] J.A. Prithi, N. Rajalakshmi, G. Ranga Rao, Nitrogen doped mesoporous carbon supported Pt electrocatalyst for oxygen reduction reaction in proton exchange membrane fuel cells, Int. J. Hydrogen Energy. 43 (2018) 4716–4725. doi:10.1016/j.ijhydene.2017.11.137.

[120] S.H. Joo, S.J. Choi, I. Oh, J. Kwak, Z. Liu, O. Terasaki, R. Ryoo, Erratum: Ordered nanoporous arrays of carbon supporting high dispersions of platinum nanoparticles (Nature (2001) 412 (169-172)), Nature. 414 (2001) 470.

[121] V. Yarlagadda, M.K. Carpenter, T.E. Moylan, R.S. Kukreja, R. Koestner, W. Gu, L. Thompson, A. Kongkanand, Boosting Fuel Cell Performance with Accessible Carbon Mesopores, ACS Energy Lett. 3 (2018) 618–621. doi:10.1021/acsenergylett.8b00186.

[122] M. Riisom, B. Gammelgaard, I.H. Lambert, S. Stürup, Development and validation of an ICP-MS method for quantification of total carbon and platinum in cell samples and comparison of open-vessel and microwave-assisted acid digestion methods, J. Pharm. Biomed. Anal. 158 (2018) 144–150. doi:10.1016/j.jpba.2018.05.038.

[123] Y. Pei, B. Zhang, R. V. Maligal-Ganesh, P.J. Naik, T.W. Goh, H.L. MacMurdo, Z. Qi, M. Chen, R.K. Behera, I.I. Slowing, W. Huang, Catalytic properties of intermetallic platinum-tin nanoparticles with non-stoichiometric compositions, J. Catal. 374 (2019) 136–142. doi:10.1016/j.jcat.2019.04.013.

[124] Y.W. Lee, S. Cha, K.W. Park, J.I. Sohn, J.M. Kim, High performance electrocatalysts based on Pt nanoarchitecture for fuel cell applications, J. Nanomater. 2015 (2015). doi:10.1155/2015/273720.

[125] A. Jorio, A.G. Souza Filho, Raman Studies of Carbon Nanostructures, Annu. Rev. Mater. Res. 46 (2016) 357–382. doi:10.1146/annurev-matsci-070115-032140.

[126] H. Okuda, R.J. Young, D. Wolverson, F. Tanaka, G. Yamamoto, T. Okabe, Investigating nanostructures in carbon fibres using Raman spectroscopy, Carbon N. Y. 130 (2018) 178–184. doi:10.1016/j.carbon.2017.12.108.

[127] C. Roy, B.P. Knudsen, C.M. Pedersen, A. Velázquez-Palenzuela, L.H. Christensen, C.D. Damsgaard, I.E.L. Stephens, I. Chorkendorff, Scalable Synthesis of Carbon-Supported Platinum-Lanthanide and -Rare-Earth Alloys for Oxygen Reduction, ACS Catal. 8 (2018) 2071–2080. doi:10.1021/acscatal.7b03972.

[128] N. Hellgren, R.T. Haasch, S. Schmidt, L. Hultman, I. Petrov, Interpretation of X-ray photoelectron spectra of carbon-nitride thin films: New insights from in situ XPS, Carbon N. Y. 108 (2016) 242–252. doi:10.1016/j.carbon.2016.07.017.

[129] V. Perazzolo, C. Durante, R. Pilot, A. Paduano, J. Zheng, G.A. Rizzi, A. Martucci, G. Granozzi, A. Gennaro, Nitrogen and sulfur doped mesoporous carbon as metal-free electrocatalysts for the in situ production of hydrogen peroxide, Carbon N. Y. 95 (2015) 949–963. doi:10.1016/j.carbon.2015.09.002.

[130] M. Escudero-Escribano, P. Malacrida, H.M. Hansen, U. Vej-Hansen, A. Velazquez-Palenzuela, V. Tripkovic, J. Schiøtz, J. Rossmeisl, I.E.L. Stephens, I. Chorkendorff, Dering That Can Enable the Engineering of Material Properties Through Spontaneous Ordering of Nanoparticles., Science (80-.). 352 (2016) 73–76.

[131] S.B. Han, D.H. Kwak, Y.W. Lee, S.J. Kim, J.Y. Lee, S. Lee, H.J. Kwon, K.W. Park, Electrodeposited nanoporous PtY alloy electrodes with enhanced oxygen reduction reaction, Int. J. Electrochem. Sci. 11 (2016) 3803–3814. doi:10.20964/110380.

[132] J.A. Bordley, M.A. El-Sayed, Enhanced electrocatalytic activity toward the oxygen reduction reaction through alloy formation: Platinum-silver alloy nanocages, J. Phys. Chem. C. 120 (2016) 14643–14651. doi:10.1021/acs.jpcc.6b03032.

[133] E.C. Wegener, Z. Wu, H.T. Tseng, J.R. Gallagher, Y. Ren, R.E. Diaz, F.H. Ribeiro, J.T. Miller, Structure and reactivity of Pt–In intermetallic alloy nanoparticles: Highly selective catalysts for ethane dehydrogenation, Catal. Today. 299 (2018) 146–153. doi:10.1016/j.cattod.2017.03.054.

6 Catalysts Synthesis

6.1 Platinum based material synthesis

Some of the most important challenges in the synthesis of carbon supported Pt-alloy nanoparticles are the different nucleation and growth rates of the platinum precursor, which are directly related to the Nanoparticles size and distribution, and thus to ORR activity. Typical platinum precursors are: $Pt(acac)_2$, H_2PtCl_4, $Pt(NO_3)_2$ or $PtCl_2$. The ligands contained in the metal precursor play a crucial role in controlling the size and shape of the metal NPs. The reduction of the Pt precursors is generally faster than other transition metals due to the very positive standard reduction potential, differently, for example from the case of Y that has a very negative one. The nucleation and sizes of Pt@C and Pt_xM alloy NPs can be tuned by several factors, including temperature, time, reduction environmental and the addition of a secondary metal precursor in the case of alloy. In the common synthesis of Platinum-Yttrium alloy materials, the different Pt precursors, the presence of the Y precursor and different temperatures contribute to variations in the formation of Pt_xY alloys and to the formation of monodisperse and homogeneous NPs. The nature of Pt precursor salt is very important to obtain nanoparticles with a small size, a narrow distribution and good dispersion on the surface of mesoporous carbon. Platinum NPs can be obtained with different synthesis methodology, as wet chemistry, sputtering, chemical reduction; the platinum reduction in each method is incomplete; platinum (0) and platinum oxide are formed. For example, the chemical reduction of $PtCl_2$ with $NaBH_4$ form big aggregates and inhomogeneous NPs distribution on the carbon support. The same result is obtained using different reduction agent or more complex ligand [114].

The preparation of Pt_xY alloy NPs has proved to be a very challenging task since, in the presence of H_2O or O_2 traces, Y_2O_3 is the most thermodynamically stable product. Pt_3Y can be prepared by chemical reduction with $NaBH_4$ in an aqueous solution of H_2PtCl_6 and $Y(NO_3)_3$ and annealing the product at 900 °C under H_2 flow. XPS analysis revealed the formation of a Platinum-Y_2O_3 mixture. Or the water-in-oil chemical route synthesis of $Pt(acac)_2$ with YCl_3 show the formation of only yttria. Actually, only sputtering techniques under UHV conditions have allowed the formation of Pt_3Y alloys in NP or film form.

A different synthetic approach was undertaken consisting in the solid state synthesis at high temperature and in a reduction atmosphere of the Pt or Pt_xY NPs directly on a MC support. Pt NPs were synthetized by solid state synthesis, the synthesis is easy, fast but especially massive [114, 134, 135].

6.1.1 Synthesis Procedure

Pt NPs were deposited on carbon support via solid state synthesis at high temperature under a reduction environmental with a mixture of hydrogen and nitrogen. The starting Pt precursor was weighed in order to obtain a catalyst powder with a final Pt loading of 30 %w for Pt@C catalysts while 27 %w in Pt-alloy@C catalysts.

In a typical experiment for Pt@C material, ca. 60 mg of $Pt(acac)_2$ and ca. 100 mg of carbon support were mixed together, dispersed in ca. 15 mL acetone, and sonicated for 1 h at 20 °C in bath sonicator. The resulting slurry was dried in an oven at 80°C for 2 h, allowing the drying of the mixture and the obtaining of a fine powder.

For Pt_xY@C, the Pt and Y salts were weighted to obtain a 3:1 molar ratio, because the alloy Pt_3Y is the best active for ORR. Generally, ca. 35 mg of $Pt(acac)_2$, and 50 mg of mesoporous carbon were mixed after dispersed in acetone and sonicated for 1 h at 15 °C. The resulting slurry was dried in an oven at 70 ° C for 4 h, allowing the drying of the mixture and the obtainment of a fine and dry powder.

Figure 51: Tubular Furnace

After that, the mixture was heat-treated in a tubular furnace (Carbolite, UK) at a suitable temperature under an H_2/N_2 flow of 2/23 sccm. Before starting the heat treatment, the quartz tube was purged with N_2 using a flux of 30 sccm for 1 h at room temperature (r.t.) to remove O_2. Then, the temperature was raised to 100 °C and kept constant for 1 h to desorb H_2O, which can react with the carbon but especially with the metal salts; at the same time H_2 was gradually fluxed into the quartz tube to the desired ratio (8%, 23 sccm N_2 and 2 sccm H_2). Finally, the temperature was allowed to increase to working temperature and kept constant for the time reaction, after which the furnace was cooled down to r.t., while the H_2 flow was switched off, allowing only N_2 to flow inside the reactor. The obtained catalyst was then removed from the quartz boat, ground by vibro-milling.

6.2 Mesoporous carbon synthesis via Hard Template

As carbon support for the Platinum NPs different carbon was tested, commercial and homemade. An typical synthesis method for obtain a mesoporous carbon support is the hard template. Hard template permits a good control on the geometry and structure of the resulting carbon. These characteristics are fundamental for the Platinum NPs deposition. Mesoporous Carbons (MCs) are very interesting materials for their proprieties such as high surface area, porous structure, good thermal and chemical stability, good conductivity and low density. MCs can be used not only as carbon support in PEM fuel cells, but also as supercapacitors and hydrogen storage material. Pores are classified according their diameter in micropores (less than 2 nm), mesopores (included between 2 and 50 nm) and macropores (bigger than 50 nm). Mesoporous range is suitable for application as carbon support in PEM fuel cells, because it allows both Pt NPs. The interactions occurring between the metal NPs and the support, directly influence the nanoparticle size and distribution, because the properties of the support directly affect the nucleation and growth processes. Furthermore, the catalyst/support chemical binding would result in enhanced durability and intrinsic catalytic activity. The morphological aspects which are most evaluated, and directly influence the platinum properties, are the surface area and the pore dimension and interconnection. In fact, high surface area is necessary for optimizing the Pt active phase dispersion, whereas wide and interconnected mesopores are desirable for improving the NPs distribution and so the active area but also reagents and products mass transport.

Hard Template involves the employment of two main reactants: an inorganic template, whose porous structure is transferred to the synthesizing material, and a carbon source, molecules which may pyrolyse to give carbon structures. A general procedure to synthesize MCs via hard template consists in the wetting of an inorganic template with a solution of a carbon precursor. The three fundamental steps of hard template process for porous carbon synthesis are: impregnation of template with the carbon precursor, pyrolysis and template etching. With a mesostructured silica, the resulting carbon structure is the negative replica of the templating agent: the pores of the silica are filled with the carbon precursor, which becomes the continuous carbon framework, while the silica becomes the pores of the carbon structure after chemical etching. The pore size of an MC obtained via hard template is influenced by the pore wall thickness of the silica. An important parameter is the pore interconnection, which consist in micropores interconnected with the main mesoporous systems. The micropores interconnected structure is fundamental for increase the mechanical resistance of the resulting carbon and prevent the structure from the collapsing. The hard template synthesis is used in the synthesis of carbon doped materials because the insertion of N heteroatoms, but also S, P, B are obtained using carbon precursors containing the respective heteroatom [135, 136].

Several model systems show how nitrogen or sulphur modified carbon can (i) interact with the active metal phase, driving the nucleation and growth of metal NPs, (ii) increase the catalytic activity due to electronic interaction between metal and support, and (iii) afford higher stability .

Nowadays the most important reason for doping carbon support employed in fuel cells is linked to the modification of the interaction between carbon support and metal nanoparticles. In particular N doping appears to be responsible for the creation of strong and favourable interaction which may enhance the catalytic properties of catalyst, and at the same time may reduce the Pt loading. According to reference, the effect of heteroatoms doping on the activity of Pt based catalyst is responsible for the following effects:

(1) Alteration of catalyst nucleation and growth behaviour. Smaller Pt NPs and narrower size distribution are obtained on doped carbon materials, also in the case when high Pt loading is realized. This indicates a fundamental role in support chemistry in the determination of dimension and distribution of Pt NPs. Generally, high rate of nucleation is realized when the surface is defective and surface energy in high.
(2) Alteration of support/catalyst binding. Nitrogen or sulphut functionalities are supposed to act chemical binding sites. This allows better dispersion and improves the stability of Pt NPs with respect to agglomeration and coarsening.
(3) Alteration of catalyst electronic structure. Doping consists in the chemical modification of carbon materials via heteroatom insertion in their structure. It consists in an important strategy to modify or improve properties of materials.

The nitrogen content in commonly used nitrogen doped carbon is in the range 1 % - 8 %; higher values lead to a resistive material of poor interest for the application as particles support. Nitrogen functional groups, produced by pyrolysis at high temperatures, can be singled out as pyridinic defects, pyrrolic defects and N-graphitic defects, even though oxidized nitrogen can be also present pyridinic and pyrrolic functional groups are of interest because they are supposed to be responsible for the strong interaction between Pt NPs and the doped carbon support.

It was largely demonstrated how nitrogen doped carbon exerts a strong interaction with the supported Pt NPs triggering their electronic properties and catalytic activity. Also, sulphur affords a clear metal support interaction between Pt NPs and the carbon support. Sulphur doped supports significantly improve the kinetics and the stability of Pt for ORR, respectively. The positive effect of sulphur in low percentage (2-4 %) is well established, however when the sulphur concentration is increased in the carbon support, the effect on the electrochemical properties and the NPs morphology is very complex. For example, it was demonstrated that the proximity of different nitrogen and sulphur functional groups, that correspond with a high density of heteroatoms, destabilizes the formation of small Pt nuclei and their catalytic activity. Condensed aromatic heterocycles were adopted as precursor materials for the synthesis of different MCs. The adopted precursors for nitrogen doped material is 1,10-phenantroline, while for sulphur material is dibenzothiophene [136, 137].

The carbon was synthetized by mixing 1 g of carbon precursor and 0.5 g of silica in acetone or ethanol (20 mL) depending by the salt solubility. After 2 h, 250 μL of H_2SO_4 was add during the impregnation process for accelerated the carbon precursor oligomerization. The solution was dried in oven overnight at 70 °C or until a completely solvent evaporation. The pyrolysis protocol is composed of 4 steps: conditioning, heating,

maintaining of pyrolysis temperature and cooling. The substrate was thermal treated in a quartz tube in an argon-controlled atmosphere; for desorb all residues as oxygen or water, the substrate was heated at 100 °C for 1 and after, pyrolyzed with a ramp of 5 °C until 750 °C or 950 °C for 2 h. The system is finally cooled down for an entire night till room temperature (r.t.) is reached. After the synthesis the silica was totally removed by etching treatment with 20 mL with sodium ethanoate in sonicator bath for 3 day. The carbon is then separated by vacuum filtration on a nylon nanometric filter (GVS, nylon 0.2 mm, 47 mm membrane diameter) [135,137, 138].

The silica used as templating agent are describe following:

- P200: mesostructured silica purchased from Sigma Aldrich, made of spherical particles with diameter of 200 nm and mesopores of 4 nm.
- P20: non porous silica spherical particles with mean diameter equal to 10 nm -20 nm, used for chromatographic applications.
- P10: non porous silica spherical particles with mean diameter equal to 5 nm - 15 nm, used for chromatographic applications

Silica P200 has a mesostructured, the carbon salt precursors entry inside the pore structure so the final carbon structure is given by the silica porosity, in contrast the carbon porosity is given by the silica structure. In the mesoporous carbon obtained with silica P20 and P10, the carbon structure is given by the silica structure after the silica removal.

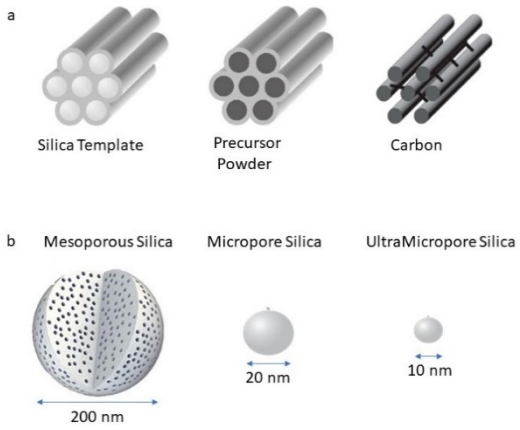

Figure 52: a) MC synthesis procedure by hard template, using a mesostructured silica; b) Silicas structure and dimension

6.3 Bibliography

[134] L. Perini, C. Durante, M. Favaro, V. Perazzolo, S. Agnoli, O. Schneider, G. Granozzi, A. Gennaro, Metal-support interaction in platinum and palladium nanoparticles loaded on nitrogen-doped mesoporous carbon for oxygen reduction reaction, ACS Appl. Mater. Interfaces. 7 (2015) 1170–1179. doi:10.1021/am506916y.

[135] V. Perazzolo, R. Brandiele, C. Durante, M. Zerbetto, V. Causin, G.A. Rizzi, I. Cerri, G. Granozzi, A. Gennaro, Density Functional Theory (DFT) and Experimental Evidences of Metal–Support Interaction in Platinum Nanoparticles Supported on Nitrogen- and Sulfur-Doped Mesoporous Carbons: Synthesis, Activity, and Stability, ACS Catal. 8 (2018) 1122–1137. doi:10.1021/acscatal.7b03942.

[136] R. Brandiele, L. Picelli, R. Pilot, V. Causin, A. Martucci, G.A. Rizzi, A.A. Isse, C. Durante, A. Gennaro, Nitrogen and Sulfur Doped Mesoporous Carbons, Prepared from Templating Silica, as Interesting Material for Supercapacitors, ChemistrySelect. 2 (2017) 7082–7090. doi:10.1002/slct.201701404.

[137] B. You, F. Kang, P. Yin, Q. Zhang, Hydrogel-derived heteroatom-doped porous carbon networks for supercapacitor and electrocatalytic oxygen reduction, Carbon N. Y. 103 (2016) 9–15. doi:10.1016/j.carbon.2016.03.009.

[138] Z. Yang, Y. Zhang, Z. Schnepp, Soft and hard templating of graphitic carbon nitride, J. Mater. Chem. A. 3 (2015) 14081–14092. doi:10.1039/c5ta02156a.

7 Pt NPs on Nitrogen doped Carbon: Metal deposition and Doping

7.1 Abstract

Pt nanoparticles (Pt NPs) are deposited on commercial high-area carbon support materials. Carbon supports with high surface area and high graphitization, provide good electrical conductivity, bring catalyst particles closer to reactants via the pore mesoporous structure and prevent particle agglomeration. The carbon structure must be mesoporous with an micropore interconnection, for host the Platinum Nanoparticles and prevent collapsing process. Furthermore, the insertion of heteroatoms, such as nitrogen, sulphur or boron, into the carbon structure has enabled to improve the chemical and physical stability of carbon-based support materials as conductivity, stability, durability. Nitrogen doping prevents the agglomeration process, improves the distribution of metal nanoparticles on carbon support, in low concentration reduce the resistivity and increase the control on the NPs growing. Nitrogen doped carbon supports not only increase the dispersion and distribution of metal nanoparticles but render increase the durability and the NPs resistivity by introducing more binding sites to the carbon surface that anchor metal precursor. These effects are fundamental for stabilized the Pt NPs on carbon, the stabilization lead to the possibility of a platinum concentration reduction. Nitrogen-doped carbon as catalyst support is expected to improve the durability, in terms to prevent detachment or leaching process, of the resultant catalysts because of the enhanced π-bonding which are increase the electron donor proprieties of nitrogen [139, 140, 141]. The nitrogen content in commonly used nitrogen doped carbon is in the range 1 % - 8%; higher values lead to a resistive material, which are incompatible with the metal deposition or with an application as catalyst for ORR. Nitrogen concentration higher than 10 % generally is used as electron blocking. Nitrogen functional groups, produced by pyrolysis at temperature higher than 600 °C, can be singled out as pyridinic defects, pyrrolic defects and N-graphitic defects, even though oxidized nitrogen can be also present. Pyridinic and pyrrolic functional groups are interesting because interact with the Pt NPs, driving the nucleation process. The common synthesis of Platinum NPs on doped carbon support are divided in two steps, (i) the synthesis of nitrogen doped carbon support by pyrolysis or graphene exfoliation (ii) the Platinum NPs deposition. The process results unfavourable for obtain a controlled nitrogen functional group distribution on the mesoporous carbon, and for maximized the interaction with the Pt NPs which area homogeneous distributed in the carbon support [142, 143, 144].

PtN@C was synthetized by solid state synthesis in reduction atmosphere with the simultaneous N doping introduction in the carbon structure. Pt metal NPs deposition and carbon support doping, by using a platinum precursor bearing a nitrogen containing ligand. The synthesis would allow to keep the metal NPs as much close as possible with the nitrogen domains, the process is fundamental for maximized the Platinum-Nitrogen interaction and increase the catalytic activity of the resulting platinum catalyst. TEM images show the effect of the Pt-N

interaction on the NPs morphology and distribution on the carbon matrix and the totally absence of agglomerate. The Nanoparticles show an narrow dimensional distribution peaked at 2.5 nm. XPS analysis confirmed that during the thermal treatment the ligand degrades, and the nitrogen is embedded in the mesoporous carbon structure, resulting in a surface modification of the carbon support with preservation of bulk conductivity and thermal stability of the carbon support [145, 146]. The nitrogen insertion has not any impact on the carbon morphology as surface area, pore structure or pore dimension.

Electrochemical characterization at a rotating disk electrode in O_2 saturated 0.1 M $HClO_4$ revealed a superior catalytic activity for ORR, in terms of $E_{1/2}$ and mass activity, in those catalysts showing higher Pt-N interaction, expressed as binding energy shift of nitrogen components. Furthermore, cyclic voltammetry analysis in Ar purged 0.1 M $HClO_4$ electrolyte showed that nitrogen doping appears to inhibit PtO formation. The influence of nitrogen incorporation in the carbon matrix on Pt NPs-support interaction was also rationalized on the basis of density functional theory simulations.

7.2 Synthesis and Chemical

Mesoporous Carbon (MC) (Sigma Aldrich, 500 nm particle size, >99.95%), $PtCl_2$ (Alfa Aesar, >99.9%), $Pt(acac)_2$ (Sigma Aldrich,>97%), $PtCl_2$(1,10-phenanthroline) (Sigma Aldrich, >95%), $PtCl_2$(2,20-bipyridyl) (Sigma Aldrich, >95%), 2,20-bipyridyl (Sigma Aldrich, >98%), 1,10-phenanthroline (Sigma Aldrich, >99%), platinum nominally 50 $\%_w$ on Carbon Black (TKK), Nafion (Sigma Aldrich, 5 wt% in EtOH), $HClO_4$ (Fluka, Traceselect®, 67e72%), 2-propanol (Sigma Aldrich, >99.8%), and NOCHROMIX, (Sigma Aldrich-Glass-Cleaning Reagent) were used as received without further purification.

For the synthesis a standard commercial carbon was used. The mesoporous carbon used for the support have a surface area, evaluated by BET, of 252 $m^2\ g^{-1}$ with a pore distribution positioned in the mesoporous range from 4 nm to 15 nm. The surface area is given at 78 % by the mesoporous structure and 22 % by the microporous structure. The carbon morphology is optimal for the Pt NPs deposition with a size of 2 nm – 4 nm. The salt used for the platinum deposition are $Pt(acac)_2$, $PtCl_2$, $PtCl_2$(1,10-phenantroline) and $PtCl_2$(2,2'-bypiridyl), Figure 53. The complexes bearing phenanthroline (after call "phen") or 2,20-bipyridyl (after call "bpy") as an ancillary ligand, acted as both Pt and nitrogen precursors.

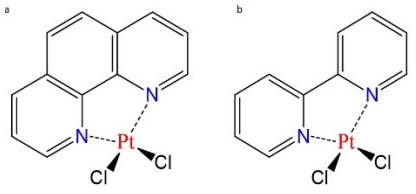

Figure 53: Chemical Structures of a) $PtCl_2$(1,10-phenantroline, b) $PtCl_2$(2,2'bypiridil)

The metal deposition occur in a tubular furnace at high temperature under a H_2/N_2 flux. Two series of catalysts was synthetized, one using a platinum complex with a nitrogen ligand as 1,10-phenantroline or 2,2'-bipyridyl and another one by mixing a platinum salt with a nitrogen source (e.g. $Pt(acac)_2$ and 1,10-phenantroline or $PtCl_2$ with bpy).

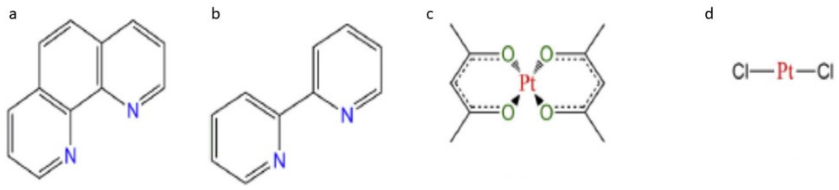

Figure 54: Chemical Structures of a) 1,10-phenantroline; b) 2,2'-bypiridile; c) $Pt(acac)_2$ and d) $PtCl_2$

In a typical experiment, a platinum precursor or a Pt complex bearing 1,10- phenantroline or 2,20-bipyridyl ligands and mesoporous carbon were mixed together in a vial, dispersed in acetone and sonicated for 1 h to favour dispersion and impregnation of the precursor inside the carbon mesopores. The dispersion in acetone is fundamental because salts precursors are soluble in this organic solvent. The amount of Pt complex was adjusted to obtain a final Pt loading of 20 $\%_w$ in the resulting catalyst. When $PtCl_2$ or $Pt(acac)_2$ was used, a stoichiometric amount of 2,20-bipyridyl or 1,10-phenanthroline was added as a source of nitrogen for the chemical doping of the carbon support. In this case the concentration of 1,10-phenantroline or 2,2'bypiridil is the same than is possible obtained when $PtCl_2$(phen) or $PtCl_2$(bpy) are used, respectively. The resulting slurry was dried directly in the quartz boat at 50 °C for 5 h. The Pt NPs were deposited with a solid state synthesis at high temperature in a reduction controlled atmosphere. Before starting the thermal treatment, the quartz tube was treated only with N_2 (30 sccm) for 1 h at room temperature (r.t.) to remove O_2 and standardized the synthesis conditions. Then, the temperature was raised to 100 °C and kept for 1 h to desorb all possible solvent by the platinum carbon powder precursor at the same time H_2 was fluxed into the quartz tube with a ratio of 8 % respect the nitrogen, the step is fundamental for remove the oxidation species which can react with the carbon or the platinum. Finally, the temperature was increase to 650 °C and kept constant for 5 h, after which the furnace was cooled down to r.t., the H_2 flow was switched off, and the N_2 flow was increased. Several experiments are conduct for evaluated the best temperature for the platinum reduction and the inclusion of the nitrogen atom in the carbon structure. At temperature lower than 600 °C, the platinum reduction resulted incomplete and the concertation was lower than 13 %, at temperature higher than 750 °C, the aggregates formation was evaluated by TEM images. The obtained catalyst was then removed from the quartz boat, ground by ball milling and dispersed in a 1 M H_2SO_4 solution. The treatment with sulphuric acid was fundamental for remove all the possible unreacted species and passivating species. The Pt catalyst powder was then separated by vacuum filtration on a nylon nanometric filter (GVS, nylon 0.2 mm, 47mm membrane diameter) and abundantly rinsed with milliQ water. Eventually, the catalyst was dried under vacuum and recovered in a glass vial.

Table 1: Synthesis condition for Platinum-Nitrogen catalysts

Catalyst	Precursor	Synthesis Temperature °C	Synthesis Time h	H_2/N_2 %	$\%^{Pt}_{teorico}$ %	$\%^{N}_{teorico}$ %
PtN1@MC	$PtCl_2$phen	650	5	8	19.6	3.5
PtN2@MC	$Pt(acac)_2$ + phen	650	5	8	20.5	5.0
PtN3@MC	$PtCl_2$ + phen	650	5	8	20.9	4.2
PtN4@MC	$PtCl_2$bpy	650	5	8	20.7	3.7
PtN5@MC	$Pt(acac)_2$ + bpy	650	5	8	19.7	4.8
PtN6@MC	$PtCl_2$ + bpy	650	5	8	19.7	4.1

The platinum content was evaluated by ICP-MS, before and after the acid treatment, which in general caused a slight decrease of platinum loading, (~0.9 $\%_w$). The nitrogen content was evaluated by Elemental Analysts, the technique can determinate also the carbon, hydrogen and sulphur content [53].

Table 2: Elemental characterization of PtN catalysts

		Platinum Loading %	C %	H %	N %
PtN1@MC		18.9 ± 0.5	75.32	0.61	2.25
	AC	16.8 ± 0.4	75.08	0.53	2.13
PtN2@MC		15.4 ± 0.4	75.67	0.35	0.97
	AC	15.1 ± 0.4	75.48	0.28	0.92
PtN3@MC		18.2 ± 0.5	83.01	0.42	1.31
	AC	16.4 ± 0.4	82.21	0.36	1.20
PtN4@MC		18.1 ± 0.5	84.21	0.39	0.97
	AC	17.3 ± 0.4	83.73	0.21	0.85
PtN5@MC		16.2 ± 0.4	72.48	0.59	0.21
	AC	15.1 ± 0.4	71.91	0.48	0.06
PtN6@MC		17.5 ± 0.4	74.11	0.46	0.41
	AC	16.8 ± 0.4	73.87	0.19	0.38

The platinum loading is very close to the theoretical value, the acid treatment reduces the metal amount of 1-2 %. The loading in the sample PtN1@C is very similar to PtN4@C and the same effect occur in the samples PtN2@C/PtN4@C and PtN3@C/PtN6@C, because the platinum salt used for the synthesis are very similar or the same. The platinum losses can be attributed also to the platinum sublimation during the thermal treatment.

In all case the ICP determination was repeated three times with different samplings. The elemental analysis shows a carbon content of 80 % and a hydrogen amount less than 1%. With the acid treatment all content degrades with an increment of the residual which can be attributed to the oxygen. After the acid treatment the catalysts shows a slight nitrogen concentration reduction. For examples, with PtN1@C before the acid treatment the material shows an nitrogen content of 2.25 % and after 2.13 %, for PtN2@C (synthetized by mixing of Pt(acac)2 and 1,10-phenantroline) show an nitrogen reduction of 1.6 %. The highest nitrogen content for the two series (1,10-phenantroline and 2,2'-bypiridil) were obtained with $PtCl_2$(1,10-phenantroline) and $PtCl_2$(2,2'-bypiridyl) with 2.13 % and 0.85 respectively. The PtN2@C and PtN3@C synthetized with $Pt(acac)_2$ show a nitrogen concentration of 0.97 % and 0.21 % for the sample obtained with 1,10-phenantroline and 2,2'bypiridil. The catalysts obtained with 2,2'-bypiridil show an nitrogen content around 0.5 %, lowest than the catalysts obtained with 1,10-phenantroline and the same platinum precursors. This type of synthesis allowed to functionalize only the carbon support surface, preserving bulk carbon properties such as the electrical conductivity and the mesoporous structure. Elemental Analysis confirmed the doping action of the 1,10-phenantroline and 2,2'bipyridyl both in the complex both in salt. The temperature synthesis permits the completely platinum deposition, a lower temperature can reduce the platinum salt but not degrade the nitrogen ligand. Several experiments were tried for reached the correct temperature and time synthesis which permit the concomitant platinum reduction and the nitrogen ligand degradation. The temperature experimented are 300 °C, 450 °C and 600 °C for 3 and 5 h. The optimum conditions for the synthesis are 650 °C for 5 h. Another easy method for valuated the degradation temperature is Thermogravimetric Analysis, TGA of $PtCl_2$Bpy, Figure 55a, showed a single wide degradation step centered at 470 °C and a complete complex degradation at 650 °C.

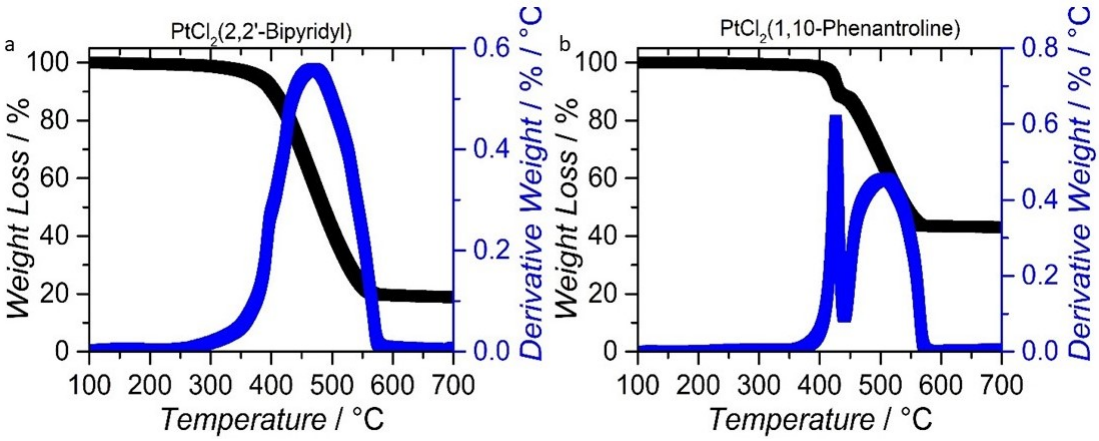

Figure 55: TGA analysis of a) $PtCl_2$(bpy) and b) $PtCl_2$(phen)

The temperature degradation range is the same for the two platinum precursors, in the case of $PtCl_2$(2,2'-bipyridyl) the chloride loss and the ligand degradation occur in the same step, while for $PtCl_2$(1,10-phenantroline), Figure 55b, the Platinum complex loss the chloride ligand at 421 °C, the 1,10-phenanthroline

degradation occur in the range 450 °C – 565 °C. The $Pt(acac)_2$ show only one peak at 198 °C, which correspond to the direct platinum sublimation.

7.3 TEM Characterization: Influence of Platinum Precursors on NPs dimension

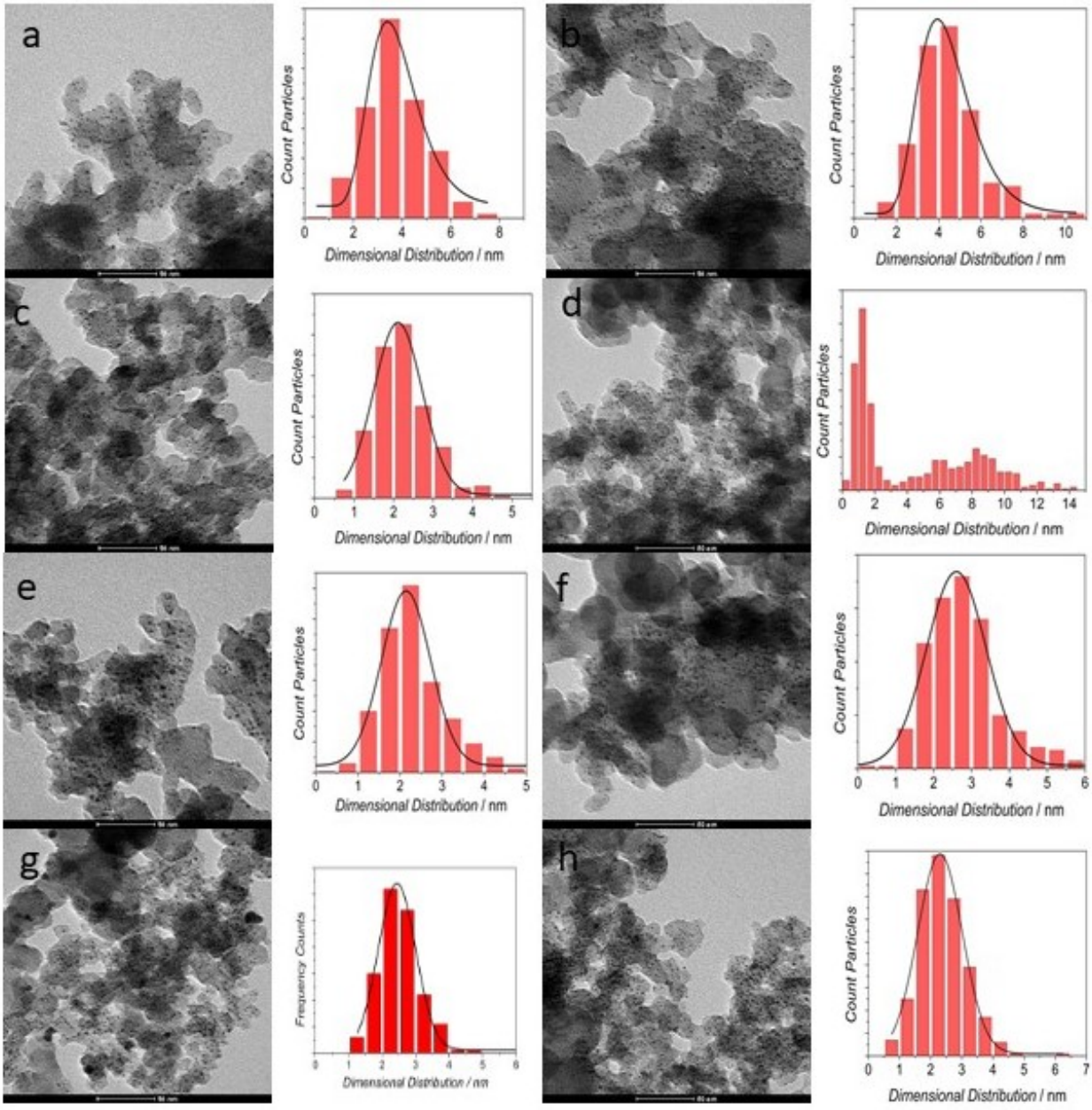

Figure 56: TEM images of a) PtN1@C; b) PtN1@C_AC; c) PtN2@C; d) PtN2@C_AC; e) PtN3@C; f) PtN3@C_AC; g) PtN4@C_AC and h) Pt/C

Figure 56 shows the TEM images for the samples PtN1@C, PtN2@C and PtN3@C before and after the acid treatment. All images show a very high population with a uniform NPs distribution on the carbon support. The corresponding particle size distributions were obtained by calculating the size of more than four hundred randomly selected particles in the magnified TEM images. For PtN1@C the mean Pt particle size diameter was centred at ca. 4 nm; in the case of PtN2@C a dual distribution was observed with mean diameters centered at 2.5 nm and 10 nm, respectively, whereas for PtN3@C even lower dimension (2.5 nm) and narrower size distribution were obtained. The catalysts PtN2@C was prepared by mixing $Pt(acac)_2$ with 1,10-phenantroline, the platinum salt has a sublimation temperature of 198 °C, evaluated by TGA. The aggregate formation and the presence of NPs with a high dimension (around 10 nm) can be correlated to the low degradation temperature. The optimum synthesis conditions for $Pt(acac)_2$ are 300 °C and 3 h, with these parameters the 1,10-phenantroline inclusion on the carbon structure is impossible. The same effect was obtained with the catalysts PtN5@C which is synthetized with the same platinum precursors and with 2,2'-bipyridyl. $PtCl_2$ is used as platinum precursor in PtN3@C and PtN6@C, the salt has an high degradation temperature, TEM images show a NPs dimension of 2.5 nm and 2.8 nm, respectively. Regarding PtN4@C, the mean Pt NPs size was similar to that of PtN1@C. However, in this case, the NPs distribution was wider and some big NPs (10 and 20 nm) were visible. The different NPs distribution and dimension are connected to the degradation temperature of the salt precursors. The degradation peak of $PtCl_2$(2,2'-bipyridyl) evaluated TGA is very splay from 420 °C to 600 °C, the chloride loss and the ligand degradation occur in one step, the peak is positioned at a temperature lower than the second degradation peak of $PtCl_2$(1,10-phenantroline). For these reason during the reduction process at 650 °C the NPs will have a higher mobility and will tend to aggregate.

The particle size distribution histograms show that the acidic wash led to a decreasing of the Pt particle dimension. It is worth noting that the treatment in H_2SO_4 decreases the Pt content in all the samples, as a result of the Pt NPs leaching and shrinking as highlighted also by the ICP analysis. Acid treatment is fundamental for remove the oxide present in the NPs surface so increase the active surface. Another utility of H_2SO_4 is the degradation of the carbon shell around the metal NPs. The carbon shell was form during the synthesis by the ligand degradation.

7.4 XPS and XRD Analysis: Platinum-Nitrogen Interaction

Nitrogen insertion on the carbon matrix was confirmed by XPS, the doping action was evaluated by the interaction with the platinum and the relative shift of its binding energy. To compare the chemical physics data the commercial carbon used as support was treated with only 1,10-phenantroline at 650 °C for 5 h in H_2 and N_2 atmosphere. The carbon catalysts is used to compare eventually binding energy shift, obtain after the platinum deposition. In **Errore. L'origine riferimento non è stata trovata.** is immediately evident how the addition of Pt NPs shifted the N 1s spectra to higher binding energies by about 0.5 eV, as indicated by the yellow highlighted area in the figure, while its FWHM remained almost unchanged in all samples (2.7 eV and 2.8 eV).

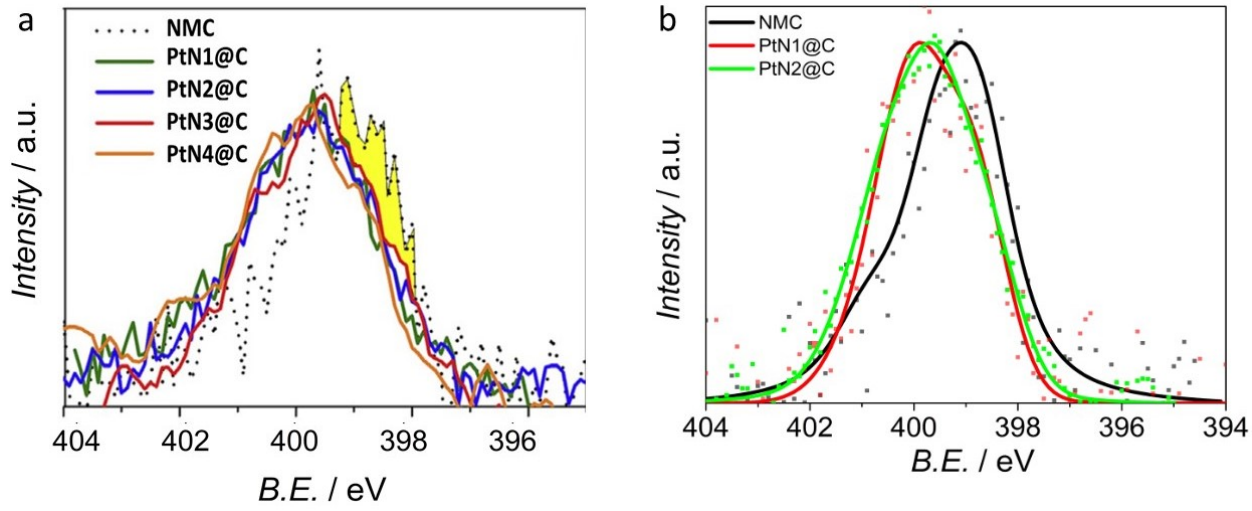

Figure 57: a) XPS spectra raw data N 1s b) XPS spectra N 1s for NMC, PtN1@C and PtN2@C

A decrease in the electron density of the Pt would result in an increase of the Pt 4f BE. The nitrogen 1s peak was fitted using three components, assigned to pyridinic, pyrrolic and graphitic nitrogen group. After the platinum deposition the binding energy of pyridinic and pyrrolic component was shifted at higher value, pyridinic group from 398.7 eV to 398.8 eV and pyrrolic group from 399.6 eV to 399.9 eV, Figure 58. The graphitic component remained unchanged before and after the platinum reduction. The different binding energy shift is connected to the different interaction between the platinum and the nitrogen group. Pyridinic and pyrrolic nitrogen have lone pairs that can be donated to Pt atoms, although the lone pair of pyrrolic nitrogen is less basic because it is part of the aromatic π system. In literature, many articles show as the graphitic nitrogen do not interact with the platinum, because its aromatic system have an energy too lower respect the platinum electronic structure.

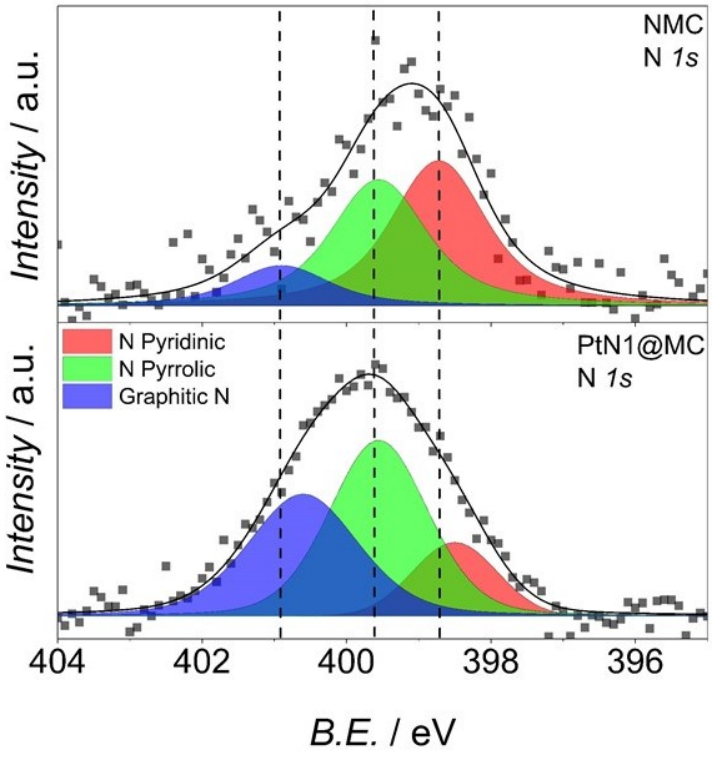

Figure 58: XPS spetra of N 1s component for NMC and PtN1@C

Pyridine complexes with Platinum showed a p back-donation/s donation ratio of 0.37 for Pt (0)-pyridine complex, meaning that the contribution of the lone pair to the N-Pt bond is higher. Nevertheless, a higher amount of back-donation from Pt to π* orbitals in the case of Pt NPs is expected so that a rather limited binding energy shift of the N 1s peak is observed. The main component in N 1s spectra of PtN@C catalysts is the pyrrolic group. Regarding the Pt 4f region, the spectra contain two peaks, which correspond to Pt $4f_{7/2}$ and $4f_{5/2}$ states from the spin-orbital splitting, and each peak was deconvoluted into three different Pt oxidation states associated to Pt(0), Pt(II) and Pt(IV).

The change in the electronic structure of the metal NPs, the specific capacitance, density of states, and electronic conductivity all depend on the N-doping, in terms of pyridinic, pyrrolic and graphitic concentration. The platinum nitrogen interaction with the metal NPs are important in order to produce highly efficient and long-term stable catalysts, and so a possible application as catalysts in the cathodic compartment of PEM-Fuel Cell. It well know that Pt favourably nucleates on pyrrole and pyridinic defect sites. The active sites for the increment of the electrochemical performance vs. Oxygen Reduction Reaction are pyrrolic and pyridinic nitrogen functional group. These functional groups induce partial charges on neighboring carbon active sites acting as defect sites for Pt nucleation but also interact directly with the platinum. In the case of the samples synthetized with 2,2-bypiridil the concentration of nitrogen Pyrrolic and Piridinic group are much lower, and the electron density of the π-conjugated system is very small. The donation/back donation decrease, for this reason, so the control on the platinum nucleation decrease, the effect was confirmed by a lower binding energy

shift between N-Pt and Pt-N. A small mean Pt NP size with a narrow size distribution is attributed to the presence of pyrdinic N-groups in the carbon structure, whereas, for the PtN@C with mainly graphitic and pyrrolic N-groups, an increase in the average Pt NP size with a broad size distribution is found. XPS and TEM images confirm, the absence of an positive interaction between the graphitic nitrogen and the platinum.

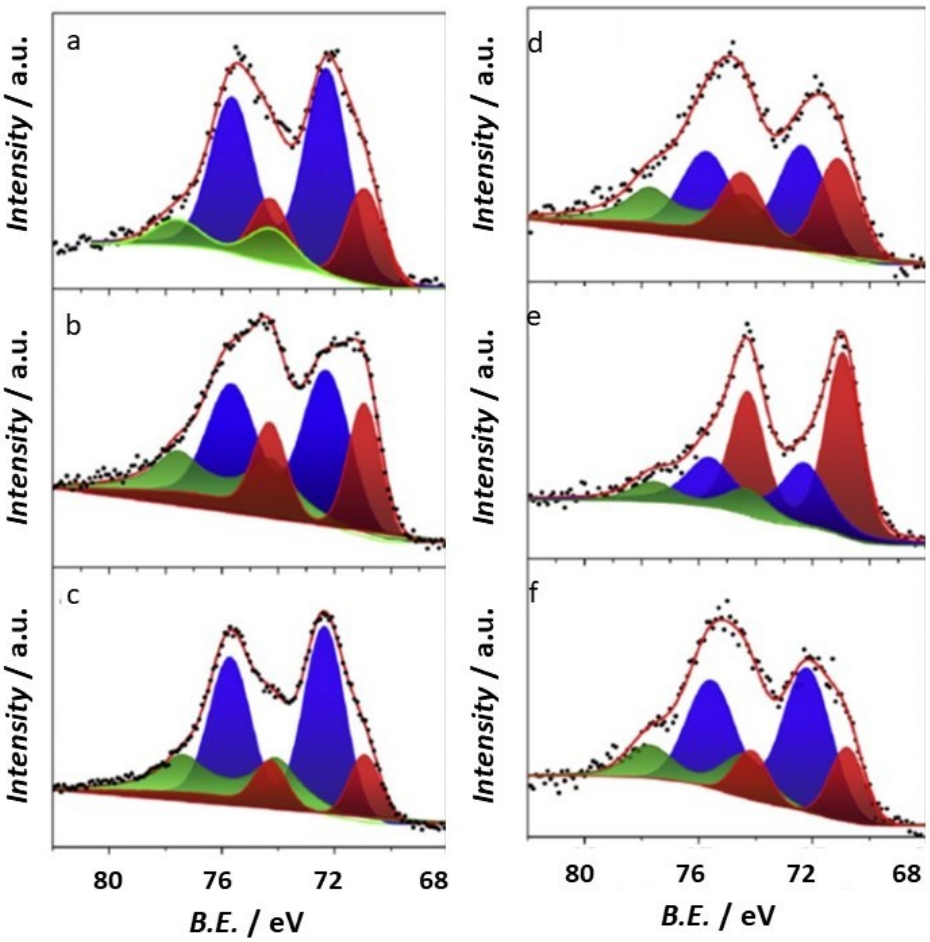

Figure 59: XPS spectra for Pt 4f component for a) PtN1@C; b) PtN2@C; c) PtN3@C; d) PtN4@C; e) PtN5@C and f) PtN6@C

Figure 59 show the Platinum 4f XPS spectra for the different catalysts. The predominant species in the Pt 4f peak is Pt^{2+}, the higher amount of Pt^{+2} species in the PtN1@C could also be interpreted as an evidence of the Pt–N interaction. All PtN@C catalysts show a variable amount of Pt(II) and Pt(IV) species, deduced at 72.1 eV and 74.6 eV. Their presence in all the samples can be attributed to the contact of the Pt NPs surface with oxidant species and show the high reactivity of the Pt NPs due to the interaction with nitrogen group. The high concentration of oxidized species is attributed to the small size of the Pt NPs, resulting in a high percentage of Pt atoms on the surface of the NPs. As already observed from TEM analysis, the NP size of the PtN@C catalysts is about 2 nm, which is very close to the 2.5 nm observed for the Pt/C standard. The Pt 4f XPS spectra of PtN1@C showed much less intense and broader peaks in the same spectral range notwithstanding a higher component of Pt^{2+}. It is worth to note that the Pt^{2+} component decreases with the decrement of the nitrogen

doping of the carbon support. It is much less intense in PtN5@C catalyst, which is the one with the lowest nitrogen content (0.06 $\%_w$) in the whole series. Therefore, it is reasonable to assert that the increased amount of Pt^{2+} for the PtN@C catalysts is due to an electron donation toward the N-groups and the carbon network and specifically a back-donation from Pt to π^* orbitals [53, 142, 144].

The increment of electron transfer from the Pt nanoparticle to the graphite support, induced by the nitrogen insertion on the carbon structure, affords a electronic density modification of the overlying Pt NPs,and so the Pt peak is expected to move towards higher binding energy. In the present case, the Platinum 4f shift is around 0.1 eV and 0.2 eV, which is close to the experimental sensitivity, thus it is complex to evaluate and the comparison with Pt 4f component in Pt/C standard is useless. The Pt binding energy modification due to N-doping maybe the principal reason for the improved Pt catalytic activity and durability for a Platinum NPs on Nitrogen carbon catalyst, compared to an undoped Pt/C system.

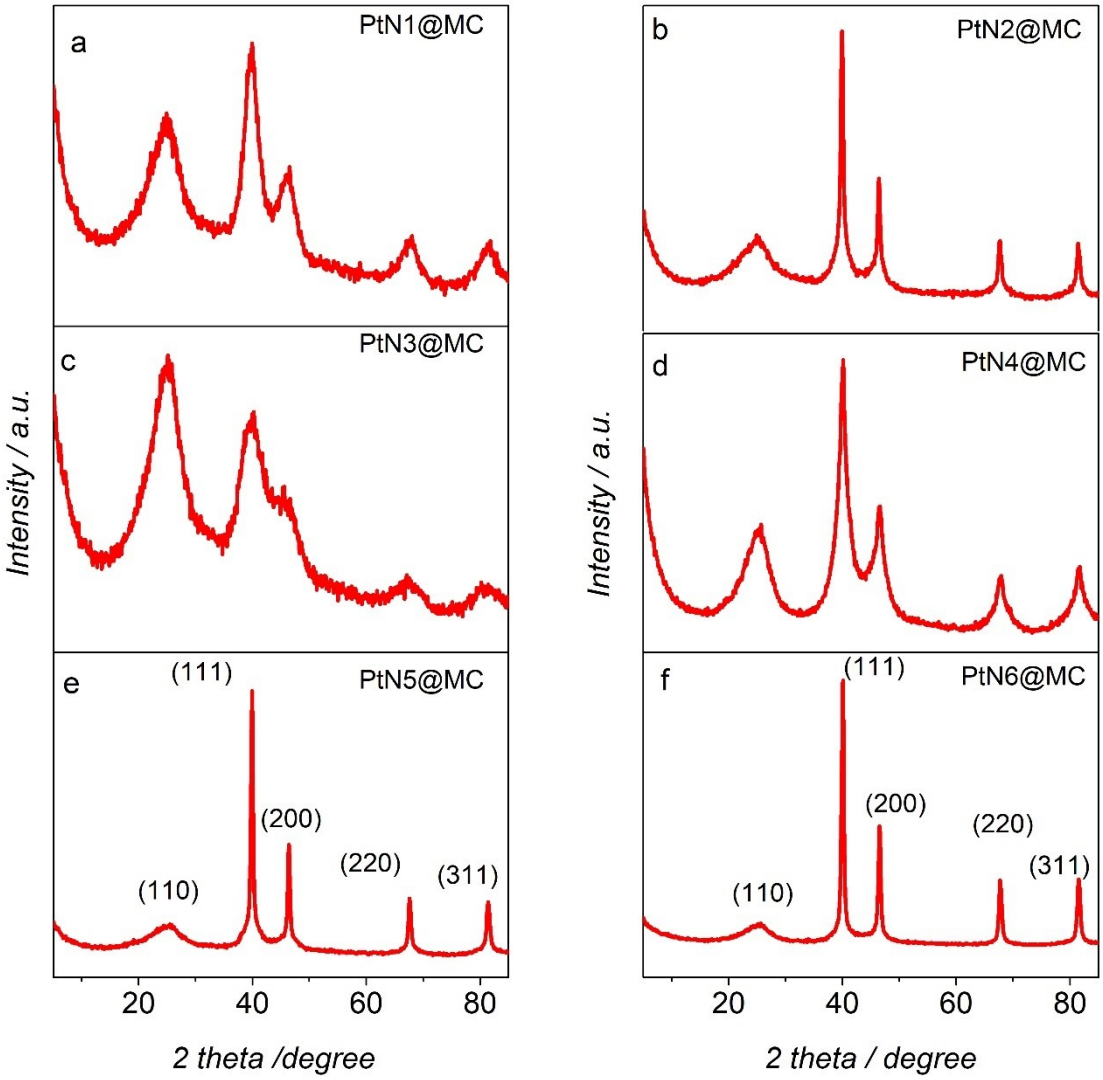

Figure 60: XRD spectra for a) PtN1@C; b) PtN2@C; c) PtN3@C; d) PtN4@C; e) PtN5@C and f) PtN6@C

The PtN@C catalysts show the typical platinum diffraction peaks, as show in Figure 60. The lattice parameter, calculated from the (220) and (311) diffraction peak position, and the average particle size, calculated using the full-width at half-maximum of the (220) diffraction and the Debye–Scherrer equation, are presented in the Table 3. The X-ray diffraction (XRD) profile displayed the typical Pt face centred cubic peaks. By applying the Scherrer equation to the Pt(220) and Pt(311) peaks, average Pt nanoparticle sizes were calculated to be for PtN1@MC (synthetized with $PtCl_2$phen) 2.19 nm and 2.12 nm; for PtN3@MC ($Pt(acac)_2$ + phen) 1.63 nm and 1.78 nm and for PtN5@MC (from $PtCl_2$ + phen) 1.48 nm and 1.66 nm, respectively. The diameter of the crystallites obtained from XRD follows the same trends derived from TEM measurements. These values are in close agreement, albeit slightly larger than the calculated average nanoparticle sizes based on transmission electron microscopy (TEM) image measurements of 2.19 nm and 1.77 nm for PtN1@MC and PtN3@MC, respectively. The particle size distribution, calculated from PtN5@MC, shows that the mean particle size is about 2.43 nm in diameter, which is slightly larger than the value calculated from XRD.

Table 3: Crystallite dimension of PtN@C evaluated on 220 and 331 Pt crystallographic peak

	d_{220}	d_{331}
	nm	nm
PtN1@MC	2.76 ± 0.14	2.21 ± 0.11
PtN2@MC	1.63 ± 0.09	1.78 ± 0.09
PtN3@MC	1.43 ± 0.07	1.66 ± 0.08
PtN4@MC	1.26 ± 0.06	1.31 ± 0.07
PtN5@MC	4.62 ± 0.23	4.19 ± 0.21
PtN6@MC	1.87 ± 0.09	1.86 ± 0.09

7.5 Electrochemical Characterization of PtN@C catalysts

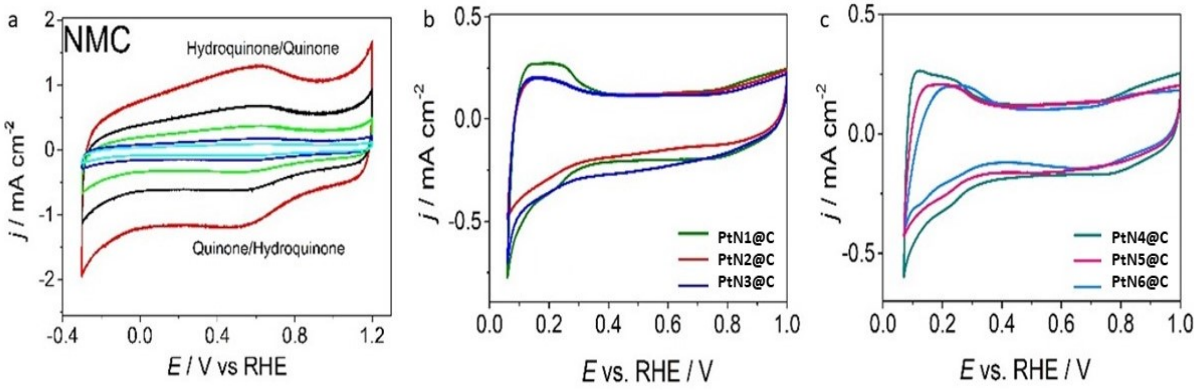

Figure 61: Cyclic Voltammetry a) NMC at different scan rate; b) CV for PtN1@C, PtN2@C and PtN3@C at 50 mV s^{-1} and c) PtN4@C, PtN5@C and PtN6@C at 50 mV s^{-1} in Ar saturated $HClO_4$ 0.1 M solution

Figure 61 report the cyclic voltammetry of standard NMC in Argon saturated $HClO_4$ 0.1 M solution at different scan rate. The nitrogen content is 0.6 $\%_w$, evaluated by Elemental analysis. The peak at 0.55 and 0.6 V vs RHE are assigned to the redox couple Quinone/Hydroquinone. NMC show an pseudocapacitive character, which can be connected to the nitrogen and oxygen present in the carbon matrix. Figure 61b and Figure 61c show the cyclic voltammetry in Argon saturated $HClO_4$ 0.1 M solution at 50 mV s^{-1} for the samples obtained from the 1,10-phenantroline and 2,2'-bipyridyl. The catalysts show a similar electrochemical response, the hydrogen adsorption/desorption region between 0.35 V and 0.05 V is not well defined, and the CV do not show the typical crystallographic peaks of a platinum catalysts. The capacitive current for the catalysts is very similar. PtN1@C and PtN2@C synthetized with $PtCl_2$(1,10-phenantroline) and $PtCl_2$(2,2'-bipyridil) show the higher hydrogen adsorption/desorption region [147].

In Table 4 are present the EPSA and ECSA value for the samples synthetized before and after the acid treatment. The EPSA value of each catalyst increase after the treatment, this effect is due to the oxide removal from the NPs surface, which decrease the NPs dimension and increase the concentration of active sites. PtN1@C show a EPSA of 0.63 cm^2 before and 2.18 cm^2 after, the same trend is observed for the other samples. The EPSA increment is due to the platinum oxide removal, the effect on the platinum oxide reduction is confirm by XPS analysis and ICP analysis.

The EPSA, for PtN@C obtained after the acid treatment, decrease in the following order PtN1@C > PtN2@C > PtN3@C for the catalysts where the nitrogen source is 1,10-phenantroline and the same trend is obtained with the second series, PtN4@C > PtN5@C > PtN6@C where the nitrogen doping is obtained with 2,2'bypiridil. The same progress is observed for the catalysts obtained without the acid washing. The EPSA for the 1,10-phenantroline series is higher than the samples obtained by 2,2'-bypiridil. PtN1@C and PtN4@C shows an EPSA of 2.18 cm^2 and 0.78 cm^2 which correspond to a EPSA value of 74.1 $m^2\ g^{-1}$ and 24.1 $m^2\ g^{-1}$. ECSA depends on both dispersion and size of the Pt NPs; it is also affected by the electrical contact between Pt and the underlying carbon support. The low EPSA obtained in PtN2@C and PtN3@C is connected to the big cluster and aggregates obtained. The error associated to the EPSA and ECSA is very low, around 5%, which can confirm the high reproducibility of these material.

Table 4: Electrochemical results, EPSA and ECSA, for PtN@C catayst before and after the acid treatment

		Platinum and Nitrogen	***EPSA*** cm^2	***ECSA*** $m^2\ g^{-1}$
PtN1@C		$PtCl_2Phen$	0.63 ± 0.05	21.4 ± 1.8
	AC	$PtCl_2Phen$	2.18 ± 0.13	74.1 ± 4.4
PtN2@C		$Pt(acac)_2$ + Phen	0.38 ± 0.03	12.9 ± 1.1
	AC	$Pt(acac)_2$ + Phen	1.48 ± 0.13	50.3 ± 4.3
PtN3@C		$PtCl_2$ + Phen	0.37 ± 0.03	12.6 ± 1.1
	AC	$PtCl_2$ + Phen	1.26 ± 0.11	42.9 ± 3.6
PtN4@C		$PtCl_2Bpy$	0.57 ± 0.05	19.4 ± 1.6
	AC	$PtCl_2Bpy$	0.71 ± 0.06	24.1 ± 2.1
PtN5@C		$Pt(acac)_2$ + Bpy	0.30 ± 0.03	10.2 ± 0.9
	AC	$Pt(acac)_2$ + Bpy	0.48 ± 0.04	16.3 ± 1.4
PtN6@C		$PtCl_2$ + Bpy	0.32 ± 0.03	10.9 ± 0.9
	AC	$PtCl_2$ + Bpy	0.37 ± 0.03	12.6 ± 1.1

The different capacitive current between the Pt/C and PtN1@C is associated to the nitrogen content, because the heteroatoms increase the capacitive characters of the carbon. Another different is the platinum oxide formation/reduction potential, Pt/C show a very well defined Platinum oxide formation peak at 0.94 V vs RHE, while the PtN1@C a small peak at the same potential. The current intensity remains constant if the upper vertex potential is increase from 1 V vs. RHE to 1.6 V vs. RHE both in Pt/C both in PtN1@C. When the potential is increase from 1 V vs RHE tp 1.6 V vs. RHE also the PtO_x stripping have a very low intensity compared with Pt/C. The cathodic peak at 0.75 V in the reverse sweep increases with the increase of the anodic inversion potential both in Pt/C then in PtN1@C, the effect is more evident in the Pt/C than PtN1@C

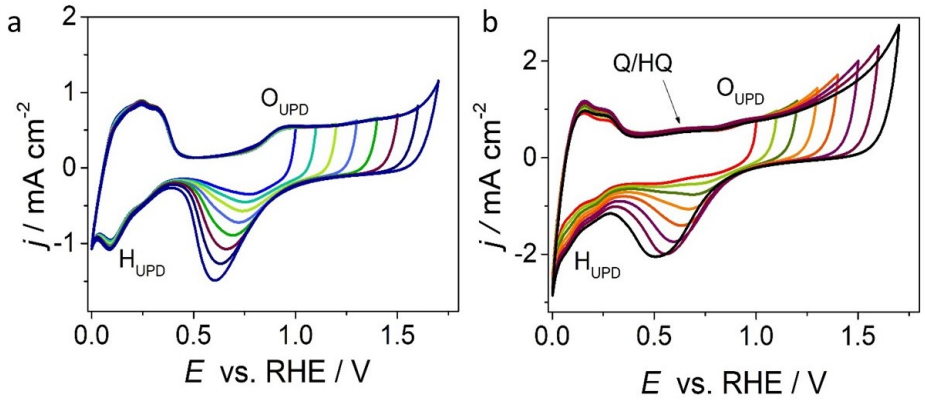

Figure 62: Cyclic Voltammetry at different upper vertex potentials in Ar saturated $HClO_4$ 0.1 M solution at 50 mV s^{-1} for a) Pt/C and b) PtN1@C

Figure 62 show the cyclic voltammetry at 50 mV s^{-1} at different upper vertex potential, recorded in acid electrolyte solution, for the standard platinum on carbon catalyst and the best catalysts obtained, PtN1@C. The figure show the typical platinum oxide reduction due to the increment of the upper vertex potential

The hydrogen adsorption/desorption area is slightly bigger when the upper vertex potential is increased, while in the Pt/C remain constant with the increment of upper vertex potential. Obviously, with the increment of the potential in the cathodic scan, the peak, associated to the PtO_x stripping, accounting both the reduction of the small amount of O_2, produced by the $HClO_4$ electrolyte discharge during the anodic sweep both the PtO_x stripping. The platinum oxide formation is hindered in the PtN@C catalysts. Therefore, it may be concluded that the nitrogen doped support deeply affects the electrochemical behavior of Pt NPs. In particular, the electronic effect arising from charge back donation of Pt to the carbon support, hampers the formation of PtO_x.

Table 5 show the electrochemical results for the oxygen reduction reaction in terms of limited density current, half wave potential, kinetic current, mass activity and specific activity. The electrochemical activity of the synthetized PtN@C catalysts toward ORR was evaluated by LSV with RDE at 1600 rpm and 20 mV s^{-1} in O_2 saturated 0.1 M $HClO_4$ solution. PtN1@C show a very similar mass activity before and after the acid treatment, the high SA value obtained in the untreated sample is associated to the low EPSA obtained from CV in Argon. The treated samples show a higher half wave potential than the unwashed catalyst. In other word the kinetic rate of the sample is faster after the acid treatment because are removed fewer active species. PtN1@C and PtN2@C show a slight increment of Mass Activity after the acid treatment. The sample obtained with $PtCl_2$ and 1,10-phenantroline show a doubling of the mass activity after the acid washing respect the untreated catalyst, 44 A g^{-1} and 93 A g^{-1}, respectively. PtN4@C and PtN5@C show an increment of mass activity after the acid treatment, PtN4@C show a MA of 156 A g^{-1} before the acid washing and of 316 A g^{-1} after, the Mass activity of PtN5@C increase from 71 A g^{-1} to 101 A g^{-1}. The TEM image of PtN6@C shows the aggregate formation of 50 nm, the acid treatment in this case can't help in the MA improvement [52, 143, 148] .

Table 5:. Electrochemical results for PtN@C catalysts in O_2 saturated HClO4 0.1 M solution.

		$\|j_L\|$			$E_{1/2}$ vs. RHE			i_k			*MA*			*SA*		
		mA cm^{-2}			V			mA			A g^{-1}			mA cm^{-2}		
PtN1@C		6.02	±	0.13	0.899	±	0.004	1.60	±	0.13	544	±	44	2.539	±	0.419
	AC	6.43	±	0.14	0.912	±	0.005	1.59	±	0.13	541	±	43	0.730	±	0.101
PtN2@C		5.77	±	0.13	0.865	±	0.004	0.73	±	0.06	248	±	20	1.919	±	0.317
	AC	6.27	±	0.14	0.870	±	0.004	0.71	±	0.06	242	±	19	0.481	±	0.079
PtN3@C		5.89	±	0.13	0.828	±	0.004	0.13	±	0.01	44	±	4	0.350	±	0.058
	AC	6.19	±	0.14	0.854	±	0.004	0.27	±	0.02	93	±	7	0.217	±	0.036
PtN4@C		6.09	±	0.14	0.878	±	0.004	0.46	±	0.04	156	±	12	0.804	±	0.133
	AC	5.87	±	0.13	0.855	±	0.004	0.93	±	0.07	316	±	25	1.309	±	0.216
PtN5@C		6.33	±	0.14	0.828	±	0.004	0.21	±	0.02	71	±	6	0.697	±	0.115
	AC	5.95	±	0.13	0.831	±	0.004	0.30	±	0.02	101	±	8	0.619	±	0.102
PtN6@C		6.02	±	0.13	0.781	±	0.004	0.13	±	0.01	45	±	4	0.413	±	0.068
	AC	6.27	±	0.14	0.800	±	0.004	0.12	±	0.01	40	±	3	0.318	±	0.052

Considering the catalysts obtained after the acid treatment, the catalytic activity, based on $E_{1/2}$, showed the following trend: PtN1@C (0.912 V) > PtN2@C (0.870 V) > PtN4@C (0.855 V) > PtN3@C (0.854 V) > PtN5@C (0.831 V) > PtN6@C (0.798 V),

Pt/NMC1 show a better catalytic activity in terms of half wave potential than the Pt/C benchmark by at least 40 mV. The same trend can be obtained with the Mass Activity and the kinetic current. In term of MA the best sample was obtained with $PtCl_2$(1,10-phenantroline) and $PtCl_2$(2,2'-bipyridyl), with 541 A g^{-1} and 316 A g^{-1}, respectively. The catalysts obtained from the platinum complex show the higher catalytic activity for the oxygen reduction reaction. The samples synthetized with $Pt(acac)_2$ and 1,10-phenantroline or 2,2'-bipyridil show the second value of MA, 242 A g^{-1} and 101 A g^{-1}, respectively. PtN5@C and PtN6@C given their big NPs and the aggregate formation show a low mass activity, 101 A g^{-1} and 40 A g^{-1}.

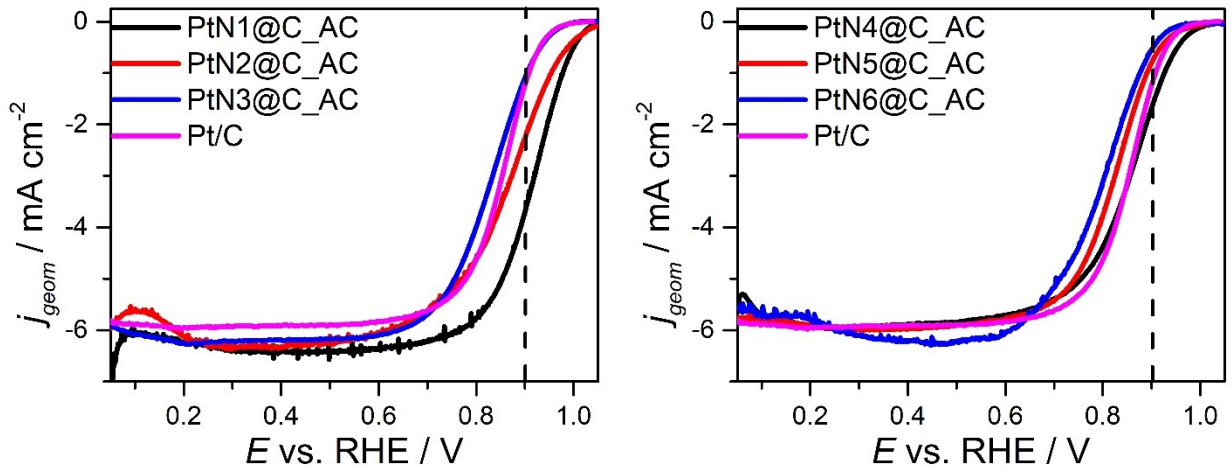

Figure 63: Linear Sweep Voltammetry with RDE recorded at 1600 rpm and 20 mV s^{-1} in O2 saturated HClO4 0.1 M solution, for a) 1,10-phenantroline series and b) 2,2'-bypiridil series

Figure 63 show the Linear Sweep Voltammetry in oxygen saturated electrolyte for the catalysts treated with sulphuric acid. The Tafel slope for PtN1@C show two different slope of 68 mV dec^{-1} and 108 mV s^{-1} at high potential. The value obtained from Linear Sweep Voltammetry with RDE is similar to the theoretical value of 60 mV dec^{-1} and 120 mV dec^{-1} which corresponds the first to an easy chemisorption of oxygen in the platinum active sites and to a totally active surface without species than can interact with oxygen and slow down the kinetics reaction. All the investigated materials including the benchmark Pt/C showed similar double Tafel slopes and therefore a similar reduction mechanism is expected. Figure 64a reports a tentative correlation between $E_{1/2}$ and binding energy of pyridinic and pyrrolic groups as extrapolated from the N 1s XPS peak. It is interesting that the catalytic activity increases with increment of pyrrolic and pyridinic binding energy. Therefore, it appears that the catalytic activity of PtN@C catalysts arises from the interaction between Pt NPs and the nitrogen functional groups in the carbon support. Furthermore, the interaction between active metal phase and the support is more efficient when Pt NPs are deposited as 1,10- phenanthroline Pt complex, possibly due to a better control over the formation of Pt-N_x active site or the higher nitrogen concentration. 2,2'-bipyridil have a less impact on the nitrogen doping, when this precursor is used the NPs distribution in the final catalysts is widened. The low mass activity resulting is influence by interaction grade between the platinum and nitrogen but also from the NPs dimension and thei distribution in the carbon support.

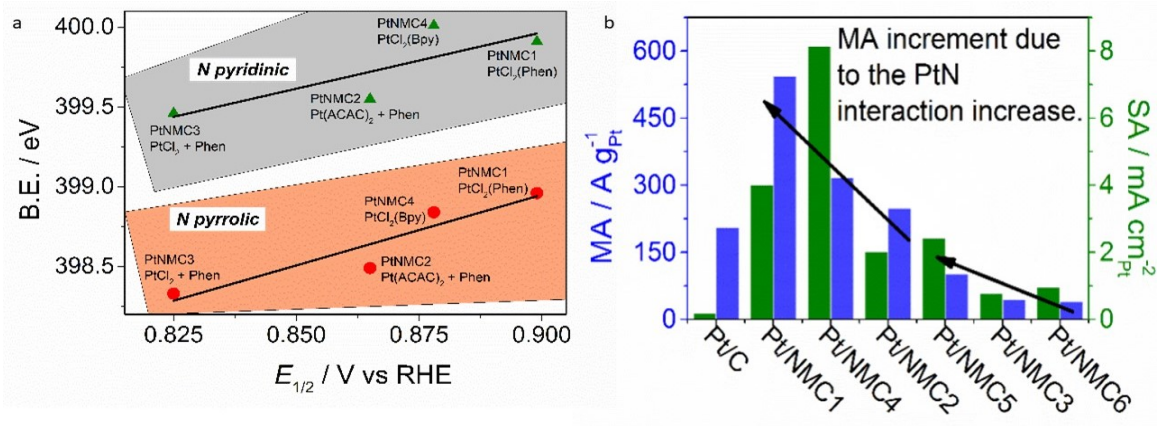

Figure 64: a) Correlation between the Nitrogen pyridinic and pyrrolic binding energy peaks with half wave potential; b) Mass Activity hystogram for the PtN@C catalysts

For the 1,10-phenantroline series the pyrrolic binding energy pass from 399.0 eV to 398.4 eV and the pyridinic group from 399.9 eV to 399.5 eV with the following trend:

PtN1@C > PtN2@C > PtN3@C.

PtN1@C show the highest binding energy shift for pyrrolic and pyridinic nitrogen peak and the best electrochemical performance for the Oxygen Reduction Reaction. Despite the present of aggregate in PtN4@C, the catalysts have a very high Mass Activity and $E_{1/2}$, this effect can be connected to the strong interaction between the platinum and nitrogen. The same trend isn't observed with SA because the catalysts synthetized show an inactive adsorption/desorption hydrogen region.

7.6 Conclusion

Platinum NPs on nitrogen doped carbon was successfully synthetized with a solid state synthesis at high temperature in a reduction atmosphere. The platinum deposition and the nitrogen doping were obtained in one step using particular platinum complex contain nitrogen ligand. The platinum reduction was obtained with a temperature of 650 °C with an atmosphere composed by 2 sccm of hydrogen and 23 sccm of nitrogen. Lower synthesis temperature does not permit both the nitrogen insertion on the carbon structure both the completely platinum salt reduction. XPS show the nitrogen insertion in the carbon matrix and the interaction with the platinum domains, especially in the catalysts where 1,10-phenantroline is used as nitrogen source. The nitrogen content is maximum when the Platinum-Nitrogen complex is used, 2.13 % in PtN1@C and 0.85 % in PtN4@C, these two catalysts was synthetized with $PtCl_2$(1,10-phenantroline) and $PtCl_2$(2,2'-bipyridil), respectively. 1,10-phenantroline result have a more impact on nitrogen content than 2,2'-bipyridyl. Carbon Black was used as support, the carbon shows a mesoporous structure with pore peaked at 4 nm, 9 nm and 14 nm, the surface area is 264 m^2 g^{-1} due to, predominately, to the mesoporosity. The graphitization grade, the surface area and the structure make it a good support for the platinum NPs. The insertion of nitrogen in the carbon structure

increase the carbon conductibility and decrease the electrochemical capacitance of the resulting material. These effects have impact on the platinum electrochemical activity, in fact the platinum NPs show an high stability, in terms of platinum oxidation and reduction. The reduction of the platinum oxide formation is due to the carbon modification by the insertion of nitrogen. The catalyst shows a good NPs dispersion and distribution in the carbon support; an aggregate formation is observed when $Pt(acac)_2$ and $PtCl_2$ are used as platinum precursors, due to the higher temperature used for the synthesis. Pt NPs of 3 nm were formed with $PtCl_2$(1,10-phenantroline). XPS analysis of N 1s and Pt 4f peaks shows a strong interaction between platinum and nitrogen. The interaction creates a partial positive charge on Platinum atoms which increase the formation of Pt(II).
Electrochemical characterization shows an inhibition of PtO_2 formation and stripping on PtN catalysis, and a inactivity on hydrogen adsorption/desorption. The inhibition process was evaluated increasing the upper vertex potential until 1.6 V vs. RHE. The best sample was synthetized with $PtCl_2$(1,10-phenantroline). The electrochemical performances were tested before and after an acid treatment, act to remove the impurities such as oxide by the NPs external surface. PtN1@C show an high catalytic activity versus the Oxygen Reduction Reaction, with an $E_{1/2}$ of 0.912 V vs RHE, a MA of 542 A g^{-1} and a SA of 710 μA cm^{-2}. The electrochemical performances of PtN1@C are higher than the standard Pt/C, which show a Mass Activity of 205 A g^{-1} and a Specific Activity of 0.273 mA cm^{-2}. The PtN catalyst show typical direct reduction process for the Oxygen. The electrochemical results are in good correlation with the binding energy shift of pyrrolic and pyridinic N 1s peaks. In conclusion is confirmed the effective influence of nitrogen doping on the catalytic activity of a platinum catalysts [65, 148, 149].

7.7 Bibliography

[139] S. Pylypenko, A. Borisevich, K.L. More, A.R. Corpuz, T. Holme, A.A. Dameron, T.S. Olson, H.N. Dinh, T. Gennett, R. O'Hayre, Nitrogen: Unraveling the secret to stable carbon-supported Pt-alloy electrocatalysts, Energy Environ. Sci. 6 (2013) 2957–2964. doi:10.1039/c3ee40189h.

[140] H.S. Kim, Y. Lee, J.G. Lee, H.J. Hwang, J. Jang, S.M. Juon, A. Dorjgotov, Y.G. Shul, Platinum catalysts protected by N-doped carbon for highly efficient and durable polymer-electrolyte membrane fuel cells, Electrochim. Acta. 193 (2016) 191–198. doi:10.1016/j.electacta.2016.02.057.

[141] Y. Zhou, K. Neyerlin, T.S. Olson, S. Pylypenko, J. Bult, H.N. Dinh, T. Gennett, Z. Shao, R. O'Hayre, Enhancement of Pt and Pt-alloy fuel cell catalyst activity and durability via nitrogen-modified carbon supports, Energy Environ. Sci. 3 (2010) 1437–1446. doi:10.1039/c003710a.

[142] S.H. Liu, M.T. Wu, Y.H. Lai, C.C. Chiang, N. Yu, S. Bin Liu, Fabrication and electrocatalytic performance of highly stable and active platinum nanoparticles supported on nitrogen-doped ordered mesoporous carbons for oxygen reduction reaction, J. Mater. Chem. 21 (2011) 12489–12496. doi:10.1039/c1jm11488c.

[143] L. Yang, S. Jiang, Y. Zhao, L. Zhu, S. Chen, X. Wang, Q. Wu, J. Ma, Y. Ma, Z. Hu, Boron-doped carbon nanotubes as metal-free electrocatalysts for the oxygen reduction reaction, Angew. Chemie - Int. Ed. 50 (2011) 7132–7135. doi:10.1002/anie.201101287.

[144] J. Melke, B. Peter, A. Habereder, J. Ziegler, C. Fasel, A. Nefedov, H. Sezen, C. Wöll, H. Ehrenberg, C. Roth, Metal-Support Interactions of Platinum Nanoparticles Decorated N-Doped Carbon Nanofibers for the Oxygen Reduction Reaction, ACS Appl. Mater. Interfaces. 8 (2016) 82–90. doi:10.1021/acsami.5b06225.

[145] Y. Zhou, T. Holme, J. Berry, T.R. Ohno, D. Ginley, R. O'Hayre, Dopant-induced electronic structure modification of HOPG surfaces: Implications for high activity fuel cell catalysts, J. Phys. Chem. C. 114 (2010) 506–515. doi:10.1021/jp9088386.

[146] M. Del Cueto, P. Ocón, J.M.L. Poyato, Comparative study of oxygen reduction reaction mechanism on nitrogen-, phosphorus-, and boron-doped graphene surfaces for fuel cell applications, J. Phys. Chem. C. 119 (2015) 2004–2009. doi:10.1021/jp512588r.

[147] K.J.J. Mayrhofer, D. Strmcnik, B.B. Blizanac, V. Stamenkovic, M. Arenz, N.M. Markovic, Measurement of oxygen reduction activities via the rotating disc electrode method: From Pt model surfaces to carbon-supported high surface area catalysts, Electrochim. Acta. 53 (2008) 3181–3188. doi:10.1016/j.electacta.2007.11.057.

[148] D.A. Bulushev, M. Zacharska, A.S. Lisitsyn, O.Y. Podyacheva, F.S. Hage, Q.M. Ramasse, U. Bangert, L.G. Bulusheva, Single Atoms of Pt-Group Metals Stabilized by N-Doped Carbon Nanofibers for Efficient Hydrogen Production from Formic Acid, ACS Catal. 6 (2016) 3442–3451. doi:10.1021/acscatal.6b00476.

[149] E.L. Kolsbjerg, M.N. Groves, B. Hammer, Pyridine adsorption and diffusion on Pt(111) investigated with density functional theory, J. Chem. Phys. 144 (2016). doi:10.1063/1.4947225.

8 Pt NPs on Sulphur doped Carbon: Effect of Sulphur content and Surface area on ORR activity

8.1 Abstract

Several papers agree on the fact that the interactions occurring between the metal NPs and the support play a crucial role in the final composite structure, in terms of nanoparticle size and distribution, morphology, crystallography because the properties of the support directly affect the nucleation and growth processes during preparation. Furthermore, the catalyst/support chemical binding would result in enhanced durability and intrinsic catalytic activity because stabilized the NPs and prevent the platinum detachment. The morphological aspects most heavily investigated are the high surface area and the pore dimension and interconnection between the pore. In fact, high surface area is necessary for optimizing the Pt active phase dispersion, whereas wide and micro-meso interconnected pores are desirable for improving the reagents and products mass transport and increase the mechanical resistance[150, 151]. The modification of the support chemical properties generally consists in the introduction on the carbon surface of heteroatoms such as nitrogen, boron, phosphorus, and sulfur, a process that is commonly known as doping. Among many carbon materials, mesoporous carbons (MC) are ideal materials for electrocatalysis, since they have large surface area and show a mesoporous structure, furthermore they have uniform and adjustable pore size (which allows for favourable mass transport). Another important propriety of mesoporous carbon is the easy doping [152, 153]. The sulphur mesoporous carbon was modified with Pt NPs. For understand the interaction mechanism between the sulphur doped carbon and the platinum, several sulphur carbon support was synthetized by hard template method with same precursors but a different concentration of heteroatoms, the synthesis procedure permits to control the morphological proprieties such as surface area, pore dimension and pore distribution. Another important parameter is the carbon characteristic as surface area or pore distribution, in this case the SMC was post treated for increase these parameters. The platinum deposition preparation was investigated changing the impregnation method of the platinum salt on the doped support. The platinum deposition is fundamental because influence directly the NPs distribution over the carbon and the NPs dimension. Increase the control on the NPs proprieties permits to increase the electrochemical performance in terms of activity and stability. The impregnation is an important step for the platinum NPs distribution, because the salt precursors must entry in the carbon pore [154].

8.1.1 Impact of the preparation methods on the catalytic activity

The sulfur doped carbons were synthetized by hard template methods, using a commercial mesoporous silica P200 as templating agent and dibenzothiophene as sulphur source. The precursor powder was pyrolyzed at 750 °C for 3h in a Argon atmosphere. The synthesis procedure was explicated in the previous chapter. Pt NPs distribution and dimension are the main factors for the catalytic activity vs. ORR increasing. The synthesis procedure must be optimized for obtain a total control on the nanoparticles' morphology. The solid state synthesis at high temperature in a reduction atmosphere permit a good control in the NPs growing but haven't any impact on the distribution on the carbon. The main parameters in a solid state synthesis are the temperature, the time, the platinum precursors and the precursor homogenization treatment.

For obtained a good NPs distribution, the carbon pore dimensions must be bigger than the Platinum NPs otherwise the distribution would be only in the external surface. $Pt(acac)_2$ was used as platinum precursor, the Platinum NPs was deposited at 300 °C with a time synthesis of 3h. The carbon support used as support show different pore dimension at 3 nm, 6 nm, 8 nm and 14 nm, this morphology makes it a good candidate for the platinum deposition. The nitrogen adsorption/desorption analysis show an surface area higher than 1000 $m^2 g^{-1}$. The homogenization process between the platinum salt precursor and the carbon support is a fundamental step because the platinum salt precursor solution must entry on the carbon pores for increase during the synthesis the NPs formation inside the pores [155, 156, 157].

8.1.2 Probe Sonicator, Bath Sonicator and Ball Milling

The platinum precursor, $Pt(acac)_2$, was weighted for obtained a final platinum loading of 27 % on the carbon support. The homogenization process adopted was probe Sonicator, Bath Sonicator and Ball Milling.

In probe Sonicator and Bath Sonicator, $Pt(acac)_2$ was dissolved in 15 mL acetone and after mixed with the sulphur doped mesoporous carbon, while in ball milling the mixing is a dry method, where the catalyst precursors are mixed without any solvent.

- In Probe Sonicator, the catalyst powder was treated for 10 minutes using a power of 10 %.
- In Bath Sonicator, the precursor powder was mixed for 3 h in a water bath at 20 °C. After the sonication, the slurry was deposited in the quartz boat at 80 °C, until the completely solvent evaporation.
- The Mixing in Ball Milling happen in 3 step each lasting of 30 minutes. In the first step the vibration frequency was set at 20 Hz and after was increase at 25 Hz in the second step and at 30 Hz in the last one. After, the carbon/salt mixing the dry powder was transfer in quartz boat.

After the homogenization process the precursor powder was treated in a tubular furnace at 300 °C for 3 h with reduction flux composed by 2 sccm of H_2 and 23 sccm of N_2. Before starting the heat treatment, the furnace was purged by fluxing only N_2 (30 sccm) for 1 h at room temperature. Then, the temperature was allowed to increase to 300 °C and kept constant for 3 h; at the same time, H_2 was gradually fluxed into the quartz tube to the desired ratio. Finally, the furnace was allowed to cool down to room temperature, while the H_2 flow was switched off, allowing only N_2 to flow inside the reactor.

Pt@SC_B was synthetized by mixing the $Pt(acac)_2$ and the Sulfur doped carbon with Bath Sonicator, Pt@SC_P was obtained with Probe Sonicator and in Pt@SC_V the homogenization process was conduct in Ball Milling.

This study is fundamental for understand how increase the platinum salt dispersion inside the carbon pore, purpose to obtain a good NPs dispersion and distribution after the synthesis but especially reduce the aggregate formation or the clusterization process. The impact of the homogenization process on the NPs size and distribution was evaluated with TEM. The influence of the treatment on the carbon support was analysed with N_2 adsorption/desorption analysis. And finally, the chemical-physic results were correlated to the electrochemical result [153].

8.1.3 NPs dimension and carbon modification

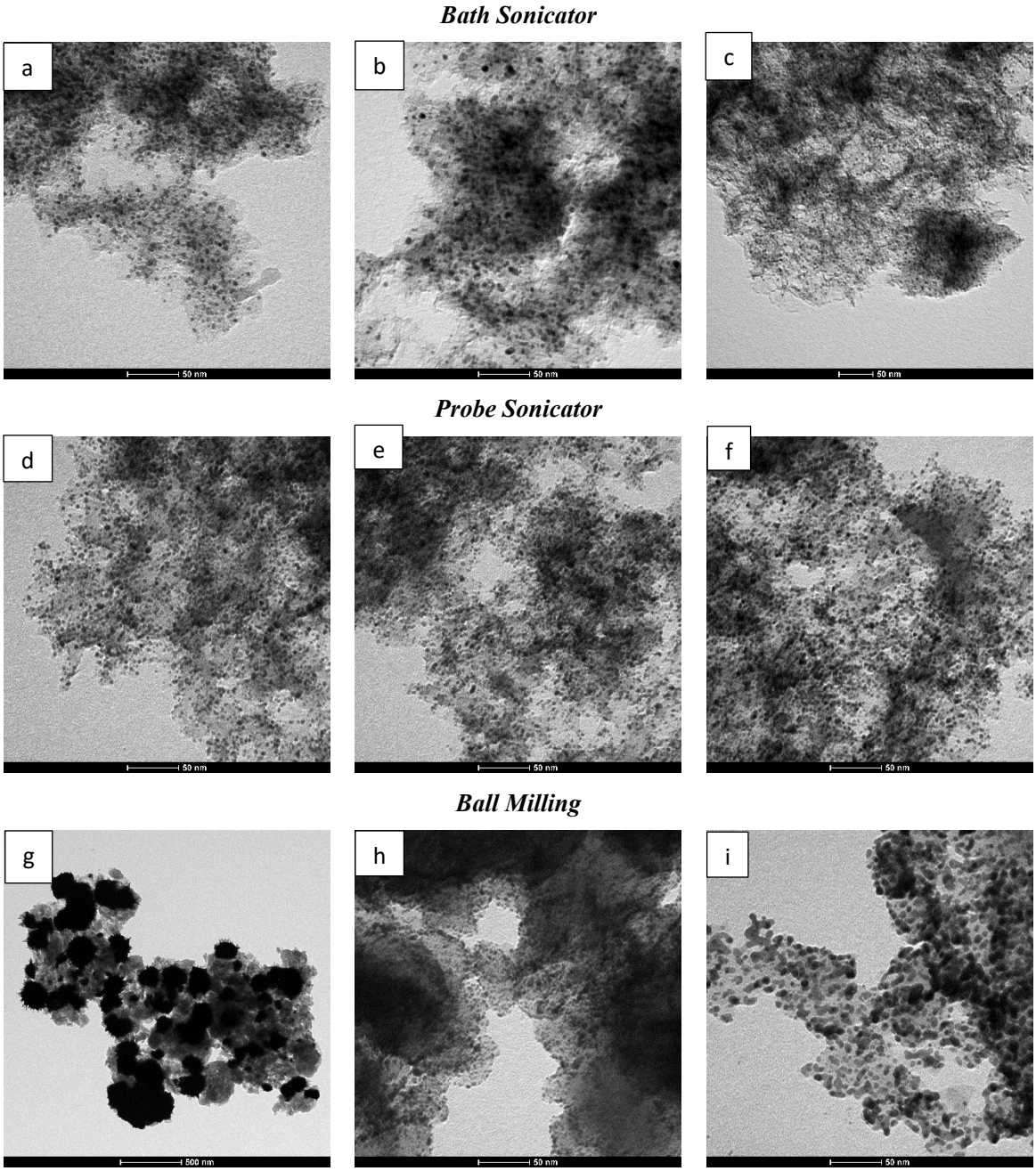

Figure 65: TEM images for a,b,c) Pt@SC_B; d,e,f) Pt@SC_P and g,h,i) Pt@SC_V

TEM image for the sample obtained by Bath Sonicator (Figure 65 a,b,c) shown a very good distribution in the carbon matrix without the aggregate formation. The NPs have a dimension of 2 nm - 3 nm (Figure 66 a), with the sporadic present of bigger particles around 10 nm. The sample Pt@SC_P show an optimal NPs dispersion (Figure 65 d,e,f) in all the support, the totally absence of aggregate or cluster, the dimensional distribution is arrow and centred at 3.5 nm (Figure 66 b). Pt@SC_B is obtained with ball milling homogenization procedure, TEM image (Figure 65 g,h,i) show different NPs distribution and the formation of metal cluster with a

dimension of 70 nm – 90 nm. At higher magnification are visible two different dimensional distribution, one at 2.7 nm and another one at 12.7 nm. Ball milling not permits the entrance of platinum salt in the pore of the carbon support, in addition the aggregate formation can be associated to the incomplete salt dispersion in all the matrix. TEM images shows the typical carbon structure obtained with the silica P200.

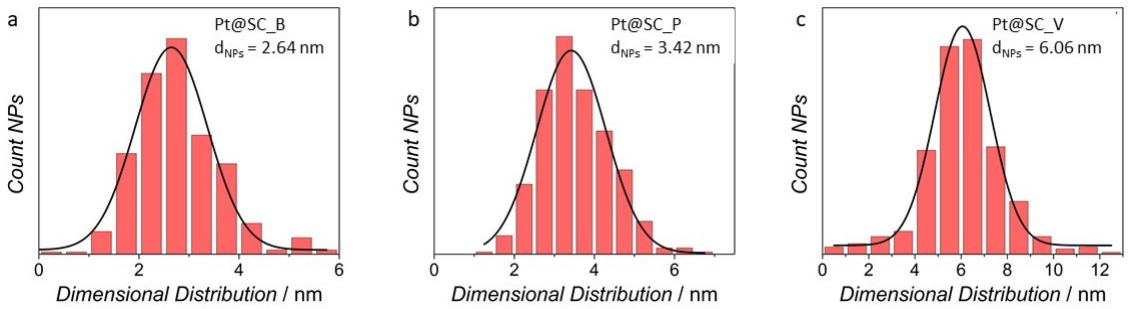

Figure 66: Platinum NPs dimensional distribution for a) Pt@SC_B; b) Pt@SC_P and c) Pt@SC_V

The influence of homogenization process on the carbon morphology was studied with N_2 adsorption desorption @77 K analysis, Figure 67. The surface area obtained in Pt@SC_B and Pt@SC_P was compared with the carbon used as support for the platinum NPs.

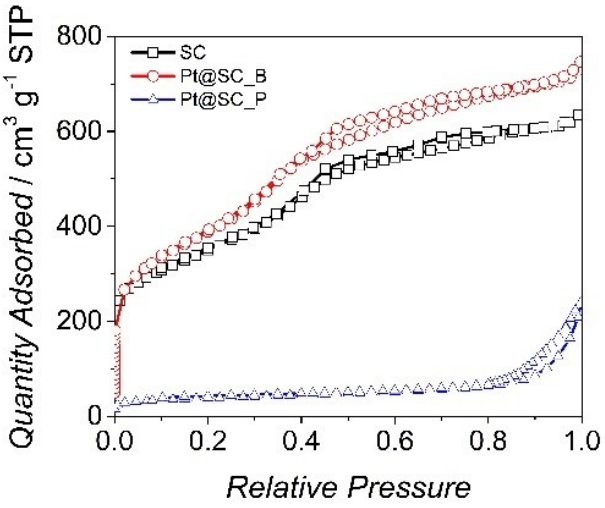

Figure 67: Isotherm of sulfur doped carbon, Pt@SC_B and Pt@SC_P

The carbon support SC was synthetized with mesostructured silica P200, the carbon obtained happen an high surface area of 1011 m^2 g^{-1}, the pore distribution is almost totally positioned in mesoporous range at 4 nm, 7 nm and 13 nm. The Sulphur doped Carbon show an external surface area is 921 m^2 g^{-1} and a very low micropore volume. In Pt@SC_B, after the platinum deposition the surfaces area is increase due to the NPs formation, the final surface area is 1203 m^2 g^{-1}, the increment of microporosity at the expense to a reduction of external area is due to the morphology of the NPs, which have a high roughness than interfered with the nitrogen adsorption. The situation is completely different in Pt@SC_P, which have a drastically surface area reduction, from 1011 m^2 g^{-1} in the pristine

carbon support to 128 $m^2\ g^{-1}$ in the final catalyst. The mesopore volume in SC and Pt@SC_B is ~85 % of the total porosity, while in Pt@SC_P is of 50%.

Table 6: Morphological characterization for Sulphur doped Carbon (SC), Pt@SC_B and Pt@SC_P

	S_{BET}	V_{pore}	V_{micro}	V_{meso}	S_{micro}	S_{ext}
	$m^2\ g^{-1}$	$cm^3\ g^{-1}$	$cm^3\ g^{-1}$	$cm^3\ g^{-1}$	$m^2\ g^{-1}$	$m^2\ g^{-1}$
SC	1011	0.864	0.086	0.778	521	921
Pt@SC_B	1203	0.821	0.112	0.709	478	871
Pt@SC_P	128	0.128	0.076	0.052	21	94

The probe Sonicator with its high vibration frequency damage the carbon support which loss the morphology proprieties. The pore distribution for SC and Pt@SC_B are very similar, the pore distribution is multimodal distribution with 5 peaks centred at 2.3 nm, 6.4 nm, 9.2 nm, 14.5 nm and 17.1 nm. Pt@SC_P show a three modal distribution at 1.3 nm, 3.6 nm and 7.1 nm. The NPs are distributed only in the external surface since the pore absence. The chemical-physics characterization show as the bath Sonicator is the best homogenization method for mixing the carbon support and the platinum salt. The NPs happed a good distribution in the carbon support and the matrix keep its proprieties of surface area and pore distribution.

8.1.4 Electrochemical Characterization

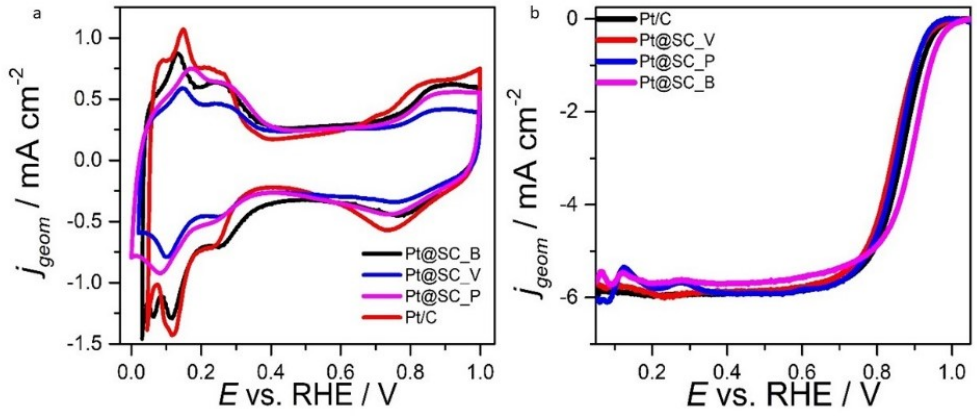

Figure 68: a) Cyclic Voltammetry at 50 mV s^{-1} in Ar saturated $HClO_4$ 0.1 M and b) LSV with RDE at 1600 rpm and 20 mV s^{-1} in O_2 saturated solution

Figure 68a show the cyclic voltammetry recorded in Argon saturated $HClO_4$ 0.1 M solution at 50 mV s^{-1} for the Pt@SC catalysis obtained by Bath Sonicator (B), Ball Milling (V) and Probe Sonicator (P), the voltammetry can be divided in three zone. From 0.65 V vs RHE to 1 V vs. RHE, the cyclic voltammetry show the typical the Pt-Oxide formation and stripping, the materials show the same Pt oxidation potential and PtO_x

reduction [158, 159]. Between 0.4 V vs RHE and 0.65 V vs RHE is possible identify the capacitive current due to double layer charging. All catalysts show a similar capacitive current, the capacitive current for Pt@SC catalysts is slightly higher than the reference Pt/C. And at potential less than 0.3 V vs RHE is present the hydrogen adsorption/desorption region. The Cyclic Voltammetry show the typical peaks of adsorption and desorption of H_2, but the intensity is lower than the peaks presents in the Pt/C voltammetry. The effect is due to a lower crystallinity in the Pt@SC catalysts than the platinum standard. The peak at 0.14 V vs. RHE and 0.23 V vs. RHE in the H_2 desorption region are associated to Pt 110 and Pt 111.

Table 7: Electrochemical results for Pt@SC catalysts and Pt/C, the data were calculated by Cyclic Voltammetry at different scan rate in Ar saturated $HClO_4$ 0.1 M solution

	Homogenization Treatment	***Pt$_{ICP}$*** $\%_w$	***EPSA*** cm^2	***ECSA*** $m^2\ g^{-1}$
Pt/C	-	49.2 ± 1.2	2.24 ± 0.15	76 ± 5
Pt@SC_B	Bath Sonicator	26.1 ± 0.7	1.52 ± 0.12	52 ± 4
Pt@SC_P	Probe Sonicator	25.9 ± 0.6	1.38 ± 0.14	47 ± 5
Pt@SC_V	Ball Milling	26.4 ± 0.7	0.76 ± 0.11	26 ± 4

The platinum loading was evaluated by IC-MS, and it is very close to the theoretical value of 27 %. From the cyclic voltammetry recorded in argon saturated solution is possible calculated the Electrochemical Platinum Surface Area. The commercial standard Pt/C show an EPSA value of 2.24 cm^2 which correspond to 76 $m^2\ g^{-1}$. The sample synthetized happens a lower EPSA with the following trend

Pt@SC_B (52 $m^2\ g^{-1}$) > Pt@SC_P (47 $m^2\ g^{-1}$) > Pt@SC_V (26 $m^2\ g^{-1}$).

The low value obtained from ball milling is connected to the aggregate formation, which reduce the external active surface area. The samples synthetized with Bath and Probe Sonicator shows a similar EPSA value, considering the error associated to the measurement. TEM image for Pt@SC_B and Pt@SC_P show a good NPs distribution in the carbon matrix. The difference obtained respect the Pt/C are connected to the NPs dimension of the standard which resulting be 2.1 nm.

Table 8: Electrochemical results evaluated by LSV with RDE in O_2 saturated $HClO_4$ 0.1 M solution at 1600 rpm and 20 mV s^{-1}

	Homogenization Treatment	$\lvert j_L \rvert$ $mA\ cm^{-2}$	$E_{1/2}$ **vs. RHE** V	i_k mA	***MA*** $A\ g^{-1}$	***SA*** $mA\ cm^{-2}$
Pt/C	-	5.91 ± 0.01	0.864 ± 0.005	0.81 ± 0.03	275 ± 5	0.36 ± 0.03
Pt@SC_B	Bath Sonicator	5.70 ± 0.11	0.891 ± 0.006	0.90 ± 0.05	306 ± 14	0.59 ± 0.06
Pt@SC_V	Ball Milling	5.86 ± 0.13	0.845 ± 0.007	0.18 ± 0.01	61 ± 4	0.13 ± 0.02
Pt@SC_P	Probe Sonicator	5.91 ± 0.09	0.854 ± 0.003	0.25 ± 0.03	85 ± 7	0.33 ± 0.06

The Pt@SC catalysts was synthetized with the same procedure unless the homogenization treatment. The catalyst shows a similar limited density current, very close to the theoretical value. The activity evaluated as Mass Activity follow the next trend:

$$Pt@SMC\_B\ (306\ A\ g^{-1}) > Pt/C\ (275\ A\ g^{-1}) > Pt@SC\_V\ (85\ A\ g^{-1}) > Pt\ @SC\_P\ (61\ A\ g^{-1}).$$

The same trend can be obtained considering the $E_{1/2}$, Pt@SC_P and Pt@SC_V show a half wave potential lower 10 mV and 19 mV than Pt/C. Pt@SC_B show the best catalytic activity vs. ORR, with an half wave potential and a Masse Activity higher than commercial standard Pt/C. Pt@SC_V show a very low catalytic activity, the bad performance is connected to the absence of small NPs on the carbon support and at the aggregate formation. Despite the good NPs distribution and dimension, Pt@SC_P show a MA of 85 A g^{-1} and a Specific Activity of 0.33 mA cm^{-2}, moreover the reproducibility is very low, the effect is connected to the low surface area of the carbon support and on the absence of a mesoporous structure which generally increase the NPs stability and prevent the detachment process of platinum NPs.

Summarize, the platinum salt dispersion with bath sonicator results the best procedure. The sonication permits a completely dispersion of $Pt(acac)_2$ in the carbon matrix. The platinum NPs, obtained after the synthesis, are distributed homogeneously in the support without the aggregate formation. The NPs show a dimension of 3 nm and an arrow dimensional distribution. Nitrogen Adsorption/Desorption Analysts show an surface area increment after the platinum deposition respect the carbon material for Pt@SC_B, from 1011 $m^2\ g^{-1}$ to 1203 $m^2\ g^{-1}$, and an surface area decrement for Pt@SC_P, due to the strong power of the technique. Pt@SC_B show the best performance in term of half wave potential and mass activity for the oxygen reduction reaction. The aggregate formation has a strong impact on the electrochemical performance, in fact Pt@SC_V show a Mass Activity of 61 $m^2\ g^{-1}$ and a Specific Activity three times lower than the Pt/C.

8.2 Effect of Sulphur of a Pt@SdC catalyst on the catalytic activity for ORR

8.2.1 Abstact

The carbon functionalization is an interesting process for modify the electronic and morphologic proprieties, generally when a metal is deposited in a doped carbon support the present of heteroatoms can increase the stability and the activity of the active phase. Heteroatoms as sulphur, boron or nitrogen have a strong impact on the NPs growing and their shape and dimensions. The doping most commonly used are sulphur and nitrogen. However, the heteroatoms concentration plays a fundamental role in the increment or decrement of the catalyst performance. For example, in the case of nitrogen, sulphur or co-doping, it was demonstrated that a high density of heteroatoms, i.e. closely separated nitrogen and sulphur functional groups, disfavours the formation of small Pt NPs and so the catalytic activity decrease drastically. In a carbon support, a sulphur content between 5 % and 14 % increases the conductibility of the resulting material, instead higher concentration than 18 %, the electronic transfer from the heteroatoms to the carbon saturated the electronic gap and de-active the material [142, 135, 154].

Different sulfur doped mesoporous carbons were synthetized with different heteroatoms concentration, but the same carbon morphology as pore distribution. For evaluate the effect of the sulphur doping on the NPs morphology is fundamental that the carbon support show the same morphology. Hard template is an easy method for synthetized doped mesoporous carbon, using an carbon salt precursor with an aromatic structure, moreover the carbon structure can be easy tuned using the template agents [160]. The effect of sulphur concentration and surface area were evaluated after the platinum deposition. The target is understanding the correlation between the doping and the morphological characteristic of the carbon support, but especially correlate the Platinum nanoparticles dimension, distribution and the sulphur concentration with the electrochemical activity for the Oxygen Reduction Reaction[161, 162, 157, 163].

8.2.2 Synthesis and Chemical

Mesoporous silica (Sigma−Aldrich, 200 nm particle size, 4 nm pore size), sucrose (Sigma−Aldrich, >99%), dibenzothiophene (Sigma−Aldrich, 98%), $Pt(acac)_2$ (Sigma−Aldrich, >97%), Nafion (Sigma Aldrich, 5 wt.% in EtOH), $HClO_4$ (Fluka, Traceselect® 67-72%), Pt/C Tanaka (TKK) standard and acetone (Fluka, HPLC grade) were used as received without further purification.

The synthesis of sulphur doped mesoporous carbon (SMC) was accomplished following a hard template approach with a commercial mesoporous silica P200 as a templating agent, sucrose (Figure 69 a) and dibenzothiophene (Figure 69 b) as a carbon doped and undoped precursors.

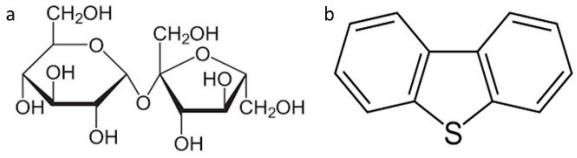

Figure 69: Chemical structures of a) sucrose and b) dibenzothiophene

Sulphur doped mesoporous carbons with different concentration of sulphur were prepared, starting from different dibenzothiophene/sucrose ratios, for example 100/0, 70/30, 50/50, 30/70 and 0/100.
The syntheses of sulphur doped mesoporous carbons, at different heteroatom contents, was accomplished by pyrolysis at 750 °C of the mixtures of dibenzothiophene and sucrose with a silica P200, which was removed after the pyrolysis by chemical etching in EtOH/NaOH 2M solution. The precursor powder was pyrolyzed in solid state using an Argon atmosphere, before the pyrolisis treatment, the system is conditioned using a nitrogen flux of 50 sccm at room temperature, after the temperature is increased at 100 °C and kept constant for 2 h, the process is used for desorbing the H_2O and O_2 from the carbon structure which when the temperature is increased, they can react with the carbon and modify the morphology. The temperature is increase until the pyrolysis temperature, 750 °C, with a ramp of 5 °C min^{-1} and kept constant for 3 h [129, 136].

$Pt(acac)_2$ was deposited via impregnation with Bath Sonicator on the sulphur doped carbon support. The catalyst powder precursors were treated in a reduction atmosphere at 300 °C for 3 h. The obtained Pt loaded mesoporous carbons are labelled as Pt@SC100, Pt@SC70, Pt@SC50, Pt@SC30, and Pt@SC0. The starting Pt precursor was weighed in order to obtain a catalyst powder with a final Pt loading in the range 25 % and 30 %. The obtained catalyst was then removed from the quartz boat and ground Ball Milling. The catalysts after were treated with sulphuric acid for 1h at room temperature under stirring for remove the impurities and reduce the platinum oxide concertation. The catalyst, after, was filtered on a nylon nanometric filter (GVS, nylon 0.2 μm, 47 mm membrane diameter) and carefully washed with milli-Q water. Finally, after drying the sample in

an oven at 80 °C overnight, the catalyst was finely ground in an agate mortar and preserved in a glass vial [136].

8.2.3 AE and N_2 Adsorption/ Desorption Analysis: Sulphur Content vs. Surface Area

The obtained Sulphur doped carbon contained 13.8%, 8.6%, 6.87%, 4.2% and <1.0% of sulfur and will be indicated in the text as SC100, SC70, SC50, SC30, and SC0, respectively. Using sucrose alone led a carbon material containing < 1% sulfur; in this specific case, the sulphur derived from sulfuric acid used, in a small amount (~250 µL), to catalyse the oligomerization of the carbon precursor. From now on, catalysts are named in the text and figures as Pt@SCx, where x assumes the values 100, 70, 50, or 30 and refers to the dibenzothiophene/sucrose ratio 100/0, 70/30, 50/50 and 30/70, respectively. Instead, the sample prepared from sucrose alone is indicated as Pt@SC0.

Table 9: Morphological proprieties of sulphur doped carbon

	Sucrose	***Dibenzothiophene***	S_{BET}	d_{p1}	d_{p2}	d_{p3}	V_p^{MESO}	***C***	***H***	***S***	***O***
	%	%	$m^2\ g^{-1}$	nm	nm	nm	$cm^3\ g^{-1}$	%	%	%	%
SC100	0	100	1103	1.1	3.8	5.1	0.864	68.11	2.29	13.79	15.81
SC70	30	70	1010	2.15	4.3	5.9	0.889	74.21	1.15	8.64	16.00
SC50	50	50	1002	1.9	4.9	6.2	0.873	73.81	1.67	6.83	17.69
SC30	70	30	999	2.1	4.4	5.6	0.989	75.27	1.13	4.21	19.39
SC0	100	0	953	1.1	3.8	5.7	0.801	70.97	1.29	1.01	26.73

The Brunauer–Emmett–Teller specific surface areas (S_{BET}), were in the range from 953 to 1103 $m^2\ g^{-1}$ and a good correlation was found between the sulphur concentration and the S_{BET} (Figure 70b). Increasing the sulphur doping the surface area increase from 953 $m^2\ g^{-1}$ in SC0 to 1103 $m^2\ g^{-1}$ in SC100, the pore distribution is very similar for the different SC samples, the porosity is given manly by the silica used as templating agent, the pore distribution shows a multimodal distribution picked at 2 nm, 4.5 nm and 6 nm.

The mesoporous volume is ~0.8 $cm^3\ g^{-1}$. The silica content on the SC was evaluated with TGA, the residual at 1000 °C is connected to the unremoved silica. The resulting carbon after the etching treatment shows a template content of 1% - 2%. This result confirms the efficiency of the etching process. The Elemental Analysis shows a very similar carbon content, 70% for all sulphur doped carbon. For the doped material the oxygen concentration is in the range 15%-20%, while the undoped carbon the content it is increased until 27 %. Elemental Analysis show the sulfur decrement with the decrement of dibenzothiophene/sucrose ratio. The SC100, synthetized with dibenzothiophene, show a sulphur content of 13.8 %.

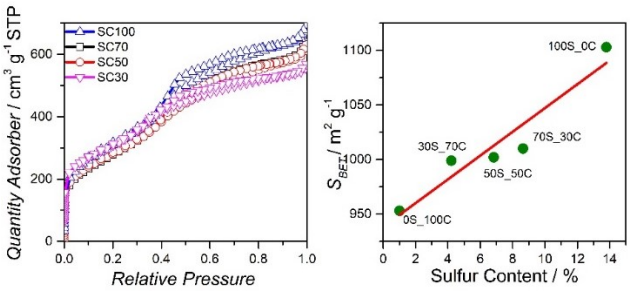

Figure 70: a) Isotherm of adsorption/desorption of N2 at 77 K of sulfur doped carbon and b) Linear correlaion between the surface area and the sulfur concentration

Figure 70a shows the nitrogen adsorption/desorption isotherms for the doped carbon support. All of the catalysts follow a type IV isotherm according to IUPAC classification and the presence of an accentuated hysteresis classifies them as mesoporous materials. The Figure 70b show the correlation between the total surface are and the sulphur concentration.

8.2.4 TEM and SEM: Influence of Sulphur Content on NPs distribution and dimension

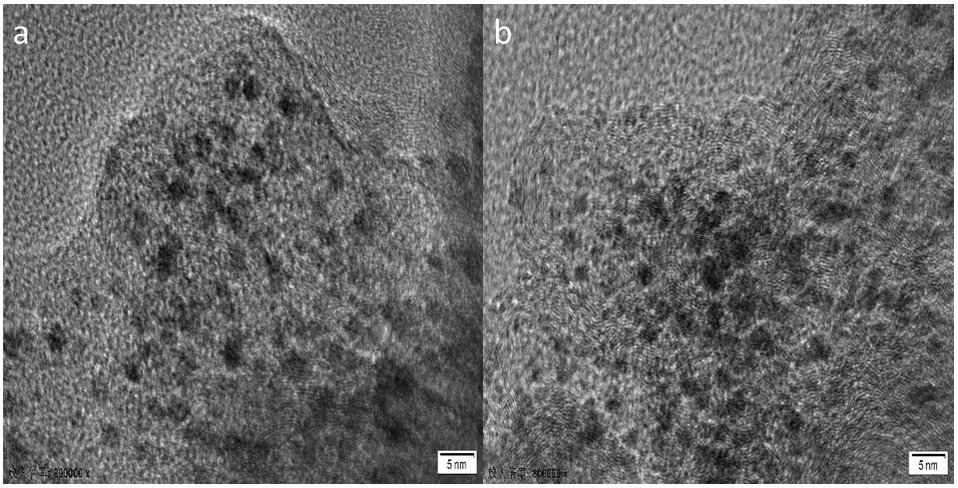

Figure 71: TEM images of a) Pt@SC100 and b) Pt@SC100_AC

After the platinum deposition the catalysts were treated with acid sulphuric 1 M under stirring at room temperature, 25 °C. The procedure is necessary for remove the impurities and the oxide from the NPs external surface. The acid treatment does not affect the morphological texture of the carbon support, in fact BET analysis show the same Surface Area, Mesoporous Volume and Pore distribution before and after the treatment. It is evident that the mean particle size distribution remains close to 2 nm before and after the acid wash even if in the latter case the Laurentia profile of the histogram assumes a wider width with respect to the unwashed

catalyst. Figure 71 report the TEM images of Pt@SC before and after the acid treatment. The TEM images show the typical carbon structure where the pore are orderly distributed. The EDX maps confirm the presence of Pt and S before and after the acid wash, as already determined by thermal elemental analysis and ICP-MS investigation, which are more accurate as analytical techniques. The Figure 72 show the Pt NPs distribution for both samples; it is evident that the mean particle size distribution slightly decreases, upon the acid wash, since the center of Lorentzian profile of the histogram shifts from 2 nm in the unwashed catalyst to 1.5 nm. This behaviour was explained by considering that the acid treatment can decrease NPs dimension by eroding the particle surface (most probably PtO_x), while the resulting metal ions or small cluster can redeposit affording smaller NPs. The TEM images clearly show that small Pt NPs are embedded inside the carbon support, while some bigger nanoparticles randomly form over the carbon sphere surface as evidenced by the SEM analysis.

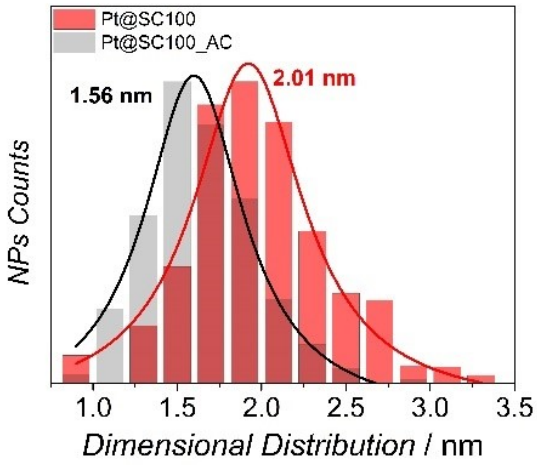

Figure 72: NPs dimensional distribution for Pt@SC100 and Pt@SC100_AC

TEM image of Pt@SC catalysts show a very good small NPs distribution in the carbon support, Figure 73. Pt@SC100_AC and Pt@SC70_AC shows round-shaped Pt NPs with high loading and uniformly dispersed throughout the samples, without the formation of aggregates. The aggregates formation happens when the sulphur content less than 5 %, in fact in Pt@SC30_AC and Pt@SC0_AC are present cluster with a dimension of 20 nm – 30 nm. This NPs dimensional distribution confirms the strong confinement effect exerted by the carbon support, which limits the growth of metal NPs when they nucleate inside the support pores. At high magnification, TEM imagine shows the carbon texture given by the silica P200 used as templating agent. The average pore diameter of mesopores and micropores is constant with a value around 3 and 1 nm, respectively, evaluated by TEM images. The carbon support consists of hollow spherical carbon particles, as good replica of the templating silica, along with other collapsed and fractured particles that give rise to a heterogeneous morphology. The average diameter of the spheres is about 300 nm - 400 nm. Pores are uniformly located to construct the whole sphere, achieving a loosely packed nanostructure. In fact, several three-dimensionally interconnected bright spots can be observed on the sphere surfaces indicating the presence of mesopores, whereas the dark contrast that characterizes the edges confirms their hollow nature. The corresponding particle

size distribution were obtained by calculating the size of 400 particles, randomly selected and distributed in the carbon support. Pt@SC100, Pt@SC70 and Pt@SC50 show a NPs dimension in the range 2 nm – 2.3 nm Instead, Pt@SC30 and Pt@SC0 show a NPs diameter of 3.8 nm and 4.4 nm, respectively. The undoped material show a sporadic NPs distribution with a widen dimensional distribution from 1.2 nm to 7.8 nm. After the acid treatment, Pt@SC100 show NPs with a dimension of 1.56 nm. The NPs dimension for Pt@SC70_AC, Pt@SC50_AC, Pt@SC30_AC are 2.3 nm, 2.5 and 2.8 nm, respectively. The platinum standard, Pt/C, shows a perfect NPs distribution in the carbon support, without any evidence of aggregates formation, the resulting NPs have a very arrow dimensional distribution at 2.6 nm. The multimodal distribution of Pt NPs dimension in Pt@SC0 is a clear indication that, for a very low content of sulphur, there is no control on the nanoparticle diameter. Conversely, in Pt@SC narrow size distributions were observed, as well as a clear tendency to form smaller NPs as the sulphur content increased.

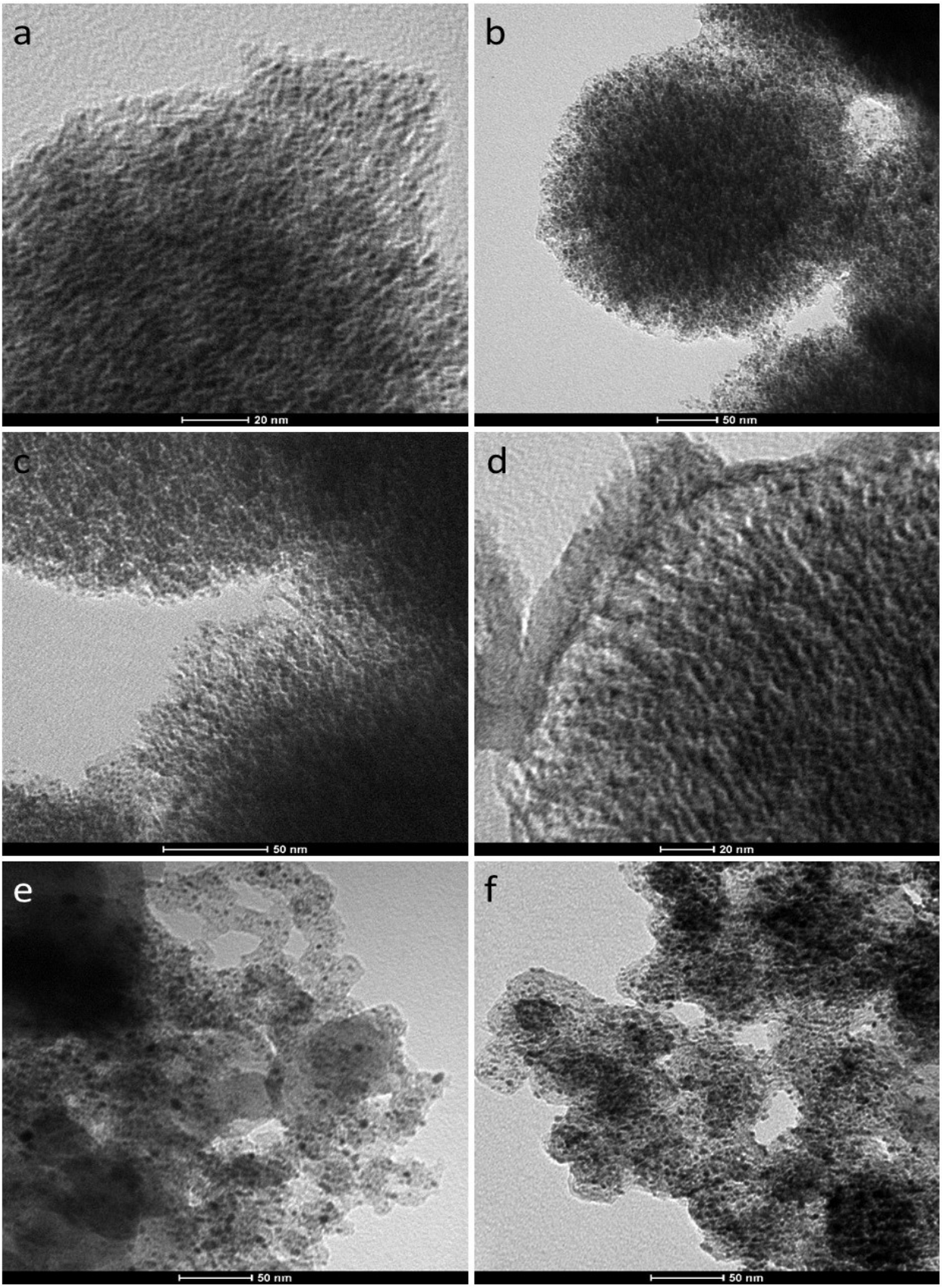

Figure 73: TEM images of a) Pt@SC100_AC; b) Pt@SC70_AC; c) Pt@SC50_AC; d) Pt@SC30_AC ; e) Pt@SC0_AC and f) Pt/C

8.2.5 XPS and XRD Analysis: Platinum-Sulphur Interaction

For evaluate the interaction between the platinum and sulphur, XPS is revealed itself an crucial technique, the interaction between the Pt-S can be studied as binding energy shift in the Pt 4f spectra or S 2s spectra.
The S 2p photoemission peak can be deconvoluted by a single component peaked in the range 163.4 eV and 163.9, which represents the thiophenic group, often know as sulphide -C-S-C-. Increasing the sulfuric concentration, the thiophenic binding energy shift from 163.5 eV in Pt@SC30 to 163.9 eV in Pt@SC100, as show in Figure 74 a,c,e,g. The thiophenic sulphur peak in Pt@SC50 and Pt@SC70 is positioned at middle value between 163.4 eV and 163.9 eV. The binding energy shift is correlated at the interaction with the platinum and the variation of electron density on the sulphur atoms. XPS confirm the influence of sulphur on the electronic proprieties of the platinum. The comparison of the S 2p region before and after Pt deposition does not reveal any particular change of the S 2p peak signal. This confirm the attack of the sulfuric acid only on the platinum NPs and not on the carbon structure. Also, the Pt 4f peak shows different binding energy passing from Pt@SC30_AC to Pt@SC100_AC (Figure 74 b,d,f,h). Pt 4f peak can be deconvoluted with three different components peaked at 71.0 eV, 72.4 eV and 74.9 eV, which are associated to Pt(0), Pt^{2+} and Pt^{4+}. The more intensity component result be Pt(0), followed by Pt(II) and Pt(IV). The Pt^{0} peak in Pt@SC30 is close to the theoretical value, while with the sulphur increment the component shift to higher binding energy value, from 71.05 eV in Pt@SC30_AC to 71.24 eV in Pt@SC100_AC. In addiction the intensity of the component at 72.5 eV, associated to Pt(II), increases on going from Pt-SMC30 to Pt-SMC100. The Platinum peak at 72.5 eV can be associated both to PtO species, both to PtS species; the common binding energy for these group are 72.8 and 72.5 eV. No binding energy variation are founded for the components at 74.3 eV (Pt^{4+}) which is connected to Pt(IV).

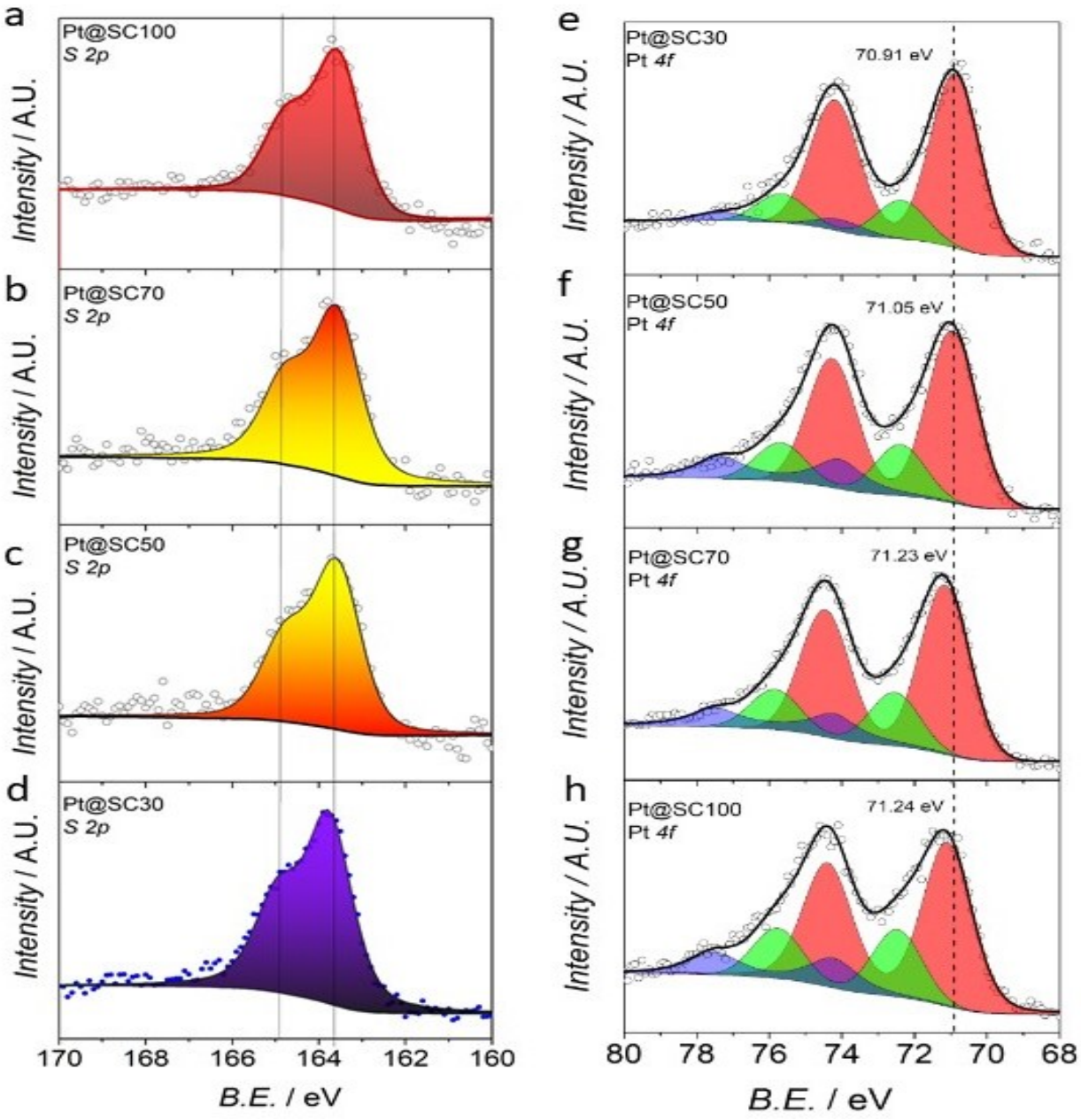

Figure 74: XPs spectra for a) S *2p* Pt@SC100, b) S *2p* Pt@SC70, c) S *2p* Pt@SC50, d) S *2p* Pt@SC30, e) Pt *4f* Pt@SC30, f) Pt *4f* Pt@SC50, g) Pt *4f* Pt@SC70 and h) Pt *4f* Pt@SC100

Figure 75 show the XRD pattern for Pt@SC catalysts. All of the doped samples exhibit a wide diffraction peak at ca. 29.3°, which is related to graphitic materials and is indicative of the presence of amorphous carbon and small graphitic domains. The diffraction peaks evaluated at the Bragg angles of 46 °, 54 ° 67 °, 81° and 109 ° correspond to the (111), (200), (220), (311) and (222) facets of Pt, respectively, which suggests that Pt NPs on all the samples have the same face centered cubic (fcc) crystal structure.

Platinum nanoparticle sizes were evaluated, as done previously, by using the Debye - Scherrer equation and the full width at half-maximum (FWHM) of the Pt (220) diffraction peaks in the XRD spectra. The crystallite dimension trend is the following:

Pt@SC70_AC (6.1 nm) > Pt@SC0_AC (6.6 nm) > Pt@SC30_AC (3.4 nm) > Pt@SC100_AC (1.8 nm) > Pt@SC_50_AC (1.7 nm).

Pt@SC0_AC and Pt@SC70_AC exhibit narrower peaks than the other samples, denoting an average crystallite size of Pt NPs in the range of 6 nm - 7 nm. Smaller Pt NPs were found for Pt@SC100 and Pt@SC50, with estimated crystallize sizes of ca. 1.8 nm, and 3.4 nm for Pt-SMC30. It is worth noting that X-ray diffraction data refer to bulk samples encompassing all Pt NPs without distinguishing between NPs embedded inside carbon pores and bigger NPs formed over the carbon surface. An average size of 2 nm denotes that the major part of Pt NPs has coherently diffracting domains smaller than the pores of the carbon support. An average size of 6 nm indicates that a fraction of crystalline Pt exists with larger coherent diffracting domains and is expected to form over the carbon surface. The large peak broadening of Pt@SC100 and Pt@SC50 diffraction patterns hampers the fitting procedure in line profile analysis and for these catalysts' deconvolution of micro strain and size effects was not feasible. Single reflection analyses with the Langford method have also been performed fitting the (220) single peak with a Voigt function. With the Langford method the Gaussian and Lorentzian contributions to peak broadening are related to strain and size effects, respectively. In this case, it was possible to estimate the micro strain contribution for all samples. The obtained results indicate a higher strain contribution in the Pt NPs associated to sulfur containing carbon (estimated strain of 2.2%, 1.1% and 0.3% for Pt-SMC100, Pt-SMC50 and Pt-MC, respectively).

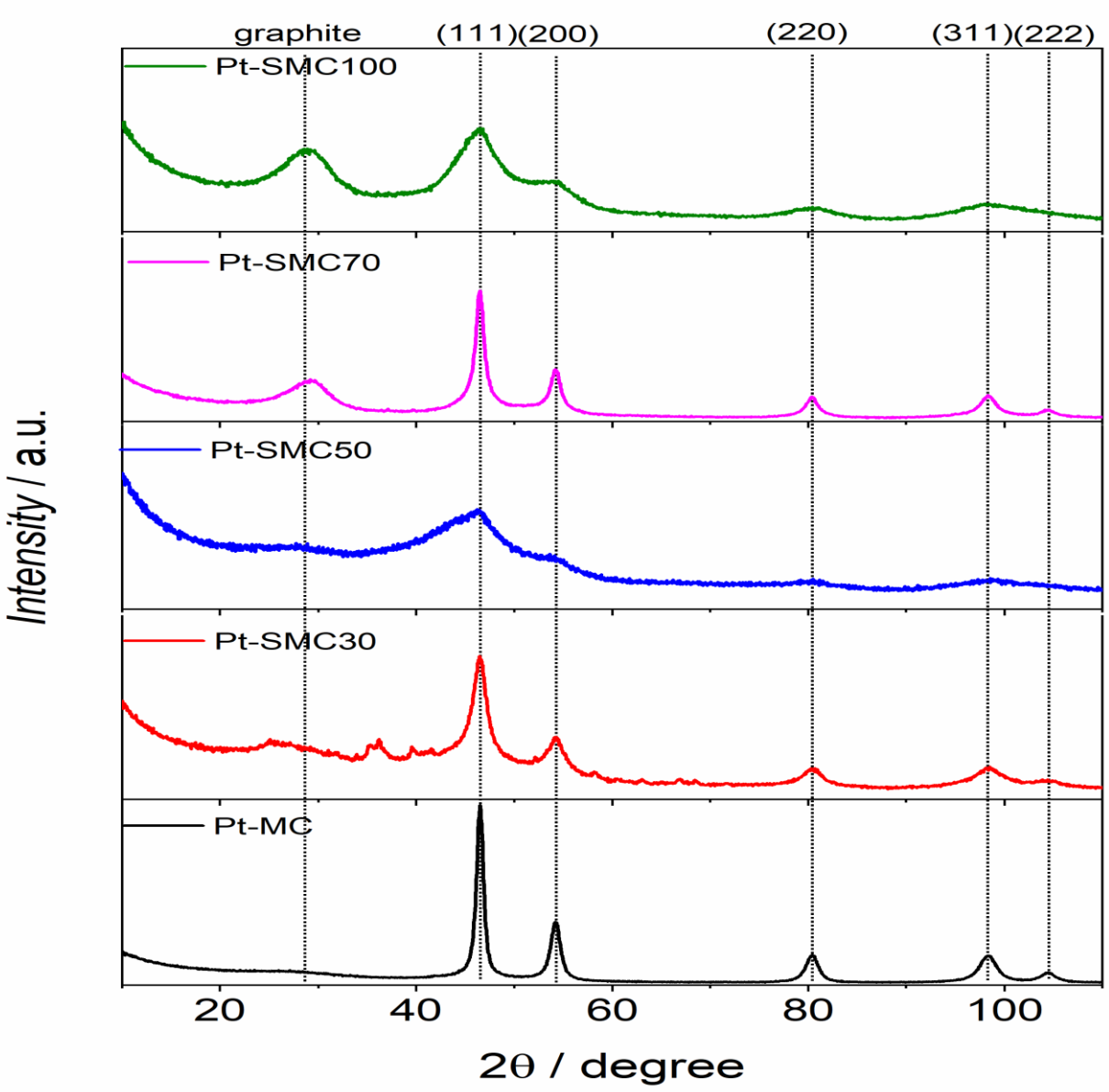

Figure 75: XRD analysis for Pt@SC catalysts

8.2.6 Electrochemical Characterization: activity vs. sulphur content

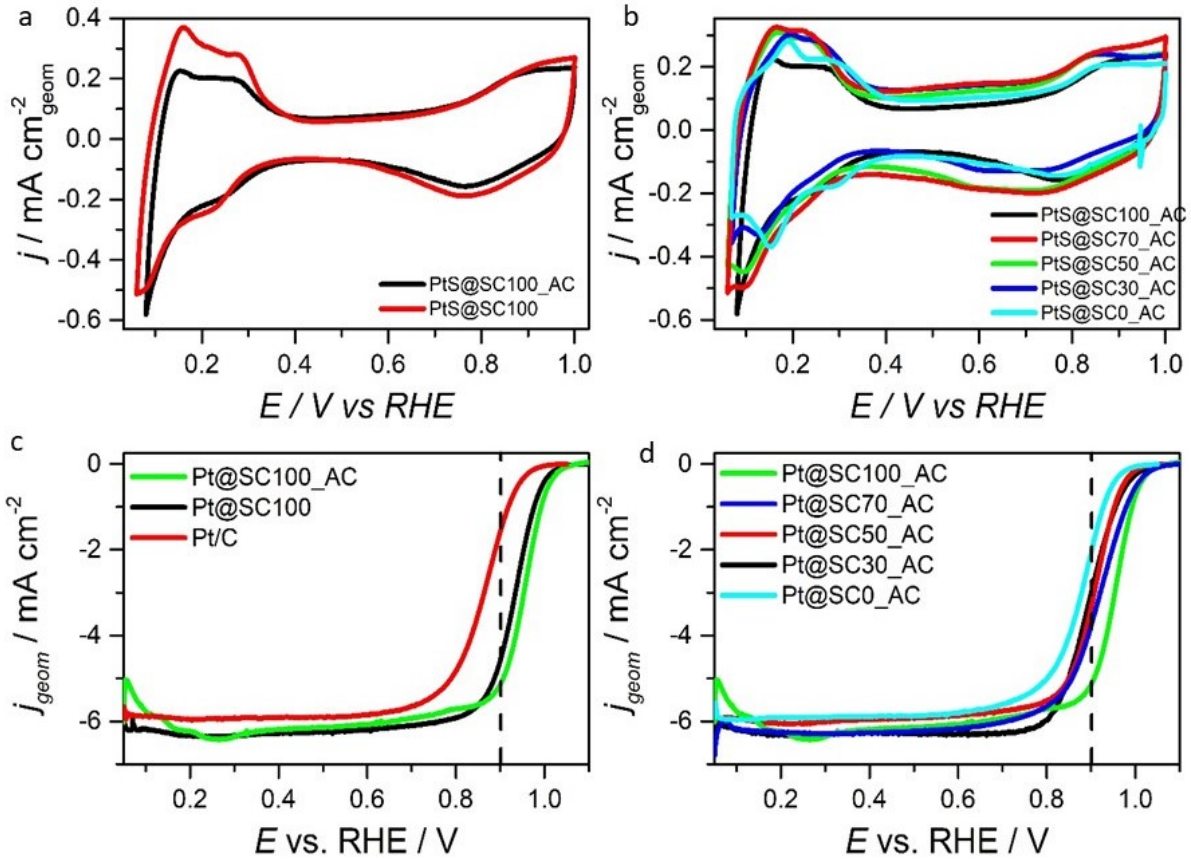

Figure 76: a) Cyclic Voltammetry at 50 mV s^{-1} in Ar saturated $HClO_4$ 0.1 M solution for Pt@SC100 before and after the acid treatment; b) Cyclic Voltammetry at 50 mV s^{-1} in Ar saturated $HClO_4$ 0.1 M solution; c) LSV with RDE at 1600 rpm and 20 mV s^{-1} in O_2 saturated $HClO_4$ 0.1 M solution for Pt@SC100 catalysts before and after the H_2SO_4 treatment and d) LSV with RDE at 1600 rpm and 20 mV s^{-1} in O_2 saturated $HClO^4$ 0.1 M solution for Pt@SC100_AC catalysts.

Cyclic voltammetry (CV) and linear sweep voltammetry (LSV) at a rotating disk electrode (RDE) were performed in 0.1 M $HClO_4$ in a three electrode cell at 25 °C, using a Biologic SP200 potentiostat instrument. Figure 76a show the cyclic voltammetry for Pt@SC100 before and after the acid treatment at 50 mV s^{-1}. The capacitive current and the Platinum Oxide formation/stripping peak are very similar for all two samples. The Hydrogen desorption area of Pt@SC100 results be similar than Pt@SC100_AC, the hydrogen adsorption area appears slight reducedafter the acid treatment. This different can associated to an deactivation of platinum sites due to the treatment. Small particles are also more susceptible to acid leaching or to ripening phenomena during the acid wash, as evidenced by the TEM and by XRD analyses, most likely with a decrease of EPSA. The values of EPSA for Pt@SC are listed Table 10; all catalysts showed very high EPSA values in the range 1.20 cm^2 – 2.50 cm^2 comparable with the value obtained for the Pt/C benchmark (2.11 cm^2 and 75 m^2 g^{-1}). The Pt@SC catalysts after the acid treatment show an EPSA reduction. For example, Pt@SC100 show an EPSA of 2.44 cm^2 while Pt@SC100_AC of 1.27 cm^2; the EPSA evaluated for Pt@SC70 and Pt@SC70_AC result

be 2.11 cm^2 and 1.94 cm^2, respectively. For the catalysts obtained after the acid treatment The EPSA increase from Pt@SC0_AC to Pt@SC70_AC (from 1.17 cm^2 to 1.94 cm^2) and after decrease (from 1.94 cm^2 to 1.27 cm^2).

Table 10: Electrochemical results for Pt@SC catalyst before and after the H_2SO_4 treatment evaluated by LSV with RDE at 1600 rpm and 20 mV s^{-1} in O_2 saturated $HClO_4$ 0.1 M solution.

Sample	j_L	$E_{1/2}$	j_k	*EPSA*	*ECSA*	*MA*	*SA*
	mA cm^{-2}_{geom}	V vs RHE	mA cm^{-2}_{geom}	cm^2	$m^2\ g^{-1}$	A g^{-1}	mA cm^{-2}
Pt@SC100	6.31	0.908	7.06	2.44	83.12	470.9	0.57
$\Delta_{Pt@SC100}$	0.06	0.008	0.04	0.15	5.36	3.2	0.04
Pt@SC100_AC	6.28	0.911	8.26	1.27	43.32	551.0	1.27
$\Delta_{Pt@SC100\_AC}$	0.06	0.005	0.08	0.09	3.00	5.5	0.12
Pt@SC70	6.43	0.868	3.32	2.11	71.77	221.4	0.31
$\Delta_{Pt@SC70}$	0.07	0.006	0.04	0.14	3.00	5.0	0.01
Pt@SC70_AC	6.68	0.914	7.31	1.94	65.99	487.2	0.74
$\Delta_{Pt@SC70\_AC}$	0.07	0.007	0.09	0.11	2.37	5.2	0.06
Pt@SC50	6.05	0.862	1.67	1.83	62.24	111.5	0.18
$\Delta_{Pt@SC50}$	0.06	0.050	0.13	0.15	5.00	4.7	0.03
Pt@SC50_AC	6.31	0.900	6.54	1.60	54.59	436.2	0.80
$\Delta_{Pt@SC50\_AC}$	0.05	0.003	0.05	0.12	4.00	8.0	0.02
Pt@SC30	6.28	0.843	1.69	1.34	45.58	112.5	0.25
$\Delta_{Pt@SC30}$	0.06	0.080	0.04	0.10	4.00	3.0	0.02
Pt@SC30_AC	6.14	0.881	4.02	1.21	41.20	267.9	0.65
$\Delta_{Pt@SC30\_AC}$	0.04	0.006	0.11	0.09	3.00	7.3	0.24
Pt@SC0	6.07	0.842	1.27	1.31	44.56	84.7	0.19
$\Delta_{Pt@SC0}$	0.08	0.007	0.12	0.12	4.54	7.3	0.04
Pt@SC0_AC	5.87	0.881	3.20	1.17	39.86	213.2	0.53
$\Delta_{Pt@SC0\_AC}$	0.11	0.004	0.15	0.10	3.52	8.0	0.04

Pt/C show an ECSA of 75 $m^2\ g^{-1}$, Pt@SC100 and Pt@SC70 owns an ECSA very similar to the standard, 83 $m^2\ g^{-1}$ and 73 $m^2\ g^{-1}$. Decreasing the sulphur content, the ECSA decrease from 70 $m^2\ g^{-1}$ to 39 $m^2\ g^{-1}$ for the undoped samples. The acid untreated sample show a EPSA decrement with sulphur content decrease. The catalytic activity of Pt@SC catalysts towards ORR was evaluated by linear sweep voltammetry at a rotating disk electrode in O_2-saturated 0.1 M $HClO_4$. It was observed that acid washing improved the ORR catalytic performance of the tested materials, especially in samples containing higher density of sulfur functional groups. The Mass Activity increase from 470 A g^{-1} to 550 A g^{-1} for Pt@SC100. In Pt@SC70 the electrochemical activity pass from 221 A g^{-1} to 487 A g^{-1}. The same increment was observed for the other

Pt@SC catalysts. If we consider the half wave potential $E_{1/2}$ as a parameter for evaluating the catalytic activity, instead of the more questionable and unrelible onset potential, all Pt@SC electrodes catalysed the ORR and are more active than the commercial standard Pt/C TKK. The $E_{1/2}$ increases in the order

Pt@SC0 < Pt@SC30_AC < Pt@SC50_AC < Pt@SC70_AC < Pt@SC100_AC.

It is worth noting that $E_{1/2}$ increases with increment of the sulfur defect density on the carbon support. The mean values of Specific Activity (SA) and Mass Activity (MA) clearly increase with increasing sulfur site density. It is worth noting that in Pt@SC50, Pt@SC70 and Pt@SC100, the mean MA values reach or even overtake the United States Department of Energy target of 440 A g^{-1} at 0.9 V vs. RHE. The Mass Activity evaluated for Pt@SC100_AC and Pt@SC70_AC result be 550 A g^{-1} and 487 A g^{-1}, respectively. The untreated sample respect the same trend of MA and SA with the sulfur content, but the activity is lower than Pt@SC_AC series. it is clear that sulfur functional groups play an active role in the nucleation and growth on Pt NPs and, as a consequence, also in their catalytic activity, so that a metal support interaction can be clearly claimed, even though small B.E. shifts were observed by XPS investigation on Pt 4f and S 2p peaks.

8.2.7 Conclusion

The support plays a role in both preparation and stability of Pt NPs; in particular, sulphur heavily affect both the nucleation and growth of Pt NPs, but partially fail in stabilizing Pt NPs, since TEM images show the formation of NPs with a size of 6 nm – 8 nm, which are less active in the ORR. Carbon doping in a method for increase the electrochemical performance of Pt NPs and it help reach the DOE target. For an real application in the PEM-Fuel cell, the catalysts must show a Mass Activity higher than 440 A g^{-1} and a Specific Activity higher than 0.250 mA cm^{-2}. Sulphur doping increase the kinetic current of a Platinum material, and this would allow one to lower the Pt loading on the electrode. Five different mesoporous carbons with similar morphological properties but different sulfur contents were synthetized according to a hard template approach employing a commercial mesoporous silica [154, 155]. The hard template results a good method for obtained carbon with a similar structure but using different carbon precursor, since the porous structure is given by the templating agent. Pt NPs were deposited on the resulting mesoporous carbons by high temperature reduction of $Pt(acac)_2$ and the resulting catalysts were investigated with XRD, XPS, TEM, Elemental Analysis and Electrochemistry.

It was demonstrated that Pt NPs interact with the carbon active site and the interaction depends by the density of sulphur thiophenic group in the support. Increasing the sulfur content in the support increased the extent of interaction as evidenced by the gradual shift of the XPS signal of Pt 4f towards higher binding energy of 0.3 eV; the same binding energy shift was evaluated for the S 2p. Furthermore, increased S doping induces an increase of strain on Pt NPs. It is known that both strain and electronic effects influence the catalytic properties of Pt NPs catalysts. Pt@SC catalysts are resulted active towards ORR, with catalytic activity clearly increasing with the extent of the sulfur doping. An acid treatment was used for trying to increase the electrochemical

performance. With an acid treatment, the EPSA was reduced but the mass activity of the resulting material increases due to the platinum oxide removing from the external surface of NPs [156, 157, 163]. In particular, Pt@SC100, with a sulfur content of 14%, showed much higher mass activity (Mass Activity 550 A g^{-1}) and more positive $E_{1/2}$ = 0.951 V vs. RHE than the commercial standard Pt/C (MA = 275 A g^{-1} and $E_{1/2}$ = 0.864 V vs. RHE).

In conclusion, this study demonstrated the existence of an important metal-support interaction between sulfur doped carbon support and Pt NPs, and how this effect can influence the catalytic activity of Pt NPs towards ORR. Furthermore, it was shown that the interaction can be boosted by acting on the sulfur content.

8.3 Effect of Surface Area of a Pt@SdC catalyst on the catalytic activity for ORR

8.3.1 Abstact

Carbon based material are the most material investigated as NPs support for the catalysis in all their form, nanospheres, fibres, nanotubes or sheet. In addition, for their good conductivity combined with mechanical, chemical and electrochemical stability, they are widely used in electrocatalysis as well as in energy storage and generation systems. In recent years, the interest on the synthesis of porous carbon materials is increased, for their intrinsic characteristic as controlled and uniform pore sizes, which confer high surface area and large pore volume to the material [154, 156]. Porous carbon materials are usually synthesized using various methods, including

(i) pyrolysis of a carbon precursor synthetized with inorganic template (hard template approach)

(ii) pyrolysis of co-polymers composed by a sacrificial polymer and by a "structural" polymer (soft template approach)

(iii) hydrothermal synthesis from organic precursors as biomass.

The hard template synthesis is of interest because it is a fast and reproducible method for obtained a carbon with a well-defined structure. Consists in the mixing of an inorganic template such as zeolite or silica with an carbon precursor. The carbon precursor is allowed to permeate into the pores of the template. After pyrolysis, the removal of the template generates porous carbon materials with an interconnected pore. Even though many porous carbon materials have been developed according to the hard template approach, the synthesis of uniform porous carbon materials is still very challenging. Therefore, several types of templates and carbon precursors are continuously investigated to optimize particle and pore dimensions, surface area and surface chemistry. Furthermore, pore structure can be tuned at high temperature using oxidizing gas such as O_2, CO_2, Cl_2 or water vapor, or by chemical activation of carbon with KOH, H_3PO_4 or $ZnCl_2$ [75, 75, 164].

In a platinum NPs based material several factor can stabilize the NPs for increase the activity and the stability. In previous part was analysed the influence of heteroatoms on the catalytic activity and the interaction between the metal and the sulfur. The platinum NPS were deposited in mesoporous carbon obtained by hard template. The support owns a very controlled and ordered porosity with different pore distribution, external surface area, pore volume and surface area. The main problem in a Pt NPs based material is the NPs dispersion in the carbon support, the NPs must be distributed not only in the external surface ma also inside the pore. The pore dimension must be bigger than the NPs. Since the deposition method used for the synthesis, the NPs can grow also inside the pore, so the pore dimensions become a critical factor for obtaining an optimal NPs distribution. For these reasons several sulphurs doped mesoporous carbon was thermal treated for increase the pore

dimension so the surface area. After the platinum deposition by solid state synthesis, the resulting catalysts were fully characterized for evaluate the connection between the sulphur concentration and the carbon morphology on the electrochemical performance vs. ORR [153, 161].

8.3.2 Synthesis and Chemical

Mesoporous silica (Sigma−Aldrich, 200 nm particle size, 4 nm pore size), dibenzothiophene (Sigma−Aldrich, 98%), $Pt(acac)_2$ (Sigma−Aldrich, >97%), Nafion (Sigma Aldrich, 5 wt.% in EtOH), $HClO_4$ (Fluka, Traceselect® 67-72%), Pt/C Tanaka (TKK) standard and acetone (Fluka, HPLC grade) were used as received without further purification.

Usually, hard template synthesis of mesoporous carbons uses very expensive silica particles employed as a sacrificial template for obtaining a negative carbon replica. Silica P200 consists in mesostructured SiO_2 nanoparticles (NPs, 200 nm) that act as a porogen agent during the formation of the carbon texture.
Sulphur doped mesoporous carbons were synthetized by hard template method using dibenzothiphene and silica P200 in ratio 2:1. The SC (Sulfur doped Carbon) was pyrolized at 750 °C for 2 h in Argon atmosphere. After pyrolysis at 750 °C, the resulting crude product was treated with an etching solution (EtOH/KOH 2M) in Bath Sonicator for 3 day to remove the SiO_2 NPs, leaving wide open pores of the same dimensions of the solid structure of the SiO_2 NPs.
The sulphur doped mesoporous carbon was, after, post-treated in a tubular furnace (Carbolite, UK) with a 50 sccm N_2 flux at 100 °C for 1 h for eliminated all impurities which can interact with the treatment, after which the temperature was raised up to 850 °C with a rate of 5 °C min^{-1} and kept at constant for different stream treatment time. The steam flux used for all thermal post treatment was set of 1 mL min^{-1}. Several time steam treatments were adopted, 5 min, 20 min, 40 min and 60 min. After the carbon treatment the platinum was deposited by heated the mixture of the support and the $Pt(acac)_2$ in a reduction H_2 atmosphere (8% H_2) at 300 °C for 3 h. The resulting catalysts were dispersed in a 1 M H_2SO_4 solution at room temperature for 10 minutes and after filter under vacuum and washed with milliQ water [127, 156, 165].

8.3.3 Elemental Analysis and N_2 Absorption/ Desorption Analysis: Surface Area vs. Sulphur Content

Table 11: Morphological results for Pt@SC_St catalysts

	S_{AE}	Pt_{ICP}	S_{BET}	d_{p1}	d_{p2}	d_{p3}	d_{p4}	$S_{micropore}$	$S_{mesopore}$	$V_{micropore}$	$V_{mesopore}$
	%	%	$m^2\ g^{-1}$	nm	nm	nm	nm	$m^2\ g^{-1}$	$m^2\ g^{-1}$	$cm^3\ g^{-1}$	$cm^3\ g^{-1}$
Pt/C	0.75	49.2	218	1.78	4.87	7.98	14.01	65	153	0.030	0.038
$\Delta_{Pt/C}$	0.04	2.5	11	0.09	0.24	0.40	0.70	3	8	0.002	0.002
Pt@SC_St0_	10.04	27.8	1103	1.10	3.80	4.90	7.20	146	957	0.014	0.864
$\Delta_{Pt@SC\_St0}$	0.50	1.4	55	0.06	0.19	0.25	0.36	7	48	0.001	0.043
Pt@SC_St5	9.12	28.9	1278	2.30	4.10	6.34	15.95	138	1140	0.045	0.765
$\Delta_{Pt@SC\_St5}$	0.46	1.4	64	0.12	0.21	0.32	0.80	7	57	0.002	0.038
Pt@SC_St20	5.34	26.9	1489	2.94	3.88	6.02	16.47	94	1395	0.098	0.984
$\Delta_{Pt@SC\_St20}$	0.27	1.3	74	0.15	0.19	0.30	0.82	5	70	0.005	0.049
Pt@SC_St40	3.46	29.6	1510	3.10	4.36	6.75	17.11	121	1389	0.187	1.388
$\Delta_{Pt@SC\_St40}$	0.17	1.5	76	0.16	0.22	0.34	0.86	6	69	0.009	0.069
Pt@SC_St60	1.97	29.1	1674	3.00	4.17	6.09	15.94	196	1478	0.374	2.183
$\Delta_{Pt@SC\_St60}$	0.10	1.5	84	0.15	0.21	0.30	0.80	10	74	0.019	0.109

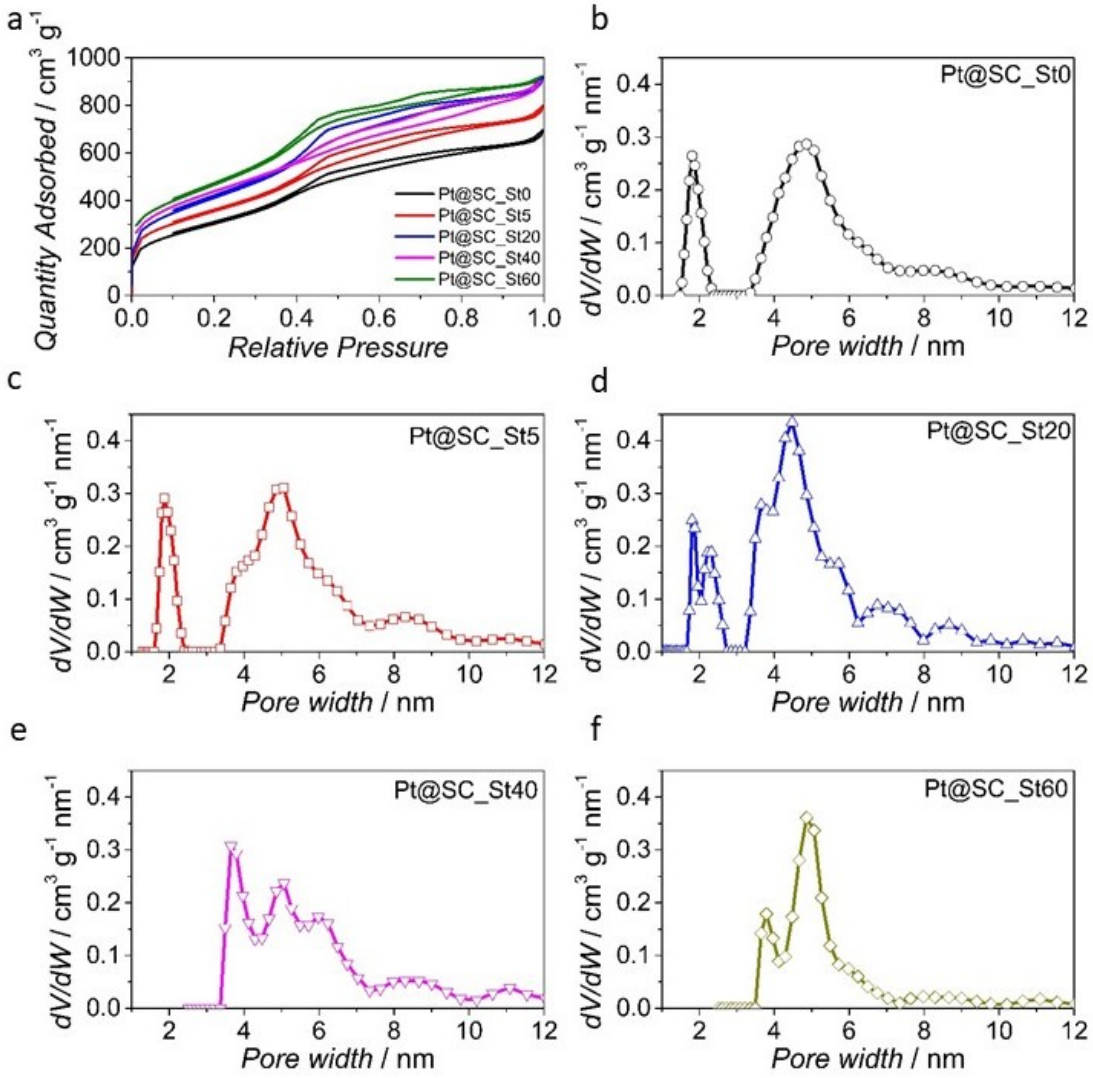

Figure 77: a) Adsorption/Desorption Isotherm for Pt@SC_St; b) Pore distribution Pt@SC_St0; c) Pore distribution Pt@SC_St5; d) Pore distribution Pt@SC_St20; e) Pore distribution Pt@SC_St40 and f) Pore distribution Pt@SC_St60

Elemental Analysis show a sulfur content decrement with the increasing of steam time treatment. Pt@SC_St0 show a sulfur content of 10.04 %, after the percentage decrease until 1.97 % with 60 min of steam treatment. The effect of steam treatment on the carbon surface is increase the porosity and so the surface area; it is based on controlled combustion process. The surface area of sulphur doped carbon increase with the increment of the time treatment. The untreated sample have a surface of 1103 m^2 g^{-1}, with the steam treatment the surface area increases with the following trend:

Pt@SC_5 (1278 m^2 g^{-1}) < Pt@SC_20 (1489 m^2 g^{-1}) < Pt@SC40 (1510 m^2 g^{-1}) < Pt@SC60 (1674 m^2 g^{-1}).

The pore distribution are shows in Figure 77. The pore dimension, especially d_{p1}, increase with the increment of the steam treatment time. The mesoporous surface area increase passing from 5 min to 60 min of steam

treatment. The micropore pore volume increase with the time treatment from 0.01 $cm^3\ g^{-1}$ to 0.34 $cm^3\ g^{-1}$; because the process forms new porosity in the carbon particles. The mesoporous volume in Pt@SC_St0, Pt@SC_St5 and Pt@SC_St20 is 0.86 $cm^2\ g^{-1}$, 0.76 $cm^2\ g^{-1}$ and 0.98 $cm^2\ g^{-1}$, respectively. The mesoporous volume can be considered constant for these catalysts. Instead, the sample Pt@SC_St40 and Pt@SC_St60 show an mesoporous volume increment from 0.984 $cm^3\ g^{-1}$ to 2.18 $cm^3\ g^{-1}$. The Nitrogen adsorption desorption analysis confirm the impact of the steam treatment of the mesoporous carbon. The surface area increment follows a linear trend with the sulphur content decrement. The platinum loading was evaluated by ICP-MS, the platinum content is close to the theoretical value of 30 % for all catalysts.

8.3.4 TEM and SEM: Influence of Surface Area and Pore distribution on the PLATINUM NANOPARTICLES

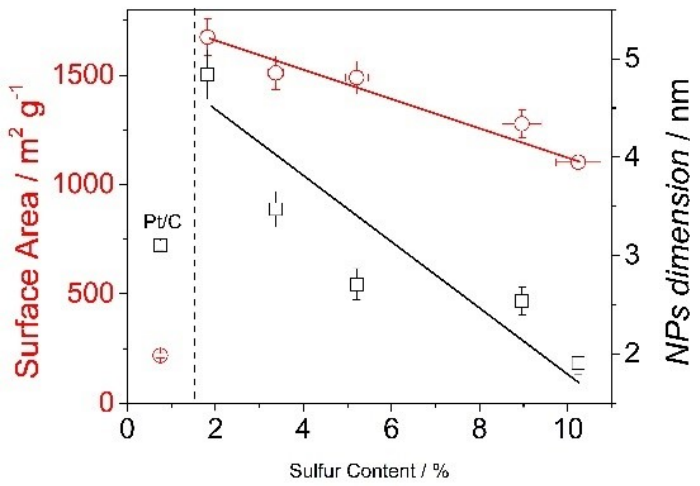

Figure 78: Correlation between Surface Area and the Platinum NPs with the Sulphur concentration.

NPs dimension was evaluated by counting of 350 NPs randomly distributed in TEM images, after the distribution was fitted by a Lorentzian a or Gaussian. The NPs dimension distribution increase with the increment of steam treatment or, in another point of view, with the decrement of sulphur content, as show in Figure 78. The catalyst Pt@SC_St0 show a sulfur content of 10.04 % and a NPs dimension of 1.91 nm, the NPs dimension decrease with the following trend, Pt@SC_60 (4.84 nm, 1.82 $\%_S$) < Pt@SC_40 (3.47 nm, 3.37 $\%_S$) < Pt@SC20 (2.71 nm, 5.21 $\%_S$) < Pt@SC5 (1.91 nm, 10.24 %s). The commercial platinum Pt/C used for the electrochemical comparison show a NPs distribution picked at 3.10 nm and a sulphur content of 0.75 %.

Table 12: NPs dimension for Pt@SC_St catalysts before and after the H_2SO_4 treatment

	d_{NPs}	$^{AC}d_{NPs}$
	nm	nm
Pt/C	3.1	2.8
$\Delta_{Pt/C}$	0.1	0.1
Pt@SC_St0	2.1	1.9
$\Delta_{Pt@SC\_St0}$	0.1	0.1
Pt@SC_St5	2.8	2.5
$\Delta_{Pt@SC\_St5}$	0.1	0.1
Pt@SC_St20	3.2	2.7
$\Delta_{Pt@SC\_St20}$	0.1	0.2
Pt@SC_St40	4.0	3.5
$\Delta_{Pt@SC\_St40}$	0.1	0.2
Pt@SC_St60	5.4	4.8
$\Delta_{Pt@SC\_St60}$	0.1	0.3

Several articles in literatures confirm the influence of sulfur doping on the stabilization of Platinum Nanoparticles, high sulfur content around 14 % can stabilize low metal nanoparticles and prevent aggregation phenomena. This effect is connected to the incredible electrochemistry stability of the Pt NPs on Sulphur doped Carbon for the oxygen reduction reaction. Figure 79 show the SEM image for the samples obtained with the different steam treatment, the NPs are randomly distributed in the external carbon surface. SEM images show the presents of some aggregates. Figure 80 show the TEM images, it is clear the good NPs distribution around the nanoparticles and inside the pore. The carbon particles can be described as perfect spheres with a cylinder porosity that develops from the external surface to the bulk. The images show the totally absence of aggregate or cluster with high dimension. The NPs have a very narrow dimensional distribution. The EDX maps confirm the presence of Pt and S heteroatoms before and after the acid wash. TEM images and EDX maps show that round shaped Pt NPs are, in both cases, well distributed all over the carbon support. The mean particle size distribution slightly decreases after the acid wash, since the center of Lorentzian profile of the histogram shifts down of 0.5 nm – 0.7 nm.

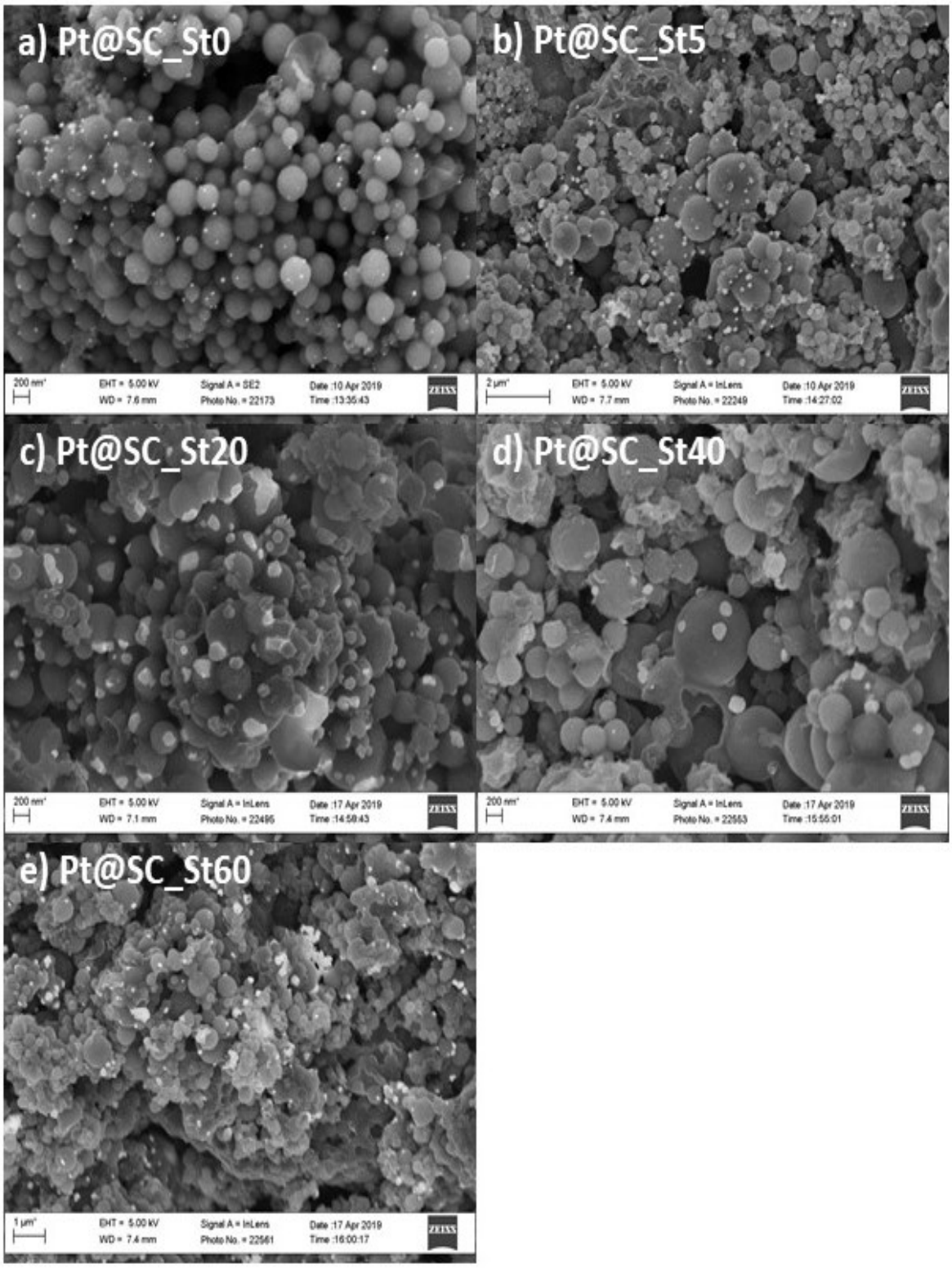

Figure 79: SEM characterization of Pt@SC catalysts; a) Pt@SC_St0; b) Pt@SC_St5; c) Pt@SC_St20; d) Pt@SC_St40 and e) Pt@SC_St60

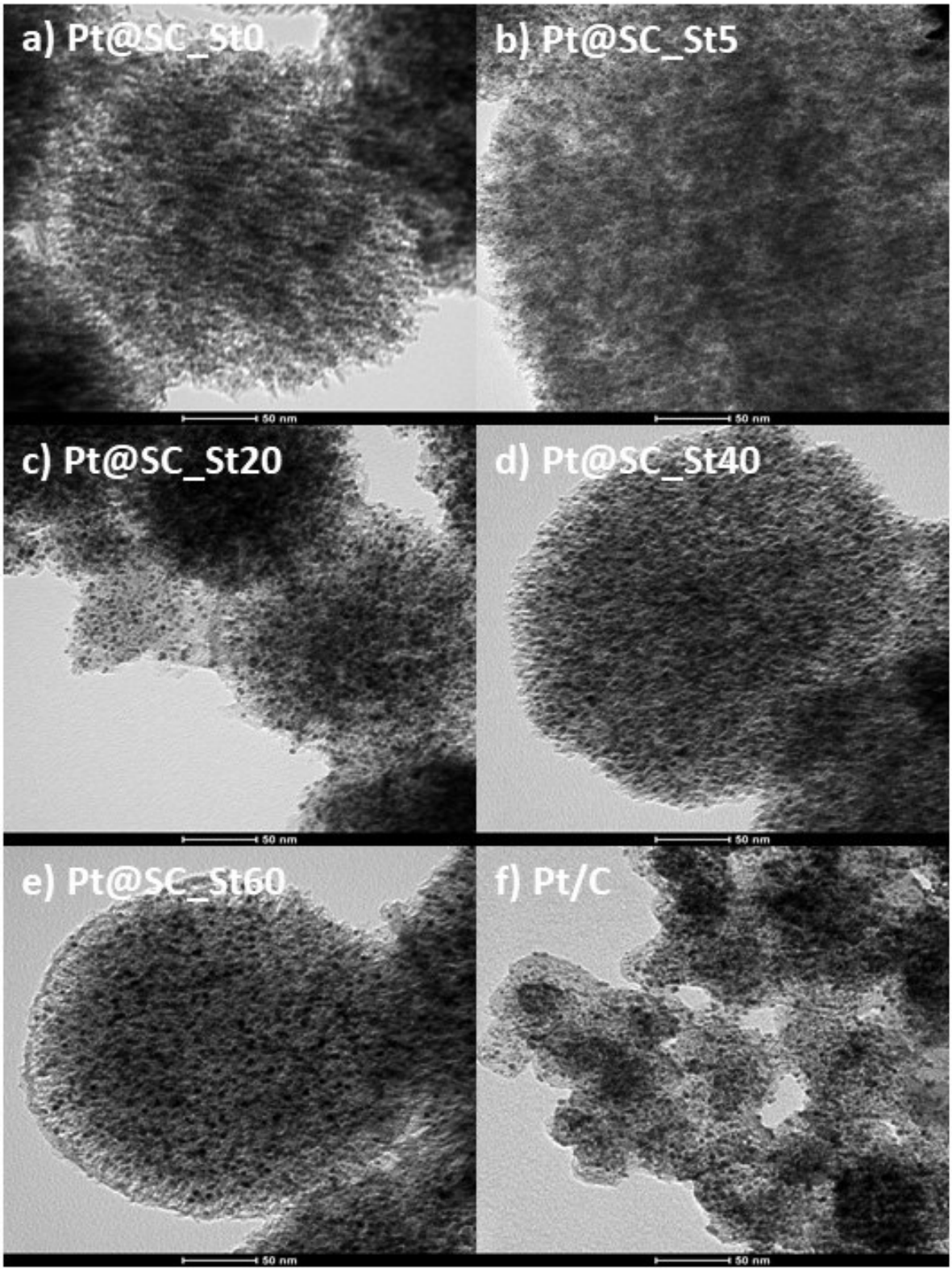

Figure 80: TEM characterization of Pt@SC catalysts; a) Pt@SC_St0; b) Pt@SC_St5; c) Pt@SC_St20; d) Pt@SC_St40; e) Pt@SC_St60 and Pt/C

8.3.5 XRD Analysis: effect of the carbon surface area on the platinum nanoparticles

Figure 81 show the XRD spectra for the different sample, the peak position was associated with the following correlation, 29° C 002, 46° Pt 111, 54° Pt 200, 81° Pt 220, 99° Pt 311 and 105° Pt 105. The large peak broadening of Pt@SC_St0 and Pt@C_St60 diffraction patterns hampers the fitting procedure in line profile analysis and for these samples deconvoluting micro-strain and size effects with the W-H plot method was impossible. The diffraction peak in samples Pt@SC_St0 and Pt@SC_St60 is less pronounced because of the different maximum values of the intensity axes.

Table 13: Crystallite dimension evaluated with Scherrer Equation for the different Pt difraction peaks for the Pt@SC_St catalysts

		Pt@SC_St0	Pt@SC_St5	Pt@SC_St20	Pt@SC_St40	Pt@SC_St60	Pt@C_St60
	Signal	***d***	***d***	***d***	***d***	***d***	***d***
	2 θ	**nm**	**nm**	**nm**	**nm**	**nm**	**nm**
	27	-	1.0	23.7	10.1	11.8	1.7
C 002	29	1.7	-	1.9	1.8	1.6	3.8
Pt 111	46	1.8	8.4	8.4	5.8	5.4	4.4
Pt 200	54	1.4	5.2	6.6	4.4	5.6	4.9
Pt 220	81	1.9	5.1	7.0	3.3	4.0	3.3
Pt 311	99	1.3	5.1	7.1	3.1	3.9	3.4
Pt 222	105	-	3.7	7.5	3.0	3.6	2.6

The crystallite dimension was calculated with Scherrer Equation for all diffraction peaks, Generally the most reliable results ad associated to 220 and 311 peaks. The dimension obtained from XRD profile is very similar. From 0 minutes of Steam Treatment to 20 minutes the crystallite dimension increases from 1.5 nm to 7 nm. Pt@SC_St40 and Pt@SC_St60 show a similar dimension of 3 nm – 4 nm. These results suggest how the carbon morphology as surface area or pore dimension/distribution but also the sulphur content have a strong impact on the NPs growing and on the platinum crystallography. At 29° is observed the 022 face of carbon support, increasing the time treatment the intensity is increased, confirming an influence also in the carbon graphitization. Interesting is the comparison between Pt@SC_St60 and Pt@C_St60, the undoped material show an lower platinum crystallography than Sulphur doped catalysts, the crystallite dimension obtained was 3.9 nm and 3.4 nm, respectively. Pt@SC_St20 show an high definition peak, so an high crystallography of platinum. For all catalysts the most intensive peak is the Pt 111, the most active also, as active site, for the Oxygen Reduction Reaction. The size values, reported in table xx, refer to average values not accounting for sample inhomogeneity through crystallite size distributions. An average size of 2 nm denotes that the major part of Pt NPs has coherently diffracting domains smaller than the pores of the carbon support. An average

size of 6 nm indicates that a fraction of crystalline Pt exists with larger coherent diffracting domains and is expected to form over the carbon surface. With the Langford method the Gaussian and Lorentzian contributions to peak broadening are related to strain and size effects, respectively. In this case, it was possible to estimate the micro strain contribution for all samples. The obtained results indicate a higher strain contribution in the Pt NPs associated to sulfur containing carbon which decrease with the increment of Steam Treatment on the Carbon support.

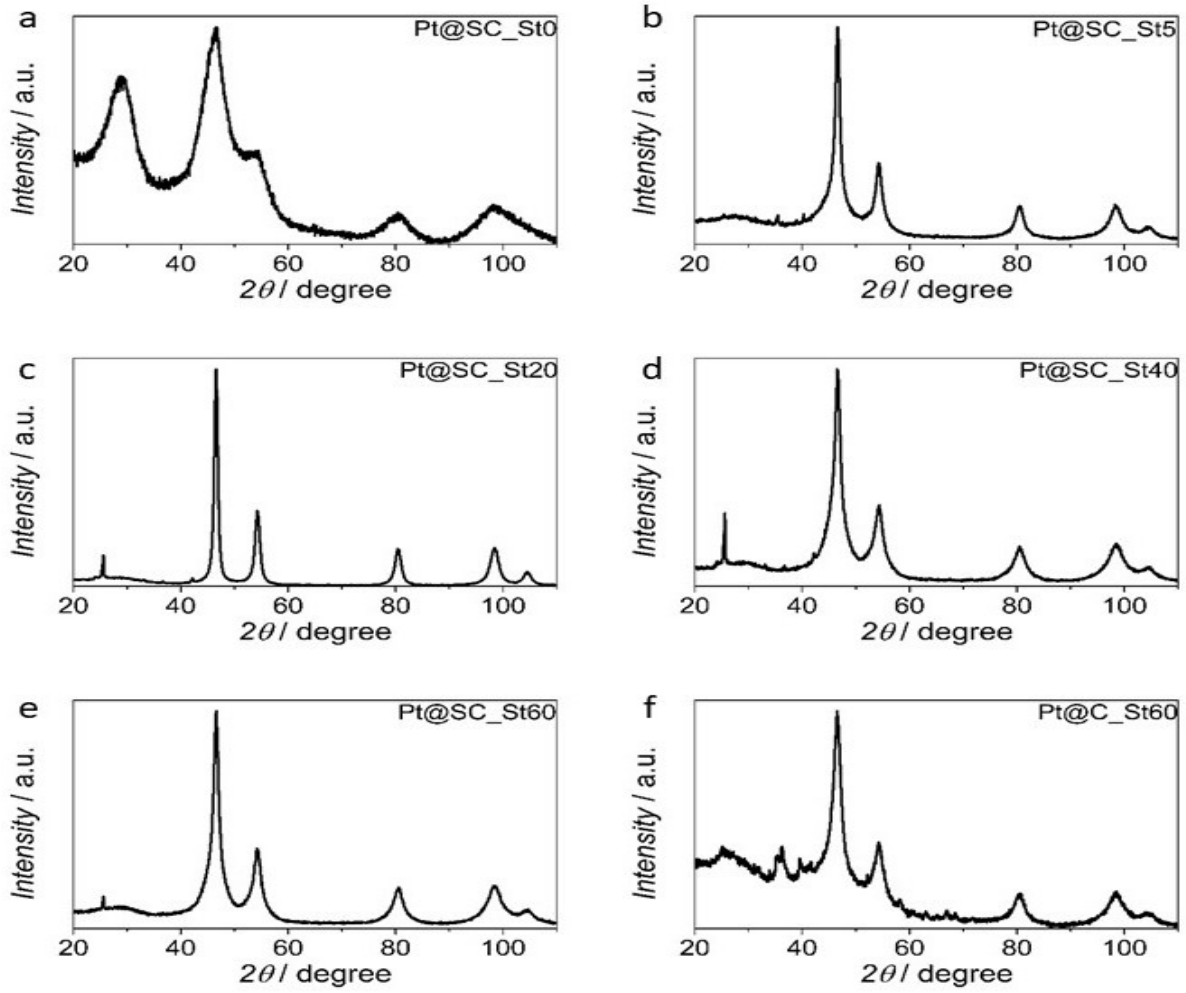

Figure 81: XRD pattern for a) Pt@SC_St0; b) Pt@SC_St5; c) Pt@SC_St20; d)Pt@SC_St40; e) Pt@SC_St60 and f) Pt@C_St60

8.3.6 Electrochemical Characterization: Surface Area and pore distribution vs. ORR

Pt@SC_St before and after the acid treatment were tested in $HClO_4$ 0.1 M electrolyte. The double characterization is due to for understand the effective influence of the treatment on the resulting catalytic activity vs. ORR. In the Figure 82 are reported the cyclic voltammetry in argon saturated solution. Pt/C show an EPSA of 2.16 cm^2 which correspond to an ECSA of 73 $m^2\ g^{-1}$. The cyclic voltammetry shows well defined adsorption and desorption H_2 region. The catalysts synthetized without the acid treatment show an EPSA increment from 1.6 cm^2 to 2.49 cm^2 passing from Pt@SC_St0 to Pt@SC_St5, also Pt@SC_St20 show an high platinum area (2.34 cm^2). After the EPSA decrease with the increasing of the steam treatment used for modifying the carbon support. Same trend is observed after the acid treatment. The Acid Treatment reduce the NPs dimension in all catalyst, the EPSA increase after the H_2SO_4 washing. Sample Pt@SC_St5 and Pt@SC_St20 show an EPSA higher than pure platinum commercial standard, 2.75 cm^2 and 2.46 cm^2, respectively. When SC_St60 is used as support, the low sulfur content cannot stabilize the NPs during the platinum deposition. The EPSA, in Pt@SC_St60, is 1.79 cm^2 before the acid treatment and 1.83 cm^2 after. The EPSA decrement is due to the increment of the NPs dimension and the aggregate formation. The EPSA increment follow the next trend:

Pt@SC_St5 > Pt@SC_St20 > Pt@SC_St40 > Pt@SC_St60 > Pt@SC_St0

Carbon structure and sulphur doping have a strong impact on the NPs growing. With 5 and 20 minutes of steam treatment the carbon mesoporous structure is considerably increased (respect the Pt@SC_St0) but at the same time the sulphur content remain high. The mesoporosity increment result be fundamental in the NPs stabilization, in fact the EPSA evaluated for Pt@SC_St5 is higher than the Pt@SC_St0. Considering the EPSA trend, the carbon morphology in terms of mesostructure have an impact on the EPSA greater than the sulfur concentration. The steam treatment in the carbon support do not modify the capacitive current of the resulting material. The peaks of platinum oxide formation and stripping in all sample after and before the H_2SO_4 washing are at the same potential but have different current intensity. Passing from Pt@SC_St0 to Pt@SC_St60, the hydrogen evolution occurs at lower potential, this phenomenon is associated to the reduction of graphitization which occur during the steam treatment.

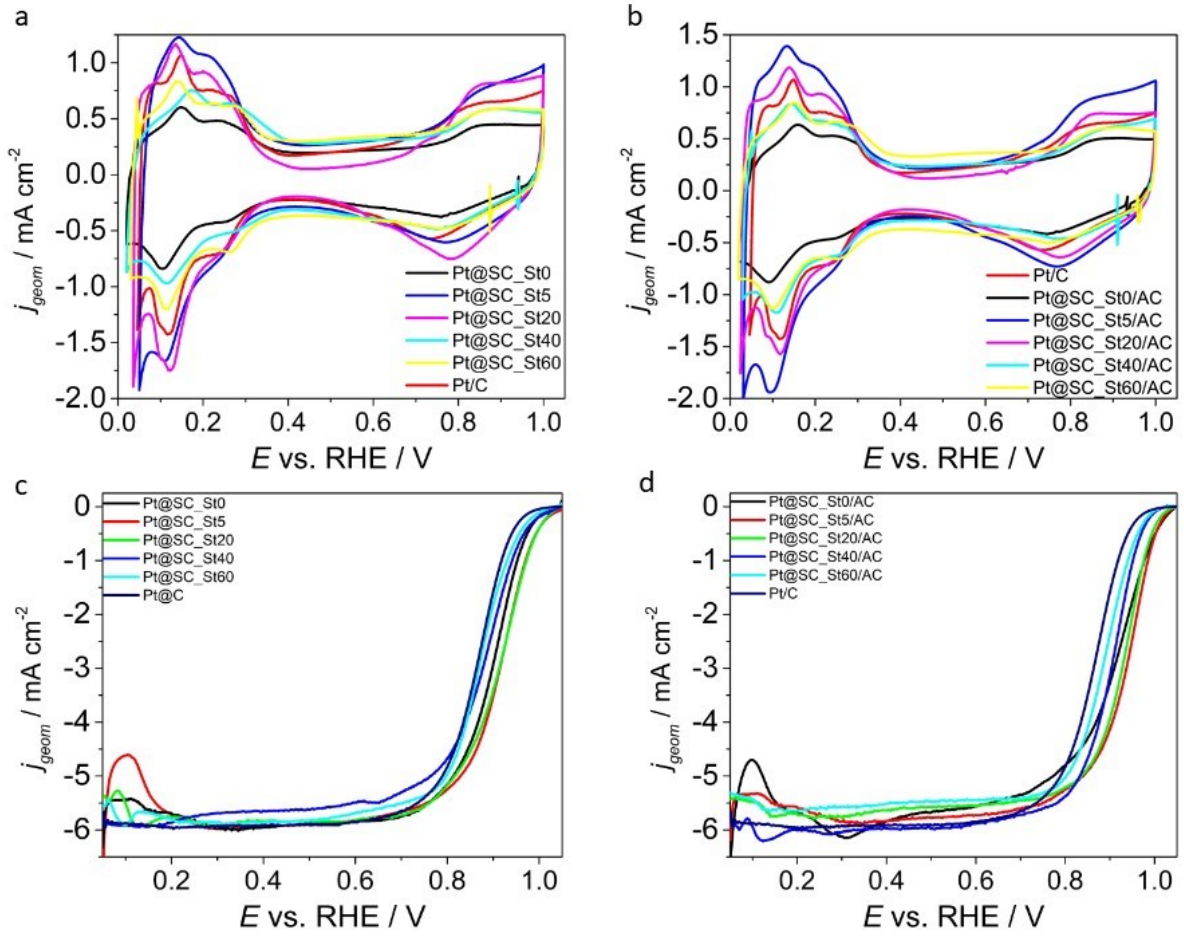

Figure 82: a) Cyclic Voltammetry in Ar saturated $HClO_4$ 0.1 M solution at 50 mV s^{-1} for Pt@SC_St catalysts before the acid treatment; b)Cyclic Voltammetry in Ar saturated $HClO_4$ 0.1 M solution at 50 mV s^{-1} for Pt@SC_St catalysts after the acid treatment; c) LSV with RDE in O_2 saturated solution at 1600 rpm and 20 mV s^{-1} for Pt@SC_St materials before the H_2SO_4 treatment and d) LSV with RDE in O_2 saturated solution at 1600 rpm and 20 mV s^{-1} for Pt@SC_St/AC materials

Figure 82 c, d show the linear sweep voltammetry for the Pt@SC catalysts untreated and treated with sulphuric acid. The Pt@SC_St catalytic before and after the Sulphuric Acid treated was tested in a classic three electrode electrochemical cell. The electrochemical data were calculated from LSV with RDE in anodic scan at 20 mV s^{-1} and 1600 rpm. Platinum content was evaluated by ICP, the value obtained is close to 30 %, typical value for Platinum based material in PEM Fuel Cell. For the acid untreated materials, Pt@SC_St0 show an $E_{1/2}$ of 0.896 V vs RHE, 29 mV higher than platinum commercial reference. From Pt@SC_St0 to Pt@SC_St20 the half wave potential pass from 0.896 V vs RHE to 0.923 V vs RHE; same trend was observed for kinetic current, Mass Activity and Specific Activity. The best sample was synthetized with the support obtained with 20 minutes of steam treatment, the surface area obtained is 1489 m^2 g^{-1} and a sulphur content of 5.34 $\%_w$. The platinum based material shows 536 A g^{-1} of MA, 1.58 mA of i_k and 0.723 mA cm^{-2} of Specific Activity. The electrochemical performance in term of kinetic current and Mass Activity is 2.6 times higher than Pt/C 50 %. From Pt@SC_St20 to Pt@SC_St60 the catalytic activity decrease, Pt@SC_St60 show a lower MA and similar SA than pure platinum, (MA= 169 A g^{-1} vs. 201 A g^{-1} and 0.283 mA cm^{-2} vs. 0.273 mA cm^{-2}).

Considering $E_{1/2}$ and MA, the Pt@SC_St performance follow the next trend:

Pt@SC_St20 > Pt@SC_St5 > Pt@SC_St0 > Pt@SC_St40 > Pt/C > Pt@SC_St60

Table 14: Electrochemical results for Pt@SC_St catalysts evaluated in HClO4 0.1 M electrolyte solution.

	S_{AE}	Pt_{ICP}	$E_{1/2}$	$\Delta E_{1/2}$	i_k	EPSA	ECSA	MA	SA	Ts
	%	%	V	mV	mA	cm^2	$m^2\ g^{-1}$	$A\ g^{-1}$	$mA\ cm^{-2}$	$mV\ dec^{-1}$
Pt/C	0.75	49.2	0.867	0	0.59	2.16	73	201	0.273	59
$\Delta_{Pt/C}$	0.04	2.5	0.005	0	0.03	0.12	4	10	0.014	3
Pt@SC_St0	10.04	27.8	0.896	29	1.09	1.60	54	369	0.697	63
$\Delta_{Pt@SC\_St0}$	0.50	1.4	0.006	1	0.06	0.17	6	20	0.037	5
Pt@SC_St5	9.12	28.9	0.922	55	1.56	2.49	85	529	0.580	72
$\Delta_{Pt@SC\_St5}$	0.46	1.4	0.007	3	0.04	0.23	8	12	0.013	7
Pt@SC_St20	5.34	26.9	0.923	56	1.58	2.34	79	536	0.723	81
$\Delta_{Pt@SC\_St20}$	0.27	1.3	0.003	3	0.06	0.16	5	21	0.029	9
Pt@SC_St40	3.46	29.6	0.883	16	0.73	1.87	64	250	0.387	67
$\Delta_{Pt@SC\_St40}$	0.17	1.5	0.004	1	0.02	0.09	3	7	0.010	3
Pt@SC_St60	1.97	29.1	0.872	5	0.50	1.79	61	169	0.283	71
$\Delta_{Pt@SC\_St60}$	0.10	1.5	0.005	0	0.02	0.09	3	5	0.009	7

Table 15 show the electrochemical data obtained after the sulphuric acid washing, the treatment is crucial for remove the oxide layer around the NPs which is naturally formed during the synthesis and reduce the number of active sites for the Oxygen Reduction Reaction. The platinum content evaluated by ICP-MS, the platinum concentration is close to 30 %w, after the sulfuric acid treatment the platinum concentration decrease of 7 % due to the platinum oxide dissolution. After the Acid treatment the performance vs. ORR are increased. Pt@SC_St20/AC show an $E_{1/2}$ of 0.934 V vs RHE, 12 mV higher than the respectively untreated material, and 64 mV than Platinum commercial standard. The trend obtained after the H_2SO_4 washing is the same obtained in the previous case, from Pt@SC_St0/AC to Pt@SC_St20/AC the electrochemical performances are increased, both in term of $E_{1/2}$ from 0.906 V vs. RHE to 0.934 V vs. RHE, both in terms of MA from 551 A g^{-1} to 578 A g^{-1}. The Specific Activity decrease from Pt@SC_St0/AC to Pt@SC_St60/AC, from 0.863 cm^2 to 0.430 cm^2. The best sample in terms of Mass Activity, Specific Activity and $E_{1/2}$ results be Pt@SC_St20. From Pt@SC_St40 to Pt@SC_St60, the catalytic activity decrease. Pt@SC_St60 show a MA of 271 A g^{-1} and a $E_{1/2}$ of 0.889 V vs. RHE. Considering the XRD analysis, the electrochemical performance increase with the crystallite dimension, in fact the dimension obtained are 1.3 nm, 5.1 nm and 7.1 nm for the samples Pt@SC_St0, Pt@SC_St5 and Pt@SC_St20, respectively; for the same catalysts, the Mass Activity calculated are 551 A g^{-1}, 583 A g^{-1} and 578 A g^{-1}. The electrochemical performance increase after the oxide dissolution, the effect is crucial in Pt@SC_St0, the half wave potential and Mass Activity increase from 0.806 V vs. RHE

to 0.906 V vs. RHE and from 369 A g^{-1} to 551 A g^{-1}. The specific activity depends by the EPSA and the i_k, the resulting Specific Activity, in Pt@SC_St0/SC, calculated after the washing with H_2SO_4 is 0.863 mA cm^2, 1.5 times higher the initial value. The samples Pt@SC_St5/AC and Pt@SC_St20/AC show a very similar electrochemical performance, the sulphur reduction in Pt@SC_St20/AC than Pt@SC_St5/AC is compensated by the increment of the mesoporous surface area. The sulphur concentration and the mesoporous structure result fundamental for the NPs growing and stabilization. Pt@SC_St60 show a MA increment from 169 A g^{-1} to 271 A g^{-1} after the treatment with H_2SO_4, and $E_{1/2}$ higher of 15 mV than the untreated catalysts with a double Specific Activity.

Table 15: Electrochemical results for Pt@SC_St/AC catalysts evaluated in $HClO_4$ 0.1 M electrolyte solution

Acid Treatment	S_{AE}	Pt_{ICP}	$E_{1/2}$	$\Delta E_{1/2}$	i_k	EPSA	ECSA	MA	SA	Ts
H_2SO_4 1 M r.t.	%	%	V	mV	mA	cm^2	$m^2\ g^{-1}$	A g^{-1}	mA cm^{-2}	mV dec^{-1}
Pt/C	0.75	49.2	0.867	0	0.592	2.16	73	201	0.273	59
$\Delta_{Pt/C}$	0.04	2.5	0.005	0	0.031	0.12	4	10	0.014	3
Pt@SC_St0/AC	10.24	27.1	0.906	39	1.619	1.85	63	551	0.863	57
$\Delta_{Pt@SC\_St0/AC}$	0.51	1.4	0.008	2	0.091	0.12	4	31	0.049	3
Pt@SC_St5/AC	8.96	27.8	0.931	64	1.714	2.75	94	583	0.625	81
$\Delta_{Pt@SC\_St5/AC}$	0.45	1.4	0.005	3	0.140	0.16	5	48	0.051	9
Pt@SC_St20/AC	5.21	26.2	0.934	67	1.699	2.46	84	578	0.658	73
$\Delta_{Pt@SC\_St20/AC}$	0.26	1.3	0.008	3	0.092	0.56	19	31	0.036	8
Pt@SC_St40/AC	3.37	28.3	0.904	37	1.101	2.03	69	374	0.529	67
$\Delta_{Pt@SC\_St40/AC}$	0.17	1.4	0.007	2	0.058	0.15	5	20	0.028	3
Pt@SC_St60/AC	1.82	27.8	0.889	22	0.797	1.83	62	271	0.430	87
$\Delta_{Pt@SC\_St60/AC}$	0.09	1.4	0.005	1	0.113	0.10	3	39	0.061	9

The histogram in Figure 83 show the EPSA and the ECSA before and after the sulfuric acid treatment, a slight increment is observed for all materials. This confirm the influence on the NPs, and on the platinum oxide layer removal. An NPs dimension reduction involves an external surface area increment and an increment of the number of the active sites. Passing from Pt@SC_St5 to Pt@SC_St60, the EPSA relative increment decrease.

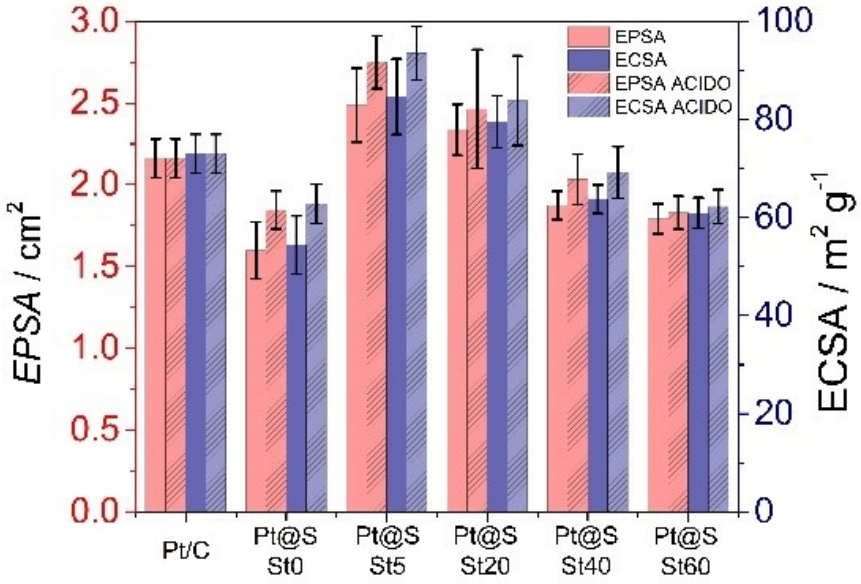

Figure 83: EPSA and ECSA for the differents Pt@S catalysts before and after the acid treatment

The histogram in Figure 84a show the relation between $E_{1/2}$ and i_k with the different samples synthetized; the Figure 84b show the histogram correlation between the MA and SA with the steam time treatment in the Pt@SC catalysts. The histograms are referred to the electrochemical value obtained in Pt@SC materials after the H_2SO_4 treatment. The catalytic activity vs. ORR, in term of $E_{1/2}$, i_k and Mass Activity before increase from Pt@SC_St0 to Pt@SC_St20 and after reducing from Pt@SC_St20 to Pt@SC_St60. Specific Activity, SA, decrease from Pt@SC_St0 to Pt@SC_St60. The Nanoparticles and crystallite dimension increase from Pt@SC_St0 to Pt@SC_St20 (from a crystallite dimension of 1.9 nm to 7 nm) and after decreases. The NPs dimensions are strong connected to the sulphur content and to the surface area (in terms of mesoporous area) obtained with the steam treatment.

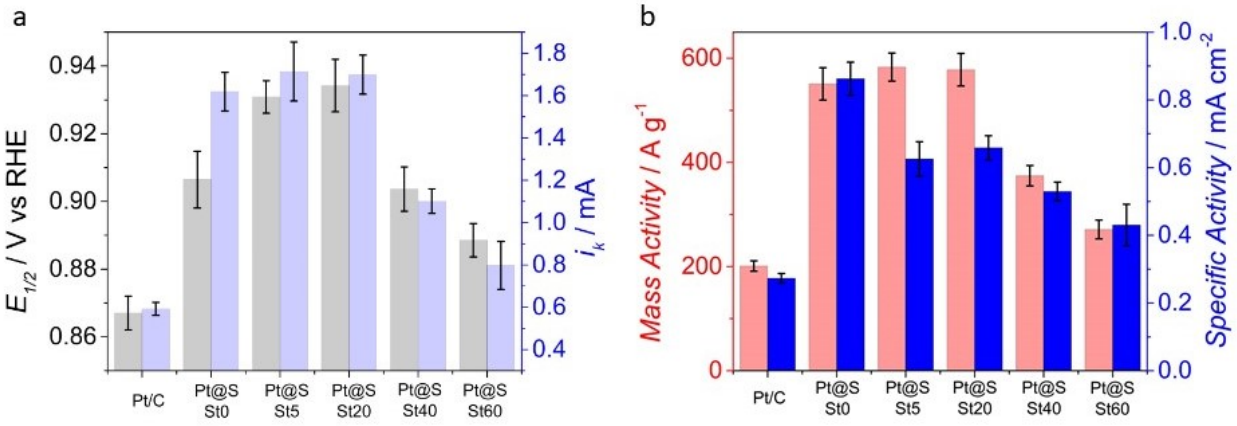

Figure 84: Histograms for a) $E_{1/2}$ and i_k and b) Mass Activity and Specific Activity for the Pt@SC_St/AC catalysts

8.3.7 Conclusion

Generally, the mesoporous carbon synthetized by hard template show a high capacitance due to the low graphitization grade, the common method for increase the conductibility such as thermal treatment cannot be applied because it caused a decrement of surface area and an increment of hydrophobicity. The decrement of surface area is a dangerous process because favourable the NPs aggregate formation, the increment of hydrophobicity makes difficult the material dispersion during the electrode preparation, and the resulting film in the electrode is in-homogeneous. A Easy method for increase the carbon conductivity is the sulphur doping, in fact a sulphur concentration of 0.2 % can increase the carbon conductivity.

The sulphur doped mesoporous carbon were synthetized by hard template method, using silica P200 as templating agent and dibenzothiophene as carbon precursor and heteroatoms source. The morphology modification was obtained treated the SC with steam at high temperature. The surface area for the different mesoporous carbon was evaluated by Nitrogen adsorption/desorption analysis at 77 K, increasing the steam treatment the surface area increases from 1103 $m^2\ g^{-1}$ to 1600 $m^2\ g^{-1}$ and the sulphur concentration decrease from 13 % to 1 %. Platinum NPs were deposited on the mesoporous carbon via high temperature solid state synthesis in a reduction atmosphere using a temperature of 300 °C for 3 h. TEM image show a good NPs distribution in the carbon support without the aggregate formation; NPs dimension increase with the decrement of the sulphur concentration and the increment of surface area. XRD analysis show a crystallite dimension increment from 1 nm to 7 nm and after a reduction. Corckendorf et all have showed how the best crystallite dimension for Pt NPs are from 6 to 9 nm. The electrochemical results have showed a great catalytic activity (536 A g^{-1} and 0.723 mA cm^2) for the sample Pt@SC_St20/AC which have the biggest crystallite, the crystallite dimensions depend both by a good compromise between the surface area (1489 $m^2\ g^{-1}$) and both the sulphur content (5.34 %). For increase the electrochemical performance the catalysts were washed with Sulphuric Acid, for remove, from the NPs, the external platinum oxide layer, in fact during the treatment 3% of Pt is loosed. After the treatment, the catalytic activity is increase, Pt@SC_St20 show a Mass Activity of 586 A g^{-1} and a Specific Activity of 0.658 mA cm^{-2}. Comparing the electrochemical result of Pt@SC catalysts with the reference Pt/C 50 %, after the acid treatment all materials have an higher catalytic activity than the standard (201 A g^{-1} and 0.283 mA cm^{-2}). The Pt@SC catalyst show a direct reduction mechanism from oxygen to water, in other word a direct 4 electron reduction. In conclusion, this study demonstrated the existence of an important metal-support interaction between sulfur doped carbon support and Pt NPs, and how this effect can influence the catalytic activity of Pt NPs towards ORR. Furthermore, it was shown that the interaction can be boosted by acting on the sulfur content, i.e., the higher the sulfur content, the stronger the interaction and hence the higher the catalytic activity.

8.4 Bibliography

[149] K.J.J. Mayrhofer, D. Strmcnik, B.B. Blizanac, V. Stamenkovic, M. Arenz, N.M. Markovic, Measurement of oxygen reduction activities via the rotating disc electrode method: From Pt model surfaces to carbon-supported high surface area catalysts, Electrochim. Acta. 53 (2008) 3181–3188. doi:10.1016/j.electacta.2007.11.057.

[150] J. Li, L. Li, M.J. Wang, J. Wang, Z. Wei, ScienceDirect Alloys with Pt-skin or Pt-rich surface for electrocatalysis, (2018) 60–67. doi:10.1016/j.coche.2018.01.006.

[151] M. Shao, Q. Chang, J. Dodelet, R. Chenitz, Recent Advances in Electrocatalysts for Oxygen Reduction Reaction, (2016). doi:10.1021/acs.chemrev.5b00462.

[152] M. Ahmadi, H. Mistry, B.R. Cuenya, Tailoring the Catalytic Properties of Metal Nanoparticles via Support Interactions, (2016). doi:10.1021/acs.jpclett.6b01198.

[153] D. Higgins, A. Hoque, M.H. Seo, R. Wang, F. Hassan, J. Choi, M. Pritzker, A. Yu, J. Zhang, Z. Chen, Development and Simulation of Sulfur-doped Graphene Supported Platinum with Exemplary Stability and Activity Towards Oxygen Reduction, (2014) 4325–4336. doi:10.1002/adfm.201400161.

[154] K. Kwon, S. Jin, C. Pak, H. Chang, S. Hoon, H. Ik, J. Hoe, J. Man, Enhancement of electrochemical stability and catalytic activity of Pt nanoparticles via strong metal-support interaction with sulfur-containing ordered mesoporous carbon, Catal. Today. 164 (2011) 186–189. doi:10.1016/j.cattod.2010.10.030.

[155] C. Liang, Z. Li, S. Dai, Mesoporous carbon materials: Synthesis and modification, Angew. Chemie - Int. Ed. 47 (2008) 3696–3717. doi:10.1002/anie.200702046.

[156] R. Brandiele, M. Zerbetto, M.C. Dalconi, G.A. Rizzi, A.A. Isse, C. Durante, A. Gennaro, Mesoporous Carbon with Different Density of Thiophenic-Like Functional Groups and Their Effect on Oxygen Reduction, ChemSusChem. 12 (2019) cssc.201901568. doi:10.1002/cssc.201901568.

[157] V. Perazzolo, C. Durante, A. Gennaro, Nitrogen and sulfur doped mesoporous carbon cathodes for water treatment, J. Electroanal. Chem. 782 (2016) 264–269. doi:10.1016/j.jelechem.2016.10.037.

[158] L. Su, W. Jia, C.-M. Li, Y. Lei, Mechanisms for Enhanced Performance of Platinum-Based Electrocatalysts in Proton Exchange Membrane Fuel Cells, ChemSusChem. 7 (2014) 361–378. doi:10.1002/cssc.201300823.

[159] Y. Garsany, J. Ge, J. St-Pierre, R. Rocheleau, K. Swider-Lyons, ORR Measurements Reproducibility Using a RRDE, ECS Trans. 58 (2013) 1233–1241. doi:10.1149/05801.1233ecst.

[160] S. Sun, F. Jaouen, J.P. Dodelet, Controlled growth of Pt nanowires on carbon nanospheres and their enhanced performance as electrocatalysts in PEM fuel cells, Adv. Mater. 20 (2008) 3900–3904. doi:10.1002/adma.200800491.

[161] S. Sun, G. Zhang, Y. Zhong, H. Liu, R. Li, X. Zhou, X. Sun, Ultrathin single crystal Pt nanowires

grown on N-doped carbon nanotubes, Chem. Commun. (2009) 7048–7050. doi:10.1039/b916080a.

[162] J.E. Park, Y.J. Jang, Y.J. Kim, M.S. Song, S. Yoon, D.H. Kim, S.J. Kim, Sulfur-doped graphene as a potential alternative metal-free electrocatalyst and Pt-catalyst supporting material for oxygen reduction reaction, Phys. Chem. Chem. Phys. 16 (2014) 103–109. doi:10.1039/c3cp54311k.

[163] D.W. Kim, O.L. Li, N. Saito, Enhancement of ORR catalytic activity by multiple heteroatom-doped carbon materials, Phys. Chem. Chem. Phys. 17 (2015) 407–413. doi:10.1039/c4cp03868a.

[164] X.H. Song, R. Xu, A. Lai, H.L. Lo, F.L. Neo, K. Wang, Preparation and characterization of mesoporous activated carbons from waste tyre, Asia-Pacific J. Chem. Eng. 7 (2012) 474–478. doi:10.1002/apj.544.

[165] R. Brandiele, C. Durante, M. Zerbetto, N. Vicentini, T. Kosmala, D. Badocco, P. Pastore, G.A. Rizzi, A.A. Isse, A. Gennaro, Probing the correlation between Pt-support interaction and oxygen reduction reaction activity in mesoporous carbon materials modified with Pt-N active sites, Electrochim. Acta. 277 (2018) 287–300. doi:10.1016/j.electacta.2018.04.182.

9 Platinum Yttrium Alloy NPs on Carbon

For reduce the economic impact and the cost of the platinum based material on the PEM-Fuel Cell cost, one solution is increasing the catalytic performance vs. the Oxygen Reduction Reaction. Increasing the activity given the possibility to reduce the amount of catalyst. One promising catalyst which show an high electrocatalytic activity vs. ORR is platinum alloy material in particular Pt_3Y alloy. Several techniques can be used for the synthesis of Pt_3Y alloy NPs. The synthesis result be difficult because yttrium is an instable element, which form easily and fastly Y_2O_3 if in the reaction environmental are present oxidant species [166, 167]. Generally, the Pt_3Y are synthetized in UHV for reduce the yttria content. The synthesis in Ultra High Vacuum have a strong limitation on the amount of catalysts that can be synthetized, in fact can be considered a micro synthesis. For increase the amount of catalysts and maintain an high platinum yttrium alloy concentration several methods were tested as solid state synthesis, dry inorganic chemistry or chemical reduction. The Platinum yttrium alloy was synthetized by solid state synthesis at high temperature, the main parameters which influence the platinum and yttrium salt reduction are the temperature, the time synthesis, platinum and salt precursors, the stoichiometric ratio between the metals but also the preparation methods of the powder precursor, for example the homogenization methods between Pt and Y salts. The solid state synthesis is an important synthesis method because fast, easy, massive, do not use solution which can contaminate the catalyst, the synthesis parameters are easily controlled, and it is an secure method [168].

The study on the synthesis parameters is crucial for evaluated the conditions which permits to obtain the Platinum Yttrium alloy with the stoichiometric ration of 3. The Pt_xY alloy formation was evaluated by XPS and XRD. The NPs dimension was analysed by TEM and SEM images. The catalysts were electrochemical tested in $HClO_4$ 0.1 M for the Oxygen Reduction Reaction, an acid post treatment for the catalytic activity increasing was tested.

9.1 Material Preparation: Bath Sonicator, Probe Sonicator and Ball Milling

The protocol for the solid state synthesis at high temperature expected before the mixing of platinum and yttrium salt precursors and after the thermal treatment for the metals' reduction. The mixing procedure in terms of homogenization is very important because the NPs distribution is directly connected to the catalytic activity. The impregnation process can be divided in two class: wet impregnation and dry impregnation. In wet impregnation the platinum and yttrium salts were, before, mixing in acetone, and after, in a second step, the carbon support was added. The metal precursors solution must entry in the carbon porosity. After the homogenization process the acetone was removed by thermal treatment in oven at 60 °C until the completely

solvent evaporation. In solid impregnation process the salts precursors and the carbon matrix were mixed without any solvent, the homogenization happens only by physical mixing. Since the homogenization is a step directly connected to the NPs size and distribution, several mixing steps were evaluated, Bath Sonicator, Probe Sonicator and Ball Milling. Bath Sonicator and Probe Sonicator were used for the wet impregnation process while Ball Milling for the dry homogenization process. The homogenization in bath Sonicator expected the salt precursors dissolution in 10 mL of acetone and the sonication in a vial for 2 h with a temperature lower than 20°C. With Probe Sonicator the platinum and yttrium salts are dispersed in 20 mL of acetone. The mixing procedure is composed by two steps, before the mixture was mixed under stirring for 20 min at 200 rpm, and after in Probe Sonicator for 10 minutes with 10 % Power. The sonication happens in an ice bath for control the temperature, the problem with Probe Sonicator are the local hot spots. In Ball Milling, the solid powder precursors (platinum precursor salt, yttrium precursor salt and carbon support) are transfer in steel jar and after ground. The procedure is divided in 4 different steps of 10 minutes each one. The vibration frequency is increase until each treatment from 10 Hz to 25 Hz. The last steps at 30 Hz expected a duration of 25 minutes. Several catalysts were synthetized with different mixing procedure.

9.1.1 Synthesis and Chemical

$Pt(acac)_2$ and $Y(NO_3)_3$ were used as platinum and yttrium salts precursors. The support used for the synthesis is the Vulcan XC-72. The carbon support owns a very high mesoporosity and a surface area of 412 $m^2\ g^{-1}$. Generally, 35 mg of $Pt(acac)_2$ are dissolute in acetone after 10 mg of $Y(NO_3)_3$ was added, finally 40 mg of carbon was added. The synthesis is developed to obtain a P_xY catalysts with a Pt loading of 27, an Yttrium loading of 3.5 % and a molar ratio of 3. The thermal treatment in furnace for the platinum yttrium salts precursors reduction expected a pre-condition (at r.t. for 1 h with a nitrogen flux of 25 sccm) for eliminate every external impurity as Oxygen, Water, Oxidizing agents or poisoning. In the second step the temperature was increased at 100 °C and the nitrogen flux was reduced to 23 sccm and 2 sccm of Hydrogen was add. This step is necessary for remove the eventually water adsorb on the powder. In the thermal reduction for these catalysts the temperature was increase to 600 °C and kept constant for 5 h. Finally, the system was cooled until room temperature, the hydrogen flux was switched off and the nitrogen concentration was increase at 25 sccm [91,168]. For evaluated the homogenaization treatment, three catalysts were synthetized, Pt_xY@C_B where is used the Bath Sonicator, Pt_xY@C_V obtained with Ball milling and Pt_xY@C_P with Probe Sonicator.

9.1.2 TEM and Absorption/Desorption N_2 Analysis: Carbon degradation and Nanoparticles aggregation

Table 16 show the conditions for the synthesis of the catalysts, the platinum content and the NPs dimension. For Pt_xY@C_B, Pt_xY@C_V and Pt_xY@C_P show a platinum concentration very similar to the theoretical value of 27 %. The synthesis conditions, 600 °C and 5 h, are the best condition for the reduction of $Pt(acac)_2$ and $Y(NO_3)_3$. Considering the platinum concentration, evaluated by ICP, is evident as the homogenization treatment do not influence the platinum amount. During pre-treatment the loss of precursor salt and therefore of metal phase was not observed. The NPs dimension increase with the following trend, as visible in the TEM image in Figure 85.

$$Pt_xY@C\_V > Pt_xY@C\_P > Pt_xY@C\_B$$

NPs dimension are obtained measurement the dimension of 500 NPs randomly distributed in the carbon surface in three different TEM images. Pt_xY@C_V show a NPs size of 7.1 nm and the formation of aggregate with high dimension, 50 nm – 60 nm. The NPs are homogeneously distributed in the carbon matrix with a constant density in all surface. Pt_xY@C_P show spherical NPs with a lower dimension, around 5.5 nm. The aggregate concertation in the carbon surface is higher than Pt_xY@C_V. Pt_xY@C_B show very small NPs with a dimensional distribution picked at 3.5 nm. The NPs have an high density distribution, the TEM images show the totally absence of aggregate or cluster [70, 84, 169].

Table 16: Synthesis condition for Pt_xY@C catalysts. Effect of the Homogenization Treatment.

	Homogenazation Treatment	Platinum Precuror	Yttrium Precursor	Temperature °C	Time h	Pt_{ICP} %	d_{NPs} nm
PtxY@C_B	Bath Sonicator	$Pt(acac)_2$	YCl_3	600	3	26.7	3.5
PtxY@C_P	Probe Sonicator	$Pt(acac)_2$	YCl_3	600	3	25.9	5.5
PtxY@C_V	Ball Milling	$Pt(acac)_2$	YCl_3	600	3	26.1	7.1

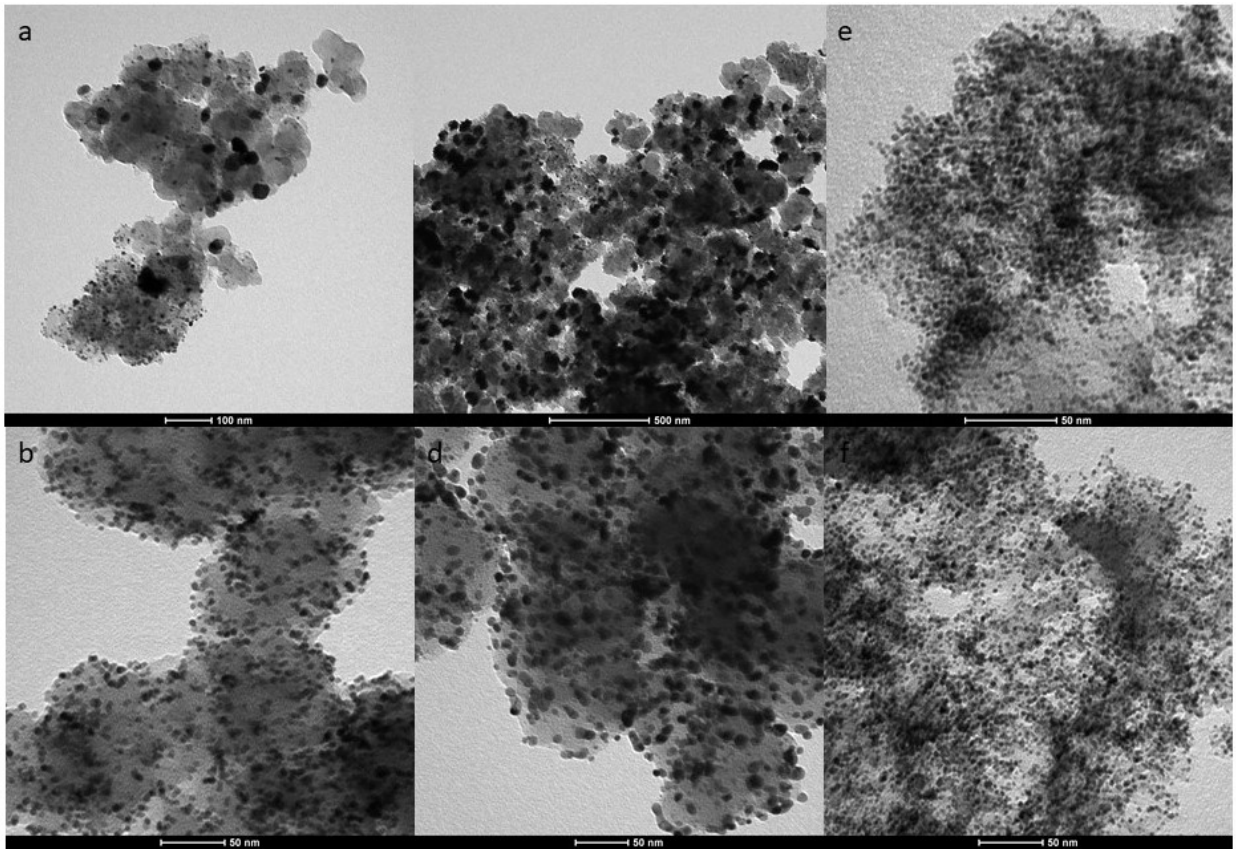

Figure 85: TEM images for the PtxY@C catalysts; a,b) Pt_xY@C_P; c,d) Pt_xY@C_V and e,f) Pt_xY@C_B

Table 17 show the morphology proprieties for the carbon support and for the different catalysts. The carbon support shows a BET surface area of 412 $m^2\ g^{-1}$ equi distributed between mesoporosity and microporosity (R_{meso} = 52.1 %), after the Pt_xY deposition with Bath Sonicator the surface area is increase at 467 $m^2\ g^{-1}$, the increment is due to the NPs deposition. The Mesoporosity ratio is increase at 61.9 %, the increment is due to the thermal treatment which influence the carbon morphology. Pt_xY@C_V (Ball Milling) shows a less increment of surface area since the TEM images show bigger NPs and the aggregated formation, the ratio S_{meso}/S_{BET} evaluated in this case is 62.1 %. When Probe Sonicator is used as homogenization treatment the resulting surface area is 124 $m^2\ g^{-1}$. The porosity is predominately microporous. The total pore volume decreases from 0.595 $cm^3\ g^{-1}$ (in the carbon support) to 0.189 $cm^3\ g^{-1}$ in Pt_xY@C_P. The decrement is observed both for the mesoporous and both for microporous volume. Pt_xY@C_B and Pt_xY@C_V show a mesoporous volume of 0.426 $cm^3\ g^{-1}$ and 0.412 $cm^3\ g^{-1}$, while a microporous volume of 0.113 $cm^3\ g^{-1}$ and 0.101 $cm^3\ g^{-1}$. The slight decrement of pore volume is due to the NPs formation inside the pore which reduce the final dimension. This explanation is valid for Pt_xY@C_V and Pt_xY@C_B, the data obtained for Pt_xY@C_P are compatible with a pore collapse. The carbon degradation is due to the high energy in the Probe Sonicator method [107].

Table 17: Nitrogen Adsorption/Desorption analysts of Pt_xY@C catalysts and the carbon support. Effect of the Homogenization Treatment.

	S_{BET}	V_{pore}	V_{micro}	V_{meso}	S_{meso}	S_{micro}
	$m^2\ g^{-1}$	$cm^3\ g^{-1}$	$cm^3\ g^{-1}$	$cm^3\ g^{-1}$	$m^2\ g^{-1}$	$m^2\ g^{-1}$
C	412	0.595	0.086	0.509	215	196
Pt_xY@C_B	467	0.426	0.113	0.313	286	181
Pt_xY@C_P	124	0.189	0.011	0.178	40	84
Pt_xY@C_V	434	0.412	0.101	0.311	273	161

Table 18 show the pore distribution for the carbon support and for the different Pt_xY catalysts. The carbon matrix shows 6 different pore distribution at ca. 1.2 nm, 3.6 nm, 5.5 nm, 7.7 nm, 9.4 nm and 10.8 nm. Pt_xY@C_P show a pore dimensional reduction for all dimensional distribution [139].

Table 18: Pore dimension distribution for Pt_xY@C catalysts and carbon support. Effect of the Homogenization Treatment.

	d_{p1}	d_{p2}	d_{p3}	d_{p4}	d_{p5}	d_{p6}
	nm	nm	nm	nm	nm	nm
C	1.2	3.57	5.46	7.73	9.41	10.73
Pt_xY@C_B	1.22	3.56	5.28	7.74	9.31	10.06
Pt_xY@C_P	1.04	2.12	5.11	6.66	8.43	13.09
Pt_xY@C_V	1.32	3.65	4.96	7.56	9.31	10.11

9.1.3 Electrochemical Characterization

The cyclic Voltammetry in Argon saturated solution at 50 mV s^{-1} and the Linear Sweep Voltammetry in Oxygen saturated electrolyte at 20 mV s^{-1} 1600 rpm are reported in Figure 86. The cyclic voltammetry shows a completely different behaviour. The Pt_xY@C_B show a well-defined PtO_x formation and stripping at 0.82 and 0.78 v vs. RHE, respectively. The hydrogen adsorption/desorption region owns a good resolution, showed the different crystallographic peak of platinum. The capacitive current obtained in Pt_xY@C_B is comparable to Pt/C commercial standard. The Pt_xY@C_V show an low EPSA both calculated with the adsorption region both with the desorption, the Pt absorption peak are not defined as in Pt_xY@C_B. The Platinum oxide reduction and the PtO_x formation peak are at the same potential 0.81 and 0.77 V vs. RHE. The capacitive current is a tenth of Pt_xY@C_B.

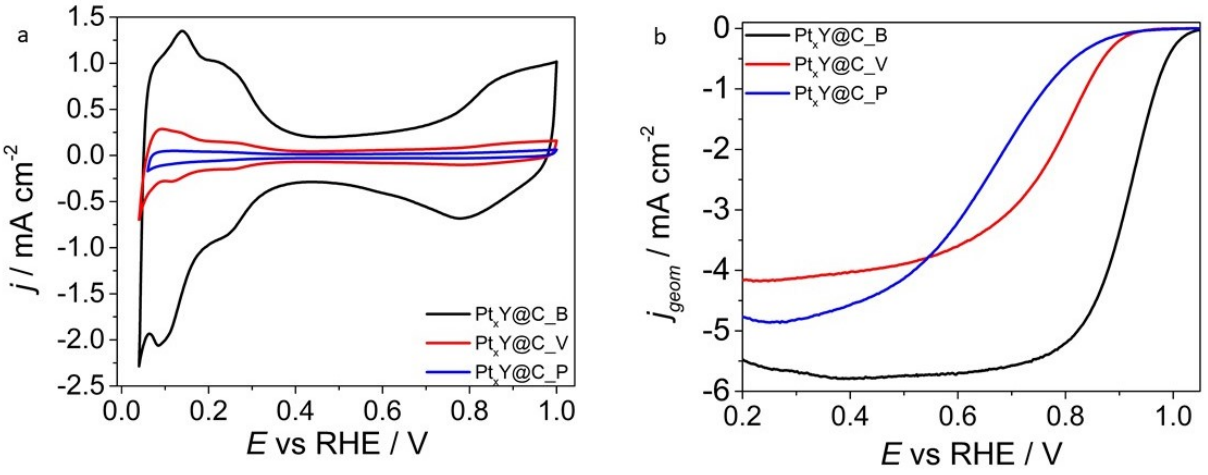

Figure 86: a) Cyclic Voltammetry in Ar saturated $HClO_4$ 0.1 M solution at 50 mV s^{-1} and b) LSV with RDE at 20 mV s^{-1} and 1600 rpm in O_2 saturated solution

The standard platinum on carbon catalysts show an EPSA of 2.06 cm^2 which correspond to an ECSA of 73.5 m^2 g^{-1}. The EPSA evaluated for Pt_xY@C_B is 2.51 cm^2, when Probe Sonicator and Ball Milling are used as homogenization process the EPSA decrease at 0.09 cm^2 in Pt_xY@C_P and 0.73 cm^2 in Pt_xY@C_V. In Pt_xY@C_P was observed the platinum detachment during the electrochemical measurement and a low electrochemical stability, in fact cycling the catalysts the current continuously to decrease. Pt_xY@C_V show a EPSA of 0.73 cm^2 and a ECSA of 24.3 m^2 g^{-1}, the problem in is the low capacitive current, the capacitive current is connected to the carbon collapse and degradation derived by the Probe Sonicator [127, 170].

Table 19: Electrochemical results for Pt_xY catalysts obtained by different homogenization treatments

	Pretreatment	***Pt_{ICP}***	***$\|j_L\|$***	***$E_{1/2}$* vs. RHE**	***i_k***	***EPSA***	***ECSA***	***MA***	***SA***
		%	mA cm^{-2}	V	mA	cm^2	m^2 g^{-1}	A g^{-1}	mA cm^{-2}
Pt_xY@C_B	Bath Sonicator	26.7	5.77	0.893	1.76	2.51	85.4	598.3	0.701
$\Delta_{PtxY@C}$		0.2	0.11	0.006	0.07	0.12	4.1	23.8	0.010
Pt_xY@C_P	Probe Sonicator	25.9	4.67	0.651	0.024	0.09	3.1	8.2	0.268
$\Delta_{PtxY@C}$		0.3	0.23	0.011	0.003	0.01	0.3	1.0	0.034
Pt_xY@C_V	Ball Milling	26.1	4.10	0.781	0.043	0.73	24.8	14.8	0.059
$\Delta_{PtxY@C}$		0.1	0.20	0.008	0.003	0.08	2.7	1.0	0.012

The electrochemical activity for ORR was evaluated with Linear Sweep Voltammetry at 20 mV s^{-1} and 1600 rpm, in anodic scan. The catalyst synthetized with bath Sonicator show a very high $E_{1/2}$ and Mass Activity. The Half wave potential is higher of 28 mV than platinum on carbon, Pt_xY@C_B show a Mass Activity of 598 A g^{-1}, 2.1 times higher than Pt/C. The Catalytic Activity is connected to the Platinum alloy formation and to the good Pt_xY NPs distribution. The TEM images shows a size of 3.5 nm, without the cluster formation and the platinum yttrium alloy formation was evaluated by XPS and result be 41 %. The Mass Activity obtained

in Pt_xY@C_P and Pt_xY@C_V are 2.1 A g^{-1} and 24.8 A g^{-1}. The linear Sweep voltammetry do not show a constant density current limit in the usual potential range, 0.6 V vs. RHE and 0.2 V vs. RHE. The specific activity obtained in Pt_xY@C_P is due to the low EPSA obtained, while the SA evaluated in Pt_xY@C_V is 4 times lower than Pt/C [171, 172].

The low catalytic performance obtained are connected to the carbon degradation in Pt_xY@C_P and to the aggregate formation in Pt_xY@C_V. The carbon degradation shows a strong impact on the final electrochemical performance, the decrement of conductibility, the pore dimension reduction and the pore collapse are responsible to the low kinetic during the Oxygen Reduction Reaction. For increase the electrochemical performance the catalysts were treated in H_2SO_4 1M under stirring at room temperature for 30 minutes. The treatment is used for removing all impurities and the oxide layer of platinum and/or yttrium which are present in the external surface of the NPs. XPS analysis was used for evaluated the Pt_xY alloy concentration in the catalysts after the treatment. Table 20 show the platinum and yttrium concentration of the different oxidation state for the different catalysts. In Pt_xY@C_B the platinum (0) concentration increase after the acid treatment, the same trend was observed for Pt_xY@C_P. and Pt_xY@C_V. A Pt(II) and Pt(IV) decrement was observed for all catalysts. However, XPS show a similar platinum content, ca. 65 %. The Platinum yttrium alloy content evaluated ad metal Y at 156.3 eV decrease after the acid treatment. Pt_xY@C_B show a Pt_xY concentration of 41 % while after the treatment with sulphuric acid of 39.5 %. The Platinum yttrium alloy amount evaluated in the Pt_xY@C_P and Pt_xY@C_V is very low, 1.2 % and 3.4 %, respectively. After the treatment, XPS show a Pt_xY concentration for Pt_xY@C_P of 5 % while for Pt_xY@C_V of 7.9 %.

Table 20: Pt 4f and Y 3d concentration for Pt_xY@C catalysts

		71.0 eV Pt(0) %	72.4 eV Pt(II) %	74.9 eV Pt(IV) %	156.3 eV Y(0) %	156.9 eV Y_2O_3 %	157.7 eV Y-Carbide %
Pt_xY@C_B	Bath Sonicator	63	21	16	41	34	25
Pt_xY@C_B_A	Bath Sonicator	66.1	19.3	14.6	39.5	60.5	0
Pt_xY@C_P	Probe Sonicator	52.4	14.9	32.7	1.2	64.7	34.1
Pt_xY@C_P_A	Probe Sonicator	69.2	17.4	13.4	5	45.3	49.7
Pt_xY@C_V	Ball Milling	64.2	18.7	17.1	3.4	57.8	38.8
Pt_xY@C_V_A	Ball Milling	67.9	18.2	13.9	7.9	52.5	39.6

Figure 87 show the XPS spectra for the catalysts after the sulphuric acid treatment. Interesting is the decrement of yttrium oxide due the dissolution in the acid solution and the increment of the yttrium carbide concentration. The XPS show also C 1s and O 1s, the concentration of the element evaluated are 85 % and 15 %, the component evaluated by the fitting are the same before and after the acid treatment.

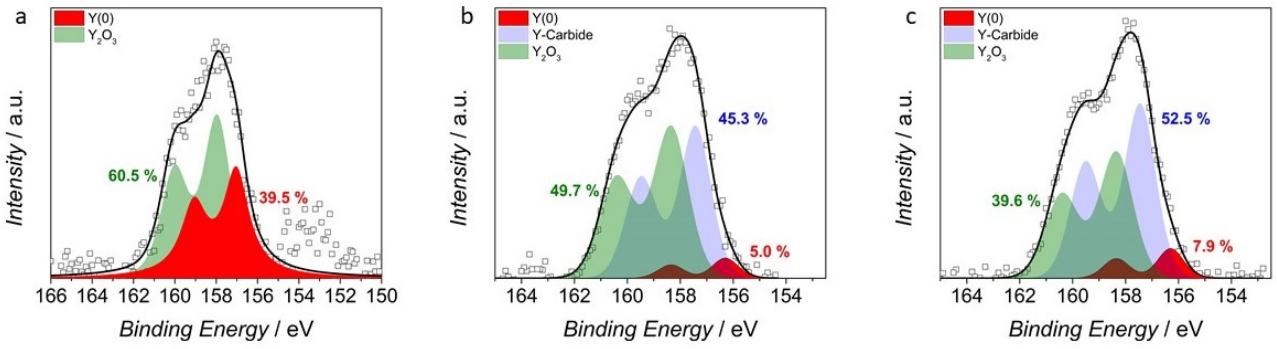

Figure 87: XPS Y 3d spectra of Pt_xY catalysts; a) Pt_xY@C_B; b) Pt_xY@C_P and c) Pt_xY@C_V

The impact of the sulfuric acid on the metal particles is, also, confirmed by the ICP-MS, after the acid treatment the platinum concentration is reduced by 20 %. Pt_xY@C_B before the acid treatment show 26.7 % of metallic platinum while after the acid washing of 24.9 %. The same trend is observed for Pt_xY@C_V and Pt_xY@C_P, the final platinum amount is 23.9 % and 22.1, respectively. The Electrochemical Platinum Surface Area is increased after the H_2SO_4 treatment, in Pt_xY@C_B the increment is lower than Pt_xY@C_V and Pt_xY@C_P. In Pt_xY@C_B, the EPSA pass from 2.51 cm^2 to 2.64 cm^2. The relatives ECSA, calculated considering the platinum loading, are 85.4 $m^2\ g^{-1}$ and 89.8 $m^2\ g^{-1}$, respectively. For Pt_xY@C_P and Pt_xY@C_B the EPSA after the H_2SO_4 treatment result be 0.19 cm^2 and 0.94 cm^2. H_2SO_4 treatment influence the NPs dimension and consequently the Hydrogen adsorption/desorption region, the treatment does not appear any influence on the capacitive current [173, 174, 175].

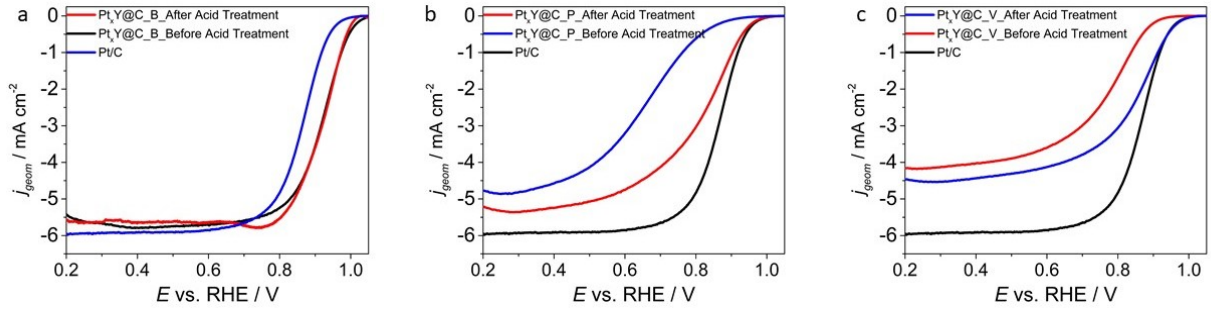

Figure 88: LSV with RDE at 1600 rpm and 20 mV s^{-1} in O_2 saturated $HClO_4$ electrolyte solution for a) Pt_xY@C_B; b) Pt_xY@C_P and c) Pt_xY@C_V

Figure 88 show the Linear Sweep Voltammetry recorded in the standard conditions for Pt/C, the different catalysts before and after the acid treatment. The catalysts Pt_xY@C_B_A and Pt_xY@C_B shows very similar electrochemical results, the $E_{1/2}$ is slight increased from 0.912 V vs. RHE to 0.918 V vs. RHE. Considering the error calculated by the different LSV with RDE, the kinetic current is the same for all two catalysts. The same consideration can be applied on Mass Activity and Specific Activity. The MA calculated before the acid treatment for Pt_xY@C_B is 598 A g^{-1} while for Pt_xY@C_B_A result be 624 A g^{-1}. The Specific Activity evaluated for the Pt_xY@C_B and Pt_xY@C_B_A are 701 µA cm^{-2} and 695 µA cm^{-2}. Pt_xY@C_P_A show an

higher electrochemical performance than Pt_xY@C_P. The $E_{1/2}$ is increased of 170 mV after the acid treatment, Pt_xY@C_P_A show a half wave potential of 0.823 V vs. RHE. The kinetic current pass from 0.09 mA to 0.23 mA. The MA obtained in Pt_xY@C_P_A is 3 times higher than Pt_xY@C_P. Interesting is the reduction of the resistivity of the material, in fact a limited current is observed at higher potential respect Pt_xY@C_P, the slope in the mixed electron transfer is higher. PtxY@C_V show the same previous trend, in fact the electrochemical activity in terms of $E_{1/2}$, i_k and Mass Activity is increased after the acid treatment. Pt_xY@C_V_A show an Half Wave Potential, a kinetic current and a Mass Activity of 0.864 V vs. RHE, 0.35 mA and 119 A g^{-1}.

Table 21: Electrochemical Results for Pt_xY@C catalysts before and after the acid treatment. Effect of the Homogenization Treatment.

	Treatment	***Pt$_{ICP}$***	***|j$_L$|***	***E$_{1/2}$* vs. RHE**	***i$_k$***	***EPSA***	***ECSA***	***MA***	***SA***
		%	mA cm^{-2}	V	mA	cm^2	m^2 g^{-1}	A g^{-1}	mA cm^{-2}
PtxY@C_B	Bath Sonicator	26.7	5.77	0.912	1.76	2.51	85.37	598.64	0.701
$\Delta_{PtxY@C}$		0.2	0.11	0.006	0.07	0.12	4.08	23.81	0.010
PtxY@C_B_A	Bath Sonicator	24.9	5.64	0.918	1.84	2.64	89.80	624.30	0.695
$\Delta_{PtxY@C}$	Acid Treatment	0.1	0.14	0.009	0.09	0.13	4.42	30.61	0.009
PtxY@C_P	Probe Sonicator	25.9	4.67	0.651	0.02	0.09	3.06	8.16	0.267
$\Delta_{PtxY@C}$		0.3	0.23	0.011	0.00	0.01	0.34	1.02	0.034
PtxY@C_P_A	Probe Sonicator	22.1	5.35	0.823	0.26	0.19	6.46	87.09	1.348
$\Delta_{PtxY@C}$	Acid Treatment	0.1	0.18	0.007	0.09	0.05	1.70	30.61	0.014
PtxY@C_V	Ball Milling	26.1	4.10	0.781	0.04	0.73	24.83	14.63	0.059
$\Delta_{PtxY@C}$		0.1	0.21	0.008	0.00	0.08	2.72	1.02	0.012
PtxY@C_V_A	Ball Milling	23.9	4.46	0.864	0.35	0.94	31.97	119.68	0.374
$\Delta_{PtxY@C}$	Acid Treatment	0.2	0.13	0.006	0.11	0.11	3.74	37.41	0.031

Figure 89 show the TEM images for the Pt_xY NPs before and after the acid treatment. Pt_xY@C_B show a slight size reduction from 3.5 nm to 3.3 nm; the population density is equal for Pt_xY@C_B and Pt_xY@C_B_A. The situation is very different in Pt_xY@C_V and Pt_xY@C_P. In Pt_xY@C_V the NPs density increase after the acid treatment, Pt_xY@C_V_A shows a reduction of the aggregates' number. The NPs dimension pass from 7.1 nm to 6.7 nm. Finally, the Pt_xY@C_P show a drastically reduction of the number of NPs, the NPs dimension remain unchanged, but is visible a reduction of cluster or big partiles with a dimension higher than 12 nm.

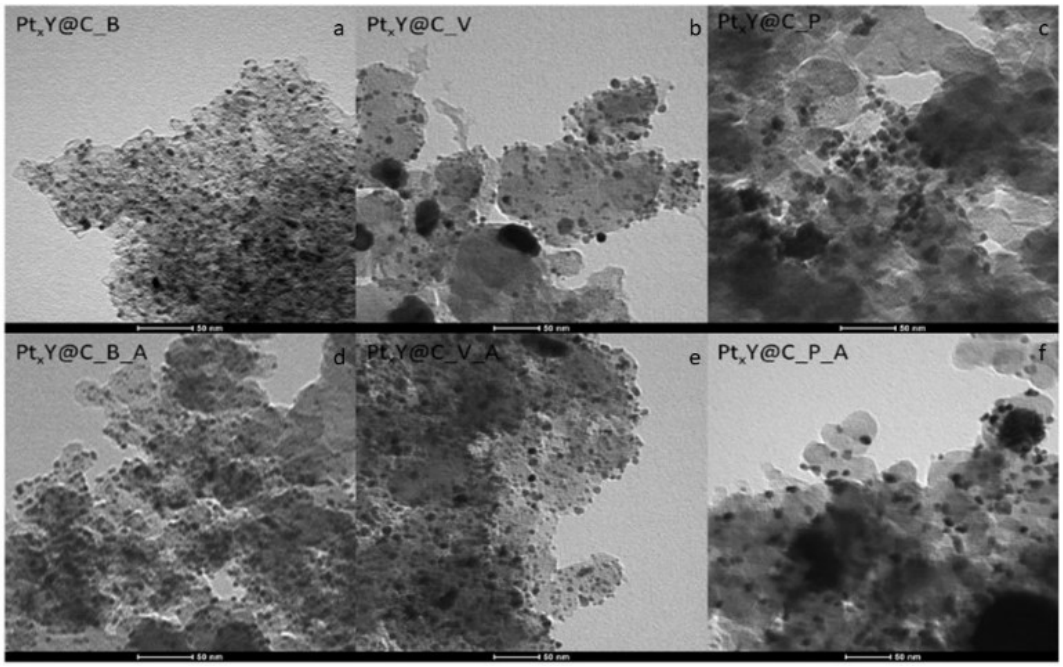

Figure 89: TEM images for a) Pt_xY@C_B: b) Pt_xY@C_B; c) Pt_xY@C_P; d) Pt_xY@C_B_A; e) Pt_xY@C_V_A and f) Pt_xY@C_P_A

9.1.4 Conclusion

The Pt@Y NPs were synthetized using different homogenization treatment for the metal precursors, bath Sonicator, Probe Sonicator and Ball Milling. The different homogenization technique shows a strong impact on the alloy formation, on the NPs size/distribution, on the carbon morphology and on the resulting electrochemical activity. The catalysts were synthetized with solid state synthetises in reduction atmosphere using the same condition and the same precursors, $Pt(acac)_2$, YCl_3 at a temperature of 600 °C for 3 h. When Bath Sonicator is used for mixing the platinum, yttrium and carbon precursors, the resulting NPs are good distributed in the carbon matrix and show a very arrowed NPs distribution picked at 3.5 nm. The XPS show an high Pt_xY alloy content, 41 %. With Probe Sonicator and Ball milling, the NPs show an higher dimension at 5 and 7 nm, respectively; and the aggregates formation. With Probe Sonicator, nitrogen absorption/desorption analysis show a carbon pore collapse and a drastically decrement of surface area, while in Pt_xY@C_B and Pt_xY@C_V the surface area increases respect the carbon support for the NPs formation. The alloy content is less than 10 % in Pt_xY@C_P and Pt_xY@C_V. Pt_xY@C_B show a high Mass Activity, 598 A g^{-1}, 2 times higher than platinum on carbon. The electrochemical activity for Pt_xY@C_P and Pt_xY@C_V is very low; the mass activity is lower than 20 A g^{-1} and the $E_{1/2}$ is lower than platinum on carbon of 150 mV. The best homogenization treatment for mixed the precursors result be the Bath Sonicator. For increase the catalysts activity, the catalysts were treated with H_2SO_4, for remove the metal oxide from the NPs surface. After the acid treatment the electrochemical performance increase but only for Pt_xY@C_P and Pt_xY@C_V. in Pt_xY@C_B the acid treated do not have effect on the electrochemical proprieties, the Mass Activity increase slight respect the untreated sample [166, 168, 171].

9.2 Influence of Platinum and Yttrium salt precursors on platinum yttrium alloy formation

Platinum yttrium alloy NPs with a stoichiometry 3 to 1 have an incredible electrochemical activity vs. ORR. Chorchendorff and Stephen have synthetized the platinum yttrium alloy in UHV, through pure metals sputtering with an alloy formation of 72 % evaluated in situ by XPS. The resulting material was tested, in situ, as catalyst in Oxygen Reduction, the electrochemical measurement showed an Mass Activity of 3000 A g^{-1} and a Specific Activity of 1.45 mA cm^{-2}. The actual research is focused on the synthesis of Pt_3Y alloy NPs with a very arrow dimension distribution. For a real utilization of this material, the synthesis must be massive, easy, rapid and the catalyst must preserve its incredible activity. The solid state synthesis is a good solution for these requests. The main parameters which influence Platinum Yttrium alloy formation and NPs dimension in this kind of synthesis are: the platinum and yttrium precursors, the temperature and the time. In this chapter the Platinum yttrium alloy was synthetizes by solid reduction at high temperature. For understand the influence of the yttrium precursors on the alloy formation several yttrium precursor salts were tested. As platinum precursor, $Pt(acac)_2$ was used; Platinum acetylacetonate result be the best platinum salt precursors because owns a low sublimation temperature, 198 °C, and a low reduction potential. Perazzolo et all. show as platinum (II) acetylacetonate can being easy reduced in hydrogen atmosphere to metallic platinum, and the resulting NPs owns a dimension in the range 6 nm to 9 nm [134, 135, 167].

9.2.1 Synthesis and Chemical

Figure 90 shows the thermogravimetric analysis for platinum (II) acetylacetonate and 5 different yttrium precursors, yttrium (III) acetylacetonate, Y (III) acetate, Y (III) nitrate, Y (III) chloride and Y (III) trifluoromethansulphonate. The TGA was recorded in a nitrogen atmosphere with a temperature ramp of 1°C min^{-1} from 100 °C to 750 °C. Before starting the analysis, the temperature is kept constant for 15 minutes at 100 °C for desorb any impurities from the precursor salt. The TGA is necessary for understand the better temperature to applied during the platinum yttrium synthesis. Platinum (II) acetylacetonate show only one peak at 198 °C and the residual after the peak is 0 % (black line). $Pt(acac)_2$ sublime at temperature higher than 198 °C. The yttrium salts precursors show different degradation peak at different temperature which correspond to the ligands' degradation, the residual generally obtained at temperature higher than 600 °C are associated to a mixture of metallic yttrium and yttria.

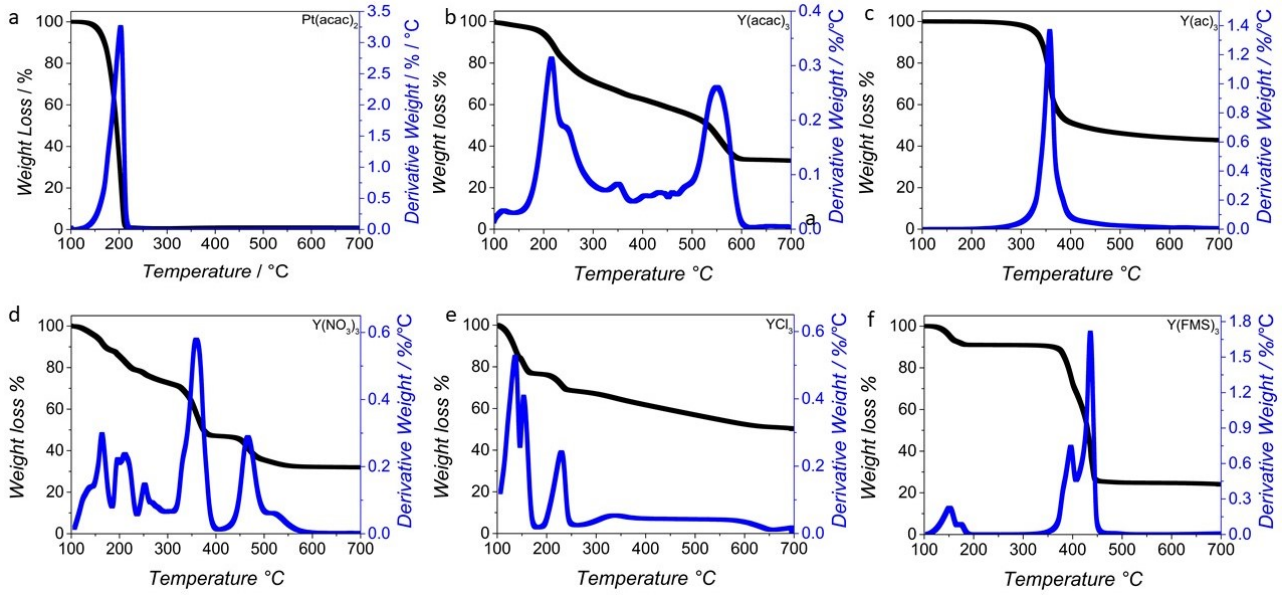

Figure 90: Thermogravimetric analysis for a) $Pt(acac)_2$; b) $Y(acac)_3$; c) $Y(ac)_3$; d) $Y(NO_3)_3$; e) YCl_3 and f) $Y(FMS)_3$

Yttrium acetylacetone shows four different degradation temperature at 214 °C, 249 °C, 348 °C and 350 °C; the residual evaluated at 616 °C is 33.46 % and can be explained by a mixture of 55% of yttrium (0) and 45 % of yttria. The degradation of yttrium (III) acetate happens at 357 °C, and the residual can be calculated at a temperature of 539 °C and correspond to a mixture of of 68 % of Y (0) and 32 % if Y_2O_3. Yttrium nitrate show different degradation peak, the nitrate degradation is a very complex process. For $Y(NO_3)_3$ is possible individuate six different temperature, 162 °C, 196 °C, 211 °C, 252 °C, 359 °C and 466 °C. The residual at 572 °C correspond to 100 % of Y (0). Yttrium (III) chloride show three different peaks associated to the chloride ligand losses. The TGA show the degradation peaks at 136 °C, 153 °C and 228 °C. From 337 °C to 627 °C, the salt shows a constant mass decrement from 68 % to 54%. The residual can be calculated at 652 °C as a mixture of 86 % of elemental yttrium and 14 % of yttrium oxide. $Y(FMS)_3$ show two couples of degradation peaks at 150 °C, 156 °C and a second one at 396 °C and 435 °C. The residual is 24.77 % and start from 461 °C, the residual value obtained can be associated to 60 % of yttrium (0) and 40 % of yttrium oxide [176, 177, 178].

Table 22: Synthesis condition and platinum/ yttrium concentration evaluated by ICP-MS

	Platinum Precursor	Yttrium Precursor	Time h	Temperature °C	Pt^{theor} %	Pt^{ICP} %	$\%Y^{theor}$ %	$\%Y^{ICP}$ %	Pt/Y -
PtxY1@C	$Pt(acac)_2$	$Y(ACAC)_3$	5	348	26.4	20.6	4.0	2.7	3.5
PtxY2@C	$Pt(acac)_2$	$Y(AC)_3$	5	357	26.0	23.0	4.2	3.2	3.8
PtxY3@C	$Pt(acac)_2$	$Y(NO_3)_3$	5	600	26.2	20.9	4.1	2.6	3.7
PtxY4@C	$Pt(acac)_2$	YCl_3	5	228	26.3	23.4	4.2	1.8	5.9
PtxY5a@C	$Pt(acac)_2$	$Y(FMS)_3$	5	396	25.9	22.0	4.1	3.4	3.0
PtxY5b@C	$Pt(acac)_2$	$Y(FMS)_3$	5	496	26.3	15.0	4.3	4.0	1.7

Table 22 show the different synthesis temperature used for the different yttrium precursors. The temperature used for the synthesis is the starting residual temperature, at this value the ligand degradation is complete. Platinum acetylacetonate is adopted as platinum precursor and a reduction time of 5 hours in tubular furnace was used. The platinum and yttrium amount were evaluated by ICP-MS.

9.2.2 TEM Analysis: NPs dimension and distribution

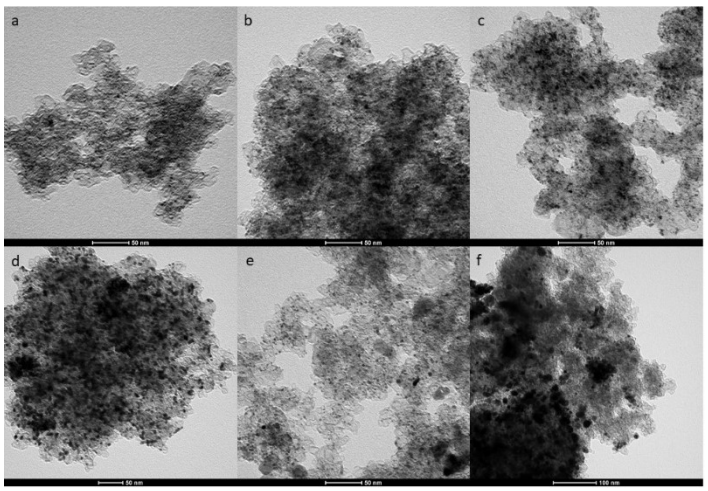

Figure 91: TEM images of a) Pt_xY1@C; b) Pt_xY2@C; c) Pt_xY3@C; d) Pt_xY4@C; e) Pt_xY5a@C and f) Pt_xY5b@C

Figure 91 show the TEM image for the samples obtained by the different yttrium salts precursors and Figure 92 show the NPs dimension distribution.. The support used for the deposition is a common commercial mesoporous carbon black with a surface area of 264 m^2 g^{-1} and without a microporosity network. Pt_xY1@C and Pt_xY2@C shows a good NPs distribution with a similar size, without an aggregate or cluster formation. In Pt_xY3@C, the NPs have a higher dimension than the catalysts obtained with $Y(acac)_3$ and $Y(ac)_3$; 2.85 nm, 1.58 nm and 2.18 nm, respectively. The situation changes drastically in Pt_xY4@C, the NPs tend to aggregate, TEM images show particles with a dimension of 20 nm. Pt_xY5a@C show a sporadic NPs distribution on the mesoporous carbon with the formation of aggregates, the aggregates formation increases when the temperature synthesis was increased at 496 °C. The NPs dimension follow the next trend:

$$Pt_xY4@C > Pt_xY3@C > Pt_xY5b@C > Pt_xY2@C > Pt_xY5a@C > Pt_xY1@C$$

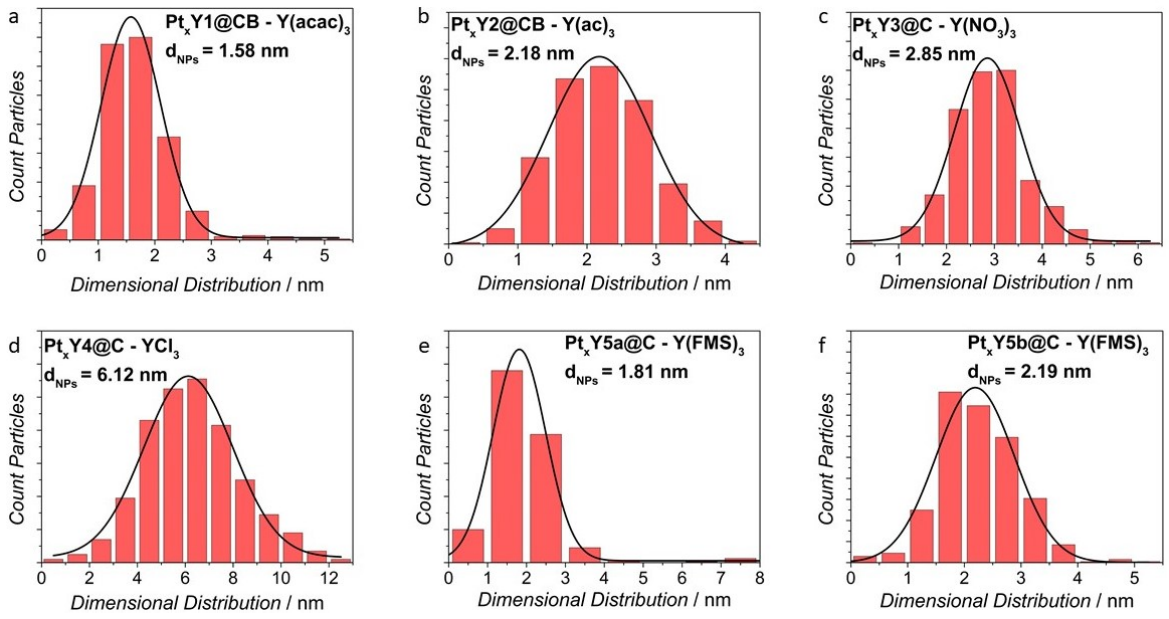

Figure 92: NPs dimensional distribution for a) Pt_xY1@C; b) Pt_xY2@C; c) Pt_xY3@C; d) Pt_xY4@C; e) Pt_xY5a@C and f) Pt_xY5b@C

9.2.3 XPS analysis, alloy formation

The alloy formation was evaluated and calculated by XPS, the platinum yttrium alloy content was connected to the amount of metallic yttrium in alloy form, at 156.3 eV. XPS confirm the presence of platinum alloy in all catalysts with different concentration, Figure 93. The temperature used for the synthesis permits the degradation of the yttrium's ligand, so favour the yttrium (III) reduction to yttrium (0). The yttrium content in alloy form follows the next trend:

$$Pt_xY3@C > Pt_xY1@C > Pt_xY2@C > Pt_xY5b@C > Pt_xY4@C > Pt_xY5a@C$$

The best sample in terms of yttrium metallic in alloy form is Pt_xY3@C, synthetized with $Y(NO_3)_3$ at 600 °C, XPS shows an yttrium content of 67 %, respect the total yttrium. Pt_xY1@C and Pt_xY2@C shows an Pt_xY content of 37 % and 31 %. The samples obtained with YCl_3 and $Y(FMS)_3$ at 396 °C and 496 °C show a yttrium alloy content lower than 25 % (19 %, 9 % and 23 %, respectively). The Y *3d* spectra were fitted with only two components at 156.3 eV and 171.1 eV, which correspond to yttrium (0) and yttria. The Pt *4f* spectra is very similar for each catalyst, a band shift in the platinum spectra is difficult to revealed due to the NPs dimension. The Table 23 show the platinum and yttrium content [91, 179, 180].

Table 23: XPS analysis of Pt 4f and Y 3d peaks, Platinum and Yttrium concentration

	Pt(0)	Pt(II)	Pt(IV)	Y(0)	Y(III)	Pt/Y
	%	%	%	%	%	-
Pt_xY1@C	70	19	11	37	63	3.94
Pt_xY2@C	62	27	11	31	69	2.93
Pt_xY3@C	65	21	14	67	33	3.42
Pt_xY4@C	69	26	5	19	81	4.13
Pt_xY5a@C	59	31	10	9	91	5.10
Pt_xY5b@C	53	37	10	23	77	2.85

Platinum metallic content is in the range 60 % - 70 % for all catalysts, except in PtxY5@C which shows a platinum (0) amount lower than 60%. The platinum yttrium ratio obtained in Pt_xY@2 and Pt_xY@C3 is close to 3. The stochiometric ratio is connected to a mixture of different alloy, Pt_2Y, Pt_3Y and Pt_4Y.

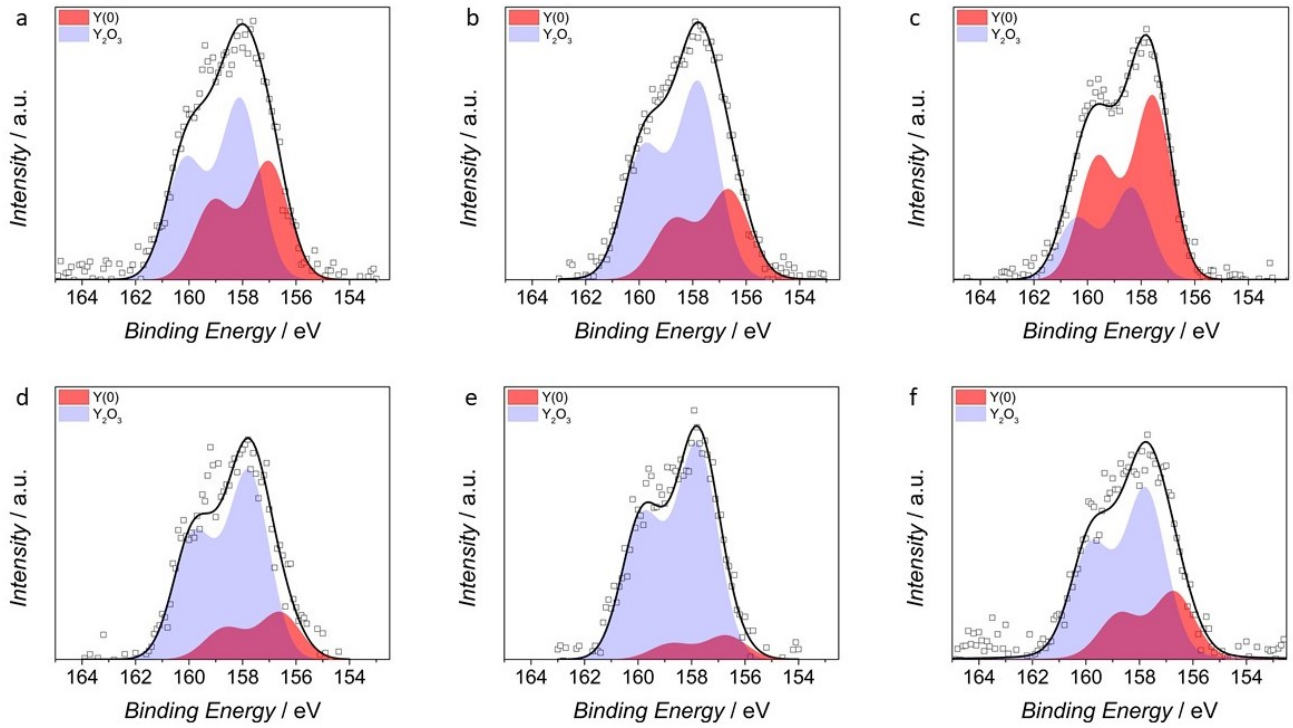

Figure 93: XPS spectra of Y 3d component for a) Pt_xY1@C; b) Pt_xY2@C; c) Pt_xY3@C; d) Pt_xY4@C; e) Pt_xY5a@C and f) Pt_xY5b@C

9.2.4 Electrochemical Characterization

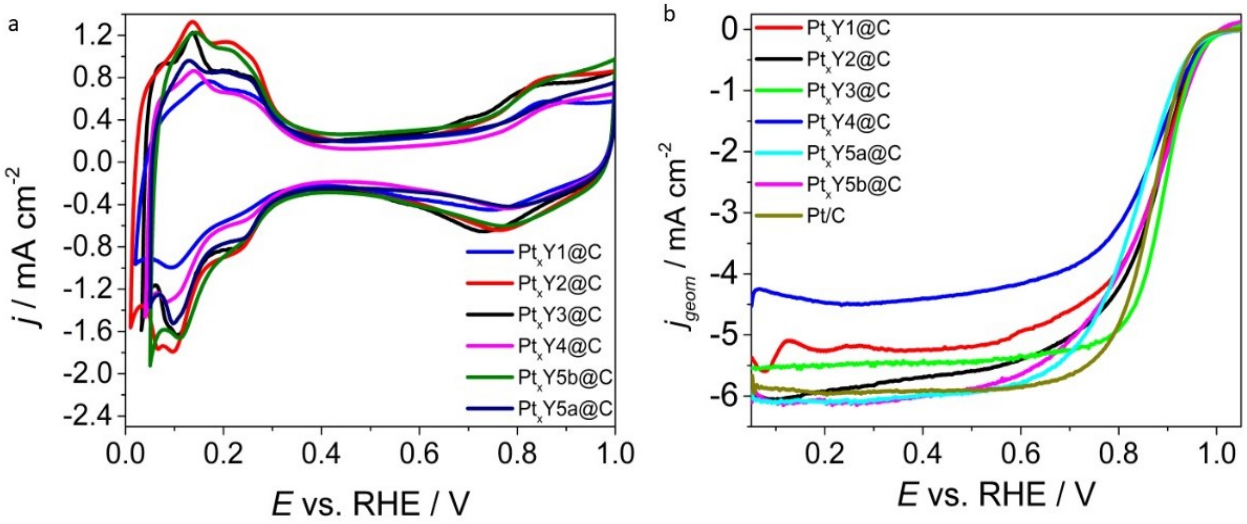

Figure 94: a) Cyclic Voltammetry at 50 mv s^{-1} in Ar saturated $HClO_4$ solution and b) LSV with RDE at 1600 rpm and 20 mV s^{-1} in O_2 saturated $HClO_4$ 0.1 M electrolyte

Figure 94a show the cyclic voltammetry recorded in Argon saturated $HClO_4$ solution at 50 mV s^{-1}. The cyclic voltammetry shows the typical regions of capacitive current and the platinum oxide formation/reduction obtained in a platinum based material. The hydrogen zone shows the typical platinum peaks, corresponding to the different crystallographic faces in which the hydrogen can easily adsorbed. EPSA were calculated considering only the hydrogen desorption area. $Pt_xY2@C$ and $Pt_xY3@C$ shows an EPSA higher than commercial platinum, 2.51 cm^2 and 2.25 cm^2, respectively. TEM images revealed NPs dimension for $Pt_xY4@C$ of 6.18 nm, the corresponding EPSA and ECSA are 1.50 cm^2 and 51 m^2 g^{-1}. In $Pt_xY5@C$ increasing the synthesis temperature, the NPs increase their dimension; the corresponding EPSA, instead, increase reducing the temperature; from 1.55 cm^2 to 1.93 cm^2. The errors associated to the EPSA and ECSA are calculated by standard deviation of nine different measurement.

Table 24: Platinum loading and the electrochemical results for Pt_xY catalysts

Y	***T***	***Pt_{ICP}***	***EPSA***	***ECSA***
	°C	$\%_w$	cm^2	m^2 g^{-1}
		49.1 ± 1.2	2.16 ± 0.12	73.5 ± 4.1
$Y(ACAC)_3$	600	25.9 ± 0.6	1.18 ± 0.09	40.0 ± 3.0
$Y(AC)_3$	400	26.0 ± 0.7	2.51 ± 0.18	85.3 ± 6.0
$Y(NO_3)_3$	600	28.1 ± 0.7	2.25 ± 0.09	76.5 ± 3.2
YCl_3	400	28.1 ± 0.7	1.50 ± 0.11	51.0 ± 3.7
$Y(FMS)_3$	400	23.7 ± 0.2	1.55 ± 0.01	52.9 ± 0.5
$Y(FMS)_3$	600	21.9 ± 0.4	1.93 ± 0.16	65.6 ± 5.6

Figure 94b shows the linear sweep voltammetry recorded at 20 mV s^{-1} in Oxygen saturated solution. Table 25 show the electrochemical value obtained, and the Mass Activity and Specific Activity for the different catalysts. Considering the Mass Activity and the $E_{1/2}$, the catalytic activity follow the next trend;

$$Pt_xY3@C > Pt_xY1@C > Pt/C > Pt_xY2@C > Pt_xY5b@C > Pt_xY5a@C > Pt_xY4@C$$

The best sample is $Pt_xY3@C$, which show a Mass Activity of 525 A g^{-1} and a $E_{1/2}$ higher than 40 mV respect the standard platinum on carbon. The electrochemical performances confirm the higher catalytic activity of platinum yttrium alloy than the pure platinum. The Specific activity obtained is two times than the Pt/C, 0.687 mA cm^{-2} and 0.274 mA cm^{-2}, respectively. $Pt_xY1@C$ and $Pt_xY2@C$ show a very similar electrochemical performances, in terms of $E_{1/2}$ (0.874 V vs. RHE and 0.871 V vs. RHE) and MA (206 A g-1 and 192 A g-1). The low Mass Activity obtained in $Pt_xY5a@C$ and $Pt_xY5b@C$ is connected to the bad NPs distribution in the carbon support, to the aggregate formation and to the low concentration of yttrium in alloy form. The high EPSA is connected to the second NPs population with a dimension of 2 nm. $Pt_xY4@$ C show an low kinetic current, the half wave potential is lower than Pt/C, the NPs dimensional is in good correlation with several articles in which show as 6 nm – 9 nm are the best dimension for Pt_3Y alloy NPs.

Table 25: Electrochemical results for PtxY@C catalysts, Effect of the yttrium salt precursor

	$\|j_L\|$	$E_{1/2}$ **vs. RHE**	i_k	***MA***	***SA***
	mA cm^{-2}	V	mA	A g^{-1}	mA cm^{-2}
Pt/C	5.94 ± 0.14	0.867 ± 0.005	0.59 ± 0.01	201 ± 3	0.274 ± 0.019
PtxY1@C	5.22 ± 0.09	0.874 ± 0.005	0.61 ± 0.04	206 ± 13	0.515 ± 0.072
PtxY2@C	5.92 ± 0.15	0.871 ± 0.007	0.57 ± 0.03	192 ± 10	0.225 ± 0.027
PtxY3@C	5.46 ± 0.27	0.891 ± 0.009	1.54 ± 0.08	525 ± 26	0.687 ± 0.063
PtxY4@C	4.18 ± 0.21	0.860 ± 0.006	0.29 ± 0.01	100 ± 5	0.195 ± 0.024
PtxY5a@C	6.10 ± 0.12	0.829 ± 0.007	0.32 ± 0.01	107 ± 4	0.203 ± 0.009
PtxY5b@C	6.10 ± 0.14	0.855 ± 0.003	0.52 ± 0.01	176 ± 5	0.268 ± 0.030

9.2.5 Conclusion

Several catalysts were synthetized with different yttrium precursors, the synthesis temperature was modified in reference to the TGA of the yttrium salts. The time synthesis and the platinum precursor are the same for each sample, 5 h and $Pt(acac)_2$. TEM images show the formation of NPs with a dimension lower than 3 nm, expect in the synthesis with YCl_3, where the dimensional distribution is picked at 6 nm. The electrochemical activity is in good correlation with the platinum yttrium alloy amount, in fact the catalytic activity vs. ORR increase with the increment of the alloy content. The best sample was synthetized at 600 °C with $Y(NO_3)_3$, show a MA of 542 A g^{-1} and a $E_{1/2}$ of 0.891 V vs. RHE. The platinum yttrium concentration result be 63%. Platinum yttrium alloy NPs were successfully synthetized with $Y(acac)_3$ and $Y(ac)_3$, but the catalytic activity is similar to the standard Pt/C, ca. 200 A g^{-1}. The aggregation process shows an catalytic activity decrement because reduce drastically the number of active sites. Obviously other temperature must be analysed for understand which the best condition for the Pt_xY@C alloy formation, not only in terms of concentration but also in terms of NPs dimension and distribution. Increase the temperature or reduce the temperature synthesis have a strong impact on the NPs growing and on the reduction grade of the metal precursors. The best NPs dimension are obtained with YCl_3, but the temperature used for the synthesis do not permit the alloy formation, In the next paragraph YCl_3 was used as yttrium precursor and the temperature synthesis was increase for increase the interaction with the platinum and increase the electrochemical performance versus the Oxygen Reduction Reaction.

9.3 Influence of the temperature on Pt_3Y alloy formation

The yttrium precursors are the one of the most important variables which can influence the performance in terms of NPs dimension or alloy formation and the its concentration. Pt_xY NPs show a core shell structure, where the core is, mainly, constituted by a mixture of platinum and yttrium in metallic form, the shell, instead, shows a mixture of platinum an yttrium oxide. The reduction rate of platinum and yttrium salts play a fundamental role in the NPs dimension, in particular in the core and shell size. The temperature is fundamental on the reduction grade, the temperature can influence the formation of different kind of NPs, homogeneous, heterogeneous, core/shell. Several temperatures were analysed for the best yttrium precursors, the study is necessary for obtaining a catalyst with an high platinum yttrium amount in alloy, for modulated the NPs dimensional distribution and for obtain a Pt_xY catalyst with a stoicmetric ratio very close to 3. The synthesis was performed in a tubular furnace using $Pt(acac)_2$ as platinum precursors [60].

Table 26: Synthesis condition for Pt_xY@C catalysts. Effect of the temperature.

	Pt Salt	***Y Salt***	***T*** °C	***t*** h
Pt_xY1@600°5h	$Pt(acac)_2$	$Y(acac)_3$	400	5
Pt_xY1@400°5h	$Pt(acac)_2$	$Y(acac)_3$	600	5
Pt_xY3@400°5h	$Pt(acac)_2$	$Y(NO_3)_3$	400	5
Pt_xY3@600°5h	$Pt(acac)_2$	$Y(NO_3)_3$	600	5
Pt_xY3@300°5h	$Pt(acac)_2$	$Y(NO_3)_3$	600	5
Pt_xY3@600°3h	$Pt(acac)_2$	$Y(NO_3)_3$	600	3
Pt_xY3@750°3h	$Pt(acac)_2$	$Y(NO_3)_3$	750	3
Pt_xY3@900°3h	$Pt(acac)_2$	$Y(NO_3)_3$	900	3
Pt_xY4@400°5h	$Pt(acac)_2$	YCl_3	400	5
Pt_xY4@600°5h	$Pt(acac)_2$	YCl_3	600	5
Pt_xY4@600°3h	$Pt(acac)_2$	YCl_3	600	3

Several temperatures were analysed for $Y(NO_3)_3$, in previous paragraph yttrium nitrate show the best electrochemical performance for the Oxygen Reduction Reaction but TEM images showed a low NPs dimension. Pt_xY NPs were synthetized with yttrium nitrate at different temperature and different time, such as 3 h or 5 h. For the synthesis at 3 h, the temperatures analysed was 400 °C , 600 °C, 750 °C and 900 °C. Platinum yttrium alloy was synthetized with Yttrium chloride at two different temperatures (400 °C and 600 °C) and two different times (3 h and 5 h), in the previous paragraph this precursor shows a low catalytic activity but the best NPs dimension for the alloy. The low electrochemical performance obtained in Pt_xY4@C are

connected to a low reduction grade of platinum and yttrium precursors, which do not permit the alloy formation [44, 93, 123, 181].

9.3.1 TEM Analysis: Nanoparticles dimensions and distributions

All the catalysts showed round-shaped Pt NPs with high loading, uniformly dispersed throughout the samples, without a big formation of aggregates, except the synthesis employed at higher temperature. The corresponding particle size distributions were obtained by calculating the size of more than two hundred randomly selected particles in the TEM images. When $Pt(acac)_2$ and $Y(NO_3)_3$ were reduced in H_2 atmosphere for 3 h, the general effect of increasing the temperature is the obtainment of a wider size distribution (Figure 95 a,b,c,d and Figure 96 a,b,c,d). Narrow NP distributions were observed preferentially at low temperature with a size distribution centered at 2.1 nm which slightly increases to 5.7 nm passing from 300 °C to 900 °C. However, when the temperature effect was evaluated for longer reaction times (5 h instead of 3 h), the temperature plays a fundamental role, since the particle dimension sensitively increases by passing from 300 to 900 °C, the NPs show a size growing from 1.9 nm to 8.4 nm. In particular, the catalyst prepared at 600 °C shows a narrow particle size distribution peaked at 4.2 nm and is therefore suitable for ORR investigation, Figure 95f and Figure 96f. When 900 °C is used, very big crystals are formed with a very poor distribution over the carbon support, the aggregates show very different dimension, from 50 nm to 140 nm. The best results, in terms of particle dimensions, dispersion, distribution and absence of aggregate over the carbon support, were obtined by employing $Pt(acac)_2$ and Yttrium nitrate at 600 °C for 3 h or 5 h. The synthesis Pt_xY3@750°3h show well dispersed NPs inside and outside the MC pores can be obtained with the sporadic formation of aggregates and crystals of larger dimensions [181].

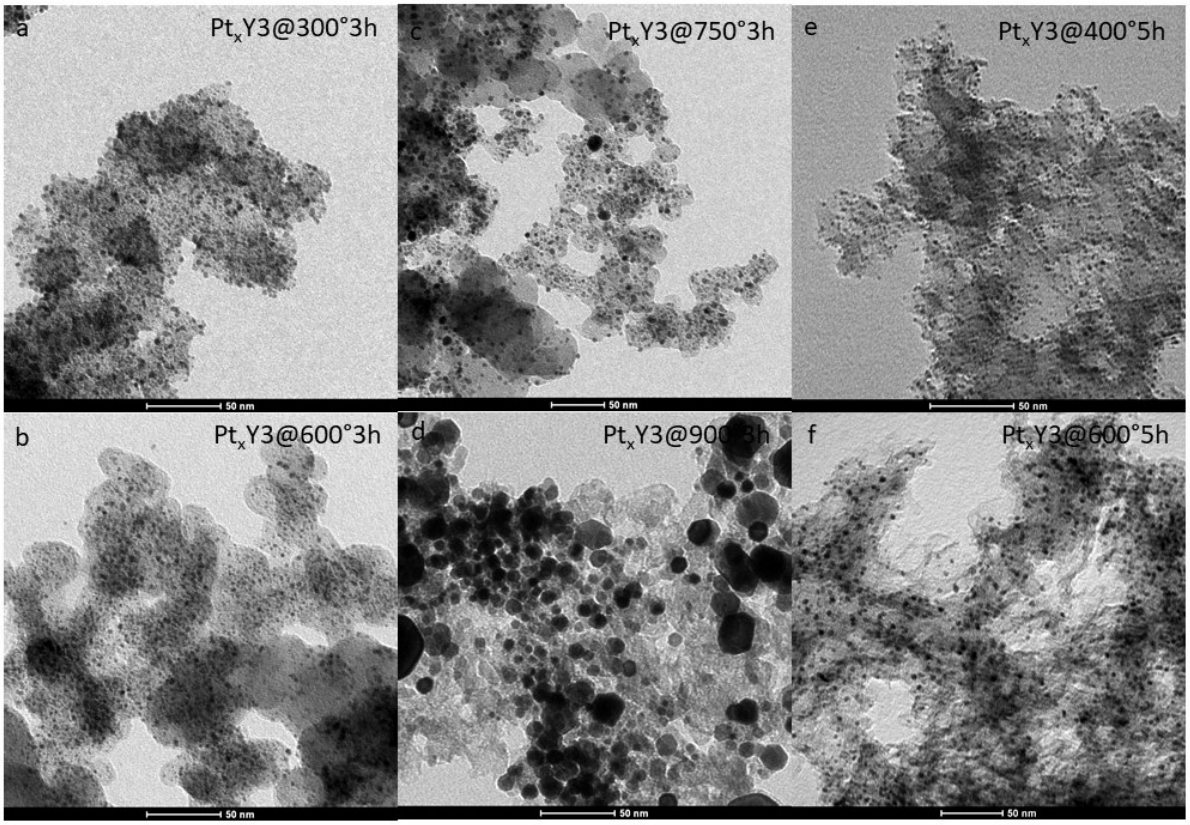

Figure 95: TEM images for a) Pt_xY3@300°3h; b) Pt_xY3@600°3h; c) Pt_xY3@750°3h; d) Pt_xY3@900°3h; e) Pt_xY3@400°5h and f) Pt_xY3@600°5h

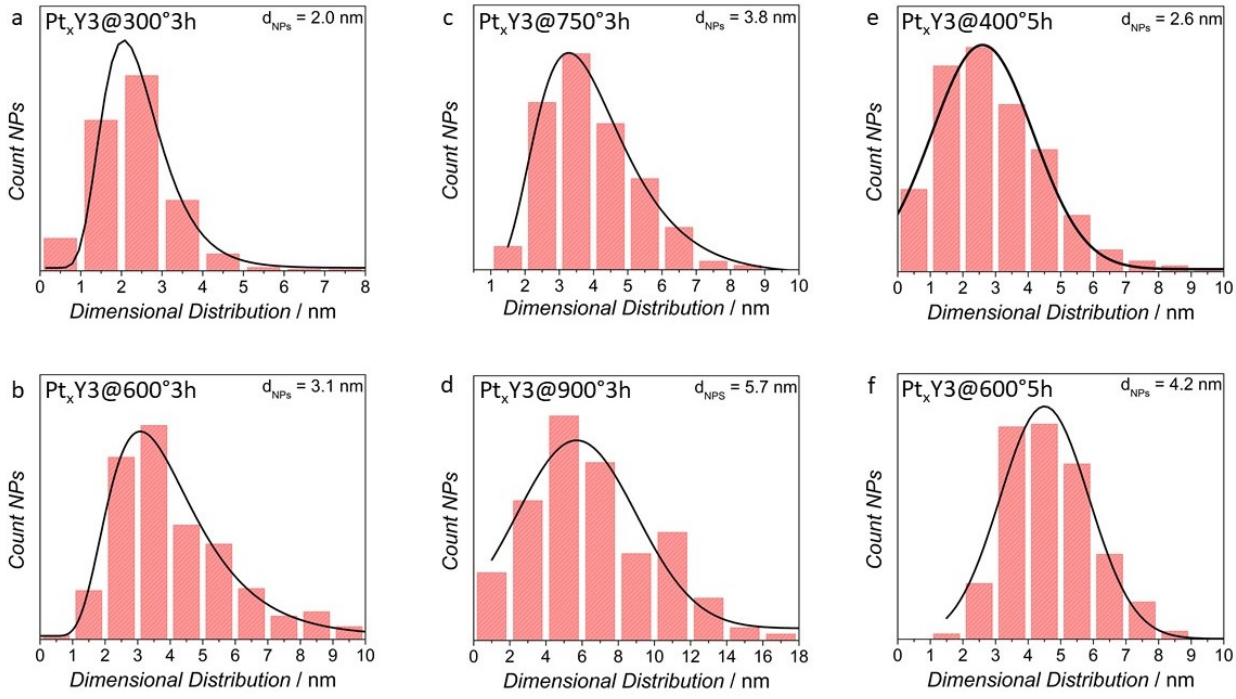

Figure 96: NPs dimensional distribution for a) Pt_xY3@300°3h; b) Pt_xY3@600°3h; c) Pt_xY3@750°3h; d) Pt_xY3@900°3h; e) Pt_xY3@400°5h and f) Pt_xY3@600°5h

For Pt_xY4@400°5h the mean Pt particle size diameter was centered at ca. 4.5 nm, Figure 96 d and Figure 97 d; in the case of Pt_xY4@600°5h (Figure 96 e and Figure 97 e)a dual distribution was observed with mean diameters peaked at 4.5 nm and 10 nm, whereas for Pt_xY4@600°3h even lower dimension (3.5 nm) and narrower size distribution were obtained. Increasing the temperature, a second population was formed, the NPs size range is from 2 nm to 18 nm, however TEM images show the total absence of aggregates or cluster. In the case of standard Pt/C, an even smaller dimension (2.9 nm) and narrower size distribution were obtained (Figure 96 f and Figure 97 f). The synthesis with Yttrium (III) acetylacetonate shows a small nanoparticle, increasing the temperature from 400 °C to 600 °C the size, suffers, a slight increment from 2.7 nm to 2.9 nm (Figure 96 a,b and Figure 97 a,b). The different NPs dimension obtained in the same temperature and time condition, explain the strong impact of the yttrium precursor on the platinum yttrium alloy [150, 167].

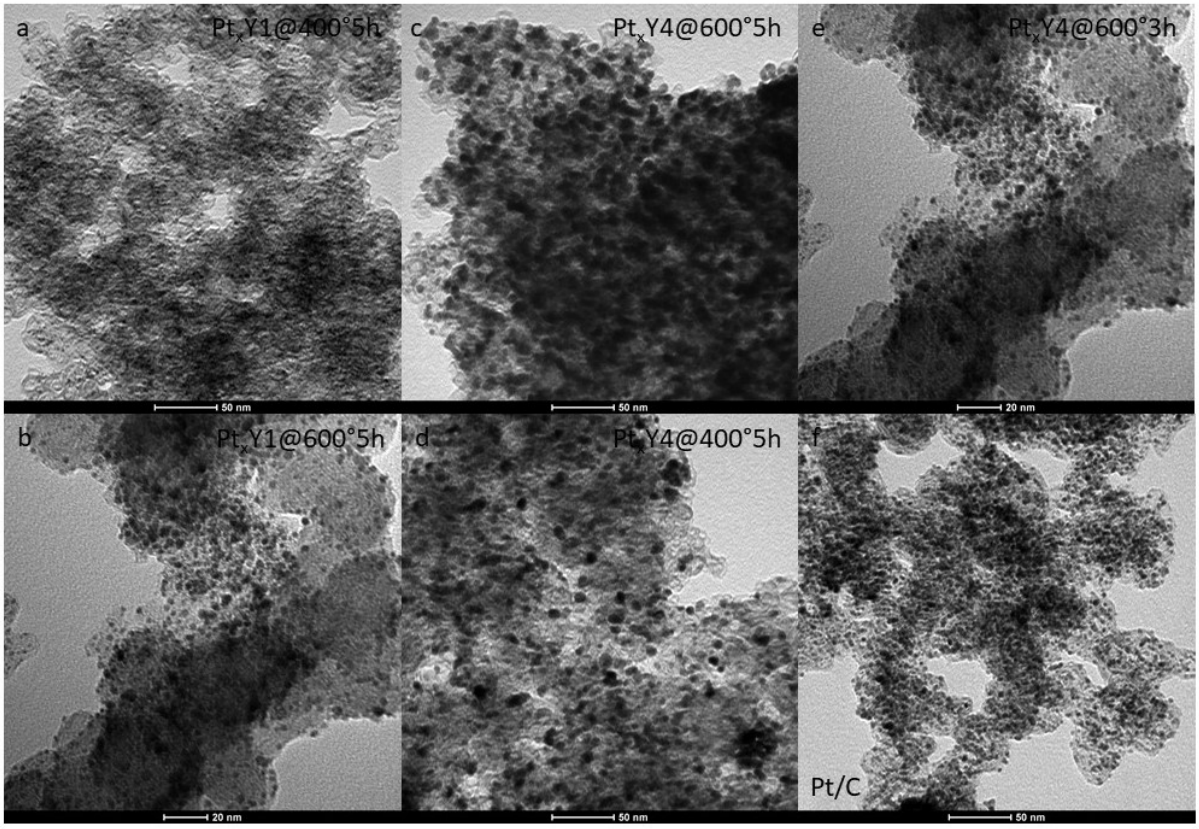

Figure 97: TEM images for a) Pt_xY1@400°5h; b) Pt_xY1@600°5h; c) Pt_xY4@600°5h; d) Pt_xY4@400°5h; e) Pt_xY1@600°3h and f) Pt/C

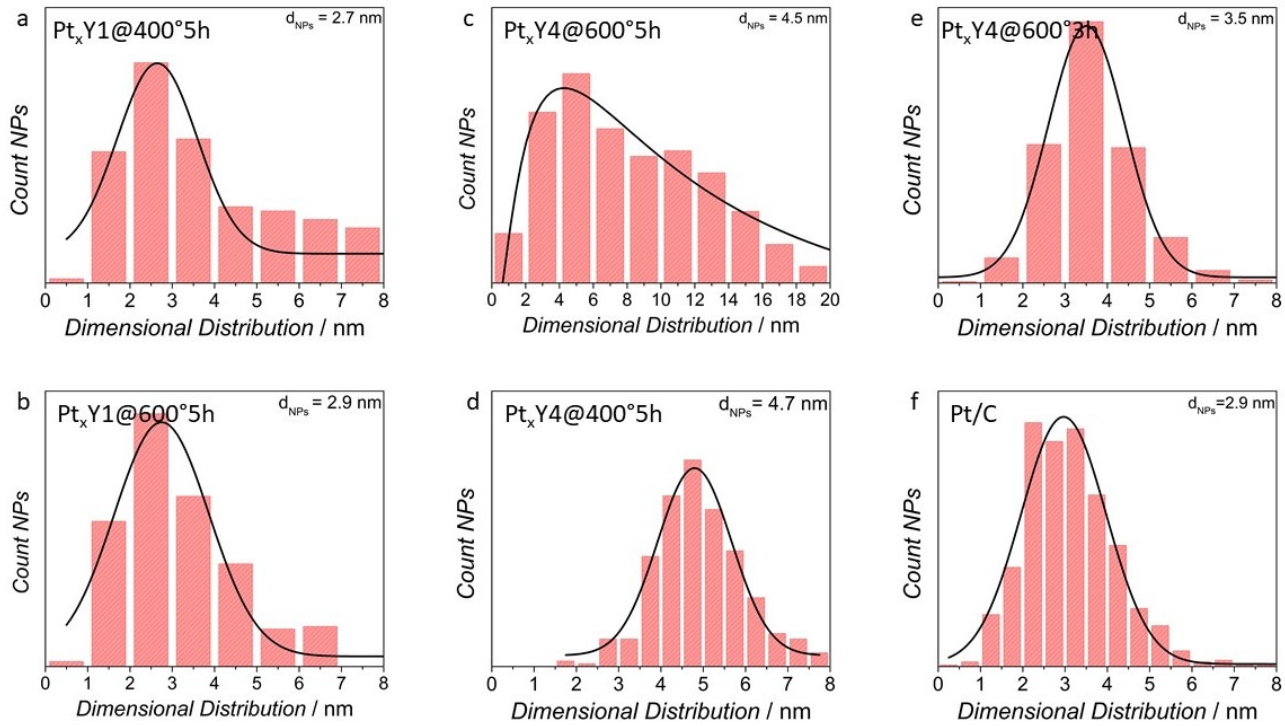

Figure 98: Dimensional distribution for a) PtxY1@400°5h; b) PtxY1@600°5h; c) PtxY4@600°5h; d) PtxY4@400°5h; e) PtxY1@600°3h and f) Pt/C

9.3.2 XPS analysis

Table 27: XPS analysis of Pt_xY catalysts. Effect of the temperature

	71.0 eV Pt(0) %	72.4 eV Pt(II) %	74.9 eV Pt(IV) %	156.3 eV Y(0) %	156.9 eV Y(III) %	157.7 eV Y-C %	Pt/Y -
Pt_xY1@600°5h	70	19	11	17	63	20	3.94
Pt_xY1@400°5h	62	27	11	20	42	38	3.11
Pt_xY3@400°5h	65	12	23	32	33	35	2.63
Pt_xY3@600°5h	65	21	14	67	14	19	4.42
Pt_xY3@300°3h	79	11	10	16	35	49	3.46
Pt_xY3@600°3h	77	2	21	43	23	34	2.87
Pt_xY3@750°3h	68	23	9	6	65	29	4.63
Pt_xY3@900°3h	72	24	4	0	45	55	5.11
Pt_xY4@400°5h	69	26	5	19	5	76	4.13
Pt_xY4@600°5h	53	32	15	3	49	48	3.37
Pt_xY4@600°3h	63	21	16	41	34	25	3.18

The electrochemical proprieties are connected to the NPs size (and their distribution on the carbon matrix) and to the platinum alloy concentration. XPS was used for evaluated the concentration of platinum and yttrium (0) in alloy form. The concentration after are connected to the resulting catalytic activity for the ORR.
Platinum 4f peak was deconvoluted by three signals associated to Pt(0) at 71.0 eV, Pt(II) at 72.4 eV and Pt(IV) at 74.9 eV. The Yttrium 3d peak was fitted by three components associated at yttrium metallic in alloy form, yttria and yttrium carbide, the component was evaluated at 156.3 eV,156.9 eV and 157.7 eV, respectively [91]. Table 27 shows the XPS component for platinum 4f and yttrium 3d, and the platinum yttrium ratio. For $Y(acac)_3$ (Pt_xY1@C), when the temperature was increased from 400 °C to 600 °C, XPS show the metal platinum increment and the reduction of platinum (II). The increment of the temperature during the synthesis increase the reduction grade of the platinum acetylacetonate. Passing from Pt_xY1@400°5h to Pt_xY1@600°5h, the metal yttrium, which is associated to the platinum yttrium alloy content, is slightly increased, from 17 % to 20 %. The yttrium carbide content decrease from 38 % to 20 % and at the same time yttria increase from 42 % to 63 %. The most stable yttrium form is yttrium oxide, so obviously, increasing the temperature, in $Y(acac)_3$, the yttrium reacts with the oxygen group present in the carbon matrix forming Y_2O_3. The platinum yttrium content increased with the temperature, passing from 3.11 to 3.94. In the catalysts Pt_xY3, which are synthetized with $Y(NO_3)_3$, the Pt (0) before, decrease passing from 300 °C to 750 °C and after, increase in the synthesis employed at 900 °C. Pt_xY3@300°3h and Pt_xY3@600°3h shows a platinum oxide concentration of 11 % and 2 %, respectively. When the temperature synthesis is increased higher than 750 °C, the Pt_xY catalysts show a PtO concentration of 23 % at 750 °C and 24 % at 900 °C. The platinum yttrium alloy increase from 16 % to 43 % when the temperature is increased from 300 °C to 600 °C, after the Pt_xY concentration drastically decrease until 16 % (in the synthesis at 750 °C) and after at 0 % when the temperature synthesis is increased at 900 °C. The yttrium carbide concentration is quite constant until 750 °C, after increase with the increment of the temperature. The synthesis employed at 600 °c for 3 h show a platinum yttrium ratio very close to 3, with the reduction of the platinum yttrium alloy concentration the Pt/Y move away from theoretical value. When yttrium (III) acetylacetonate is used as yttrium precursors, increasing the synthesis temperature from 400 °C to 600 °C (for 5 h), the yttrium (0) in alloy form amount is reduced from 19 % to 3 %, the yttrium carbide concentration passes from 5 % to 49 %. The Pt (0) component show a reduction from 69 % to 53 %. Pt_xY4@600°3h show a Pt (0) concentration of 63%, and a PtO and PtO_2 of 21 % and 16 % respectively.

9.3.3 Electrochemical Characterization

The catalysts were characterized in $HClO_4$ 0.1 M, using a standard electrochemical cell composed by a Working Electrode (Rotating Disk Electrode in Glassy Carbon), a Counter Electrode (commercial platinum ring) and an Reference Electrode (Reversible Hydrogen Electrode) [61, 149, 182]. The electrochemical measurements were performed with a Pt loading of 15 μg cm^{-2}. The correct platinum concentration in the catalysts was evaluated by ICP-MS. The Table 28 show the conditions for the catalysts' synthesis, in term of

yttrium precursors, time and the temperature. The platinum content is very close to 27 %, the slight decrement is due to the sublimation of the $Pt(acac)_2$, in fact in Pt_xY3@3h, increasing the temperature for the synthesis the sublimation process is faster, so the platinum concentration decreases from 24.9 % at 300 °C to 23.9 % at 900 °C. The electrochemical results were compared with a platinum standard, Pt/C, which own a platinum content of 49.1 %.

Table 28: Synthesis condition, platinum concentration and electrochemical results for PtxY catalysts,

	Y	***T***	***t***	***Pt_{ICP}***		***EPSA***		***ECSA***	
		°C	h	$\%_w$		cm^2		$m^2\ g^{-1}$	
Pt/C				49.1	± 1.2	2.16	± 0.12	73.5	± 4.1
Pt_xY1@600°5h	$Y(ACAC)_3$	600	5	26.8	± 0.7	1.82	± 0.15	62.0	± 5.0
Pt_xY1@400°5h	$Y(ACAC)_3$	400	5	25.9	± 0.6	1.18	± 0.09	40.0	± 3.0
Pt_xY3@400°5h	$Y(NO_3)_3$	400	5	25.8	± 0.4	1.03	± 0.11	35.2	± 3.7
Pt_xY3@600°5h	$Y(NO_3)_3$	600	5	23.7	± 0.6	1.35	± 0.11	45.9	± 3.9
Pt_xY3@300°3h	$Y(NO_3)_3$	300	3	28.1	± 0.7	2.25	± 0.09	76.5	± 3.2
Pt_xY3@600°3h	$Y(NO_3)_3$	600	3	24.9	± 0.3	0.82	± 0.09	27.8	± 3.0
Pt_xY3@750°3h	$Y(NO_3)_3$	750	3	24.7	± 0.3	1.64	± 0.11	55.6	± 3.8
Pt_xY3@900°3h	$Y(NO_3)_3$	900	3	23.9	± 0.6	2.18	± 0.19	74.0	± 6.5
Pt_xY4@400°5h	YCl_3	400	5	28.1	± 0.7	1.50	± 0.11	51.0	± 3.7
Pt_xY4@600°5h	YCl_3	600	5	27.3	± 0.6	0.95	± 0.09	32.5	± 3.0
Pt_xY4@600°3h	YCl_3	600	3	24.9	± 0.2	2.63	± 0.18	89.3	± 6.2

The hydrogen adsorption and desorption area for calculate the Electrochemical Platinum Surface Area was evaluated in argon saturated solution. Platinum on carbon show an EPSA of 2.16 cm^2 which correspond to 73 $m^2\ g^{-1}$. Pt_xY1 show a EPSA increment with the increasing of the temperature, from 1.18 cm^2 to 1.82 cm^2, the NPs size (evaluated by TEM) show a slight increment from 2.7 nm at 400 °C to 2.9 nm at 600 °C, this bucking can be explain by the increment of the particles' number for area unit, in fact the population density in PtxY1@600°5h is higher than PtxY1@400°5h. The same trend was observed for Pt_xY3@400°5h and Pt_xY3@600°5h, which show an EPSA of 1.03 cm^2 and 1.35 cm^2, respectively. The increment of NPs density is more visible in this case than the previous; the NPs dimensions pass from 2.6 nm to 4.2 nm increasing the temperature synthesis. The ECSA value associated are 35.2 $m^2\ g^{-1}$ when the catalyst was synthetized at 400 °C and 45.9 $m^2\ g^{-1}$ when 600 °C is used as temperature synthesis. For the catalysts obtained with $Y(NO_3)_3$ and a synthesis time of 3 h, the EPSA before decrease from 2.25 cm^2 to 0.82 cm^2, passing from 300 °C to 600 °C, and after increase from 1.64 cm^2 to 2.18 cm^2 in the syntheses developed at 750 °C and 900 °C, respectively. The NPs size pass from 2.0 nm to 5.7 nm, increasing the temperature from 300 °C to 900 °C. The Platinum (0) concentration evaluated by XPS decrease increasing the temperature. In Pt_xY3@300°3h and Pt_xY3@600°3h, the NPs density is very similar, and the EPSA reduction is connected to the increment of the NPs size from 2.0 nm to 3.1 nm. After, TEM images show an size increment due to NPs agglomeration, but also NPs with a dimension lower than 2 nm which are responsible to the increment of EPSA. Pt_xY4 show a

EPSA reduction when the temperature is increase from 400 °C to 600 °C. Pt_xY4@600°3h show a EPSA of 2.18 cm^2 and a ECSA of 89.3 $m^2\ g^{-1}$, the high EPSA is due to the great NPs distribution in the carbon matrix and to the arrowed NPs distribution. Figure 99 show the cyclic voltammetry for the different yttrium precursors obtained at 50 mV s^{-1} in argon saturated 0.1 M solution.

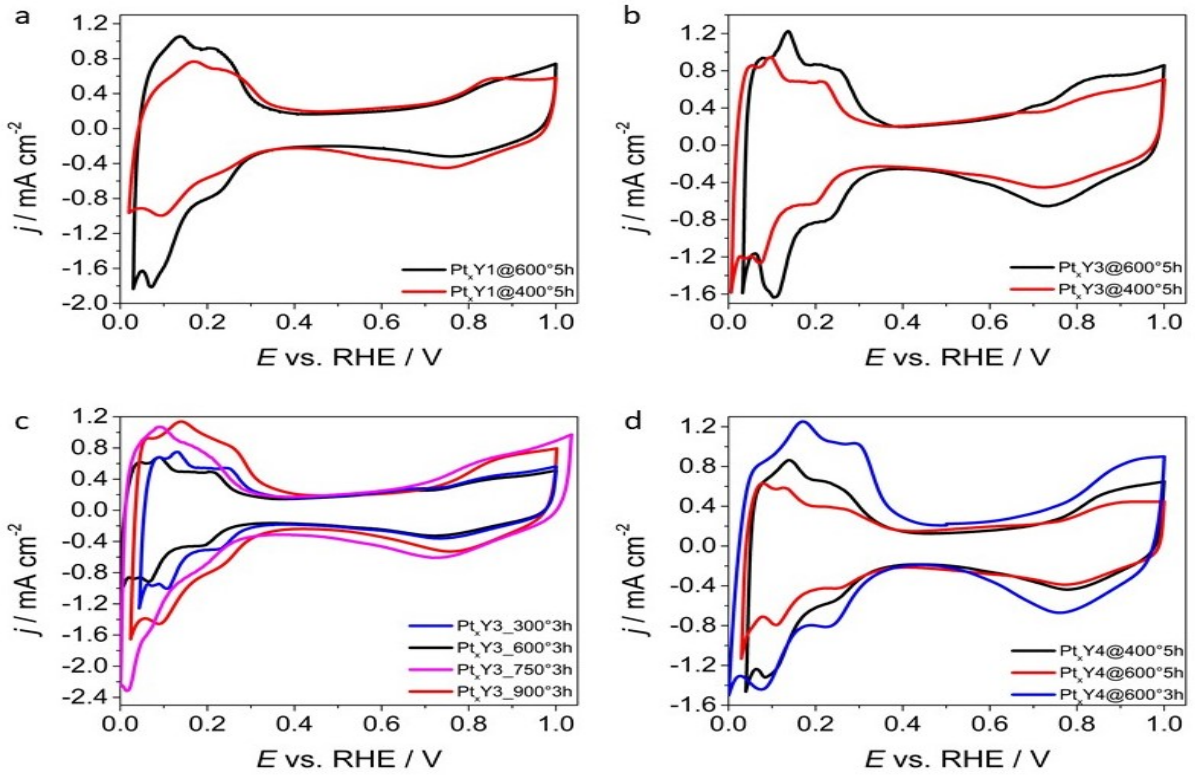

Figure 99: Cyclic Voltammetry in Ar saturated solution at 50 mV s^{-1} for a) Pt_xY1@5h; b) Pt_xY3@5h; c) Pt_xY3@3h and d) Pt_xY4

Figure 100 show the Linear Sweep Voltammetry recorded in Oxygen saturated electrolyte solution at 20 mV s^{-1} and 1600 rpm. Pt_xY@400°5h show the same Mass Activity of platinum NPs on carbon (Pt/C), 201 A g^{-1} and 206 A g^{-1} and a $E_{1/2}$ higher of 7 mV than the Pt/C. When the synthesis is employer at 600 °C, the platinum yttrium concentration evaluated by XPS is slight increase from 17 % to 20 % as the NPs dimension, from 2.7 nm to 2.9 nm. However, the catalytic performance in terms of MA and $E_{1/2}$ are considerably increase. PtxY@600°5h show a Mass Activity of 303 A g^{-1} and a half wave potential higher than 29 mV than the platinum standard. When the synthesis is employer with Yttrium (III) nitrate for 3 h. The catalytic activity of Pt_xY, expressed as $\Delta E_{1/2} = E^{catalyst}_{1/2} - E^{Pt/C}_{1/2}$, decreases as follows:

$$Pt_xY300h3 > Pt_xY600h3 > Pt_xY900h3 > Pt_xY750h3.$$

The lowest activities and limiting current densities were found for these catalysts showing a low content or even the absence of the Pt_xY alloy. In $Pt_xY300°3h$ the alloy is not present, and its deviated behavior is not easily rationalized, at 300 °C the formation of well dispersed and small Pt NPs are obtained, $Y(NO_3)_3$ in these conditions produces mainly Y_2O_3, these characteristic increase the electrochemical performance. The catalytic activity and the limiting current density decrease for synthesis temperatures higher than 600 °C, for the increasing of Y_2O_3 and the formation of bigger NPs and aggregates. When the synthesis is developed for 5h,

the performances are considerably increase, due to the Pt_xY alloy increasing and the better NPs distribution on the carbon matrix. Pt_xY3@400°5h and Pt_xY@600°5h shows a NPs size of 2.6 nm and 4.2 nm and a platinum yttrium concentration of 42 % and 67 %. The corresponding electrochemical activity in terms of MA and $E_{1/2}$ are 458 A g^{-1}, 525 A g^{-1}, 0.891 V vs. RHE and 0.866 V vs. RHE. The increment of MA is due the increment of the alloy content. In fact, the higher activity of Pt_xY3@600°5h in the ORR most likely arises from the electronic modification of Pt generated by the strain effect due to alloying with yttrium. The Specific Activity decrease for the increment of the EPSA obtained when the temperature was increased. In any case the SA obtained for Pt_xY3@400°5h and Pt_xY3@600°5h are 2 and 3 times, respectively, higher than platinum on carbon (0.276 mA cm^{-2}). Dubau et al. rationalized the best condition for an high catalytic activity (not the best) and a good electrochemical stability for the ORR is optimal in the range of 3nm - 4 nm.

Pt_xY4@400°5h and Pt_xY4@600°5h show a very low activity in terms of kinetic current, half wave potential and mass activity; TEM images shows the formation of big aggregates. The corresponding MA are 100 A g^{-1} and 65 A g^{-1}. The platinum yttrium alloy content is evaluated less than 5 %. The condition used the synthesis not permits the alloy formation and a good NPs distribution over all the carbon support. When the synthesis time was reduced at 3h, the performance change drastically, in fact Pt_xY4@600°3h show a MA three times higher than the standard Pt/C (605 A g^{-1} vs. 201 A g^{-1}), the $E_{1/2}$ is higher of ca. 80 mV than platinum standard; The alloy content reaches 67 %. The performance increment is connected to the alloy concentration and to the NPs dimension (3.5 nm) and their good distribution over the carbon matrix.

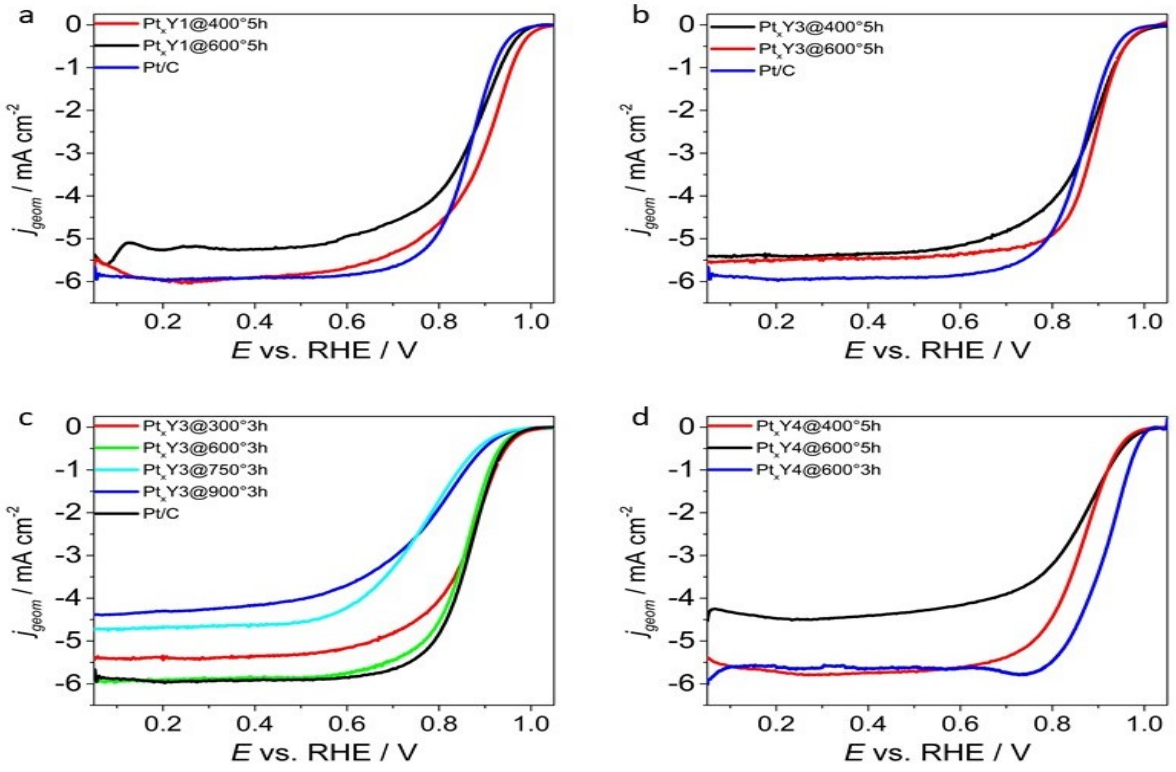

Figure 100: LSV with RDE at 20 mV s^{-1} and 1600 rpm recorded in O_2 saturated $HClO_4$ solution for a) Pt_xY1@5h; b) Pt_xY3@5h; c) Pt_xY3@3h and d) Pt_xY4

Table 29: Electrochemical results for PtxY catalysts. Effect of the temperature

	$\|j_L\|$	$E_{1/2}$ vs. RHE	i_k	*MA*	*SA*
	mA cm^{-2}	V	mA	A g^{-1}	mA cm^{-2}
Pt/C	5.94 ± 0.14	0.867 ± 0.005	0.59 ± 0.01	201 ± 3	0.274 ± 0.019
Pt$_x$Y1@600°5h	5.92 ± 0.12	0.896 ± 0.007	0.89 ± 0.04	303 ± 15	0.488 ± 0.063
Pt$_x$Y1@400°5h	5.22 ± 0.09	0.874 ± 0.005	0.61 ± 0.04	206 ± 13	0.515 ± 0.072
Pt$_x$Y3@400°5h	5.86 ± 0.15	0.866 ± 0.007	1.35 ± 0.07	458 ± 23	0.997 ± 0.134
Pt$_x$Y3@600°5h	5.46 ± 0.27	0.891 ± 0.009	1.54 ± 0.08	525 ± 26	0.687 ± 0.063
Pt$_x$Y3@300°5h	5.40 ± 0.08	0.867 ± 0.007	0.46 ± 0.06	156 ± 20	0.444 ± 0.105
Pt$_x$Y3@600°3h	5.88 ± 0.11	0.861 ± 0.005	0.33 ± 0.07	112 ± 24	0.402 ± 0.132
Pt$_x$Y3@750°3h	4.69 ± 0.11	0.771 ± 0.004	0.07 ± 0.01	23 ± 2	0.042 ± 0.007
Pt$_x$Y3@900°3h	4.31 ± 0.15	0.782 ± 0.008	0.11 ± 0.05	36 ± 16	0.049 ± 0.025
Pt$_x$Y4@400°5h	4.18 ± 0.21	0.860 ± 0.006	0.29 ± 0.01	100 ± 5	0.195 ± 0.024
Pt$_x$Y4@600°5h	5.17 ± 0.30	0.830 ± 0.009	0.19 ± 0.01	65 ± 3	0.200 ± 0.029
Pt$_x$Y4@600°3h	5.64 ± 0.09	0.942 ± 0.006	1.78 ± 0.06	605 ± 20	0.678 ± 0.070

For concluding:

- Pt$_x$Y1 was synthetized with Pt(acac)$_2$ and Y(acac)$_3$. Increasing the temperature from 400 °C to 600 °C
  - the NPs size increase from 2.7 nm to 2.9 nm and the aggregate density decrease drastically
  - Platinum content decrease from 70 % to 62 % but Pt$_x$Y alloy content increase from 17 % to 20 %.
  - MA increase from 206 A g^{-1} to 303 A g^{-1}
  - SA reduce from 0.515 mA cm^{-2} to 0.488 mA cm^{-1}
- Pt$_x$Y3 was synthetized with Pt(acac)$_2$ and Y(NO$_3$)$_3$. Increasing the temperature synthesis
  - The NPs size pass from 2 nm to 5 nm, with the aggregate formation only at 900 °C
  - The XPS alloy content is maxima at 600 °C, at lower temperature a mixture of Y2O3 and Y-Carbide is obtained.
  - The best catalyst was synthetized at 600 °C and show a MA of 525 A g^{-1} and a SA of 0.687 mA cm^{-1}
- Pt$_x$Y4 was synthetized with Pt(acac)$_2$ and YCl$_3$.
  - Increasing the temperature, the aggregate formation increases and the electrochemical performance decrease
  - Reducing the time reaction, the electrochemical activity increases drastically from 65 A g^{-1} (600°C and 5 h) to 603 A g^{-1} (600°C and 3 h)
  - Reducing the time, the aggregates formation decreases and the NPs dimension pass from 4.5 nm to 3.5 nm

9.3.4 Conclusion

The influence of the temperature and the time were analysed for understand how influence the NPs formation, growing and the platinum yttrium alloy content. The shift of Platinum and yttrium binding energy reveals the presence of a chemical interaction between the two elements. The temperature synthesis was changed for different yttrium salt precursors and each one show different behaviour, in the same way the time was analysed. In summary Pt_xY, where ca. 47 % and 61 % of Y atoms are alloyed with platinum were synthetized via high temperature solid state synthesis using $Pt(acac)_2$ and $Y(NO_3)_3$ and YCl_3. For yttrium nitrate the catalyst was synthetized at 600 °C and 5 h shows a MA of 525 A g^{-1}, $E_{1/2}$ of 0.891 V vs. RHE and a EPSA of 1.35 cm^2. The catalyst obtained by YC3 at 600 °C and 3h show a MA of 605 A g^{-1}, $E_{1/2}$ of 0.942 V vs. RHE and a EPSA of 2.63 cm^2. In particular, Pt_xY4@600°3h MA is 1.3 times the "Future Targets" DOE stack targets (440 A g^{-1}). Similar evidence was found for the specific activity, which is higher than that obtained with the conventional Pt/C catalyst. The magnitude of the ECSA obtained in these catalysts and on the Pt/C is an indication of the Pt-active site density the larger the ECSA value, the more active the catalyst layer should be. Increasing the temperature, the Platinum alloy concentration decrease and increase the yttria amount. The Yttrium carbide element is observed in all catalysts in different percentage. Each yttrium precursors can be reduced at high temperature in solid state synthesis with hydrogen atmosphere; the interaction with platinum for the alloy formation is observed only in $Y(acac)_3$, $Y(NO_3)_3$ and YCl_3.

9.4 Effect of the carbon support on alloy formation and on the catalytic activity vs. ORR

Several parameters can influence the platinum yttrium alloy formation, for example in high temperature solid state reduction the temperature or the time used for the synthesis, in wet-chemistry the solvents adopted for the chemical reduction or the inorganic/organic reduction agents used for the salt precursors reduction. In solid state synthesis the Platinum Yttrium NPs grown directly in a support, the characteristic of the matrix, in terms of doping, morphology or graphitization, can modify the NPs dimension or distribution, the shape, the crystallinity and the alloy formation [58, 118]. The carbon propriety can be divided in two class, chemical and morphological proprieties. The morphological properties are referred to the carbon physical characteristic as the surface area, the pore distribution and dimension while the chemical properties are connected to an electronegativity modification of the carbon active sites due to for examples the insertion in the matrix of heteroatoms or thermal treatment which can modify the graphitization grade [134, 142]. The chemical and morphological characteristic have a strong impact on the alloy formation, on the NPs growing and the distribution on the support. MSI (Metal-Support Interaction) describe all interaction than can establish between the carbon active site and the NPs. For understand the effective influence of MSI on the Pt_xY alloy NPs, several

commercial and homemade carbon supports were evaluated. The carbon proprieties as surface area or the heteroatoms content was evaluated, and after connected with the electrochemical performance of the resulting catalyst. Platinum yttrium NPs are deposited by solid state synthesis at high temperature in a 8% H_2 atmosphere. As platinum and yttrium precursors, $Pt(acac)_2$ and $Y(NO_3)_3$ are adopted. $Y(NO_3)_3$ is the best yttrium precursor, in fact permits to obtain a good and arrow NPs distribution over the carbon. The synthesis conditions for the salt reduction were 650 °C with a time synthesis of 3 h. The carbon proprieties were evaluated by Elemental Analysis for calculate the heteroatoms content, by N_2 Adsorption/Desorption analysis for analysis the surface area and pore distribution. The catalysts are fully electrochemical tested in $HClO_4$ 0.1 M electrolyte solution. The best five samples are characterized with TEM, XRD and XPS [154, 183].

9.4.1 Carbon Characteristic: Surface Area, Pore Distribution and Heteroatoms content

Table 30 shows the carbon support used for the platinum NPs deposition, from C1 to C9 the supports are commercial, in the table are indicated the product code and the fabrication company, and from C10 to C13 the carbons were synthetized by hard template synthesis. Several carbons are used with different characteristics, as the particle carbon dimension, for example the particles presents in C1 have a dimension lower than 500 nm while in the carbon C2 the particle have a dimension lower than 250 nm. Between C2 and C3 the graphitization grade is very different but the textural carbon properties (pore structure, pore size) are the same. C3 is a commercial carbon obtained by thermal treatment at 950 °C from C7. Two carbons support C1 and C3 were modified for increase the sulphur content, generally each commercial carbon owns 0.1 % of heteroatoms, the presence of sulphur is fundamental for increasing the electrical conductibility. C8 and C9 was obtained treated C3 and C1 at high temperature with H_2SO_4 conc. At 500 mg of carbon was added 0.25 mL of sulphuric acid and after thermal treated at 900 °C for 5 h in Argon controlled atmosphere. The treatment has the purpose of increasing the sulphur doping concentration. C10 and C11 are homemade mesoporous carbon obtained by hard template. The two carbons were synthetized with sucrose as carbon precursors and with silica P20 and P200, respectively. The silicas P20 and P200 owns a different structure, with silica P200 the resulting carbon show a more order structure with a defined pore structure, instead with P20 the carbon shows an more complex pore dimensional distribution, and an high micropore volume. The precursors powder was pyrolyzed at 750 °C for 3 h in argon atmosphere. Perazzolo at all had described the influence of the temperature and time parameters on the carbon porosity and on the graphitization grade. In these conditions the resulting carbon have a good compromised between heteroatoms content, textural properties and graphitization. Increase the temperature synthesis increase the graphitization grade but the heteroatoms content decrease as the surface area. C12 and C13 are doped homemade carbon, C12 was synthetized with dibenzothiophene so the resulting

carbon is sulphur doped while C13 was obtained by the pyrolysis of 1,10-phenantroline. For C12 and C13, the inorganic template used for the synthesis has been silica P200 .

Table 30: Carbon characteristic, Effect of the carbon support on the Pt_xY alloy formation

	Company
	-
C1	SA-1333-86-4; cod. 699632-Carbon Mesoporis Nanopowder, <500 nm particle size, 99.95%
C2	AA-1333-86-4-Carbon Black, acetylene, 100% compressed, 99.9%
C3	Carbon Black, Super P Conductive, 99+%
C4	SA-308068-56-6; cod. 724769- MWCNT, >95% carbon basis,O.D. x L 6-9 nm x 5 µm
C5	Commercial Acetylene Black
C6	SA-1333-86-4; cod. 702110; cod. Graphitized Carbon Black hydrophilic pore surface
C7	SA-1333-86-4; cod. 699640- Graphitized Carbon Black average pore diameter 100 Å, 99.95%
C8	Carbon Black, Super P Conductive, 99 % + H_2SO_4
C9	SA-1333-86-4; cod. 699632-Carbon Mesoporis Nanopowder, <500 nm particle size, 99.95% + H_2SO_4
C10	Hard Template, Silica P20_Sucrose
C11	Hard Template, Silica P200_Sucrose
C12	Hard Template, Silica P200_Dibenzothiophene
C13	Hard Template, Silica P200_1,10-Phenantroline

Table 31 describe the chemical and morphological properties of all carbon used, in terms of surface area and elemental analysis. All commercial carbons except C6 have an high carbon content, around 96 % (evaluated by Elemental Analysis). The sulphur content valued for C1 and C5 is lower than 0.05 %, while for others carbon support the heteroatoms content is higher, from 0.2 % to 0.7 %. In MWCNT and Super Conductive carbon (C4 and C3) the sulphur content is 0.24%. In C2 and C7 the elemental analysis has not revealed any heteroatoms. C8 and C9 were synthetized by thermal treatment with sulphuric acid by C1 and C3, the elemental analysis confirms the effective doping action of sulphuric acid, the sulphur content in C8 and C9 is 2.39 % and 1.12 %, respectively. The homemade mesoporous carbon show different heteroatoms content due to the carbon precursors used for the synthesis, in C10 and C11 the doping is due to the sulphuric acid used for catalysed the oligomerization process during the preparation of the precursor powder. C12 show the highest sulphur content, 13.8 %. C13 show a sulphur and nitrogen doping, the nitrogen content is connected to the carbon precursor while the sulphur, as in C10 and C11, to the sulphuric acid.

Table 31: Carbon proprieties in terms of heteroatoms concertation and morphological characteristic

	Synthesis	C_{AE}	H_{AE}	N_{AE}	S_{AE}	S_{BET}	*dp1*	*dp2*	*dp3*	*dp4*	$S_{micropore}$	$S_{mesopore}$	$V_{micropore}$	$V_{mesopore}$
	-	%	%	%	%	$m^2\ g^{-1}$	nm	nm	nm	nm	$m^2\ g^{-1}$	$m^2\ g^{-1}$	$cm^3\ g^{-1}$	$cm^3\ g^{-1}$
C1		94.81	0.73	-	0.04	254	3.17	5.84	8.35	9.81	27	227	0.082	0.317
C2		98.87	-	-	-	80	3.71	4.95	8.46	11.10	14	66	0.095	0.275
C3		88.96	0.62	-	0.24	65	1.80	2.26	4.21	5.86	12	53	0.137	0.713
C4		96.25	0.17	-	0.21	240	2.28	4.97	6.21	7.15	11	229	0.02	2.267
C5		99.36	-	-	0.05	1304	3.11	8.61	9.75	14.87	189	1115	0.004	0.936
C6		68.29	3.88	-	0.64	54	1.21	3.16	4.58	7.95	4	50	0.093	0.236
C7		99.49	-	-	-	294	4.59	6.51	8.64	11.40	7	287	0.110	0.546
C8	900 °C_5 h	87.18	0.4	-	2.39	74	2.12	2.95	4.76	6.08	6	68	0.063	0.369
C9	900 °C_5 h	95.41	0.41	-	1.12	373	4.19	6.12	9.11	10.34	26	347	0.128	0.641
C10	750 °C_3 h	70.09	2.43	-	0.96	729	1.27	3.18	5.04	14.76	359	370	0.155	0.865
C11	750 °C_3 h	67.74	0.83	-	1.12	759	3.73	4.86	8.29	11.09	57	702	0.014	0.638
C12	750 °C_3 h	68.11	1.26	-	13.8	1103	1.10	3.80	4.90	7.20	146	957	0.014	0.864
C13	750 °C_3 h	75.83	1.17	3.55	0.86	1002	1.81	4.12	6.23	8.66	124	878	0.016	0.899

The surface area, pore volume, pore distribution and pore dimension were evaluated by N_2 adsorption/desorption analysis at 77 K. The commercial carbons present different surface area connected to a different micro- or meso- porosity. C1, C4 and C7 have a similar surface area, in the range 200 $m^2\ g^{-1}$ – 300 $m^2\ g^{-1}$, due to the mesoporosity, the microporosity contribution on the total area is lower than 10 %. C2, C3 and C6 are low surface area carbon, (< 75 $m^2\ g^{-1}$) the high graphitization of these support is obtained with thermal treatment (in C6 at 1250 °C) which causes a pores occlusion, so a drastic reduction of the external surface area. The microporous and mesoporous surface area obtained in C8 is 6 $m^2\ g^{-1}$ and 68 $m^2\ g^{-1}$, respectively. The values obtained, in terms of area or pore distribution, in C8 before and after the thermal treatment with sulphuric acid is very similar. For C8, post treatment has effect only on the sulphur concentration and not on the carbon structure, the effect is explained by the high graphitization of C3. The surface area obtained in C9 are slightly higher than C1, the increment is due to the thermal treatment which modify the carbon morphology, the modification is made possible by the low graphitization of the carbon support. In other words, the high carbon graphitization obtained with high temperature pyrolysis prevent the pore dimension modification with other thermal treatments. The carbon synthetized by hard template method show a high surface area. The sample C10 synthetized with sucrose and silica P20 owns a microporous area similar to the mesoporous area. Silica P20 is unstructured silica, the carbon matrix is given by the removal of the silica NPs, and so a total structure control is hard. The situation is completely different when silica P200 is used, silica P200 have a controlled and order mesostructure. The carbon porosity is obtained by the silica structure while the carbon structure is obtained during the etching process by the silica porosity. The total surface area in C11 is 759 $m^2\ g^{-1}$, the mesoporous and microporous component are 702 $m^2\ g^{-1}$ and 57 $m^2\ g^{-1}$.

C12 and C13 shows a surface area higher than 1000 $m^2 g^{-1}$ (1103 $m^2 g^{-1}$ and 1002 $m^2 g^{-1}$), as in C11, the total area is due to the mesoporosity (the impact of the microporosity is only 9 %). Another textural propriety which influence the NPs growing is the pore dimensional distribution. The pore dimension is very important because the NPs can grow inside, and the pore dimension can control their dimension. Generally, a mesoporous carbon owns 4 pore distribution, one in microporous range (lower than 2 nm), the second at dimension higher than 10 nm and the last two at intermedium values [57, 184, 185, 186].

9.4.2 Nanoparticles distribution and Platinum-Yttrium alloy formation: TEM, XPS and XRD

Platinum yttrium alloy NPs were synthetized in tubular furnace at high temperature in a controlled reduction atmosphere. The NPs dimension and distribution were evaluated by TEM analysis. The samples characterized with TEM were Ptx@C2, PtxY@C4, PtxY@C7, PtxY@C9 and PtxY@C12; obtained using as support Carbon Black, acetylene, 100% compressed, 99.9%, MWCNT, >95% carbon basis,O.D. x L 6-9 nm x 5 µm, Graphitized Carbon Black average pore diameter 100 Å, 99.95%, Carbon Mesoporous Nanopowder, <500 nm particle size, 99.95% + H_2SO_4 and an homemade mesoporous carbon synthetized with Silica P200 and Dibenzothiophene

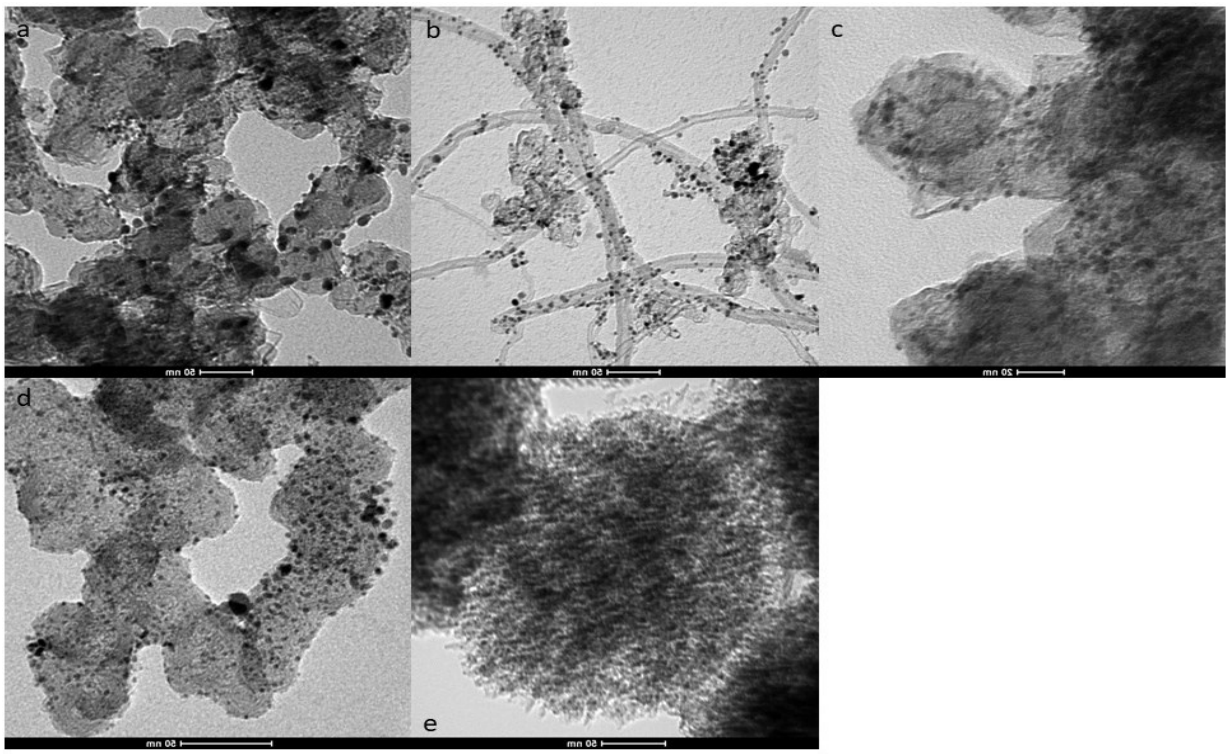

Figure 101: TEM images of a) Pt_xY@C2; b) Pt_xY@C4; c) Pt_xY@C7; d) Pt_xY@C9 and e) Pt_xY@C12

Figure 101 show the TEM images for the best five samples with the highest catalytic activity vs. ORR. Platinum Yttrium NPs have a good distribution on carbon support. Figure 101a show the formation of two NPs series with different dimension, distributed uniformly over the carbon support. The images show a spherical carbon particles with dimension in the range 50 nm – 85 nm. Figure 101b show the TEM images of Pt_xY@C4, which was synthetized with MWCNT show a good NPs distribution on the external surface of the nanotubes with a rare formation of big nanoparticles, in the size rage 12 nm -17 nm. Pt_xY@C4 show NPs with a distribution higher than Pt_xY@C2. Pt_xY@C7 show very small NPs, with a very narrow dimensional distribution. The smallest NPs are obtained with Carbon Mesoporous Nanopowder, <500 nm particle size, 99.95% + H_2SO_4, the dimensional distribution is picked at 2.31 nm, the image show the sporadic formation of aggregates with a dimension of 20 nm. Figure 101e show the typical texture for carbon obtained by hard template methods with mesostructured silica, the NPs have an average dimension of 2.77 nm, the NPs are uniformly distributed over all carbon structure. The NPs dimension follow the next trend:

Pt_xY@C9 (2.3 nm) < Pt_xY@C7 (2.7 nm) < Pt_xY@C12 (2.8 nm) < Pt_xY@C2 (3.5 nm) < Pt_xY@C4 (4.1 nm)

In Pt_xY@C12, the low NPs dimension are stabilized by the sulphur, in fact several articles show as this heteroatom prevents the NPs aggregation. The problem is the pore dimension and the micropore surface area, the low pore dimension does not permit the growing of the particles inside the structure. In fact, the pore size is very low, at 1.1 nm, 3.8 nm, 4.9 and 7.2 nm. The NPs can grow only on d_{p4} and on the external surface. In Pt_xY@C4, the high NPs dimension of 4.1 nm are given by the mesoporous structure which can stabilized the nanoparticles over-growing, in fact the mesoporous volume is 2.267 $cm^3\ g^{-1}$ and the surface area is totally given by the mesoporous structure. These values can be explained by a dense network of channels that start from the surface and reach the bulk of the particle. The morphology can stabilize the NPs during the synthesis and permits a stable growing the absence of aggregate as show in Figure 102c. Same consideration can be doing for Pt_xY@C2, the carbon present a totally mesoporous area with a pore distribution peaked at 8.5 nm and 11.1 nm, which permit an greater growth of the NPs. The size distribution shows a narrow unimodal distribution at 3.8 nm. The low NPs dimension obtained in Pt_xY@C7 and Pt_xY@C9 is associated to the microporosity network, in fact the 25 % of the total volume is microporous, so the NPs do not have space for grown and increase their dimension.

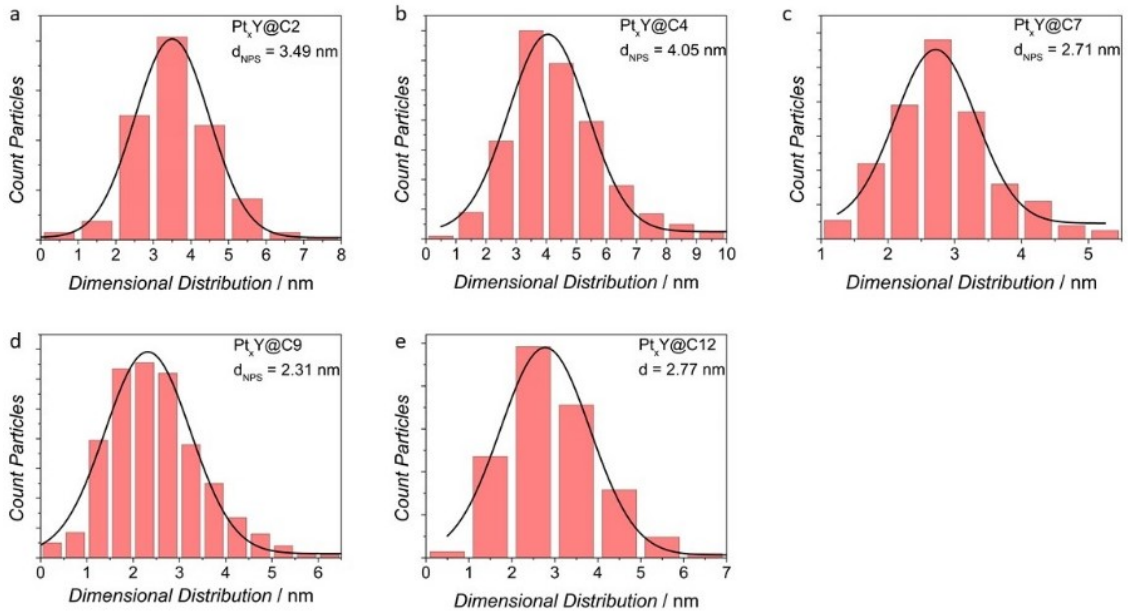

Figure 102: NPs dimensional distribution for a) Pt_xY@C2; b) Pt_xY@C4; c) Pt_xY@C7; d) Pt_xY@C9 and e) Pt_xY@C12

The Figure 103a show the Pt 4f peak of the Pt_xY@C7 NPs, the platinum NPs was deposited at 650 °C for 5 h on Carbon Black, acetylene, 100% compressed, 99.9%; the signal was fitted with 3 components: at lower B.E. the metallic Platinum; the components centered at 72.0 eV and 73.1 eV are assigned to oxidized Pt (II) and Pt(IV) species, respectively. The Pt (0) component of the Pt_xY NPs sample appears to be shifted by 0.2 eV to lower B.E. with respect the common Pt@C standard, taken as the reference. The Pt 4f shift can have various origins, including, for example, electron transfer from or to the support indicating the presence of an interaction with the support, nanoparticle size induced effect, alloy formation, etc. The Pt 4f shift is a clear evidence of the formation of a Pt_xY alloy, where the binding shift is generally attributed (in the case of alloy formation) to a change of the atoms surrounding Pt; Y in the place of Pt, therefore confirming the alloy formation. The Pt 4f spectra obtained for the different catalysts is very similar, the intensity of Pt (0) peak is higher than Pt (II) and Pt (IV), the component concentration obtained by the area comparison is very similar, Pt (0) 52 %, Pt (II) 13 % and Pt (IV) 35%. The problem is the inability to discriminate the platinum (0) in alloy form and not. A second, clearer, evidence of Pt_xY alloy formation arises from the analysis of the high resolution Y 3d photoemission peak. Y 3d peak has been fitted with 3 components of 156.3 eV, 157.4 eV and 158.4 eV [91]. The component at the highest Binding Energy can be correlate to Y_2O_3, the second one, at intermediate B.E., can be assigned to a species formed from the reaction of Y with the carbon substrate, whereas the peak at 156.3 eV is consistent with the formation of a Pt_xY alloy. Figure 103b,c,d,e and f shows the Y 3d peaks for the best five samples. The content of the yttrium in alloy form is lower than 20 % for all catalysts. The samples Pt_xY@C2 and Pt_xY@C12 present a Yttrium carbide component higher than yttrium oxide (50 and 37%, 54% and 35 %, respectively); in Pt_xY@C4 and Pt_xY@C9 the content of yttrium carbide and yttrium oxide is very similar, (43% and 49%, 41% and 48%, respectively).

Table 32: Yttrium alloy concentration calculated by Y 3d XPS spectra

	Y alloy
	%
PtxY@C2	8.5
PtxY@C4	12.6
PtxY@C7	20
PtxY@C9	17.5
PtxY@C12	6.9

Interesting is Pt_xY@C4 where MWCNT was used as support; the elemental analysis shows a sulphur content of 0.21 %. At higher binding energy respect the yttrium 3d peak is visible the S 2p peak associated to the thiophenic group. Compare the yttrium content for the catalysts is difficult because the alloy percentage obtained by the fitting is very similar. Anyway, the XPS confirm the effective alloy formation.

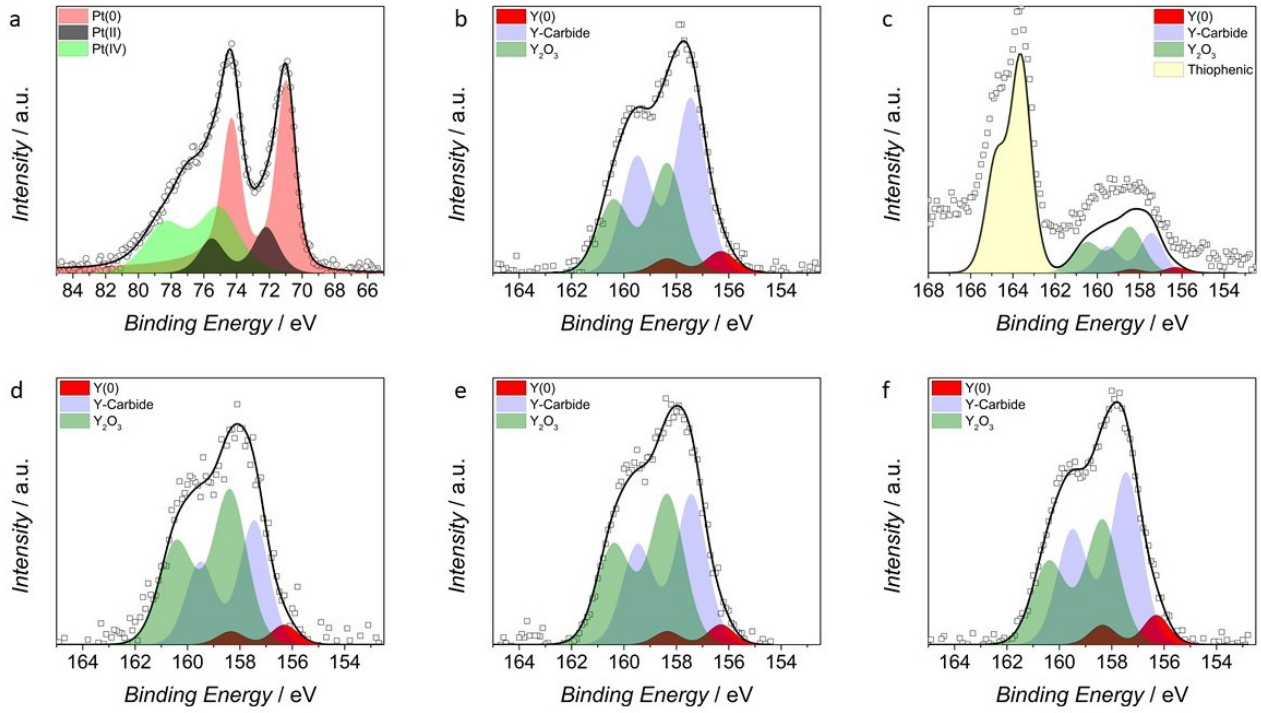

Figure 103: a) XPS spectra of Pt 4f for Pt_xY@C7; b) Y3d spectra for Pt_xY@C2; c) Y3d spectra for Pt_xY@C4; d) Y3d spectra for Pt_xY@C7; e) Y3d spectra for Pt_xY@C9 and f) Y3d spectra for Pt_xY@C12

Figure 104 show the XRD diffraction spectra for the best 4 catalysts. The diffraction peaks at the Bragg angles of 39°,46° and 67° are in good agreement with the (111), (200), (220), and (311) facets of platinum, respectively. The peak at 26° is connected to the carbon crystallography. The crystallite dimension obtained in Pt_xY@C2, Pt_xY@C9 and Pt_xY@C12 are very similar, 4.2 nm,4.5 and 3.9 nm. The dimensions are calculated by Scherrer Equation using the peak 111 and 220. The two peaks show a a very similar crystallography size for the Pt nanoparticles. Pt_xY@C7 show an crystallite dimension of 5.9 nm. In this last case the determination of the crystallite dimension is difficult due to the low intensity of Platinum peaks.

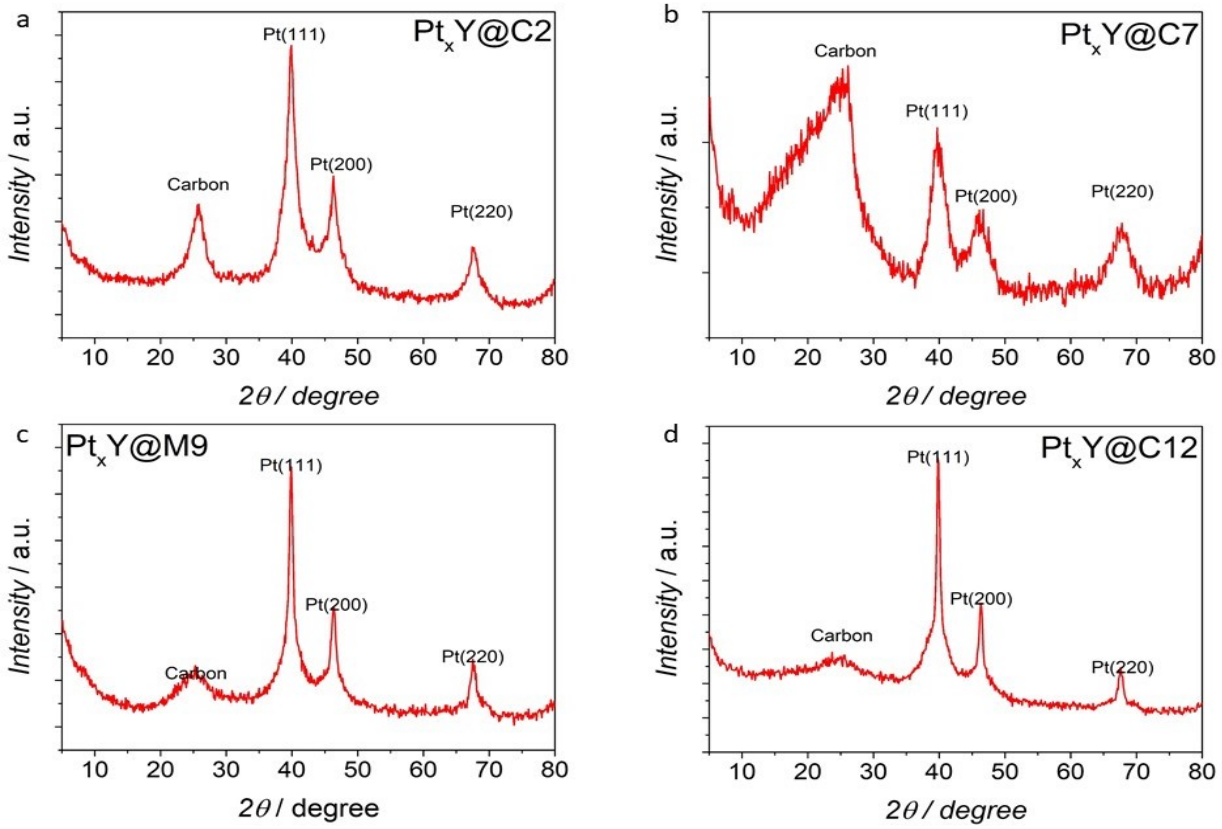

Figure 104: XRD spectra for a) PtxY@C2; b) PtxY@C7; c) PtxY@C9 and d) PtxY@C12

Yoo et al. reported that PtxY alloy diffraction peaks show a slight shift, with respect to the Pt face centered cubic (fcc) crystal structure, towards lower 2θ values and that the shift is more evident passing from Pt_9Y to Pt_1Y. Such a shift was reported to be a possible evidence for the alloy formation between Pt and Y. In the present case, the same evaluation is not straightforward, since diffraction peaks are wide due to the small crystalline domain. The determination of the actual Pt/Y ratio was not possible by XRD and so there is no indication of a definite stoichiometry [89].

9.4.3 Electrochemical Characterization

All catalysts were fully electrochemical characterized in $HClO_4$ 0.1 M electrolyte using a standard three electrode cell. The electrode set up is composited by a RDE in Glassy Carbon as working electrode, a Platinum wire commercial electrode as counter electrode and a Reversible Hydrogen Electrode as Reference. Figure 105 a, b and c show the cyclic voltammetry recorded in Argon saturated solution at 50 mV s^{-1}. The cyclic voltammetry shows the typical platinum region, the hydrogen adsorption/desorption region, the capacitive region and the Pt oxide formation and stripping. Figure 105a,b correspond to the catalysts synthetized using a commercial carbon while Figure 105c to the homemade carbon. The first different is the capacitive current between the homemade and the commercial material. The different value obtained is connected to a low graphitization grade of the carbon support obtained in the homemade carbon support.

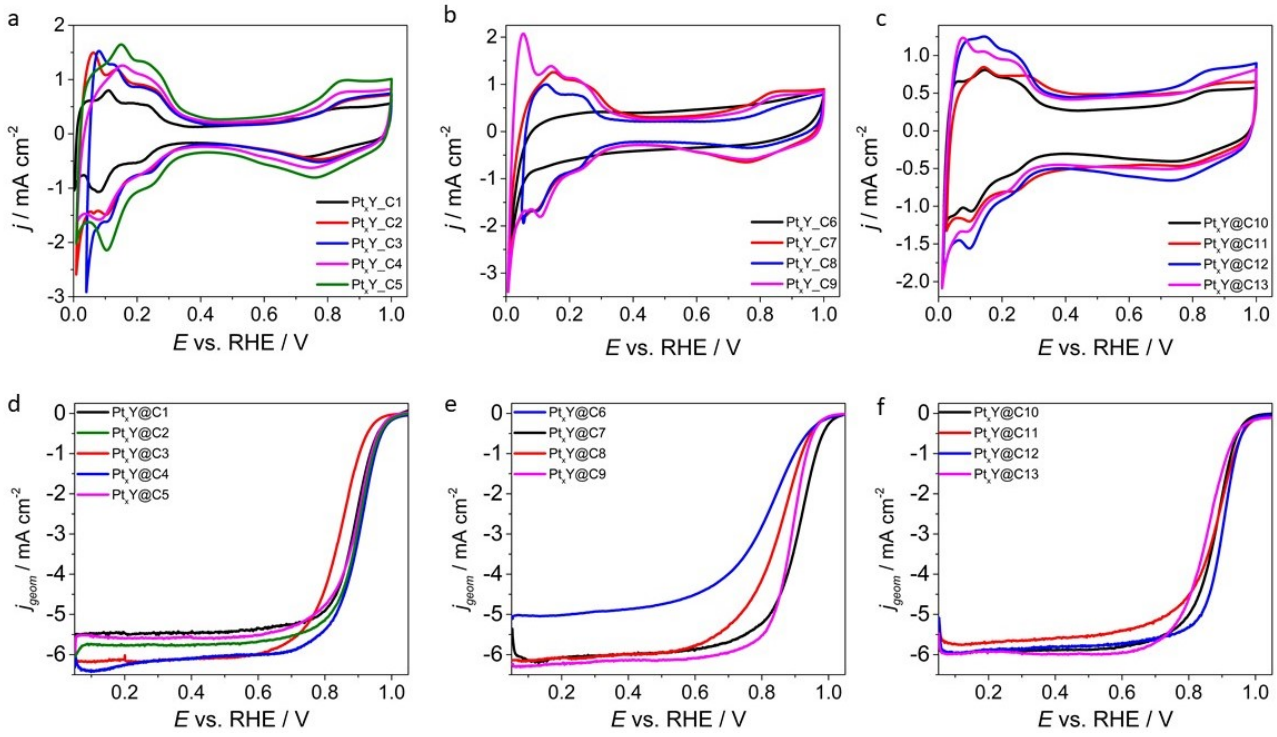

Figure 105: a,b,c) Cyclic Voltammetry at 50 mV s^{-1} recorded in $HClO_4$ 0.1 M, Argon saturated electrolyte; d,e,f) LSV with RDE at 1600 rpm and 20 mV s^{-1} in O_2 saturated electrolyte

The platinum content was evaluated by ICP-MS, the theoretical value for the synthesis was 27.0 %, The contents obtained are very similar, indicate a good reproducibility. EPSA was calculated considering the cyclic voltammetry recorded in Argon saturated solution at different scan rate. Table 33 show the corresponding value for Platinum content, Electrochemical Platinum Surface Area and Electrochemical Surface Area for the Pt_xY catalysts. The conversion from EPSA to ECSA is obtained dividing the EPSA for the platinum loading (15 µg cm^{-2}). For the best five samples the EPSA follow the next trend.

$$Pt_xY@C7 > Pt_xY@C9 > Pt_xY@C12 > Pt_xY@C4 > Pt_xY@C2$$

Pt_xY@C7, Pt_xY@C9 and Pt_xY@C12 shows and ECSA higher than 100 $m^2\ g^{-1}$, the sample obtained with Graphitized Carbon Black owns an EPSA of 3.51 cm^2. Very similar is the EPSA obtained when Mesoporous Carbon treated with sulphuric acid is used as support. The EPSA trend follow the same trend obtained with the NPs dimension, low NPs dimension correspond to an high population density of active site so a high Electrochemical Surface Area. PtxY@C6 show a particular Cyclic voltammetry, the Adsorption/Desorption peak of hydrogen are totally absence; the Carbon used for the synthesis was Graphitized Carbon Black hydrophilic pore surface, during the electrochemical measurement the low mechanic resistance and the high stability in the electrolyte solvent have caused a detachment of the material from the electrode. For concluding Pt_xY@C6 own a low mechanical and electrochemical stability due to the intrinsic characteristic of the support used for the platinum deposition. All materials present a PtO_x formation and stripping peak at the same potential. The Hydrogen Adsorption/Desorption Region is well defined, and different crystallographic peaks can be identified. In Adsorption Region from higher to lower potential, Pt(111) at potential of 0.2 V vs. RHE, Pt(110) near 0.1 V vs RHE were identified.

Table 33: Platinum content and electrochemical results for PtxY catalysts. Effect of the carbon support

	Pt_{ICP}	*EPSA*	*ECSA*
	$\%_w$	cm^2	$m^2\ g^{-1}$
Pt_xY@C1	28.1 ± 0.7	2.05 ± 0.10	69.6 ± 3.5
Pt_xY@C2	27.4 ± 0.7	1.59 ± 0.23	56.2 ± 7.8
Pt_xY@C3	27.8 ± 0.7	4.17 ± 0.21	141.7 ± 7.1
Pt_xY@C4	27.4 ± 0.7	1.96 ± 0.20	67.7 ± 6.7
Pt_xY@C5	25.3 ± 0.6	2.46 ± 0.27	85.8 ± 9.3
Pt_xY@C7	28.4 ± 0.7	3.51 ± 0.18	119.3 ± 6.0
Pt_xY@C8	26.7 ± 0.7	2.25 ± 0.11	76.6 ± 3.8
Pt_xY@C9	24.8 ± 0.6	3.38 ± 0.17	114.8 ± 5.7
Pt_xY@C10	27.4 ± 0.7	2.17 ± 0.11	73.7 ± 3.7
Pt_xY@C11	24.9 ± 0.6	1.35 ± 0.07	46.1 ± 2.3
Pt_xY@C12	26.1 ± 0.7	3.04 ± 0.15	103.4 ± 5.2
Pt_xY@C13	25.7 ± 0.6	2.81 ± 0.14	95.5 ± 4.8

Table 34 show the electrochemical results obtained from Linear Sweep Voltammetry at 1600 rpm and 20 mV s^{-1} in anodic scan in O_2 saturated $HClO_4$ 0.1 M electrolyte solution. The catalytic activity was evaluated considering the $E_{1/2}$, Mass Activity and Specific Activity. XPS have reveals the Platinum Yttrium alloy formation in the best five catalysts. The limited current density is close to the theoretical value; the half wave potential is near at 0.900 V vs. RHE for all five catalysts, the $E_{1/2}$ obtained for Pt/C was 0.867 V vs RHE, so the half wave potential for Pt_xY catalysts is higher of c.a. 30 mV than the commercial standard. Considering the $E_{1/2}$ and the the Mass Activity, the catalysts follow the next trend:

PtxY@C7 > PtxY@C4 > PtxY@C12 > PtxY@C2 > PtxY@C9

The catalytic activity obtained is influence by both the alloy formation and its amount and both by the NPs dimension. Pt_xY@C7 show a MA of 449 A g^{-1}, two times higher than Pt/C and a Pt_xY alloy content of 20 % evaluated by XPS. The NPs dimension obtained was 2.7 nm. Several articles describe as the best dimension for Pt_xY alloy NPs are between 5 nm to 9 nm; in this range the material show the best performance. Pt_xY@C4 show a lower platinum yttrium content (12.4 %, evaluated by XPS), and a NPs dimension of 4.1 nm; the mass activity and the half wave potential obtained for Pt_xY@C4 are 0.904 V vs RHE and 428 A g^{-1}. Despite the high Pt_xY content obtained in PtxY@C9 (17.5 %) the Mass Activity was 327 A g-1, the low performance is connected to the low NPs dimension obtained and to the formation of aggregates with a dimension of 20 nm as visible in TEM images. The Specific Activity obtained followed a similar trend to Mass Activity, Pt_xY@C4, Pt_xY@C7 and Pt_xY@C12 shows a SA between 0.32 mA cm^{-2} to 0.39 mA cm^{-2}, considering the error associated to the measurements the values obtained are equal. The samples Pt_xY@C2 and Pt_xY@C9 owns a Specific activity of 0.24 mA cm^{-2} and 0.29 mA cm^{-2}, respectively. The other samples show an mass activity lower than 250 A g^{-1}, the electrochemical performance is connected to the absence of platinum yttrium alloy. The catalytic activity obtained are in good correlation with the formation of platinum NPs and yttrium oxide particles. The catalytic activity higher than standard Pt/C of these samples can be describe by the low NPs dimension, less than 2.5 nm.

Table 34: Electrochemical results for Pt_xY@C catalysts. Effect of the carbon support

	$\|j_L\|$	$E_{1/2}$ vs. RHE	i_k	*MA*	*SA*
	mA cm^{-2}	V	mA	A g^{-1}	mA cm^{-2}
Pt_xY@C1	5.45 ± 0.13	0.896 ± 0.007	0.79 ± 0.04	270 ± 14	0.388 ± 0.039
Pt_xY@C2	5.77 ± 0.11	0.900 ± 0.009	1.11 ± 0.06	377 ± 19	0.241 ± 0.024
Pt_xY@C3	6.12 ± 0.10	0.853 ± 0.004	0.26 ± 0.03	89 ± 11	0.063 ± 0.011
Pt_xY@C4	6.09 ± 0.10	0.904 ± 0.007	1.26 ± 0.06	428 ± 21	0.317 ± 0.032
Pt_xY@C5	5.58 ± 0.12	0.900 ± 0.006	0.93 ± 0.09	316 ± 32	0.170 ± 0.026
Pt_xY@C7	6.09 ± 0.12	0.897 ± 0.007	1.32 ± 0.02	449 ± 7	0.376 ± 0.011
Pt_xY@C8	5.00 ± 0.10	0.818 ± 0.007	0.24 ± 0.01	81 ± 4	0.106 ± 0.011
Pt_xY@C9	5.91 ± 0.12	0.883 ± 0.008	0.96 ± 0.03	327 ± 11	0.284 ± 0.019
Pt_xY@C10	6.21 ± 0.13	0.886 ± 0.008	0.82 ± 0.08	279 ± 28	0.378 ± 0.056
Pt_xY@C11	5.65 ± 0.14	0.883 ± 0.008	0.70 ± 0.11	239 ± 39	0.519 ± 0.111
Pt_xY@C12	5.84 ± 0.12	0.903 ± 0.008	1.19 ± 0.10	405 ± 35	0.392 ± 0.053
Pt_xY@C13	5.97 ± 0.15	0.857 ± 0.007	0.38 ± 0.09	128 ± 30	0.134 ± 0.038

9.4.4 Conclusion

Surface area, graphitization grade, structure, resistivity and conductivity are the main characteristics of a carbon. For an optimal metal NPs deposition, the carbon must have an high surface area, generally higher than 100 m^2 g^{-1}, a mesoporous structure and a resistivity of 20 S m^{-1} at a pressure of 1850 kPa. The evaluation of the carbon support on the activity of platinum nanoparticles is a crucial step, because the previous expressed parameters owns a direct impact on the NPs growing and activity. The alloy formation and the electrochemical activity of Pt_xY alloy NPs were evaluated synthetized the platinum based material on different carbon support. The platinum content was evaluated by ICP-MS and the results confirm the high reproducibly of the synthesis in terms of method, protocols and chemical used. The best dimensions for Pt_xY NPs are in the range 6 nm - 9 nm; the bigger NPs were obtained with Carbon Black, acetylene, 100% compressed, 99.9% and MWCNT, >95% carbon basis,O.D. x L 6-9 nm x 5 µm, with 3.8 nm and 4.1 nm. These carbon supports own a pore distribution fixed at 3 nm, 5 nm, 8.5 nm and 11 nm. Another important characteristic is the micropore and mesopore volume, in these two supports the micropore/mesopore volume ratio is less than 0.1, so the surface area derives from the mesoporous structure. Carbon with low surface area do not permits the NPs growing and favour the aggregate formation. Carbon with an high surface area, as Pt_xY@C12, permits a perfect NPs distribution on the mesoporous carbon without any aggregate or cluster formation, but the morphological characteristics as microporosity stabilized the NPs at low dimension, the NPs show a size of 2.7 nm. The best sample was synthetized using a graphitic carbon black which show an high pore distribution at 8.8 nm and 11.8 nm and an high mesoporous volume. The carbon does not reveal pore with a dimension lower than 4.5 nm. Pt_xY@C show a Mass Activity and a Specific Activity higher than the commercial standard Pt/C 50%w (449 A g^{-1} vs 206 A g^{-1}). The electrochemical result show a 4 electron mechanism for the Oxygen Reductioon Reaction, the electron number was evaluated with RRDE and applied the Kouthechy-Levich Equation. The K-L Equation show a number of electron exchange from 3.83 to 3.95. XPS confirm the alloy formation, considering the Y 3d peak, the Pt_xY amount is 20% with a platinum yttrium ratio of 3.6.

9.5 Bibliography

[166] D. DJUROVIC, M. ZINKEVICH, F. ALDINGER, Thermodynamic modeling of the cerium–yttrium–oxygen system, Solid State Ionics. 179 (2008) 1902–1911. doi:10.1016/j.ssi.2008.06.011.

[167] J.S. Kanady, P. Leidinger, A. Haas, S. Titlbach, S. Schunk, K. Schierle-Arndt, E.J. Crumlin, C.H. Wu, A.P. Alivisatos, Synthesis of Pt3Y and Other Early-Late Intermetallic Nanoparticles by Way of a Molten Reducing Agent, J. Am. Chem. Soc. 139 (2017) 5672–5675. doi:10.1021/jacs.7b01366.

[168] C. Zhang, S.Y. Hwang, A. Trout, Z. Peng, Solid-state chemistry-enabled scalable production of octahedral Pt-Ni alloy electrocatalyst for oxygen reduction reaction, J. Am. Chem. Soc. 136 (2014) 7805–7808. doi:10.1021/ja501293x.

[169] Z. Chen, M. Waje, W. Li, Y. Yan, Supportless Pt and PtPd nanotubes as electrocatalysts for oxygen-reduction reactions, Angew. Chemie - Int. Ed. 46 (2007) 4060–4063. doi:10.1002/anie.200700894.

[170] J.N. Schwämmlein, G.S. Harzer, P. Pfändner, A. Blankenship, H.A. El-Sayed, H.A. Gasteiger, Activity and stability of carbon supported PtxY alloys for the ORR determined by RDE and single-cell PEMFC measurements, J. Electrochem. Soc. 165 (2018) J3173–J3185. doi:10.1149/2.0221815jes.

[171] M. Escudero-Escribano, K.D. Jensen, A.W. Jensen, Recent advances in bimetallic electrocatalysts for oxygen reduction: design principles, structure-function relations and active phase elucidation, Curr. Opin. Electrochem. 8 (2018) 135–146. doi:10.1016/j.coelec.2018.04.013.

[172] E. Zagoraiou, M.K. Daletou, L. Sygellou, S. Ballomenou, S.G. Neophytides, Highly dispersed platinum supported catalysts – Effect of properties on the electrocatalytic activity, Appl. Catal. B Environ. 259 (2019) 118050. doi:10.1016/j.apcatb.2019.118050.

[173] L. Lu, Nanoporous noble metal-based alloys: a review on synthesis and applications to electrocatalysis and electrochemical sensing, Microchim. Acta. 186 (2019). doi:10.1007/s00604-019-3772-3.

[174] X. Liu, E.H. Yu, K. Scott, Preparation and evaluation of a highly stable palladium yttrium platinum core-shell-shell structure catalyst for oxygen reduction reactions, Appl. Catal. B Environ. 162 (2015) 593–601. doi:10.1016/j.apcatb.2014.07.038.

[175] L.A. Estudillo-Wong, G. Ramos-Sanchez, L. Calvillo, G. Granozzi, N. Alonso-Vante, Support Interaction Effect of Platinum Nanoparticles on Non-, Y-, Ce-Doped Anatase and Its Implication on the ORR in Acid and Alkaline Media, ChemElectroChem. 4 (2017) 3264–3275. doi:10.1002/celc.201700715.

[176] Y.S. Kim, Y.R. Lee, B.J. Kim, J.H. Lee, S.H. Moon, H. Lee, Characterization of amorphous yttria layers deposited by aqueous solutions of Y-chelate alkoxides complex, Phys. C Supercond. Its Appl. 508 (2015) 42–48. doi:10.1016/j.physc.2014.10.013.

[177] M. Hosseinifard, A. Badiei, K. Ahmadi, Synthesis and characterization of yttrium aluminum garnet nanostructures by cathodic electrodeposition method, Adv. Powder Technol. 28 (2017) 411–418. doi:10.1016/j.apt.2016.10.012.

[178] P. Thakur, A. Kool, B. Bagchi, N.A. Hoque, S. Das, P. Nandy, The role of cerium(iii)/yttrium(iii) nitrate hexahydrate salts on electroactive β phase nucleation and dielectric properties of poly(vinylidene fluoride) thin films, RSC Adv. 5 (2015) 28487–28496. doi:10.1039/c5ra03524d.

[179] J. Tang, S. Jiang, Y. Liu, S. Zheng, L. Bai, J. Guo, J. Wang, Electrochemical determination of dopamine and uric acid using a glassy carbon electrode modified with a composite consisting of a Co(II)-based metalorganic framework (ZIF-67) and graphene oxide, Microchim. Acta. 185 (2018) 13–15. doi:10.1007/s00604-018-3025-x.

[180] P. Malacrida, H.G. Sanchez Casalongue, F. Masini, S. Kaya, P. Hernández-Fernández, D. Deiana, H. Ogasawara, I.E.L. Stephens, A. Nilsson, I. Chorkendorff, Direct observation of the dealloying process of a platinum-yttrium nanoparticle fuel cell cathode and its oxygenated species during the oxygen reduction reaction, Phys. Chem. Chem. Phys. 17 (2015) 28121–28128. doi:10.1039/c5cp00283d.

[181] M.K. Carpenter, T.E. Moylan, R.S. Kukreja, M.H. Atwan, M.M. Tessema, Solvothermal Synthesis of Platinum Alloy Nanoparticles for Oxygen, J. Am. Chem. Soc. 134 (2012) 8535–8542.

[182] R.T. Bonnecaze, N. Mano, B. Nam, A. Heller, On the Behavior of the Porous Rotating Disk Electrode, J. Electrochem. Soc. 154 (2007) F44. doi:10.1149/1.2403082.

[183] Y. Luo, N. Alonso-Vante, The Effect of Support on Advanced Pt-based Cathodes towards the Oxygen Reduction Reaction. State of the Art, Electrochim. Acta. 179 (2015) 108–118. doi:10.1016/j.electacta.2015.04.098.

[184] H. Tang, Y. Su, Y. Guo, L. Zhang, T. Li, K. Zang, F. Liu, L. Li, J. Luo, B. Qiao, J. Wang, Oxidative strong metal-support interactions (OMSI) of supported platinum-group metal catalysts, Chem. Sci. 9 (2018) 6679–6684. doi:10.1039/c8sc01392f.

[185] A. Fraser, Z. Zhang, G. Merle, U. Gbureck, S. Ye, J. Gostick, J. Barralet, Composite Carbon Nanotube Microsphere Coatings for Use as Electrode Supports, Adv. Funct. Mater. 28 (2018) 1–8. doi:10.1002/adfm.201803713.

[186] Y. Li, X. Zhang, S. Wang, G. Sun, Durable Platinum-Based Electrocatalyst Supported by Multiwall Carbon Nanotubes Modified with CeO 2, ChemElectroChem. 5 (2018) 2442–2448. doi:10.1002/celc.201800483.

10 Platinum and Palladium alloy NPs synthetized by Laser Ablation in Liquid

10.1 Abstract

$Pt_3(Pd_3)Y$ alloy owns an extraordinary catalytic activity when is used for catalysed the ORR reaction, the alloy formation and the control of the stoichiometric ratio between the two metals during the synthesis play a fundamental role. Several synthesis techniques were tested for increase the control on these two factors [187, 188].

Wet-Chemstry, Metal reduction with organic agents, solvothermal methods are the three main method the synthesis of $Pt_3(Pd_3)Y$ alloy NPs, the resulting catalysts show a mixture of platinum alloy and Pt-Y_2O_3. Actually, the Pt metallic and Y metallic sputtering in Ultra High Vacuum is the best method for the preparation of Pt(Pd) based alloy, the strong reaction environmental permits to limit the reaction between the yttrium and the oxidant species, for Pt_3Y, XPS show an alloy formation of 64 %. Several strategies are focused on the massive synthesis of $Pt_3(Pd_3)Y$ alloy [189].

Pd_3Y and Pt_3Y nanoparticles were for the first time successfully prepared by laser ablation synthesis in organic solvent (ethanol, acetone and *n*-hexane) and tested as active electrocatalysts in the oxygen reduction reaction in both acid and alkaline electrolytes. Laser Ablation is an particular synthesis method, a strong powered laser beam is focused on a metal target immersed in a solvent; the synthesis run at room temperature, atmosphere pressure, it is secure and not dangerous. Considering pulse time, the NPs formation is instantly, and so the metal than composed the target do not have the time for react with other species, in other world LASiS bypass the thermodynamic problem linked to the oxide formation. LASiS is an easy method for the synthesis of alloy nanoparticles, especially when these are composed of metals with different reduction potentials such as noble metals and transition metals such as Platinum, Yttrium or Palladium.

The NPs size and composition showed to be sensitive to the solvent employed for the synthesis, in fact when acetone and *n*-hexane were used, NPs form a core/shell structure with the shell being of Y_2O_3. Different solvent can be used, such as water, ethanol [190, 191, 192]

The formation of alloyed NPs was confirmed by TEM, XRD and XPS analysis. In particular, XPS analysis revealed that when ethanol was used, the superficial Pd_3Y alloy reaches it maximum (46 %) and 21 % in Pt_3Y catalysts. In the common platinum and palladium synthesis, the noble metal is present as mixture of pure platinum and in alloy form (also with different metal ratio). LASiS permit the synthesis of Pt_3Y and Pd_3Y NPs with a metal ratio very close to 3.

10.2 Palladium-Yttrium alloy NPs

10.2.1 Synthesis and Chemical

In LASiS, a colloid solution of the desired NPs is obtained by ablating with focused laser pulses a solid target dipped in a liquid solution, the synthesis sketch is show in Figure 106. Typically, the target has the same composition of the desired nanoalloys, therefore the LASiS runs at room temperature and pressure, starting just from raw materials, and it does not require precursors, stabilizers or other chemical additives, with remarkable advantages in terms of purity of products, low production costs and "green" procedure. Pd and Y form stable intermetallic compounds such as Pd_3Y, and metastable alloys in a wide range of compositions. Since the reduction potential of Y (–2.372 V from Y(III) to Y(0)) is much lower than Pd (0.915 V from Pd (II) to Pd(0)), the synthesis of Pd-Y nanostructures requires particular system as UHV with controlled atmospheres or drastic reduction conditions such as high temperature in molten hydrides or under hydrogen atmosphere. The former approaches are typically associated to agglomerated products, and the latter to the strict absence of water and oxygen, to thorough washing procedures with solvents to remove the remaining contaminants and, sometimes, also to the presence of stabilizing substrates or surface coating chemicals. The main problem is the yttrium stability, yttrium can react easy with different species formic Yttria [167, 193]. All these effects can modify the electrochemical performance of the catalyst vs. the Oxygen Reduction Reaction. The LASiS of Pd-Y NPs was performed following a well-established procedure, by focusing the pulses of a Q-switched Nd-YAG laser (1064 nm, 6 ns, 50 Hz, 100 mJ/pulse) with a 10 cm focal lens up to a fluence of 9 J cm^{-2} on a bimetallic Pd_3Y target dipped in, either, ethanol, acetone or *n*-hexane (all HPLC grade, from Sigma–Aldrich). After the synthesis, the colloids obtained in ethanol and acetone were reduced in volume by using a rotating evaporator up to a final concentration of 0.9 mg mL^{-1}. The colloid in hexane, which was not stably dispersed in the liquid over several hours, was centrifuged at 1000 rcf for 20 min, separated by the pristine liquid and re-dispersed in ethanol up to a final concentration of 0.9 mg mL^{-1}. The final colloids of Pd-Y nanoalloys were characterized by optical absorption spectroscopy, in 2 mm quartz cells, and by inductively coupled plasma assisted mass spectrometry (ICP-MS) [194, 195].

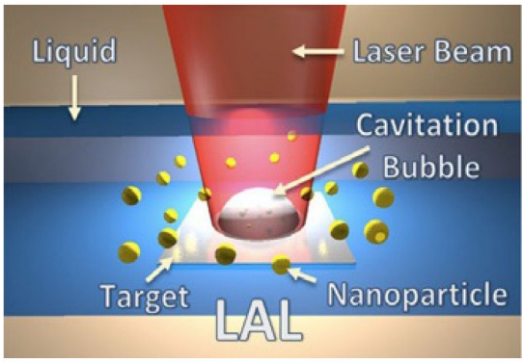

Figure 106: LASiS sketch

Data Source: B. Gökce, V. Amendola, S. Barcikowski, Opportunities and Challenges for Laser Synthesis of Colloids, ChemPhysChem. 18 (2017) 983–985. doi:10.1002/cphc.201700310.

10.2.2 Solvent Influence on Palladium-Yttrium NPs alloy formation: TEM, XPS and XRD analysis

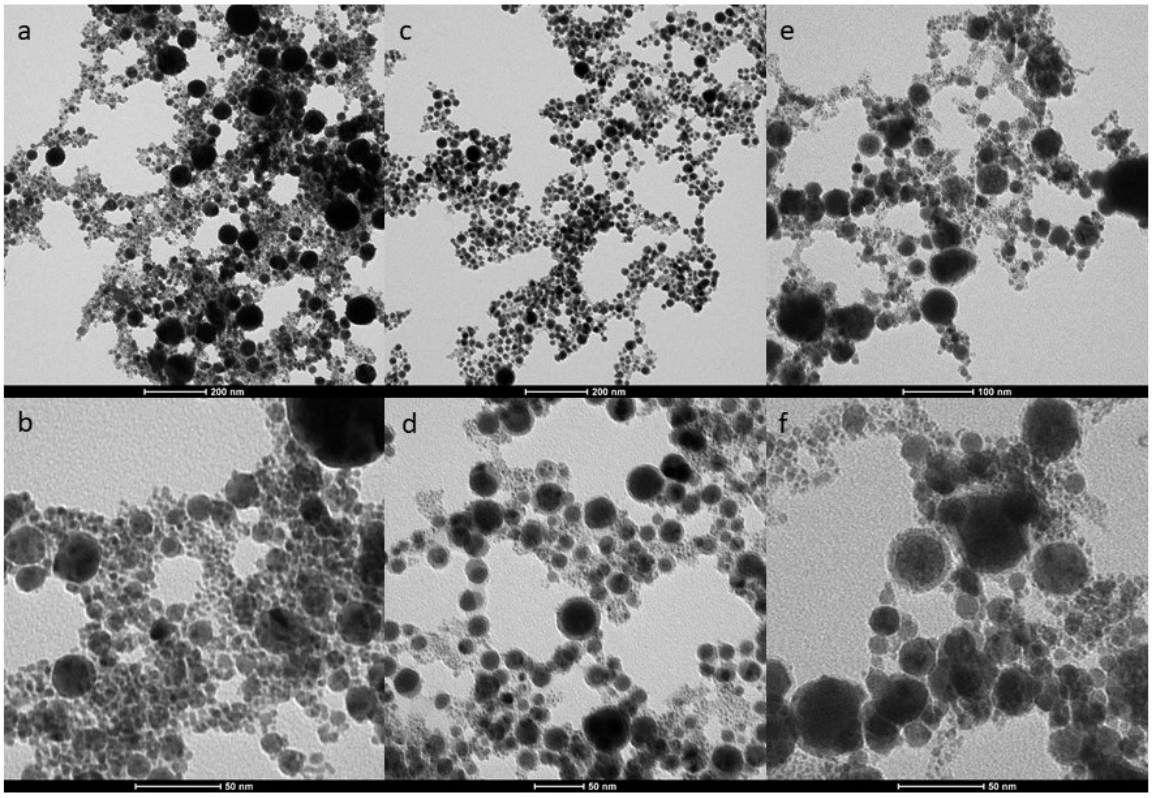

Figure 107: TEM images at different magnification for a,b) PdY-E; c,d) PdY-A and e,f) PdY-H

The TEM analysis show NPs with a size of tens of nanometers, centred at about 10 nm, 15 nm and 35 nm for, PdY-E (Figure 107 b and Figure 108 b), PdY-A (Figure 107 c and Figure 108 c) and PdY-H (Figure 107 a and Figure 108 a), respectively, although there is also a remarkable amount of small NPs in the range of 2-5 nm. The NPs synthetized by LASiS show a multimodal distribution in the range 1 nm – 50 nm [196].

Polydispersity is due to two effect, the synthesis method and is typical and intrinsic behaviour of palladium yttrium alloy. The same evidences, in term of NPs dimension and distribution, are observed for NPs obtained by chemical or physical way but in a lower dimensional range, 10 nm – 50 nm. Laser Ablation is an easy method for synthetized the metal NPs, but the control on the NPs size and distribution is impossible without a additive such as NaCl or PVP. The PdY NPs show the typical distribution for the LAL synthesis and, in addiction, the typical carbon core shell due to the organic solvent used as synthesis liquid. Modifying the synthesis parameter such as the pulsed laser or the laser power is possible control the NPs dimension in the range 100 nm – 250 nm.

The surface area derived by small NPs with a size lower than 5 nm is totally negligible respect the surface area due to the NPs with a dimension in the range 10 nm – 25 nm. PdY-E show spherical NPs with a dimension between 1 nm - 45 nm, when n-Hexane is used as synthesis solvent the resulting NPs show a size from 2.5 nm to 60 nm and in acetone the NPs show a bimodal NPs distribution, one from 1 nm to 6 nm and the second between 8 nm and 25 nm. Interestingly, the PdY-A and PdY-H catalysts, often exhibit a core-shell structure, with an electron-dense core surrounded by a nanometric thin shell with lower electronic contrast. The shell is made up to carbon, derived by the organic solvent used with the synthesis. The ratio between the shell thickness and the core diamenter is constant, an correspond to 0.12 for PdY-A and 0.18 for PdY-H [197].

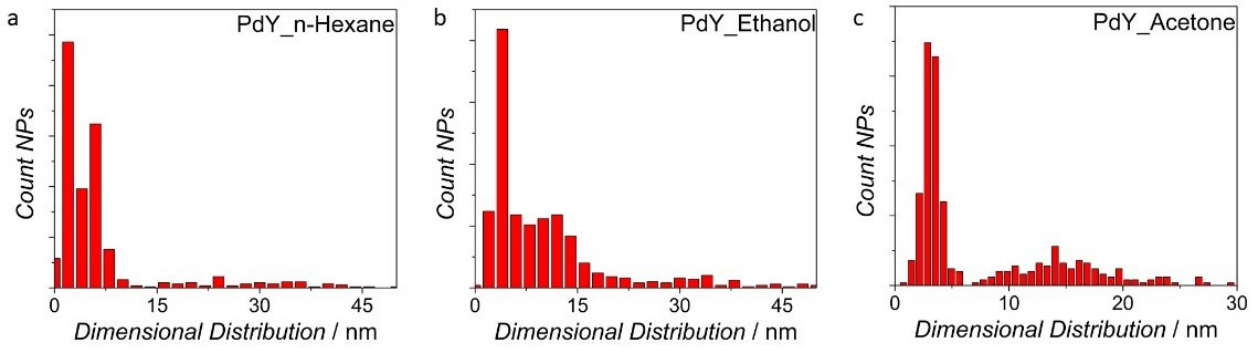

Figure 108: Dimensional distribution for a) PdY-H; b) PdY-E and c) PdY-A

XPS is a very sensitive technique for evaluate the oxidation state of the elements on the surface of the NPs, and confirm the presence of metallic Pd and Y. In particular, the Y 3d high resolution XPS spectra of can be easily deconvolute with 2 components, the signal at lower binding energy (156.3 eV) is assigned to the Pd_xY alloy, while the doublet at 157.8 eV is associated to Y_2O_3. Interestingly, the relative concentration of surface metallic Y in alloy form increases from 17% (Figure 109 e), in the case of sample PdY-H, to 38% and 46% in the case of samples PdY-A (Figure 109 f) and PdY-E (Figure 109 d) [196].

The Pd 3d peak, Figure 109 a, on the contrary, does not show any appreciable difference among the three samples, and it can be fitted with 2 doublets, one at 335.5 eV and a second one at 336.5 eV, assigned to Pd(II) and present is very low concentration (< 25 %). The component assigned to the alloy (335.5 eV) is shifted by 0.3 eV with respect to the 335.2 eV value for Pd nanoparticles normally found in the literature, Figure 109 b. Considering only the metallic component of the Y 3d signal and Pd 3d, it is possible calculate a percent abundance of Pd and Y of about 78% and 22 % ($Pd_{3.5}Y$), respectively, for samples PdY-A and PdY-H, while sample PdY-E has a Pd abundance of 72% and 28% for Y ($Pd_{2.6}Y$). The palladium and yttrium ration is very close to 3, the same trend was observed by ICP-MS.

TEM images show the carbon formation which is generated during the synthesis by interaction between the laser beam with the organic solvent. C 1s was fitted by three signal components corresponding to graphitic carbon C-C (284.4 eV) and carbonaceous species, characterized by the presence of C-O bonds (286.0 eV) and O-C=O bonds (288.2 eV), Figure 109 c. PdY-E, PdY-A and PdY-H show a very same C 1s spectra, with the same component and the same relative concetrations [197, 198].

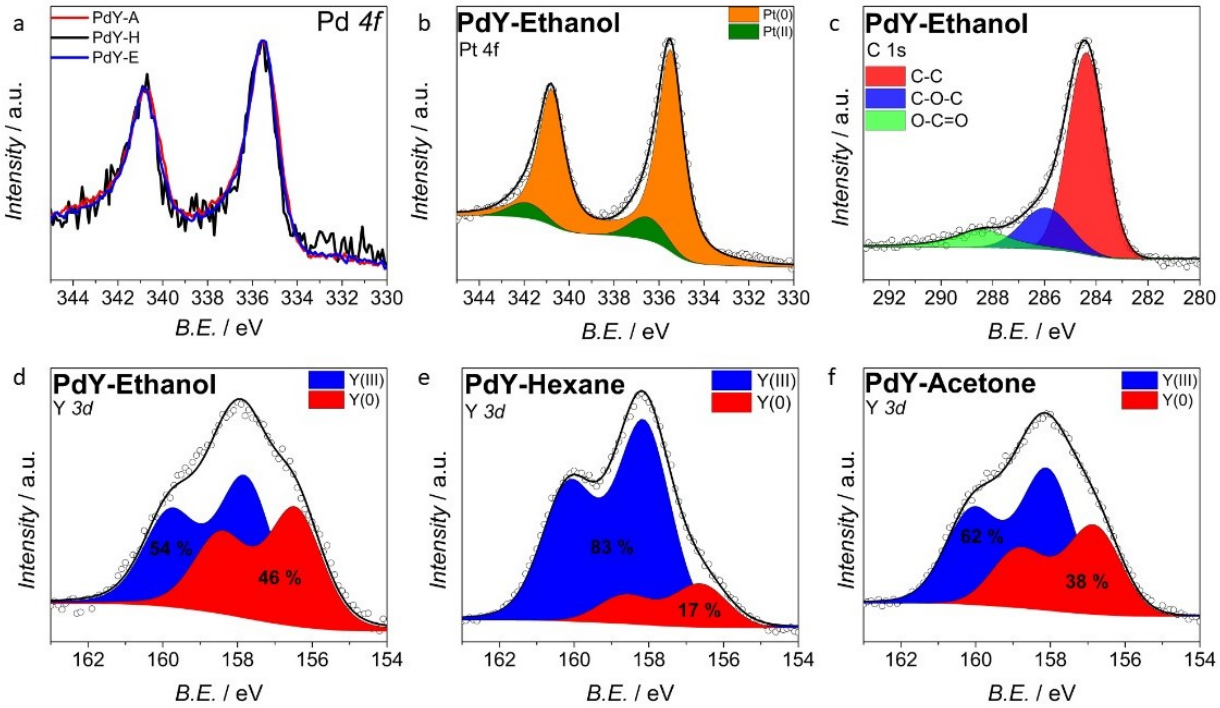

Figure 109: XPS spectra for: a) Pd 3d for PdY catalysts; b) Pd 3d spectra for PdY-E; c) C 1s for PdY-E; d) Y 3d for PdY-E; e) Y ed for PdY-H and f) Y 3d for PdY-A

The formation of a crystalline alloy structure in the PdY nanoparticles was confirmed by XRD. XRD is especially sensitive to the formation of Pd-Y alloys, because when Yttrium is present in the Palladium face centered crystal structure, the crystallographic cell appear expanded, due to the different atomic radius of the Pd(137 pm) and Y(182 pm). The cell expansion correspond to a clear shift of the diffraction pattern peaks to smaller angles [199, 200].

In the present case, the diffraction patterns of the three samples show the typical reflection peaks of the fcc cell of palladium, the XRD spectra do not show any peaks ascribable to the Yttrium

As expected, the fcc reflections are all shifted to lower angles, suggesting a larger lattice parameter and confirming the insertion of the yttrium on the palladium crystal structure and so the alloy formation. In fact, the cell parameters estimated from the Rietveld analysis resulted in 4.070 Å for PdY-H, 4.080 Å for PdY-A, and 4.079 Å for PdY-E, the cell parameters are higher than the tabled value for the Pd, 3.886 Å.

Vegaard approximation is fundamental theory for evaluating the alloy composition, in particular the metal ratio. PdY NPs synthetized by LASiS show a Pd/Y metal ratio very close to 3, in according with XPS; $Pd_{3.1}Y$ for PdY-E, $Pd_{2.9}Y$ for PdY-A, and $Pd_{3.0}Y$ for PdY-H.

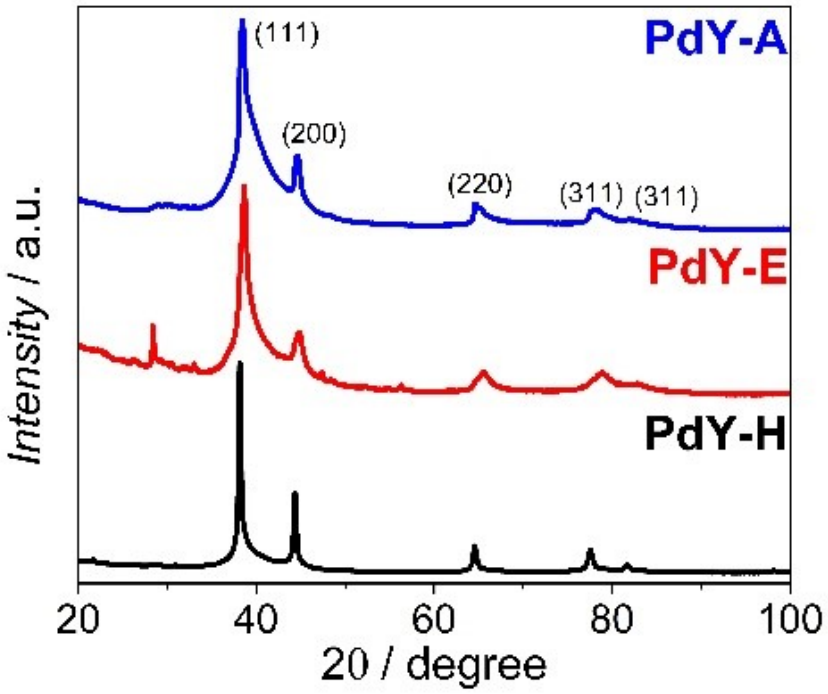

Figure 110: XRD crystallographic pattern for PdY catalysts

10.2.3 Electrochemical characterization in KOH 0.5 M

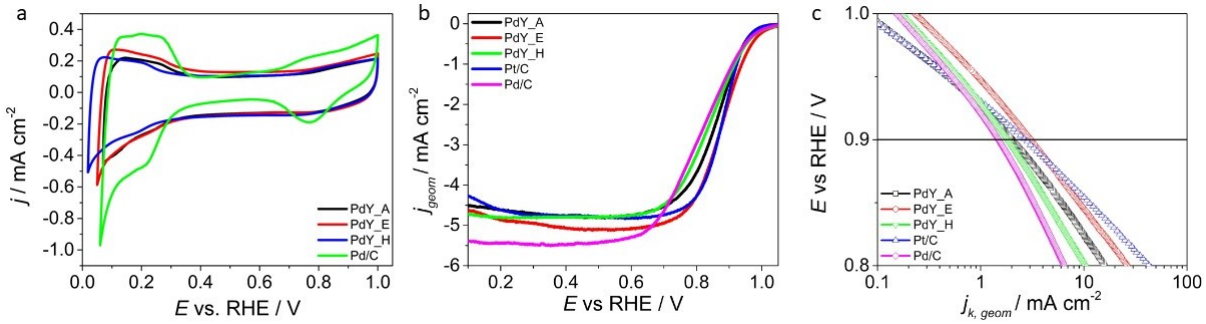

Figure 111: a) Cyclic voltammetry at 50 mV s^{-1} in Ar saturated KOH solution; b) LSV with RDE at 20 mV s^{-1} and 1600 rpm in O_2 saturated electrolyte and c) Tafel plot for PdY catalysts

The PdY NPs were characterized in alkaline solution, Figure 111a show the cyclic voltammetry at 50 mV s^{-1} for the different PdY catalysts and the commercial standard Pd/C.

The palladium oxide formation and stripping peaks are almost absent in PdY catalysts especially if compared with Pd/C which show two intensive peaks at 0.76 V vs. RHE and 0.79 V vs. RHE. The typical crystallographic peaks of the hydrogen adsorption and desorption on palladium are totally absente in PdY catalysts.

The Palladium Electrochemical Surface Area is in the range 0.3 cm^2 - 0.5 cm^2 for the PdY catalysts which are at least the half of the values obtained for the commercial Palladium Black, 1.06 ± 0.12 cm^2, and the standard

Pt/C, 1.78 cm^2 ± 0.11 cm^2. PdY-E, PdY- and PdY-H show an EPSA of 0.36 cm^2, 0.24 cm^2 and 0.51 cm^2, respectively.

PdY showed comparable NPs dimension than Palladium Black, therefore the low EPSA can be easy explained by c the presence of exposed Y_2O_3 over the NPs surface, yttria result being completely inactive to Oxygen Reduction Reaction. The presence of yttria on the NPs external surface is confirmed by the absence of a well-defined PdO_2 stripping. The commercial Palladium Black show NPs in the size range 5 nm – 20 nm. The NPs distribution in Pd/C catalysts is narrower than PdY, and the aggregation formation is more limited, for this reason the EPSA in Pd/C is higher than PdY. The same explanation can be applied for Pt/C catalyst, which shows an EPSA of 1.78 cm^2 in according the data present in literature. The cyclic voltammetry in Figure 111a in the range between 0.7 V vs. RHE and 0.85 V vs. RHE show only the capacitive current. The capacitive current in PdY catalysts is higher than Pd/C, this suggest a different resistivity between the PdY NPs obtained by Laser Ablation and the commercial standard. The carbon used as support is the same in all material, so every different are associated at the metal active phase and not to the carbon support.

The catalysts activity vs. ORR was evaluated by Linear Sweep Voltammetry with Rotating Disk Electrode, using a scan rate of 20 mV s^{-1} and a rotation rate of 1600 rpm, Figure 111b.

Half wave potential, $E_{1/2}$, for PdY is higher than the commercial standard Pd/C (PdY-E 0.889 V vs. RHE, PdY-A 0.862 V vs. RHE, PdY-H 0.842 V vs. RHE vs. 0.811 V vs. RHE in Pd/C). The limited current density agrees with the theoretical value obtaining by the Kouthecy-Levich Equation in alkaline solution KOH 0.5 M. Tafel slope determined in PdY, Figure 111c, are higher than Pt/C but lower than Pd/C, PdY catalysts shows a double Tafel slope which is known to be dependent on the formation of metal oxide on the NPs surface [201, 202].

Table 35: Electrochemical results obtained in KOH 0.5 M for PdY alloy NPs

	$E_{1/2}$	$\|j_L\|$	$j_{k,\,geom}$	Ts	$EPSA$	$ECSA$	SA	MA
	V vs RHE	mA cm^{-2}	mA cm^{-2}	mV dec^{-1}	cm^2	$m^2\ g^{-1}$	mA cm^{-2}	A g^{-1}
PdY_E	0.883	5.05	3.20	90	0.36	24	1.74	213.28
Δ_{PdY_E}	0.004	0.08	0.14	3	0.07	5	0.41	9.00
PdY_A	0.862	4.69	1.99	71	0.24	16	1.63	132.87
Δ_{PdY_A}	0.008	0.05	0.11	3	0.05	3	0.44	7.00
PdY_H	0.842	4.81	1.76	96	0.51	34	0.68	117.52
Δ_{PdY_H}	0.007	0.12	0.17	5	0.08	5	0.16	11.00
Pd/C	0.811	5.47	1.54	99	1.06	71	0.28	102.75
$\Delta_{Pd/C}$	0.006	0.15	0.11	6	0.12	8	0.05	7.00
Pt/C	0.880	4.81	2.61	63	1.78	119	0.29	174.00
$\Delta_{Pt/C}$	0.007	0.05	0.18	2	0.11	7	0.04	12.00

All PdY material synthetized by laser ablation show an electrochemical performance better than the Pd/C benchmark, PdY-E result be the catalyst with the lowest superficial Y_2O_3 content and showing the most

positive half wave potential, the highest Mass Activity and the highest limiting current density, followed by PdY-A and PdY-H. The electrochemical activity for PdY-E is almost comparable to the Pt/C. LSV indicating a comparable or even higher catalytic performance with respect to the commercial standard, Pd/C. In fact, the comparison of the mass activity determined at 0.9 V vs RHE, clearly stems the superior activity of PdY-E (213 ± 9 A g^{-1}) followed by Pt/C (174 A g^{-1}) > PdY-A (132 A g^{-1}) > PdY-H (117 A g^{-1}) > Pd/C (102 A g^{-1}). The mass activity increases with the increasing of the Pd_3Y alloy concentration. A very similar trend is obtained with the Specific Activity, the specific activity determined by considering the EPSA determined from the hydrogen adsorption/desorption region, is indicative of an outperforming behavior of PdY with respect to the benchmark materials. PdY-E and PdY-A show an incredible Specific Activity, five times higher than the SA evaluated for Pt/C and Pd/C.

PdY-E was tested with RRDE for the Hydrogen Peroxide Production, the comparison between the disk and ring current permit to determinate the electron number exchange. The electron number exchange is close to 4 (3.87). The strong electronic interaction between the palladium and yttrium in PdY alloy NPs affords better catalytic activity for PtY-X than the unalloyed Pd.

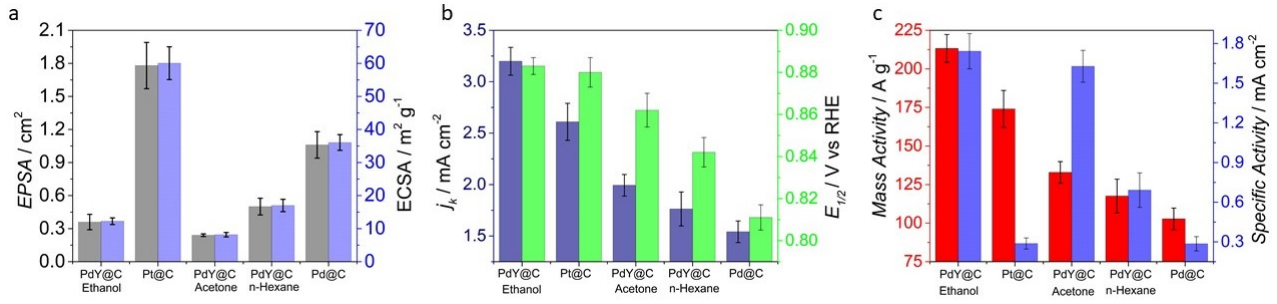

Figure 112: Electrochemical activity histogram, a) EPSA and EPSA; b) kinetic current and half wave potential; c) Mass Activity and Specific Activity

10.2.4 Electrochemical characterization in H_2SO_4 0.5 M

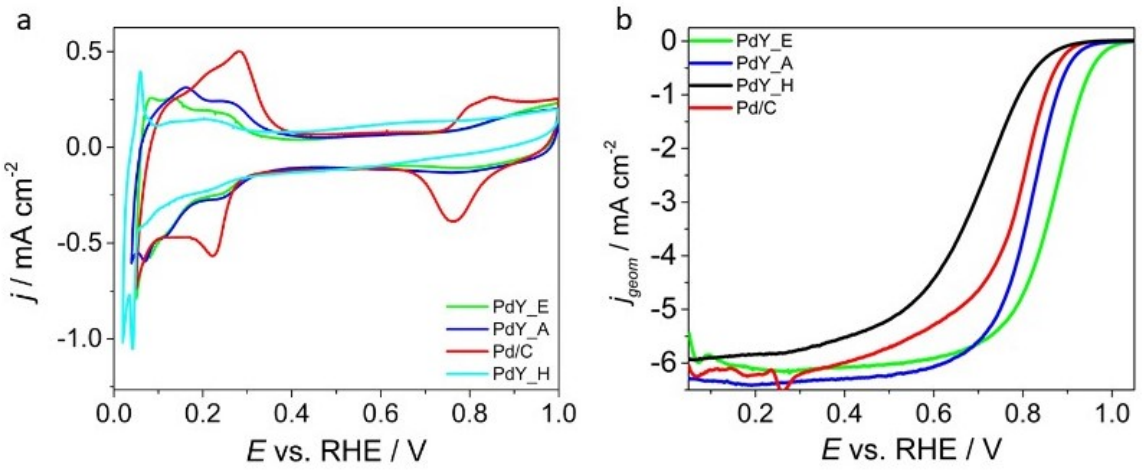

Figure 113: a) Cyclic voltammetry at 50 mV s-1 in Ar saturated H_2SO_4 0.5 M solution; b) LSV with RDE at 20 mV s^{-1} and 1600 rpm in O_2 saturated electrolyte

Figure 113a show the cyclic voltammetry at 50 mV s^{-1} in Ar saturated H_2SO_4 0.5 M solution for the catalysts synthetized by Laser Ablation and the standard Pd/C. Pd/C show the typical hydrogen adsoption desorption region and a very intensive PdO_2 of formation and stripping. The adsorption peak in H_2SO_4 are more defined than in KOH, due to the easy interaction between H^+ and palladium sites. The adsorption and desorption peaks in all material are at the same potential, which confirm the formation of the same crystallographic phases. The crystallographic peaks are well-defined for PdY-E and PdY-A. PdY-E and PdY_A show very similar EPSA value, 0.73 cm^2 and 0.89 cm^2, respectively. Considering the interaction between the hydrogen and the palladium, a correlation between NPs dimension and EPSA is easier in acid electrolyte than in alkaline electrolyte. TEM images of PdY-H show the formation of aggregate with high dimension, so the active palladium area is reduced, in fact PdY-H own an EPSA of 0.35 cm^2. Platinum and palladium commercial standard show a very high EPSA, 1.87 cm^2 and 1.31 cm^2 respectively, which correspond to an ECSA of 63 m^2 g^{-1} and 44 m^2 g^{-1}.

PdY were also tested in a O_2 saturated 0.1 M H_2SO_4 solution and results are reported in Table 36. PdY-E shows high catalytic activity versus ORR, with a half wave potential ($E_{1/2}$ = 0.851 ± 0.006 V vs RHE) comparable with the value observed for the Pt/C benchmark ($E_{1/2}$ = 0.862 ± 0.005 V vs RHE) and definitively better than Pd/C [70, 203].

Among the new catalysts the half wave potential decrease in the order

PdY-E, 0.851 V vs. RHE > PdY-A, 0.800 V vs. RHE > PdY-H, 0.699 V vs. RHE,

$E_{1/2}$ decrease with the decrement of PdY alloy concentration. In H_2SO_4 0.5 M and KOH 0.5 M the material shows the same activity trend for Oxygen Reduction Reaction. The best catalyst in terms of Mass Activity and Specific Activity result PdY-E, with 145 A g^{-1} and 0.587 mA cm^{-2}, the electrochemical performance is higher than other materials, PdY-H and PdY-A, and the commercial standard Pd/C, but lower than Pt/C which present the typical

Mass Activity of 200 A g^{-1}. The high Specific Activity value obtained for PdY-E is connected to the low EPSA determinate by Cyclic Voltammetry. It is worth noting that the MA for PdY-E determined at 0.9 V vs. RHE is slightly lower with respect to Pt/C but clearly higher than Pd/C.

Table 36: Electrochemical results obtained in H_2SO_4 0.5 M for PdY alloy NPs

	$E_{1/2}$ V vs RHE	$\|j_L\|$ mA cm^{-2}	$j_{k,\,geom}$ mA cm^{-2}	*EPSA* cm^2	*ECSA* $m^2\ g^{-1}$	*SA* µA cm^{-2}	*MA* A g^{-1}
PdY_E	0.851	6.08	2.186	0.73	24.8	587	145.7
Δ_{PdY_E}	0.006	0.13	0.12	0.09	3.1	10	7.8
PdY_A	0.800	6.11	0.54	0.89	30.3	120	36.3
Δ_{PdY_A}	0.009	0.14	0.08	0.06	2.0	5	5.3
PdY_H	0.699	5.84	0.24	0.35	11.9	134	15.9
Δ_{PdY_H}	0.011	0.09	0.07	0.07	2.4	8	4.7
Pd/C	0.789	6.18	0.22	1.31	44.6	33	14.6
$\Delta_{Pd/C}$	0.004	0.07	0.09	0.08	2.7	4	6.2
Pt/C	0.862	5.42	3.01	1.87	63.6	315	200.7
$\Delta_{Pt/C}$	0.005	0.15	0.19	0.11	3.7	6	12.9

10.2.4.1 Cl^- and ClO_4^- poisoning

The electrochemical properties of PdY NPs prepared in the Ethanol, Acetone and n-Hexane and deposited on a commercia Mesoporous Carbon was evaluated in $HClO_4$ 0.1 M. Perchloric Acid was firstly considered the best electrolyte solvent in fact ClO_4^- anions do not strongly adsorb on Pt NPs surface, so that any activity difference in the electrochemical signal can be ascribe to the electronic properties of the surfaces. The Pd/C and Pt/C cyclic voltammetry in 0.1 M $HClO_4$ electrolyte shows, typical, three distinct region: the hydrogen adsorption/desorption region between 0.0 V vs. RHE and 0.25 V vs. RHE, the double-layer region (capacitive current) between 0.25 V vs. RHE and 0.50 V vs. RHE, and the surface oxide formation/reduction region in the range 0.65 V vs. RHE and 0.8 V vs. RHE. The EPSA for Pd/C corresponding to a Pd loading of 15 µg cm^{-2} was 1.42 ± 0.05 cm^2, and 1.78 cm^2 for Pt/C [64, 204].

Comparing the cyclic voltammetry recorded in $HClO_4$ 0.1 M for the PdY NPs catalyst with the Pd/C or Pt/C, the adsorption/desorption region is less prominent than the commercial standard. Similarly, the formation and the stripping peaks for the palladium oxide are more less pronounced then Pd/C. The different electrochemical between the commercial standard and the synthetized PdY NPs can be appointed to the shell of yttrium oxide present over the nanoparticle surface which protect the palladium core and prevents its activation. The Y_2O_3 dissolution is very fast at pH 1 and especially in the potential range using for the electrochemical measurement, conversely to Y (0) that, being stable and not subject to the same effect. It is reasonable to assert that catalyst

particles expose a naked Pd surface to the acid electrolyte when the electrode is dipped in the acid electrolyte solution. The low electrochemical absorption of hydrogen and the low electrochemical performance vs. ORR might be the result of an electronic effect of the PdY alloy or of a poisoning effect. The adsorption of ClO_4^- and of the unavoidable Cl^- traces can be more accentuated on PdY, in virtue of a specific interaction arising from an electronic effect. The strong ClO^- adsorption on the Palladium could de-active the active site and so the resulting catalysts would be inactive vs. the ORR. The electrochemical performance determinate in O_2 saturated $HClO_4$ solution are very low for all catalysis, the half wave potential is lower than Pt/C and Pd/C of 300 mV, the Mass Activity is 2.0 A g^{-1}, 2.2 A g^{-1} and 2.1 A g^{-1}, for PdY-E, PdY-A and PdY-H, respectively. An current density plateau is observed only at potential lower than 0.3 V vs. RHE, the catalyst shows a very resistive comportment. The Tafel slope determinate by Linear Sweep Voltammetry at 20 mV s^{-1} and 1600 rpm are ca. 150 mV dec^{-1}, in comparison for Pt/C the Tafel Slope evaluated in the electronic transfer range is 50 mV dec^{-1}. The poisoning effect of $ClO4^-$ and Cl^- anion was evaluated added to H_2SO_4 0.5 M electrolyte solution different amount of corresponding acid, Figure 114. After every addition the EPSA was evaluated recorded a Cyclic Voltammetry ad different scan rate (50 mV s^{-1}, 20 mV s^{-1} and 10 mV s^{-1}) in Argon saturated electrolyte solution and the electrochemical activity for ORR was determinate by Linear Sweep Voltammetry at 1600 rpm and 20 mV s^{-1}. Increasing amounts of $HClO_4$ are added to the 0.1 M H_2SO_4 electrolyte; the Hydrogen Adsorption/Desorption peaks pattern disappeared reaching the same situation observed in 0.1 M $HClO_4$, Figure 114 a,c. Similarly, when HCl is added into a 0.1 M H_2SO_4 solution, the hydrogen desorption region decreases and a single peak at 0.060 V vs. RHE remains visible Figure 114 b,d. Therefore, it is evident that poisoning effects are at play when ClO_4^- or Cl^- anions are present in solution [205, 206].

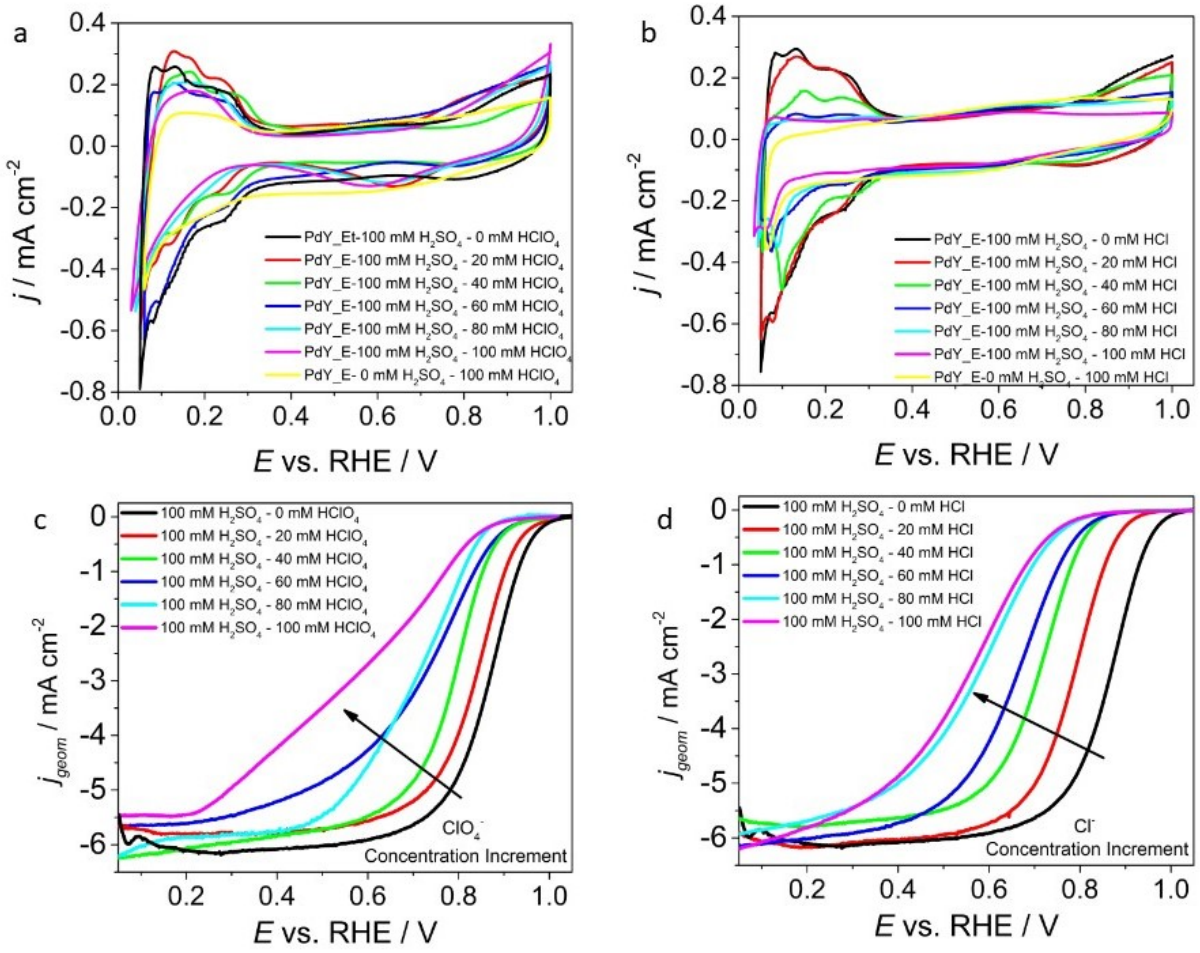

Figure 114: a) Cyclic Voltammetry at 20 mV s^{-1} at different adding of $HClO_4$ in H_2SO_4; b) Cyclic voltammetry at 20 mV s^{-1} at differt adding of HCl in H_2SO_4; c) LSv with RDE at 20 mV s^{-1} and 1600 rpm at differt adding of $HClO_4$ in H_2SO_4 and d) LSv with RDE at 20 mV s^{-1} at differt adding of HCl in H_2SO_4

The catalytic performances of PdY NPs towards the oxygen reduction reaction, in 0.1 M $HClO_4$, show a kinetic hindrance versus the ORR, the limiting current is reached only around 0.2 V vs. RHE and consequently the half wave potential is lesser positive than Pd/C reference material and Pt/C commercial catalyst which show the limiting current at 0.6 V vs. RHE and 0.7 V vs. RHE. Using the Tafel Plot is possible compare the kinetic current densities of benchmarks and PdY catalysts, PdY/C catalysts shows significant i_k only at potentials 100-150 mV less positive than commercial standards ca. 0.7 V vs. RHE),in addittion with values several orders of magnitude lower with respect to Pd/C or Pt/C. Pd/C and Pt/C show Tafel slopes of 64 mV/dec^{-1} and 58 mV/dec^{-1}, respectively (0.8 V vs. RHE - 0.9 V vs. RHE) in agreement with results obtained in literature in the same electrolyte, whereas PdY-E exhibit Tafel slopes of 180 mV dec^{-1} in the potential range 0.55 V vs. RHE and 0.7 V vs. RHE, confirming a sluggish kinetics. Higher Tafel slope valure are obtained with PdY-A and PdY-H.

In $HClO_4$ electrolyte, Palladium Pd is more susceptible to oxidize at more negative potential than Pt and so more easily poisoned by anion including ClO_4^- and other oxygen containing species than Pt.

The $E_{1/2}$ for PdY-E LSV shifts toward more negative potential at the increasing of ClO_4^- concentration and the LSV with RDE at 0.1 M ClO_4^- tends to resemble the one observed in 0.1 M $HClO_4$. A very similar behavior was observed when increasing concentrations of chloride anion were evaluated. Therefore, it can be asserted that the adsorption of anions such as ClO_4^- and Cl^- deeply affect the Pd_3Y alloy electrochemical behavior, since such anions occupy the sites for O_2 adsorption resulting in a slower ORR reaction rate than on Pd or Pt. In PdY the d-band energy is at higher level than d band in Platinum, so the Palladium alloy adsorb very strongly the oxygen molecule; the high d-band energy and the lower potential made itself very sensitive to the poisoning. SO_4^{2-} show a different hydrodynamic size, and so the absorption is less effective on Pd_3Y. In fact an high catalytic activity can be observed for the PdY catalysts in H_2SO_4 electrolyte,which is comparable with that observed on Pt/C and even higher than Pd/C.

In particular when perchloric acid was added to H_2SO_4 electrolyte solution, half wave potential shift from 0.851 V vs RHE in pure sulphuric acid electrolyte to 0.581 V vs. RHE when is added an equimolar amount of $HClO_4$. The Mass Activity decrease every addiction, from 145 A g^{-1} to 4 A g^{-1}, the same trend was observed for the Specific Activity and for EPSA. The LSV with RDE obtained after the adding of 0.1 M of $HClO_4$ at the electrolyte appears very similar to the LSV recorded directly in Perchloric Acid electrolyte, Figure 114 a,c. The performance drastically reduces when is added 0.06 M of perchloric anion. The limited current density decreases with the increment of perchloric acid[205, 206].

Table 37: Electrochemical Results for the different additions of $HClO_4$

	H_2SO_4	$HClO_4$	$E_{1/2}$	$\|j_L\|$	$j_{k,\,geom}$	*EPSA*	*ECSA*	*SA*	*MA*
	M	M	V vs RHE	mA cm^{-2}	mA cm^{-2}	cm^2	$m^2\ g^{-1}$	μA cm^{-2}	A g^{-1}
PdY_E	0.1	0	0.851	6.08	2.186	0.73	24.8	584	145.7
Δ_{PdY_E}			0.006	0.13	0.117	0.09	3.1	10	7.8
	0.1	0.02	0.841	5.79	1.279	0.71	24.1	352	85.3
			0.012	0.14	0.120	0.06	1.9	8	8.0
	0.1	0.04	0.786	5.92	0.329	0.63	21.5	102	21.9
			0.006	0.11	0.031	0.05	1.7	4	2.1
	0.1	0.06	0.749	5.63	0.276	0.52	17.6	104	18.4
			0.007	0.06	0.026	0.04	1.4	4	1.7
	0.1	0.08	0.728	5.85	0.090	0.55	18.6	32	6.0
			0.011	0.12	0.008	0.04	1.5	2	0.6
	0.1	0.1	0.581	5.46	0.067	0.43	14.7	30	4.5
			0.008	0.11	0.006	0.03	1.2	2	0.4
	0	0.1	0.453	5.42	0.025	0.36	12.2	14	1.7
			0.009	0.05	0.002	0.07	2.4	2	0.2

When Chloride anions were added the electrochemical activity decrease more drastically than HClO4. Cl^- adsorb more stronger than $ClO4^-$, for platinum but also palladium the main cause of metal deactivation is associable to the chloride present. After the first addition the Mass Activity pass from 145 A g^{-1} to 20 A g^{-1}, and after decrease until to 2 A g^{-1} when 0.1 M of HCl was added to the electrolyte solution. Specific Activity show a particular trend, before decrease from 584 μA cm^{-2} to 70 μA cm^{-2} when was added 0.08 M HCl and after increase until 103 μA cm^{-2} (in pure Chloridric acid). Specific activity was calculated as ratio between the kinetic current calculated at 0.9 V vs. RHE and the EPSA.

Table 38: Electrochemical Results for the different additions of HCl

	H_2SO_4	HCl	$E_{1/2}$	$\|j_L\|$	$j_{k,\,geom}$	*EPSA*	*ECSA*	*SA*	*MA*
	M	M	V vs RHE	mA cm^{-2}	mA cm^{-2}	cm^2	$m^2\ g^{-1}$	μA cm^{-2}	A g^{-1}
PdY_E	0.1	0	0.851	6.08	2.186	0.73	24.8	584	145.7
Δ_{PdY_E}			0.006	0.13	0.117	0.09	3.1	10	7.8
	0.1	0.02	0.789	6.12	0.320	0.70	23.7	89	21.3
			0.007	0.11	0.017	0.03	1.2	3	1.1
	0.1	0.04	0.717	5.76	0.045	0.28	9.5	31	3.0
			0.008	0.09	0.002	0.01	0.5	2	0.2
	0.1	0.06	0.663	0.15	0.053	0.13	4.4	80	3.5
			0.004	0.07	0.003	0.01	0.2	3	0.2
	0.1	0.08	0.591	5.76	0.034	0.09	3.1	74	2.3
			0.005	0.13	0.002	0.00	0.2	3	0.1
	0.1	0.1	0.571	5.88	0.029	0.07	2.4	82	2.0
			0.006	0.11	0.002	0.00	0.1	3	0.1
	0	0.1	0.569	5.47	0.024	0.05	1.6	103	1.6
			0.008	0.10	0.001	0.00	0.1	3	0.1

10.2.5 Conclusion

Pd_3Y NPs were for the first time successfully synthetized by laser ablation synthesis in ethanol, acetone and *n*-hexane. TEM measurements confirmed the formation of NPs in the range 10 nm - 20 nm, TEM show the formation of large NPs in the dimensional range 60 nm – 80 nm.

XRD spectra show the typical Palladium pattern; the crystallographic components resulted be shifted at lower angle due the insertion of the yttrium on the crystallographic structure of the palladium. XRD diffraction patterns estimated from the Rietveld analysis agree with the cell parameters of Pd_3Y alloy.

Pd_3Y NPs showed different concentration of superficial alloyed Y and Y_2O_3 depending on the synthesis solvents, in particular Pd_3Y NPs prepared in ethanol was the one with the highest superficial value of alloy (46 %). When acetone and hexane were used as solvent, 38 % and 17 % of alloy was obtained.

The electrochemical properties of Pd_3Y NPs were investigated in H_2SO_4 and KOH. The electrochemical characterization of PdY NPs confirmed high catalytic activity for ORR in both 0.1 M H_2SO_4 and 0.5 M KOH, with a clear dependence from the superficial alloy content. In H_2SO_4, PdY-E show a Mass Activity of 146 ± 8 A g^{-1} and in KOH of 213 ± 9 A g^{-1} at 0.9 V vs. RHE; resulted clearly more active than Pd black which show, in Sulphuric acid, a MA of 15 ± 6 A g^{-1} nd in KOH MA=102 ± 7 A g^{-1} at 0.9 V vs. RHE.

The different performance between the pure Pd and the alloy PdY confirming that a strong electronic effect due to the introduction of Y in the Pd lattice affords better catalytic activity for PtY-E than the unalloyed Pd.

What remains to discuss is the very different catalytic activity and EPSA found in $HClO_4$ electrolyte with respect to H_2SO_4. It is our belief that poisoning effects due to the adsorption of ClO_4^- and/or Cl^- traces in acidic electrolyte is the real discriminant for the low catalytic activity of PdY found in 0.1 M $HClO_4$ medium with respect to the high catalytic activity observed in H_2SO_4 and alkaline environment. In fact, if an electronic effect would be at play as claimed in literature by other authors, the effect would be in the same direction in all the electrolytes. In conclusion, LaSiS was confirmed as a fruitful synthetic route for the preparation of electrocatalysts for both proton and anion exchange fuel cell.

10.3 Platinum-Yttrium alloy NPs

10.3.1 Synthesis and Chemical

Generally, platinum show a catalytic activity vs. the oxygen reduction redaction higher than palladium. Platinum NPs show a higher stability than Pd NPs. Pt_3Y alloys were predicted to be the most stable Pt based binary. Pt_3Y alloys able to bind oxygen species slightly less than pure Pt, therefore showing a higher ORR activity. The synthesis of Pt_3Y alloy NPs by standard wet-chemistry approaches has proven to be challenging because of the easy formation of Y_2O_3. The main problem in the synthesis of Pt alloy nanoparticles is the different nucleation and growth rates of different elements, which are directly related to the formed NP size and their size distribution, and thus to ORR activity. Different Pt precursors, M precursor, different temperatures synthesis and different time may all contribute to variations in the formation of alloys and in the formation of monodisperse and homogeneous alloy NPs [54, 64].

Platinum yttrium alloy NPs were synthetized by Laser Ablation. In the previous chapter, PdY alloy NPs were synthetized by LASiS in different organic solvent, ethanol, n-hexane and acetone. The best PdY catalyst was obtained in ethanol, TEM images shows a good NPs distribution, the rare presence of aggregate and an high alloy content, 46%. For these reason Platinum yttrium alloy NPs were synthetized in ethanol. The synthesis procedure is the same used for PdY. The synthesis has been developed using the same laser beam, with the same frequency, time pulse and power.

Mesoporous Carbon (MC) (Sigma Aldrich, 500 nm particle size, >99.95%), Pt_3Y (Goodfellow 99.9%), Palladium black, (Alfa Aesar, 99.9%, mean particle size < 25 nm), Paltinum on Carbon (TKK, 50 %w), Nafion (Sigma Aldrich, 5 wt.% in EtOH), $HClO_4$ (Fluka, Traceselect® 67-72%), H_2SO_4 (Fluka, Traceselect® >95%), $HClO_4$ (Sigma Aldrich - ACS grade), NOCHROMIX, (Sigma Aldrich-Glass-Cleaning Reagent), ethanol, acetone and *n*-hexane (all HPLC grade, Sigma–Aldrich).

10.3.2 NPs Distribution and Morphology: core shell structure

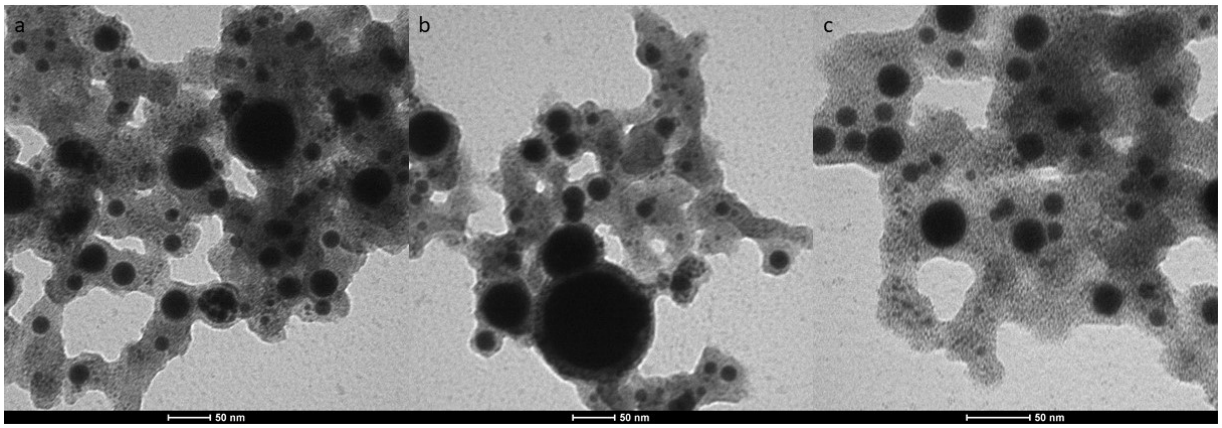

Figure 115: TEM images of PtY-E catalyst

The NPs distribution was evaluated by TEM analysis. TEM images shows a three modal distribution picked at 4.08 nm, 18.37 nm and 47.76 nm, Figure 116. The NPs dimension was determinate by calculating the diameter of three hundred NPs. The NPs are uniformly and homogeneously distributed over all carbon surface Figure 115. TEM images show the formation of spherical particles with different diameter, from 1 nm to 75 nm. The NPs show a core shell structure. Evaluating the contrast in the image, the metal NPs shows a carbon shell with different thickness, generally 5 % of diameter.

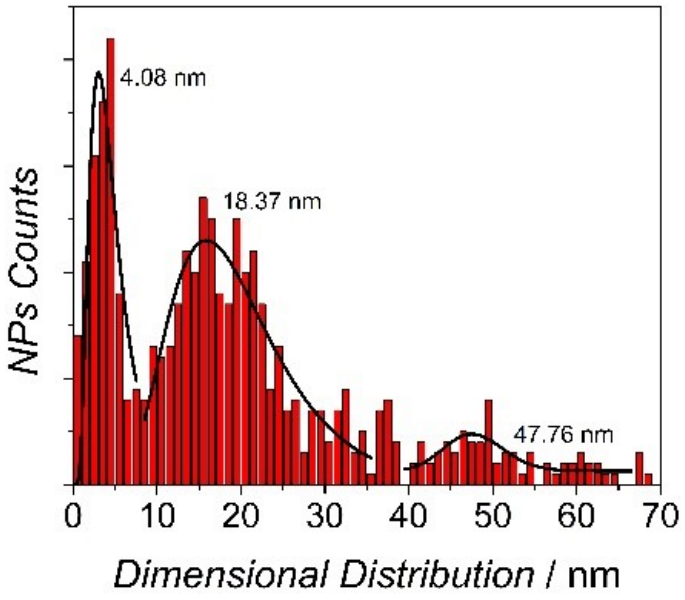

Figure 116: Dimensional distribution PtY-E catalys

10.3.3 XPS and XRD characterization: Pt_3Y alloy formation

The alloy formation and the different Platinum and Yttrium oxidation states was evaluated by XPS. The XPS spectra of PtY NPs was compared with the spectra obtained by the target which is used for the synthesis. The target is a standard PtY ingot, which was synthetized by fusion of the respective component of platinum and yttrium. The Pt 4f peak in the standard was fitted with only one component at 70.4 eV which correspond to the Pt(0), Figure 117 a. In PtY-E, the Pt 4f spectra was deconvoluted with 4 component, generally associated to the formation of Pt (0), Pt(II)O, Pt(IV)O_2 and Pt(II)OH peaked at 71.0 eV, 74.0 eV, 74.9 eV and 72.7 eV, respectively, , Figure 117 b. The concentration for the different platinum components is 38.7 %, 44.8 %, 11 % and 5.5 %, respectively [174, 180].

When Pt forms an alloy with a transition metal (with lower electronegativity), a partial d band hybridization occurs, which leads to a charge transfer from the less electronegative metal (in this case Y) to the more electronegative one, theoretically this charge transfer can be evaluated by XPS as a binding energy shift. In fact, the Pt(0) component resulted be shift in the standard of 0.9 eV and in the PtY-E NPs of 0.2 eV.

Generally, Y 3d peak can be fitted with 3 components centered at a B.E. of 156.3 eV, 157.4 eV and 158.4 eV; which correspond to metallic yttrium in alloy form, yttrium oxide and yttrium carbide.

In PtY NPs synthetized by Laser Ablation, two yttrium components were identified, at 159.9 eV and 157.9 eV, which correspond to Y metallic in alloy form and Y_2O_3. The alloy content in the standard show a concentration of Y(0) of 55 % and 45 % of Y_2O_3, the standard shows a platinum/yttrium ratio of 2.99, Figure 117 c. The same fitting was used to deconvolve the PtY-E Y 3d spectra. , Figure 117 b. The PtY-E shows a Yttrium alloy content of 18% with respect to the total Pt amount. The platinum yttrium ratio result be 2.97 [207].

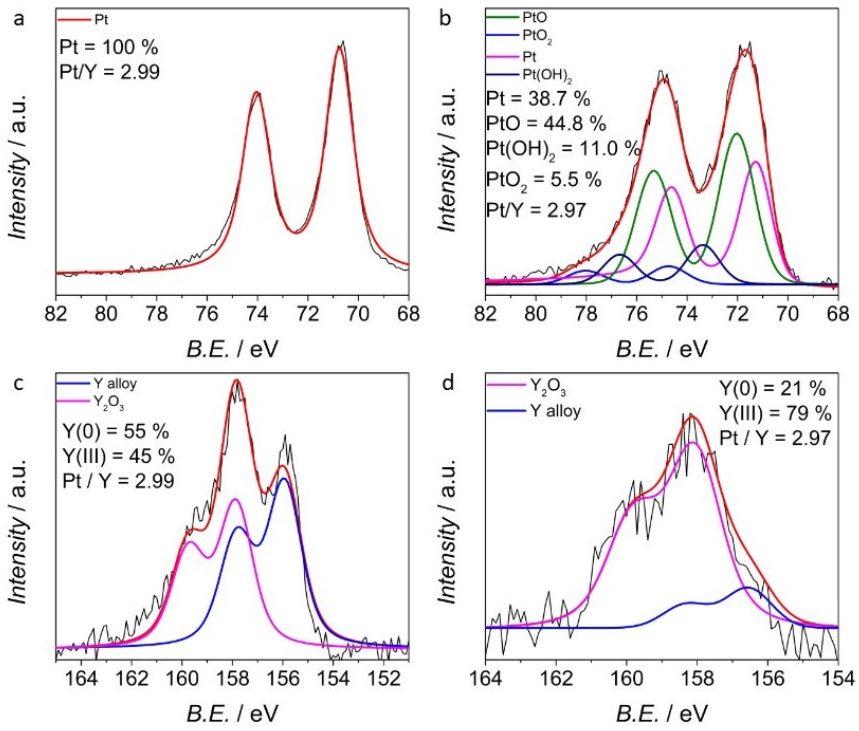

Figure 117: a) Pt 4f XPS spectra; b) Pt 4f spectra for PtY-E catalyst; C) Y 3d spectra for PtY-Standard and d) Y 3d XPS spectra for PtY-E spectra

Measured peak positions of Pt_3Y phase correspond to those of the reference pattern, whereas a systematic shift towards higher 2θ angles was observed for Pt_2Y reflections with respect to peak positions of the reference standard. Figure 118 displays the diffraction patterns of PtY-Standard and PtY_E samples. The main diffraction peaks were identified as Pt_3Y and Pt_2Y phases. A weak peak at 29° 2θ in Pt-bulk sample indicated the presence of minor PtO. The peak shifts observed for Pt_2Y correspond to a decrease in unit cell volume of 2.5% and 2.2% for PtY-Standard and PtY-E, respectively [175, 208, 209].

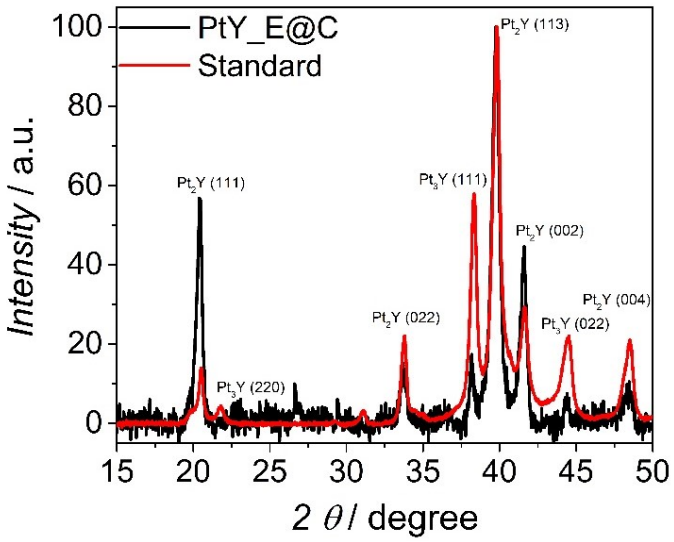

Figure 118: XRPD patterns of PtY-Standard and PtY_E

10.3.4 Electrochemical Characterization in $HClO_4$ 0.1 M and in H_2SO_4 0.1 M

Platinum yttrium alloy NPs was tested in $HClO_4$ 0.1 M and H_2SO_4 0.5 M. For comparing the catalytic activity, the H_{UPD} electrochemical surface area (ECSA), the electrochemical platinum surface area (EPSA) and all kinetics parameters of PtY_E and Pt/C are listed in Table 39. The Cyclic Voltammetry, corresponding to PtY_E and Pt/C, show in Figure 119a, are very similar, they exhibit the same capacitive current, the Pt/C show a Pt oxide formation and stripping peaks more intensive than PtY_E. The PtO_x peaks for PtY_E are shifted to higher potential than the standard Pt/C. The Hydrogen Adsorption/Desorption region show the same peaks at the same potential, indicating than are present the same crystallographic faces on the platinum.

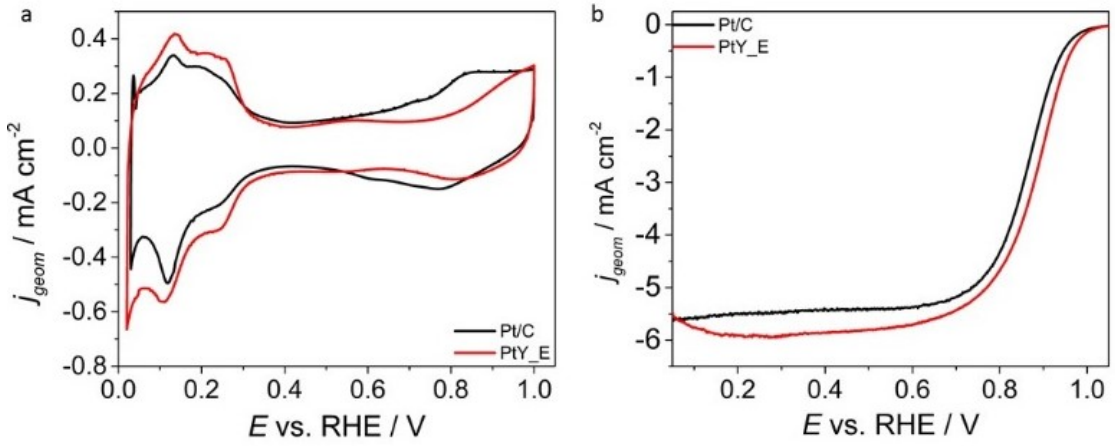

Figure 119: a) Cyclic Voltammetry in Ar saturated H_2SO_4 solution at 50 mV s^{-1} and b) LSV with RDE at 1600 rpm and 20 mV s^{-1} in O_2 saturated electrolyte

In H_2SO_4 0.1 M, PtY_E show an electrochemical platinum surface area (EPSA) of 2.31 cm^2 which correspond, considering a platinum loading of 15 µg cm^{-2} and an electrode area of 0.196 cm^2, to 79 m^2 g^{-1}. The obtaining EPSA is higher than Pt/C, which show an EPSA of 1.87 cm^2 and an ECSA of 64 m^2 g^{-1}. Figure 119b show the Linear Sweep Voltammetry with RDE at 1600 rpm and 20 mV s^{-1} in anodic scan. The Mass Activity and the Specific Activity determinate for PtY-E are 294 A g^{-1} and 0.374 mA cm^{-2}, respectively. The value obtained are higher than the corresponding value for Pt/C, 201 A g^{-1} and 0.315 mA cm^{-2}. The half wave potential of PtY_E result be highet than 25 mV than the standard Pt/C. These results confirm the electrochemical activity of Platinum Yttrium alloy vs. the Oxygen Reduction Reaction respect the pure platinum.

Table 39: Electrochemical results for Pt/C and PtY_E catalyst in H_2SO_4 0.1M

	EPSA	*ECSA*	$\lvert j_{lim} \rvert$	$E_{1/2}$	i_k	*MA*	*SA*
	cm^2	$m^2\ g^{-1}$	$mA\ cm^{-2}$	V vs RHE	mA	$A\ g^{-1}$	$mA\ cm^{-2}$
Pt/C	1.87	64	5.42	0.862	0.59	201	0.315
$\Delta_{Pt/C}$	0.11	4	0.15	0.005	0.04	13	0.038
PtY_E	2.31	79	5.87	0.887	0.87	294	0.374
Δ_{PtY_E}	0.15	5	0.09	0.004	0.05	16	0.045

As in Palladium Yttrium alloy, the PtY NPs synthetized by laser ablation show a carbon shell which do not permit the electrolyte diffusion. The electrochemical data in H_2SO_4 are in agreement with the previous one results for PdY alloy, sulfuric acid can degrade the carbon shell and permit a completely metal activation. PtY-E was tested also in $HClO_4$ 0.1 M. The electrochemical performances in terms of EPSA, $E_{1/2}$, Mass Activity and Specific Activity are lower than pure platinum, in perchloric acid the catalytic trend is inverter respect sulphuric acid. PtY_E show an Electrochemical Surface AREA of 54 $m^2\ g^{-1}$. Figure 120a shows the cyclic voltammetry for Pt/C and PtY_ obtained at 50 mV s^{-1}, the adsorption and desorption region is less defined than pure platinum. The CV show the almost total absence of the typical crystallographic peak of platinum. In the Pt/C the desorption-adsorption area ratio is 0.97 while in the PtY_E the ratio is 0.66. PtY_E show a less intensive hydrogen desorption process. The capacitive current is comparable with the Pt/C. As inH_2SO_4, PtY_E show the absence of the Pt oxide formation and stripping peaks [70, 102]

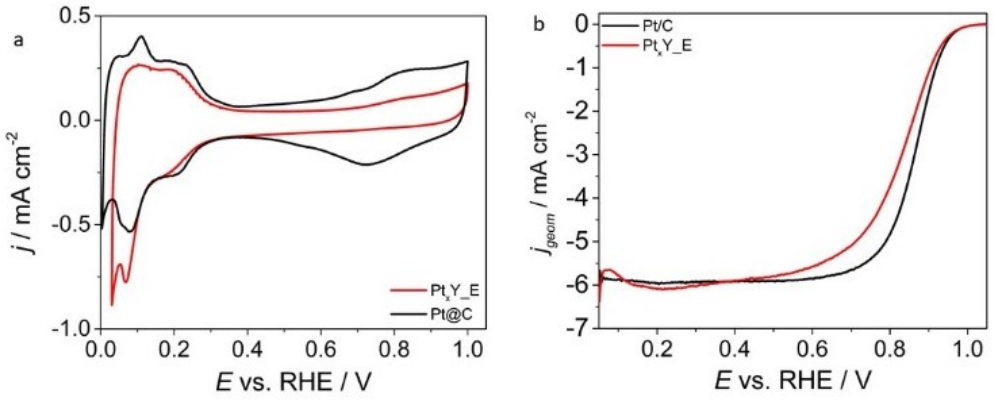

Figure 120: a) Cyclic Voltammetry in Ar saturated $HClO_4$ 0.1 M solution at 50 mV s^{-1} and b) LSV with RDE at 1600 rpm and 20 mV s^{-1} in O_2 saturated electrolyte

The limited density current obtained in Pt/C and PtY_E is very similar and close to the theoretical value, PtY_E show an higher resistivity than Pt/C in fact the catalysts have the same onset potential, but the plateau is observed at lower potential. The LSV with RDE for PtY_E is more stretched than the LSV/RDE of the benchmark. Pt/C show a $E_{1/2}$ higher than the platinum alloy NPs of ca. 40 mV. The catalytic performance evaluated with Mass Activity and Specific Activity of Pt/C are two times higher than PtY_E (201 A g^{-1} vs 94

A g^{-1} and 0.275 mA cm^{-2} vs. 0.173 mA cm^{-2}). The electrochemical performances evaluated comparing the PtY_E with the Pt/C, in $HClO_4$ are lower than H_2SO_4.

Table 40: Electrochemical results for Pt/C and PtY_E catalyst in $HClO_4$ 0.1M

	EPSA	*ECSA*	$\|j_{lim}\|$	$E_{1/2}$	i_k	*MA*	*SA*
	cm^2	$m^2\ g^{-1}$	mA cm^{-2}	V vs RHE	mA	A g^{-1}	mA cm^{-2}
PtY_E	1.60	54	5.90	0.828	0.28	94	0.173
Δ_{PtY_E}	0.19	7	0.07	0.007	0.02	7	0.034
Pt/C	2.17	74	5.92	0.867	0.60	203	0.275
$\Delta_{Pt/C}$	0.09	3	0.05	0.070	0.05	17	0.034

10.3.5 Dimensional Separation

TEM image show three dimensional distribution at 4.08 nm, 13.64 nm and 47 nm. The catalytic activity of platinum base material is connected to the NPs distribution in the support and to the NPs dimension. The Laser Ablation permit the synthesis of PtY alloy NPs, but the synthesis technique does not have a dimensional control on the NPs. Generally, decrease the pH of the synthesis solution can reduce the formation of big nanoparticles. Or, using a NaCl aqueous solution is possible obtain a homogeneous NPs growing. The problem is the yttrium stability, which in the aqueous solvent can for Y_2O_3 and so reduce the Pt_3Y concentration.

The NPs separation can be obtained also with physical methods as centrifugation or decantation. The PtY_E NPs were separated dimensionally by decantation, obtained three different fractions at 6 h (PtY_E_6h), 12 h (PtY_E_12h) and R (PtY_E_R, which correspond to the residual). In the next section the starting material will call PtY_E_0h.

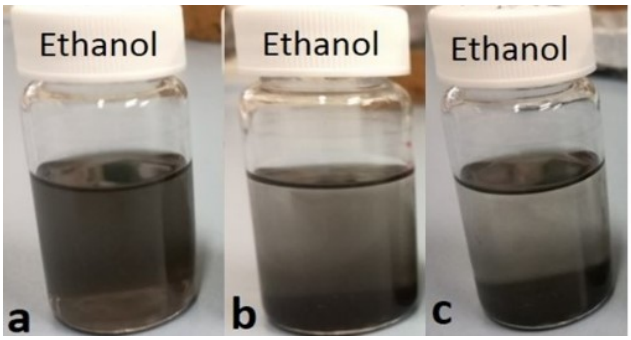

Figure 121: DImensional Separation

10.3.6 Influence of the Electrochemical Activation on the performance for ORR

The catalysts were electrochemical characterized in $HClO_4$ 0.1 M solution. The electrochemical surface area was evaluated by cyclic voltammetry in Ar saturated electrolyte solution at 50 mV s^{-1}, 20 mV s^{-1} and 5 mV s^{-1}. The EPSA increase with the following trend:

PtY_EtOH_12h (0.31 cm^2) > PtY_EtOH_6h (1.05 cm^2) > PtY_EtOH_0h (1.60 cm^2) > PtY_EtOH_R (2.23 cm^2).

The ECSA value decrease with the increment of decantation time, the highest value was obtained with PtY_E_R, 75.85 m^2 g^{-1}. PtY_E_R NPs owns dimension bigger than PtY_E_12h or PtY_E_6h. The inverted trend respects the EPSA can be explain with NPs aggregation process during the electrochemical measurement. The electrochemical performance for Oxygen Reduction Reaction follow the same trend of the ECSA. PtY_EtOH_R show and ECSA higher than the commercial standard Pt/C.

The catalytic activity vs. the ORR follow the same trend:

PtY_EtOH_12h, 21 A g^{-1} > PtY_EtOH_6h, 75 A g^{-1} > PtY_EtOH_0h, 94 A g^{-1} > PtY_EtOH_R, 469 A g^{-1}

PtY_E_R is the most active catalyst with an Mass Activity of 496 A g^{-1} and a Specific Activity of 0.619 mA cm^{-1}. The half wave potential is higher than 60 mV respect the standard Pt/C. The electrochemical performance in terms of MA and SA are two and three times higher than Pt/C (0.203 A g^{-1} and 0.274 mA cm^{-2}). The increment of the electrochemical activity is linked to the dimensional separation. However, the NPs continue to show the carbon shell, which prevent the total activation the platinum nanoparticles and limits their performance.

Table 41: Electrochemical results evaluated in $HClO_4$ 0.1M for the different dimensional fractions

	EPSA	*ECSA*	$\lvert j_{lim} \rvert$	$E_{1/2}$	i_k	*MA*	*SA*
	cm^2	m^2 g^{-1}	mA cm^{-2}	V vs RHE	mA	A g^{-1}	mA cm^{-2}
PtY_EtOH_0h	1.60	54.42	5.90	0.828	0.28	94	0.173
$\Delta_{PtY\_EtOH\_0h}$	0.19	6.63	0.07	0.007	0.02	7	0.034
PtY_EtOH_6h	1.05	35.71	6.39	0.814	0.22	75	0.211
$\Delta_{PtY\_EtOH\_6h}$	0.11	3.74	0.00	0.007	0.05	17	0.070
PtY_EtOH_12h	0.31	10.54	6.28	0.756	0.06	21	0.202
$\Delta_{PtY\_EtOH\_12h}$	0.04	1.21	0.00	0.008	0.01	4	0.063
PtY_EtOH_R	2.23	75.85	5.90	0.907	1.38	469	0.619
$\Delta_{PtY\_EtOH\_R}$	0.06	2.04	0.07	0.007	0.04	14	0.035

Several techniques can be used for removing the carbon shell, such as acid treatment with H_2SO_4 or HNO_3 at high temperature. However, this type of treatment shows a strong impact on the carbon support morphology and favourable the NPs aggregation. For remove the carbon shell without modify the catalysts proprieties an

electrochemical activation was used. Generally, the electrochemical activation is used for activating the active sites and remove the impurities as oxide. Several experiments were conduct for optimized the activation process and remove the carbon shell. E common activation process is obtained cycling at 200 mV s^{-1} between 0 V vs RHE and 1.2 V vs RHE in argon saturated solution for 100 cc. Increase the cycles number or reduce the scan rate do not have any effect on the performance of the catalyst and on the carbon shell. However, when the catalysts were activated in oxygen the situation change dramatically, the catalysts show the increment of the EPSA and of all electrochemical parameters [210, 211, 212].

Several tests were experimented for determinate the best activation condition in oxygen saturated solution. The electrochemical activity was evaluated with different activation process, increasing the upper vertex potential from 1 V vs RHE to 1.4 V vs RHE and cycling the electrodic material for 50 cc with a scan rate of 50 mV s^{-1} in oxygen saturated electrolyte solution.

In PtY_E_0h, the EPSA is reduce with the increment of upper vertex potential from 1.6 cm^2 for the un-actived material to 1.42 cm^2 when 1.4 V vs. RHE was used as upper vertex potential; the catalytic activity in terms of half wave potential, mass activity or specific activity increase until the activation at 1.3 V vs RHE and after decrease when the upper vertex potential is increased at 1.4 V vs. RHE. PtY_E_0h with an activation at 1.3 V vs RHE show a MA of 331 A g^{-1} and a SA of 0.571 mA cm^{-2}, the $E_{1/2}$ is higher than inactivated catalyst of 80 mV. With an activation procedure with a potential of 1.4 V vs RHE, the MA is reduced, from 331 A g^{-1} to 276 A g^{-1}. The deactivation process is associated to the oxidation of platinum and to the detachment process which are favourable at this potential.

Table 42: Electrochemical results for PtY_E_0h in $HClO_4$ electrolyte, using different electrochemical activation

PtY_E_0h	*EPSA*	*ECSA*	O_2-Activation	$\|j_{lim}\|$	$E_{1/2}$	i_k	*MA*	*SA*
	cm^2	$m^2\ g^{-1}$	-	mA cm^{-2}	V vs RHE	mA	A g^{-1}	mA cm^{-2}
PtY_EtOH	1.60	54	NO	5.90	0.828	0.28	94	0.173
Δ_{PtY_EtOH}	0.19	7		0.07	0.007	0.02	7	0.034
PtY_EtOH_1	1.65	56	50cc/0-1 V vs RHE	6.00	0.860	0.44	151	0.268
$\Delta_{PtY\_EtOH\_1}$	0.21	7		0.06	0.004	0.02	8	0.048
PtY_EtOH_2	1.58	54	50cc/0-1.2 V vs RHE	6.12	0.882	0.64	218	0.406
$\Delta_{PtY\_EtOH\_2}$	0.16	5		0.07	0.002	0.03	12	0.063
PtY_EtOH_3	1.53	52	50cc/0-1.3 V vs RHE	6.12	0.895	0.97	331	0.635
$\Delta_{PtY\_EtOH\_3}$	0.14	5		0.03	0.005	0.03	11	0.079
PtY_EtOH_4	1.42	48	50cc/0-1 V.4 vs RHE	6.01	0.888	0.81	276	0.571
$\Delta_{PtY\_EtOH\_4}$	0.16	5		0.03	0.003	0.05	18	0.101
Pt/C	2.17	74	NO	5.92	0.867	0.60	203	0.275
$\Delta_{Pt/C}$	0.09	3		0.05	0.070	0.05	17	0.034

PtY_EtOH_6h show same trend obtained with PtY_E_0h, the EPSA decrease from 1.05 cm^2 to 0.85 cm^2 with the increment of upper vertex potential in the activation. The EPSA decrease constantly with the increment of the electro-activation until 1.3 V vs. RHE; PtY_E_6h_4 show a drastically decrement of EPSA and ECSA due to the detachment process. The limited current density is constant in for each experimental, considering the error associated to the measurement. The Mass Activity and the $E_{1/2}$ increase from 75 A g^{-1} and 0.814 V vs RHE in the un-activated catalysts to 243 A g^{-1} and 0.867 V vs RHE when 1.2 V vs RHE is used as upper vertex potential. The electrochemical performance increase with the follow trend;

PtY_E < PtY_EtOH_4 < PtY_EtOH1 < Pt/C < PtY_EtOH_3 < Pt_EOH_2

As in PtY_E_0h, when 1.4 V vs. RHE is used as upper vertex potential in the electrochemical activation, the electrochemical performance for the ORR, drastically decrease.

Table 44 show the electrochemical results for PtY_E_12h obtained with different electrochemical activation. PtY_E_12h show a very low EPSA, the electrochemical activation does not influence the catalytic activity vs. the Oxygen Reduction Reaction. PtY_E_12h show an EPSA of 0.3 cm^2 which is constant after each activation process. The inactivity is due to the small nanoparticles which easily aggregate during the electrochemical analysis. PtY_E_12 h show a small catalytic activity in terms of $E_{1/2}$, Mass Activity or Specific Activity. Considering the error calculated by standard deviation, the electrochemical data are comparable, PtY_E_12h show a MA of 21 A g-1 and a $E_{1/2}$ of 0.756 V vs. RHE, after the best activation PtY_E_12h show an Mass Activity of 25 A g^{-1} and a half wave potential of 0.767 V vs. RHE.

Table 43: Electrochemical results for PtY_E_6h in $HClO_4$ electrolyte, using different electrochemical activation

PtY_E_6h	*EPSA*	*ECSA*	O_2-Activation	$\|j_{lim}\|$	$E_{1/2}$	i_k	*MA*	*SA*
	cm^2	$m^2\ g^{-1}$	-	mA cm^{-2}	V vs RHE	mA	A g^{-1}	mA cm^{-2}
PtY_EtOH	1.05	36	NO	6.39	0.814	0.22	75	0.211
Δ_{PtY_EtOH}	0.11	4		0.00	0.007	0.05	17	0.070
PtY_EtOH_1	1.02	35	50cc/0-1 V vs RHE	6.08	0.841	0.42	142	0.408
$\Delta_{PtY\_EtOH\_1}$	0.17	6		0.00	0.007	0.06	20	0.127
PtY_EtOH_2	1.13	38	50cc/0-1.2 V vs RHE	6.10	0.867	0.71	243	0.632
$\Delta_{PtY\_EtOH\_2}$	0.08	3		0.00	0.006	0.06	22	0.101
PtY_EtOH_3	0.98	33	50cc/0-1.3 V vs RHE	6.12	0.858	0.66	226	0.677
$\Delta_{PtY\_EtOH\_3}$	0.12	4		0.00	0.001	0.05	17	0.135
PtY_EtOH_4	0.85	29	50cc/0-1 V.4 vs RHE	6.08	0.829	0.31	105	0.362
$\Delta_{PtY\_EtOH\_4}$	0.09	3		0.00	0.008	0.04	13	0.082
Pt/C	2.17	74	NO	5.92	0.867	0.60	203	0.275
$\Delta_{Pt/C}$	0.09	3		0.05	0.070	0.05	17	0.034

Table 44: Electrochemical results for PtY_E_12h in $HClO_4$ electrolyte, using different electrochemical activation

PtY_E_12h	*EPSA*	*ECSA*	O_2-Activation	$\|j_{lim}\|$	$E_{1/2}$	i_k	*MA*	*SA*

	cm^2	$m^2\ g^{-1}$	-	mA cm^{-2}	V vs RHE	mA	A g^{-1}	mA cm^{-2}
PtY_EtOH	0.31	11	NO	6.28	0.756	0.06	21	0.202
Δ_{PtY_EtOH}	0.04	1		0.00	0.008	0.01	4	0.063
PtY_EtOH_1	0.29	10	50cc/0-1 V vs RHE	6.03	0.761	0.07	23	0.238
$\Delta_{PtY\_EtOH\_1}$	0.08	3		0.00	0.006	0.02	5	0.117
PtY_EtOH_2	0.36	12	50cc/0-1.2 V vs RHE	5.99	0.767	0.07	25	0.201
$\Delta_{PtY\_EtOH\_2}$	0.09	3		0.00	0.009	0.04	8	0.159
PtY_EtOH_3	0.25	9	50cc/0-1.3 V vs RHE	5.95	0.764	0.07	23	0.267
$\Delta_{PtY\_EtOH\_3}$	0.06	2		0.00	0.005	0.02	7	0.141
PtY_EtOH_4	0.27	9	50cc/0-1 V.4 vs RHE	6.01	0.776	0.05	19	0.203
$\Delta_{PtY\_EtOH\_4}$	0.06	2		0.00	0.007	0.02	7	0.120
Pt/C	2.17	74	NO	5.92	0.867	0.60	203	0.275
$\Delta_{Pt/C}$	0.09	3		0.05	0.070	0.05	17	0.034

The best results were obtained with the fraction, PtY_E_R. Considering the separation procedure, the catalysts show only big nanoparticles. The EPSA is almost constant with the increment of the activation potential range. PtY_E_R show an EPSA of 2.29 cm^2 when 1.2 V vs. RHE is used as upper vertex potential, the EPSA is slight increased. The density limit current is very close to the theoretical value for each sample. PtY_E_R show an MA of 469 A g^{-1} which decrease at the increment of the upper vertex potential in electro-activation.
The Mass Activity is higher than commercial standard Pt/C and show a Specific Activity three times higher than the benchmark. The half wave potential can be considering constant in al PtY_E_R catalysts.

Table 45: Electrochemical results for PtY_E_R in $HClO_4$ electrolyte, using different electrochemical activation

PtY_E_R	*EPSA*	*ECSA*	O_2-Activation	$\lvert j_{lim} \rvert$	$E_{1/2}$	i_k	*MA*	*SA*

	cm^2	$m^2\ g^{-1}$	-	mA cm^{-2}	V vs RHE	mA	A g^{-1}	mA cm^{-2}
PtY_EtOH	2.23	76	NO	5.90	0.907	1.38	469	0.619
Δ_{PtY_EtOH}	0.06	2		0.07	0.007	0.04	14	0.035
PtY_EtOH_1	2.12	72	50cc/0-1 V vs RHE	6.00	0.902	1.32	447	0.619
$\Delta_{PtY\_EtOH\_1}$	0.16	5		0.08	0.011	0.03	9	0.059
PtY_EtOH_2	2.29	78	50cc/0-1.2 V vs RHE	5.96	0.897	1.25	426	0.546
$\Delta_{PtY\_EtOH\_2}$	0.11	4		0.12	0.004	0.04	13	0.043
PtY_EtOH_3	2.19	75	50cc/0-1.3 V vs RHE	6.10	0.906	1.33	453	0.607
$\Delta_{PtY\_EtOH\_3}$	0.13	5		0.12	0.006	0.05	17	0.060
PtY_EtOH_4	2.15	73	50cc/0-1 V.4 vs RHE	6.06	0.903	1.28	436	0.597
$\Delta_{PtY\_EtOH\_4}$	0.09	3		0.09	0.004	0.04	13	0.043
Pt/C	2.17	74	NO	5.92	0.867	0.60	203	0.275
$\Delta_{Pt/C}$	0.09	3		0.05	0.070	0.05	17	0.034

PtY_E have need of an electrochemical activation for remove the carbon shell and permit a completely activation of platinum site. The best activation result being 0 V vs. RHE – 1.3 V vs. RHE. PtY_E_R show the best electrochemical performance in terms of Mass Activity, Specific Activity and $E_{1/2}$.

Figure 122 show the linear sweep voltammetry for the different dimensional fraction and the different electrochemical activation, recorded at 20 mV s^{-1} in O_2 saturated $HClO_4$ electrolyte solution. The LSV with RDE show the potential shift when the upper vertex potential is increased. The histograms in Figure 122e and f, show the i_k, $E_{1/2}$, MA and SA before and after the best activation (1.3 V vs. RHE, 50 mV s-1 and 200 cc) and the standard Pt/C. From the histogram is evident the performance increment after the electrochemical activation.

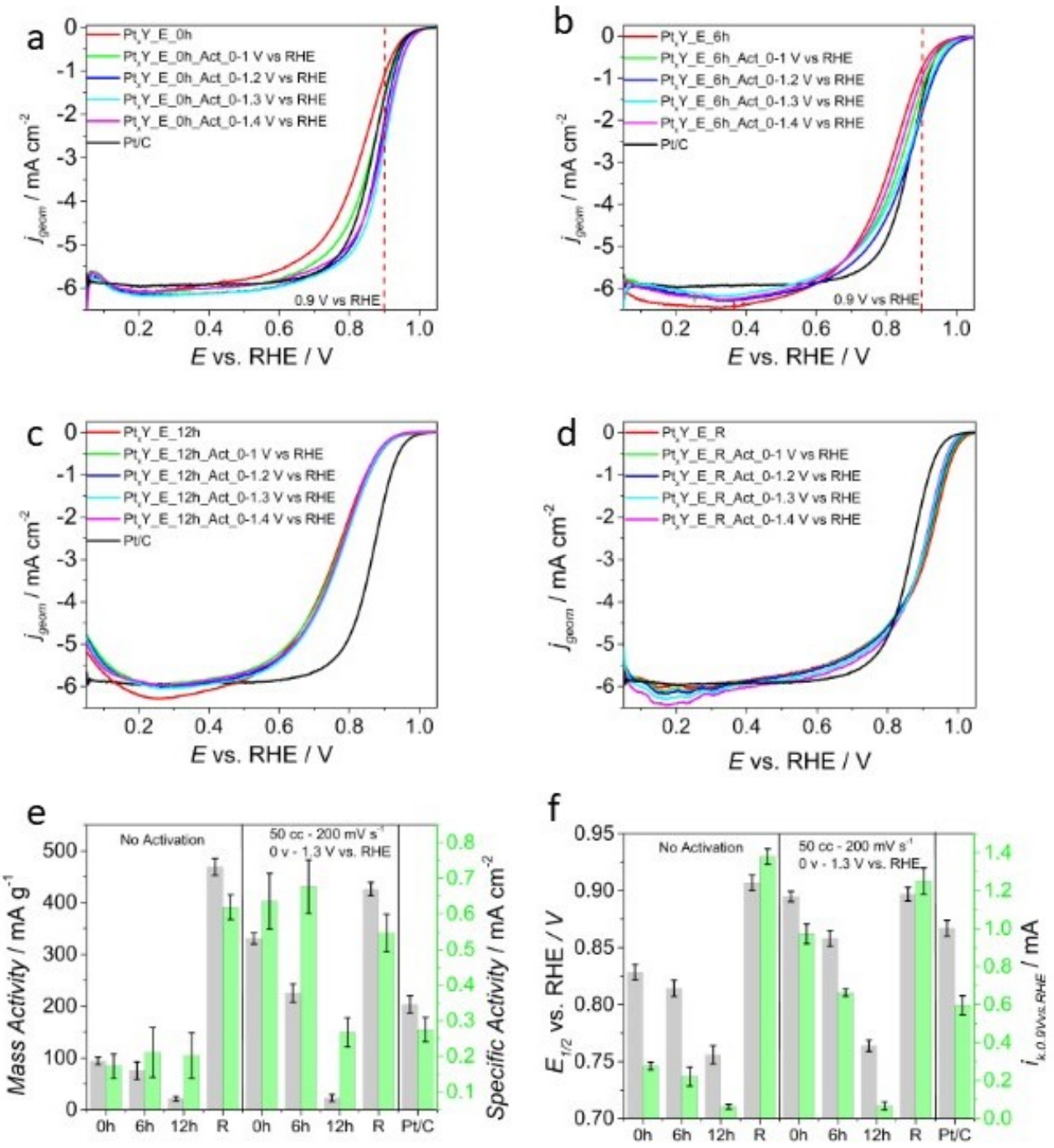

Figure 122: a) LSV with RDE at 1600 rpm and 20 mV s^{-1} for PtY_E_0h; b) LSV with RDE at 1600 rpm and 20 mV s^{-1} for PtY_E_6h; c) LSV with RDE at 1600 rpm and 20 mV s^{-1} for PtY_E_12h; d) LSV with RDE at 1600 rpm and 20 mV s^{-1} for PtY_E_R; e) Correlation between MA and SA for the different fractions before and after the best electrochemical activation and f) Correlation between $E_{1/2}$ and i_k for the different fractions before and after the best electrochemical activation

10.4 Conclusion

PtY NPs were synthetized by Laser Ablation in ethanol. XPS has confirmed the Pt_3Y alloy formation, 18 %. XRD has revelled an strain effect on the patter which confirm the presence of alloy. Pt_xY alloy synthetized by solid state synthesis, chemical reduction or solvothermal synthesis show two problems, the yttria formation and not all platinum is in alloy form. When Pt_xY alloy was synthetized by LASiS the XRD show the absence of the platinum crystallographic peaks but only signal which is attributed to Pt_3Y and Pt_2Y. The problem is the NPs dimension, LASiS do not show a NPs growing control, in fact TEM image show different dimensional distribution, from 3 nm to 50 nm, also with the aggregate formation. The NPs with an dimension higher than 10 nm show a carbon shell which protect the PtY metal core. In H_2SO_4 the PtY catalyst show a Mass Activtiy and Specific Activity higher than the standard Pt/C. The electrochemical measurement in $HClO_4$ 0.1 M has revelled a low catalytic activity vs. ORR due to the shell which do not permit the electrolyte diffusion and the completely electrochemical activation. The dimensional problem was resolved separating the NPs with decantation. After the process three fraction was obtained, PtY_E_6h, PtY_E_12h and the residual PtY_E_R. The three different sample show a NPs dimension increasing from 6 nm to 50 nm, respectively. PtY_E show a low mass activity and specific activity, 94 A g^{-1} and 0.173 mA cm^{-2}. After the dimensional separation, PtY show an increment of Mass Activity with the increment of NPs diameter. The trend suggests as the carbon shell have a strong impact on small NPs. The same trend was observed with Specific Activity and Half Wave Potential. Several procedures were tested for remove the carbon shell, as acid treatment at high temperature, but the NPs after the treatment tend easily to aggregate. An particular procedure was applied for remove the carbon shell based on the electrochemical carbon corrosion. Several electrochemical activation procedures were evaluated for degrade the carbon shell. The upper vertex potential was increase until 1.4 V vs RHE in Oxygen saturated electrolyte, at higher potential the carbon can form CO_2 or CO. The best activation results being with an upper vertex potential of 1.3 V vs RHE, at higher potential the NPs aggregate and detachment process occur. PtY_E_0h show a Mass Activity increment when the upper vertex potential is increased from 94 A g^{-1} to 331 A g^{-1}; PtY_E_6h from 75 A g^{-1} to 226 A g^{-1}. The best electrochemical results were obtained with PtY_E_R, which show an Mass Activity of 426 A g^{-1} when the best activation is used.

The effective activity of the Platinum Yttrium alloy was confirmed, in fact the catalysts after the dimensional separation and the electrochemical separation show a catalytic activity in terms of $E_{1/2}$, Mass Activity and Specific Activity higher than the commercial standard Pt/C.

Table 46: Electrochemical results for inactivated/activated Pty catalysts

	EPSA	***ECSA***	***O_2-Activation***	***$E_{1/2}$***	***i_k***	***MA***	***SA***	***Ts_1***	***Ts_2***
	cm^2	$m^2\ g^{-1}$	-	V vs RHE	mA	$A\ g^{-1}$	$mA\ cm^{-2}$	$mV\ dec^{-1}$	$mV\ dec^{-1}$
PtY_E_0h	1.60	54.42	NO	0.828	0.28	94	0.173	64	164
$\Delta_{PtY\_E\_0h}$	0.19	6.63		0.007	0.02	7	0.034	5	8
PtY_E_6h	1.05	35.71	NO	0.814	0.22	75	0.211	80	158
$\Delta_{PtY\_E\_6h}$	0.11	3.74		0.007	0.05	17	0.070	6	11
PtY_E_12h	0.31	10.54	NO	0.756	0.06	21	0.202	75	170
$\Delta_{PtY\_E\_12h}$	0.04	1.21		0.008	0.01	4	0.063	4	7
PtY_E_R	2.23	75.85	NO	0.907	1.38	469	0.619	53	276
$\Delta_{PtY\_E\_R}$	0.06	2.04		0.007	0.04	14	0.035	5	13
PtY_E_0h	1.53	52.04	50cc/0-1.3 V vs RHE	0.895	0.97	331	0.635	52	189
$\Delta_{PtY\_E\_0h}$	0.14	4.76		0.005	0.03	11	0.079	5	12
PtY_E_6h	0.98	33.33	50cc/0-1.3 V vs RHE	0.858	0.66	226	0.677	73	204
$\Delta_{PtY\_E\_6h}$	0.12	4.08		0.001	0.05	17	0.135	3	6
PtY_E_12h	0.25	8.50	50cc/0-1.3 V vs RHE	0.764	0.07	23	0.267	69	159
$\Delta_{PtY\_E\_12h}$	0.06	2.02		0.005	0.02	7	0.141	8	9
PtY_E_R	2.15	73	50cc/0-1.3 V vs RHE	0.897	1.25	426	0.546	56	236
$\Delta_{PtY\_E\_R}$	0.09	3		0.004	0.04	13	0.043	7	8
Pt/C	2.17	73.81	NO	0.867	0.60	203	0.275	59	87
$\Delta_{Pt/C}$	0.09	3.06		0.070	0.05	17	0.034	3	5

10.5 Bibliography

[187] X. Liu, E.H. Yu, K. Scott, Preparation and evaluation of a highly stable palladium yttrium platinum core-shell-shell structure catalyst for oxygen reduction reactions, Appl. Catal. B Environ. 162 (2015) 593–601. doi:10.1016/j.apcatb.2014.07.038.

[188] Y. Pan, F. Zhang, K. Wu, Z. Lu, Y. Chen, Y. Zhou, Y. Tang, T. Lu, Carbon supported Palladium-Iron nanoparticles with uniform alloy structure as methanol-tolerant electrocatalyst for oxygen reduction reaction, Int. J. Hydrogen Energy. 37 (2012) 2993–3000. doi:10.1016/j.ijhydene.2011.11.042.

[189] I.E.L. Stephens, A.S. Bondarenko, L. Bech, I. Chorkendorff, Oxygen Electroreduction Activity and X-Ray Photoelectron Spectroscopy of Platinum and Early Transition Metal Alloys, ChemCatChem. 4 (2012) 341–349. doi:10.1002/cctc.201100343.

[190] S. Reich, A. Letzel, A. Menzel, N. Kretzschmar, B. Gökce, S. Barcikowski, A. Plech, Early appearance of crystalline nanoparticles in pulsed laser ablation in liquids dynamics, Nanoscale. 11 (2019) 6962–6969. doi:10.1039/c9nr01203f.

[191] C.Y. Shih, R. Streubel, J. Heberle, A. Letzel, M. V. Shugaev, C. Wu, M. Schmidt, B. Gökce, S. Barcikowski, L. V. Zhigilei, Two mechanisms of nanoparticle generation in picosecond laser ablation in liquids: The origin of the bimodal size distribution, Nanoscale. 10 (2018) 6900–6910. doi:10.1039/c7nr08614h.

[192] A. Letzel, S. Reich, T. Dos Santos Rolo, A. Kanitz, J. Hoppius, A. Rack, M.P. Olbinado, A. Ostendorf, B. Gökce, A. Plech, S. Barcikowski, Time and Mechanism of Nanoparticle Functionalization by Macromolecular Ligands during Pulsed Laser Ablation in Liquids, Langmuir. 35 (2019) 3038–3047. doi:10.1021/acs.langmuir.8b01585.

[193] J.H. Kim, S. Chang, Y.T. Kim, Compressive strain as the main origin of enhanced oxygen reduction reaction activity for Pt electrocatalysts on chromium-doped titania support, Appl. Catal. B Environ. 158–159 (2014) 112–118. doi:10.1016/j.apcatb.2014.04.003.

[194] B. Gökce, V. Amendola, S. Barcikowski, Opportunities and Challenges for Laser Synthesis of Colloids, ChemPhysChem. 18 (2017) 983–985. doi:10.1002/cphc.201700310.

[195] S. Crivellaro, A. Guadagnini, D.M. Arboleda, D. Schinca, V. Amendola, A system for the synthesis of nanoparticles by laser ablation in liquid that is remotely controlled with PC or smartphone, Rev. Sci. Instrum. 90 (2019). doi:10.1063/1.5083811.

[196] M. Censabella, V. Torrisi, S. Boninelli, C. Bongiorno, M.G. Grimaldi, F. Ruffino, Laser ablation synthesis of mono- and bimetallic Pt and Pd nanoparticles and fabrication of Pt-Pd/Graphene nanocomposites, Appl. Surf. Sci. 475 (2019) 494–503. doi:10.1016/j.apsusc.2019.01.029.

[197] C.-H. Lee, H.-N. Park, Y.-K. Lee, Y.S. Chung, S. Lee, H.-I. Joh, Palladium on yttrium-embedded carbon nanofibers as electrocatalyst for oxygen reduction reaction in acidic media, Electrochem. Commun. 106 (2019) 106516. doi:10.1016/j.elecom.2019.106516.

[198] J. Beran, K. Mašek, RHEED and XPS study of palladium interaction with cerium oxide surface, Vacuum. 167 (2019) 438–444. doi:10.1016/j.vacuum.2019.06.023.

[199] K.J. Bryden, J.Y. Ying, Thermal stability and hydrogen absorption characteristics of palladium-yttrium nanoalloys, Acta Mater. 44 (1996) 3847–3854. doi:10.1016/1359-6454(96)00020-1.

[200] R. Brandiele, V. Amendola, A. Guadagnini, G.A. Rizzi, D. Badocco, P. Pastore, A.A. Isse, C. Durante, A. Gennaro, Facile synthesis of Pd3Y alloy nanoparticles for electrocatalysis of the oxygen reduction reaction, Electrochim. Acta. 320 (2019) 134563. doi:10.1016/j.electacta.2019.134563.

[201] T. Gao, J. Yang, M. Nishijima, H.A. Miller, F. Vizza, H. Gu, H. Chen, Y. Hu, Z. Jiang, L. Wang, L. Shuai, M. Qiu, C. Lei, A. Zhang, Y. Hou, Q. He, Evidence of the strong metal support interaction in a palladium-ceria hybrid electrocatalyst for enhancement of the hydrogen evolution reaction, J. Electrochem. Soc. 165 (2018) F1147–F1153. doi:10.1149/2.0351814jes.

[202] R.C. Sekol, X. Li, P. Cohen, G. Doubek, M. Carmo, A.D. Taylor, Silver palladium core–shell electrocatalyst supported on MWNTs for ORR in alkaline media, Appl. Catal. B Environ. 138–139 (2013) 285–293. doi:10.1016/j.apcatb.2013.02.054.

[203] H. Erikson, M. Lüsi, A. Sarapuu, K. Tammeveski, J. Solla-Gullón, J.M. Feliu, Oxygen electroreduction on carbon-supported Pd nanocubes in acid solutions, Electrochim. Acta. 188 (2016) 301–308. doi:10.1016/j.electacta.2015.11.125.

[204] M.H. Seo, S.M. Choi, H.J. Kim, W.B. Kim, The graphene-supported Pd and Pt catalysts for highly active oxygen reduction reaction in an alkaline condition, Electrochem. Commun. 13 (2011) 182–185. doi:10.1016/j.elecom.2010.12.008.

[205] L. Jiang, A. Hsu, D. Chu, R. Chen, Size-dependent activity of palladium nanoparticles for oxygen electroreduction in alkaline solutions, J. Electrochem. Soc. 156 (2009) 643–649. doi:10.1149/1.3098478.

[206] N.M. Marković, H.A. Gasteiger, B.N. Grgur, P.N. Ross, Oxygen reduction reaction on Pt(111): effects of bromide, J. Electroanal. Chem. 467 (1999) 157–163. doi:10.1016/S0022-0728(99)00020-0.

[207] E. Zamburlini, K.D. Jensen, I.E.L. Stephens, I. Chorkendorff, M. Escudero-Escribano, Benchmarking Pt and Pt-lanthanide sputtered thin films for oxygen electroreduction: fabrication and rotating disk electrode measurements, Electrochim. Acta. 247 (2017) 708–721. doi:10.1016/j.electacta.2017.06.146.

[208] H. Liu, J. Li, X. Xu, F. Wang, J. Liu, Z. Li, J. Ji, Highly graphitic carbon black-supported platinum nanoparticle catalyst and its enhanced electrocatalytic activity for the oxygen reduction reaction in acidic medium, Electrochim. Acta. 93 (2013) 25–31. doi:10.1016/j.electacta.2013.01.090.

[209] R. Cui, L. Mei, G. Han, J. Chen, G. Zhang, Y. Quan, N. Gu, L. Zhang, Y. Fang, B. Qian, X. Jiang, Z. Han, Facile synthesis of nanoporous Pt-Y alloy with enhanced electrocatalytic activity and durability, Sci. Rep. 7 (2017) 1–10. doi:10.1038/srep41826.

[210] K.H. Lim, H.S. Oh, S.E. Jang, Y.J. Ko, H.J. Kim, H. Kim, Effect of operating conditions on carbon corrosion in polymer electrolyte membrane fuel cells, J. Power Sources. 193 (2009) 575–579. doi:10.1016/j.jpowsour.2009.04.006.

[211] P. Yang, X. Wu, Z. Xie, P. Wang, C. Liu, Q. Huang, Durability improving and corrosion-resistance mechanism of graphene oxide modified ultra-thin carbon paper used in PEM fuel cell, Corros. Sci. 130 (2018) 95–102. doi:10.1016/j.corsci.2017.10.025.

[212] C.C. Hung, P.Y. Lim, J.R. Chen, H.C. Shih, Corrosion of carbon support for PEM fuel cells by electrochemical quartz crystal microbalance, J. Power Sources. 196 (2011) 140–146. doi:10.1016/j.jpowsour.2010.07.015.

11 GOAL and Future Prospective

In this PhD work two systems based on PGM material were studied, Platinum-Yttrium alloy on carbon and Platinum on doped carbon.

Platinum-Yttrium alloy show an interesting electrochemical performance for Oxygen Reduction Reaction. in the 1st year of PhD the best conditions for the alloy formation were evaluated, several temperature synthesis, time, platinum and yttrium precursors were tested. Several deposition methods and Pt/Y precursor salts were analysed, showing that the solid state deposition under hydrogen atmosphere at high temperature with $Pt(acac)_2$ and $Y(NO_3)_3$ allows to obtain the best distribution of Pt NPs over the carbon support and the alloy formation. The synthesis in Solid State of the Platinum-yttrium alloy NPs is an easy and fast method with a simple control on the synthesis parameters but especially it shows a facile scale-up.

The carbon support morphology is fundamental for modulated the NPs dimension and electrochemical activity for ORR. Several commercial and homemade carbon supports were tested, and the influence of surface area, pore distribution and pore dimension on the NPs dimension and ORR activity was evaluated. An high surface area and a mesoporous structure are fundamental for control the NPs growing and increase the electrochemical stability vs. ORR. The resulting catalysts shows a Mass Activity higher than not only the benchmark Pt/C but especially than the DOE target, which explain as a Mass Activity of 440 A g^{-1} and a Specific Activity of 0.275 mA cm^{-2}, are fundamental requirements for an real utilization and application of the catalyst on PEM-FC.

For complete the panorama on the Pt_xY alloy NPs, the last step is to evaluate the influence of heteroatoms on the catalytic activity vs. ORR. Sulphur, Nitrogen or Boron owns the ability to increase the conductibility of the carbon, can control the NPs and increase the Metal-Support Interaction stabilizing the NPs. This last step is fundamental for increase the durability and the stability of the resulting catalyst. In fact, DOE target, describe the fundamentals characteristics for a Platinum based material for Proton Exchange Membrane Fuel Cell, and describe as the catalyst must prevent the common effect of detachment and leaching.

During the 2nd PhD year, the performances of platinum on doped carbon were evaluated. The influence of sulfur and nitrogen on the platinum NPs and performance was studied. Platinum Nitrogen catalysts was synthetized by high temperature solid state synthesis in reduction atmosphere using Platinum (II) complex contained nitrogen ligand as platinum salt precursor. The catalysts show a nitrogen distribution very close to the platinum NPs, the interaction between the heteroatoms and the metal sites was confirmed by XPS. The electrochemical activity decreases with the decrement of the metal support interaction. The PtN catalysts show an electrochemical performance higher than pure platinum but especially than the DOE target for 2020.

The deposition of Pt NPs on the synthesized sulphur doped mesoporous carbon supports was investigated. The mesoporous carbons were synthetized by hard template method. Silica P200 was used as inorganic template agent and dibenzothiphene as surfer carbon precursor. Silica P200 allows to have in the final carbon a highest surface area, good pore dimensions and electrical conductivity. Different sulfur concentration was obtained using as carbon precursor a mixture of sucrose and dibenzothiophene. A pyrolysis temperature of 750 °C allows to obtain a proper amount of dopant heteroatom in the carbon structure, together with good thermal stability, an high surface area, an mesoporous structure and a good conductibility. The surface area of Sulfur doped carbon was increased with a post-treatment at high temperature using a steam flux. Platinum reduction was performed at 300 °C and 3 h using $Pt(acac)_2$. The influence of sulfur concentration and the surface area on the electrochemical activity was evaluated. XPS proved an electronic effect consisting in a charge transfer from Pt to S, which turns out to be favourable for oxygen reduction. The synergic effect between the surface area and the heteroatoms concentration is liable to the high performance obtained.

For complete the evaluation on the interaction between the sulphur and the Platinum NPs, the concentration of heteroatoms must be increased over the 17 %, the increment is fundamental for understand which is highest concentration which permits the increment of the NPs activity. The catalysts performance must be evaluated in a Electrochemical Stress Test for understanding the how the Metal-Support Interaction can influence the NPs stability and prevents the harmful processes as detachments and leaching.

During the 3rd PhD years, Platinum and Palladium yttrium alloy catalysts were synthetized by Laser Ablation in liquid. The exploration of new synthesis route is crucial for resolving the problem of the solid state synthesis. Pt_xY and Pd_xY NPs were successfully synthetized by LASiS. The NPs show an high alloy concentration, the catalysts were tested both in alkaline both in acid electrolyte and show higher performance than the standard Pt/C 50 $\%_{Pt}$ and Palladium benchmark. The main problem in LASiS synthesis is the NPs dimensional control, one way to resolve the problem is used a particular support solutions, such as water/NaCl, water and Sodium Dodecyl sulphate, Ethanol and poly(N-vinylpyrrolidone). For example, using water NaCl, increasing the Sodium Chloride is possible increase the synthesis control on NPs dimension and on their crystallinity. Pt_3Y alloy show the best catalytic activity when the NPs show a size in the range 6 nm – 10 nm, so to complete the panorama the synthesis procedure must be optimized to obtained a narrow dimensional distribution peaked in this range.

12 Appendix

12.1 Congress & Schools

1. EFCS 2019- Electrolysis and fuel Cell Discussion, 15-18 September 2019, La Grande Motte, Montpellier, FR.
    a. Oral Presentation: Pd_3Y alloyed NPs prepared by Laser Ablation: towards zero platinum in PEMFC cathode catalysts; **R. Brandiele**, A. Guadagnini, V. Amendola, G A. Rizzi, A. Gennaro, C. Durante
2. GEI2019, Giornate Italiane Elettrochimica, 8-12 September 2019, Padova (PD), Italy.
    a. Poster Contribution: Mesoporous carbon characterized by different carbon structures and a modulable density of thiophenic groups: effect on platinum NPs activity for oxygen reduction; **R. Brandiele**, M. C. Dalconi, G. A. Rizzi, A. Gennaro and C. Durante.
    b. Poster Contribution: Pd_3Y alloyed NPs prepared by Laser Ablation: towards zero platinum in PEMFC cathode catalysts; **R. Brandiele**, A. Guadagnini, V. Amendola, G A. Rizzi, A. Gennaro and C. Durante.
    c. Poster Contribution: Exploting N-doped carbon spheres for supercapacitors: **R. Brandiele**, C. Durante, F. Poli and F. Soavi.
3. Mastec, Materials for Today's Energy challenge, 3-4 June 2019, Padova, Italy
    a. Poster Contribution: Pd_3Y alloyed NPs prepared by Laser Ablation: towards zero platinum in PEMFC cathode catalysts; **R. Brandiele**, A. Guadagnini, V. Amendola, G A. Rizzi, A. Gennaro, C. Durante.
4. 69th Annual Meeting ISE International Society of Electrochemistry, 2-7 September 2018, Bologna (Italy)
    a. Oral Presentation: Nitrogen Doped Mesoporous Carbons, Prepared from Templating Propylamine Functionalized Silica, as Interesting Material for Supercapacitors; **R. Brandiele**, J. Seri, A. Gennaro, L. Picelli, G. A. Rizzi, F. Soavi and C. Durante.
    b. Poster Contribution: Pt_xY Nanocubes as Electrodic Material for ORR in PEMFC; **R. Brandiele**, G. A. Rizzi, A. Gennaro and C. Durante.
5. International Spring School of Electrochemistry, 19-23 June 2019, Castallammare del Golfo, (TP, Italy).
6. CHESS 2018, Conventional and High Energy Spectroscopies for inorganic, organic and biomolecular surfaces and interfaces, 27-30 November 2018, Florence (FI, Italy).
    a. Poster Contribution: Probing the Correlation between Pt-Support Interaction and Oxygen Reduction Reaction Activity in Mesoporous Carbon material modified with Dichloro(1,10-phenanthroline)platinum(II); **R. Brandiele**, C. Durante , G. A. Rizzi, M. Zerbetto and A. Gennaro.

7. MYCS 2017, 13-15 November 2018, Milano Marittima, Italy
    a. Oral Presentation: New evidences of Pt_xY alloyed NPs formation on carbon support and catalytic activity for ORR; **R. Brandiele**, C. Durante , G. A. Rizzi and A. Gennaro
8. GEI 2018, Giornate Italiane Elettrochimica, 21-25 January 2018 Sestriere (TO), Italy.
    a. Oral Presentation: New evidences of Pt_xY alloyed NPs formation on carbon support and catalytic activity for ORR; **R. Brandiele**, C. Durante, G. A. Rizzi and A. Gennaro
9. ENERCHEM School, 20-24 February 2018, Florence (FI), Italy
    a. Poster Contribution: Nitrogen doped mesoporous carbons, prepared from templating propylamine functionalized silica, as interesting material for supercapacitors; **R. Brandiele**, L. Picelli, G. A. Rizzi, A. Gennaro and C. Durante
10. XXXIX GE-RSEQ & 3rd E3-MS Meeting, 2-5 July 2018, Madrid, Spain.
    a. Oral Presentation: Nitrogen Doped Mesoporous Carbons, Prepared from Templating Propylamine Functionalized Silica, as Interesting Material for Supercapacitors; **R. Brandiele**, J. Seri, A. Gennaro, L. Picelli, G. A. Rizzi, F. Soavi and C. Durante
    b. Poster Contribution: Pt_xY Nanocubes as Electrodic Material for ORR in PEMFC; **R. Brandiele**, G. A. Rizzi, A. Gennaro and C. Durante
11. *SCI* 2017, Società Chimica Italiana 10-14 October 2017 Paestum (SA) Italy
    a. Oral Presentation: New evidences of Pt_xY alloyed NPs formation on carbon support and catalytic activity for ORR; **R. Brandiele**, C. Durante, G. A. Rizzi and A. Gennaro
    b. Poster Contribution: Nitrogen Doped Mesoporous Carbons, Prepared from Templating Propylamine Functionalized Silica, as Interesting Material for Supercapacitors; **R. Brandiele**, J. Seri, A. Gennaro, L. Picelli, G. A. Rizzi, F. Soavi and C. Durante
12. GEI 2016, Giornate Elettrochimica Italiana 11-14 September 2016 Gargnano (BS) Italy
    a. Oral Presentation: One Step forward to a Scalable Synthesis of Platinum-Yttrium alloyed Nanoparticles on Mesoporous Carbon for Oxygen Reduction Reaction**; R. Brandiele**, C. Durante, G. A. Rizzi, G. Granozzi and A. Gennaro
    b. Poster Contribution: Novel Platinum and Palladium Nanoparticles Synthesis on Nitrogen-Doped Mesoporous Carbon for Oxygen Reduction Reaction; **R. Brandiele**, C. Durante and A. Gennaro
13. ENERCHEM1, 18-20 Febbruary 2016 Florence (FI) Italy
    a. Poster Contribution: One Step forward to a Scalable Synthesis of Platinum-Yttrium alloyed Nanoparticles on Mesoporous Carbon for Oxygen Reduction Reaction; **R. Brandiele**, C. Durante, G. A. Rizzi, G. Granozzi and A. Gennaro

12.2 Pubblications

1. R. Brandiele, C. Durante, E. Grądzka, G.A. Rizzi, J. Zheng, D. Badocco, P. Centomo, P. Pastore, G. Granozzi, A. Gennaro, One step forward to a scalable synthesis of platinum–yttrium alloy nanoparticles on mesoporous carbon for the oxygen reduction reaction, J. Mater. Chem. A. 4 (2016) 12232–12240. doi:10.1039/C6TA04498K.
2. R. Brandiele, L. Picelli, R. Pilot, V. Causin, A. Martucci, G.A. Rizzi, A.A. Isse, C. Durante, A. Gennaro, Nitrogen and Sulfur Doped Mesoporous Carbons, Prepared from Templating Silica, as Interesting Material for Supercapacitors, ChemistrySelect. 2 (2017) 7082–7090. doi:10.1002/slct.201701404.
3. T. Gatti, G. Girardi, N. Vicentini, R. Brandiele, M. Wirix, C. Durante, E. Menna, Physico-Chemical, Electrochemical and Structural Insights Into Poly(3,4-ethylenedioxythiophene) Grafted from Molecularly Engineered Multi-Walled Carbon Nanotube Surfaces, J. Nanosci. Nanotechnol. 18 (2018) 1006–1018. doi:10.1166/jnn.2018.15250.
4. R. Brandiele, C. Durante, M. Zerbetto, N. Vicentini, T. Kosmala, D. Badocco, P. Pastore, G.A. Rizzi, A.A. Isse, A. Gennaro, Probing the correlation between Pt-support interaction and oxygen reduction reaction activity in mesoporous carbon materials modified with Pt-N active sites, Electrochim. Acta. 277 (2018) 287–300. doi:10.1016/j.electacta.2018.04.182.
5. M. Miola, X.-M. Hu, R. Brandiele, E.T. Bjerglund, D.K. Grønseth, C. Durante, S.U. Pedersen, N. Lock, T. Skrydstrup, K. Daasbjerg, Ligand-free gold nanoparticles supported on mesoporous carbon as electrocatalysts for CO_2 reduction, J. CO2 Util. 28 (2018) 50–58. doi:10.1016/j.jcou.2018.09.009.
6. G. Daniel, E. Foltran, R. Brandiele, L. Nodari, R. Pilot, E. Menna, G.A. Rizzi, A. Ahmed Isse, C. Durante, A. Gennaro, Platinum-free electrocatalysts for oxygen reduction reaction: Fe-Nx modified mesoporous carbon prepared from biosources, J. Power Sources. 402 (2018) 434–446. doi:10.1016/j.jpowsour.2018.09.060.
7. V. Perazzolo, R. Brandiele, C. Durante, M. Zerbetto, V. Causin, G.A. Rizzi, I. Cerri, G. Granozzi, A. Gennaro, Density Functional Theory (DFT) and Experimental Evidences of Metal–Support Interaction in Platinum Nanoparticles Supported on Nitrogen- and Sulfur-Doped Mesoporous Carbons: Synthesis, Activity, and Stability, ACS Catal. 8 (2018) 1122–1137. doi:10.1021/acscatal.7b03942.
8. R. Brandiele, V. Amendola, A. Guadagnini, G.A. Rizzi, D. Badocco, P. Pastore, A.A. Isse, C. Durante, A. Gennaro, Facile synthesis of Pd_3Y alloy nanoparticles for electrocatalysis of the oxygen reduction reaction, Electrochim. Acta. 320 (2019) 134563. doi:10.1016/j.electacta.2019.134563.
9. R. Brandiele, M. Zerbetto, M.C. Dalconi, G.A. Rizzi, A.A. Isse, C. Durante, A. Gennaro, Mesoporous Carbon with Different Density of Thiophenic-Like Functional Groups and Their Effect on Oxygen Reduction, ChemSusChem. 12 (2019) cssc.201901568. doi:10.1002/cssc.201901568.

10. G. A. Volpato, D. M. Arboleda, R. Brandiele, F. Carraro, G. B. Sartori, A. Cardelli, D. Badocco, P. Pastore, S. Agnoli, C. Durante, V. Amendola, A. Sartorel, Clean rhodium nanoparticles prepared by laser ablation in liquid for high performance electrocatalysis of the hydrogen evolution reaction, ***Nanoscale Adv.***, NA-COM-08-2019-000510, Submitted.

12.3 Seminars

1. Green Shades in Organic Synthesis
   4 July 2019, Prof. Luigi Vaccaro.
2. 60-Fold Ligand Equivalence in the Ubiquitous Cluster of Gold and Related Metals (I-$Au_{144}L_{60}$)
   24 June 2019, prof. L. Whetten
3. A paradigm for the electrocatalytic center through the support interaction
   20 June 2019, prof. N. A. Vante
4. Coordination Self-Assembly From the Origins to the Latest Advances
   31 May 2019, prof. M. Fujita
5. Organic materials for electronics: design by model reduction
   25 June 2019, prof. A. Troisi
6. Earth-abundant nanostructured materials for unconventional solar energy conversion devices
   18 June 2019, Dott. R. Mazzaro
7. Pressure effect on H_2O_2 electrolysis and H_2O and CO_2 co-electrolysis in high temperature
   5 February 2019, prof. F. Mauvy
8. Visualizing and Manipulating On-Surface Chemical Reaction by Atomic Force Microscopy
   19 October 2018, prof. A. Schirmeisen
9. Transmission electron microscopy: future and challenges of microscopy as analytical technique for the characterization of materials
   12 June 2018, Dr. V. Grillo,
10. From Photoinduced Electron Transfer to Charge Accumulation and New Photosensitizers,
    28 October 2017, prof. Wegner,
11. Water- and light-induced surface reactions at the semiconductor/liquid interface probed with ambient pressure photoelectron spectroscopy
    25 October 2017, Dott. M. Favaro,
12. From “free” to “controlled” radical polymerization: How to control macromolecular growth and improve catalyst removal?
    18 Octber2017, Dott. M. Fantin
13. Lectio Magistralis: “My Journey to Stockholm”
    18 December 2017, Prof. Sir Fraser Stoddart
14. Rational design of advanced catalysts for energy conversion
    13 January 2017, Dott. L. Calvillo
15. Stereoselective construction of chiral molecules: photo-organocatalysis, vinylogy and beyond
    13 January 2017, Dott. L. Dell’Amico